# Investigation of the Magnetic Vortex State for Spin-Valve Sensors

Tobias Wurft

Thesis submitted to the Faculty of Physics
of the

**Bielefeld University**

for the doctoral degree in

**Physics**

| | |
|---|---|
| Tutor: | Dr. Wolfgang Raberg |
| Referee: | PD. Dr. Hubert Brückl |
| Referee: | Prof. Dr. Günter Reiss |

Submitted: Munich, 08/27/2018

# Abstract

Many automotive applications, such as wheel speed and current sensing, require magnetic sensors with a large signal range, a negligible small hysteresis and a large linear operating range. All these requirements can be met when using a Tunneling Magnetoresistance (TMR) spin-valve sensor with a free layer (FL) that operates in the vortex state. The magnetic vortex has been intensively studied in the last two decades due to its special static and dynamic properties and promising applications. In the present work, the static properties of the magnetic vortex, especially its critical fields - nucleation field $H_n$ and annihilation field $H_{an}$ - are investigated. These fields are the key parameters regarding its implementation in a sensor. The investigated TMR spin-valve vortex sensor concept has a large potential for commercial use, for example, as speed or current sensor.

Geometrical factors such as diameter $d$ ($0.8 - 4.1\,\mu$m) and thickness $t$ ($10 - 50\,$nm) and the influence of material ($Co_{90}Fe_{10}$, $Co_{60}Fe_{20}B_{20}$, and $Ni_{81}Fe_{19}$) in circular, disk-shaped FL elements are investigated experimentally and compared to micro-magnetic simulations. The initially expected universal scaling of $H_n$ with the aspect ratio $\frac{d}{t}$ is only observed if exceeding a certain FL thickness. It is shown for a certain diameter of 1.1 µm that only above $t = 35\,$nm the stray field energy of the saturated disk drastically increases with thickness, following a linear trend as a function of $t$. This effect is linked to a significant increase of the out-of-plane magnetization at the edge of the disk with increasing thickness below $t = 35\,$nm. Phase diagrams of magnetic states - as a function of $t$ and $d$ - are extracted from micro-magnetic simulations and give information about the occurrence of different pre-vortex states. The results are consistent with experimentally observed phase transitions and allow the conclusion that for a $Co_{60}Fe_{20}B_{20}$ thickness of 20 nm the S-state delays vortex nucleation. The formation of the double vortex (DV) state is only observed for $t = 35$ and 50 nm as the formation probability increases with increasing $t$. The DV is causing a delay of the single vortex nucleation, like the S-state. It is shown that the magneto-crystalline anisotropy of $Co_{90}Fe_{10}$ is not only causing a delay of vortex nucleation but can also lead to a drastic increase of the stability of the DV as well as to the formation of hysteretic states with even more than two vortex cores. Moreover, it is demonstrated that the critical fields are also sensitive to the properties of the edge of the FL: a magnetically disturbed edge and a sloped edge lead to a drastic reduction of $H_{an}$ and edge roughness may favor or avoid the formation of intermediate states which affects $H_n$ and its distribution. In addition, a reduced change in TMR signal during vortex annihilation is observed for $Co_{90}Fe_{10}$. This effect can be explained by the introduction of an electrically inactive area at the edge of the FL.

Extrinsic factors such as temperature and magnetic bias fields are studied in terms of how they shift $H_n$ and $H_{an}$. At elevated temperatures the $H_n$ shift ($\mathit{\Delta} H_n$) is always smaller than the temperature-induced reduction of the saturation magnetization ($M_s$). For $t = 20\,\mathrm{nm}$, thermally assisted energy barrier jumps even become dominant. Thus, on average vortex nucleation is observed earlier if the temperature is raised from 35 to 150 °C. Furthermore, individual elements show in principle negative as well as positive $\mathit{\Delta} H_n$ values, depending on whether or not energy barriers delay vortex nucleation at 35 °C. Temperature-induced $H_{an}$ shifts ($\mathit{\Delta} H_{an}$) are on average always negative but individual $Co_{90}Fe_{10}$ elements also show positive values which are expected to be linked to the direction of rotation of the vortex state. For $t = 20\,\mathrm{nm}$, the average $\mathit{\Delta} H_{an}$ is almost exclusively caused by the reduction of $M_s$. For $t = 35$ and $50\,\mathrm{nm}$, the influence of thermally assisted energy barrier jumps on $H_n$ increases. Surprisingly, additionally applied in-plane bias fields, perpendicular to the field of the hysteresis loop, can facilitate vortex nucleation significantly. Three different explanations are found, depending on $t$ and the choice of material: (1) reduction of the magneto-crystalline coercivity, (2) reduction of the configurational stability, or (3) an increase of the number of possible vortex nucleation sites. For $t = 20\,\mathrm{nm}$ $Co_{90}Fe_{10}$, an average $\mathit{\Delta} H_n$ of almost 14 % is observed when applying a bias field of $H_y = 80\,\mathrm{Oe}$. For such a bias field, no positive average shifts are observed for $Co_{60}Fe_{20}B_{20}$ but individual elements show both positive and negative shifts.

# Zusammenfassung

Viele Automobilanwendungen wie zum Beispiel Raddrehzahl- und Strommessung erfordern Magnetsensoren mit einem großen Signalbereich, einer vernachlässigbar kleinen Hysterese, sowie einem großen linearen Betriebsbereich. All diese Anforderungen können erfüllt werden, wenn ein Tunnel-Magnetoresistiver (TMR) Spin-Valve Sensor verwendet wird, dessen sensitives Element (FL) sich im Vortex-Zustand befindet. Der magnetische Vortex wurde in den letzten zwei Jahrzehnten aufgrund seiner speziellen statischen und dynamischen Eigenschaften sowie den sich daraus ergebenden vielversprechenden Anwendungsaspekten intensiv untersucht. In der vorliegenden Arbeit werden die statischen Eigenschaften analysiert, insbesondere die kritischen Felder - das Nukleationsfeld ($H_n$) und das Annihilationsfeld ($H_{an}$). Diese Parameter spielen eine Schlüsselrolle bei der Umsetzung eines solchen Sensorkonzeptes. Dem untersuchten Vortex-Sensorkonzept wird ein sehr großes Potential hinsichtlich einer kommerziellen Anwendung als beispielweise Drehzahl- oder Stromsensor zugeschrieben.
Geometrische Faktoren wie Durchmesser $d$ ($0.8 - 4.1\,\mu m$) und Schichtdicke $t$ ($10 - 50\,nm$) sowie der Einfluss des verwendeten Materials ($Co_{90}Fe_{10}$, $Co_{60}Fe_{20}B_{20}$ und $Ni_{81}Fe_{19}$) wird an scheibenförmigen, kreiszylindrischen FL-Elementen (Disks) experimentell untersucht und mit mikromagnetischen Simulationen verglichen. Das anfänglich erwartete, universelle Skalieren von $H_n$ mit dem Aspektverhältnis $\frac{d}{t}$ wird nur beobachtet, wenn eine gewisse Schichtdicke überschritten wird. Für einen Durchmesser von $1.1\,\mu m$ ist zu beobachten, dass nur für $t > 35\,nm$ die Streufeldenergie der gesättigten Disk drastisch ansteigt und einen linearen Trend als Funktion von $t$ beschreibt. Diese Beobachtung ist verknüpft mit dem Effekt, dass für $t < 35\,nm$ am Rand der Disk ein deutlicher Anstieg der Magnetisierungskomponente senkrecht zur Schicht mit zunehmender Schichtdicke festgestellt werden kann. Phasendiagramme der magnetischen Zustände - als Funktion von $d$ und $t$ - werden mit Hilfe von mikromagnetischen Simulationen ermittelt und geben Auskunft über das Auftreten von verschiedenen Vorzuständen. Die Ergebnisse decken sich mit den experimentell beobachteten Phasenübergängen und lassen den Rückschluss zu, dass für $Co_{60}Fe_{20}B_{20}$ bei einer Schichtdicke von $20\,nm$ der S-Zustand die Nukleation des Vortex verzögert. Die Bildung des Doppel-Vortex (DV) wird nur beobachtet für $t = 35$ und $50\,nm$. Dabei nimmt die Wahrscheinlichkeit der DV-Bildung mit zunehmender Schichtdicke zu. Der DV verzögert die Nukleation des Vortex-Zustandes mit nur einem Kern, ähnlich wie der S-Zustand. Es wird außerdem gezeigt, dass die magnetokristallinen Eigenschaften von $Co_{90}Fe_{10}$ nicht nur eine Verzögerung der Vortex-Nukleation verursachen, sondern auch teilweise die Stabilität des DV drastisch erhöhen, sowie zur Bildung von Mag-

netisierungszuständen mit mehr als zwei Vortex-Kernen führen können. Darüber hinaus wird erörtert, wie empfindlich die kritischen Felder gegenüber den Eigenschaften des Randes der Disk sind: Ein magnetisch geschwächter Rand ebenso wie ein schräger Rand führen zu einer drastischen Reduktion von $H_{an}$. Dagegen beeinflusst die Randrauigkeit $H_n$ sowie dessen Verteilung, indem die Bildung von Zwischenzuständen begünstigt oder verhindert wird. Eine reduzierte Änderung des TMR-Signals wird darüber hinaus bei $Co_{90}Fe_{10}$ während der Vortex-Annihilation beobachtet. Dieser Effekt ist erklärbar durch die Annahme, dass ein gewisser Bereich des Randes nicht zum elektrischen Signal beiträgt. Der Einfluss äußerer Faktoren wie Temperatur und zusätzlicher, konstanter magnetischer Felder wird untersucht, indem die Verschiebung von $H_n$ und $H_{an}$ statistisch analysiert wird. Bei einer Erhöhung der Temperatur ist die Änderung von $H_n$ ($\mathit{\Delta} H_n$) immer geringer als die temperaturbedingte Reduktion der Sättigungsmagnetisierung ($M_s$). Für $t = 20\,\mathrm{nm}$ überwiegt sogar der Einfluss der thermischen Anregung hinsichtlich des Überwindens vorhandener Energiebarrieren. Folglich ist im Mittel eine frühere Vortex-Nukleation zu beobachten, wenn die Temperatur von 35 auf 150 °C erhöht wird. Außerdem sind bei einzelnen Elementen prinzipiell positive wie negative $\mathit{\Delta} H_n$ Werte zu beobachten, je nachdem ob potentielle Energiebarrieren die Nukleation bei 35 °C verzögern. Die temperaturbedingte Verschiebung von $H_{an}$ ($\mathit{\Delta} H_{an}$) ist im Mittel immer negativ, aber einzelne $Co_{90}Fe_{10}$ Elemente können auch positive Werte aufweisen. Diese Beobachtung ist vermutlich auf eine Umkehrung des Drehsinns des Vortex-Zustandes zurückzuführen. Für $t = 20\,\mathrm{nm}$ ist $\mathit{\Delta} H_{an}$ beinahe ausschließlich auf eine Reduktion von $M_s$ zurückzuführen. Für $t = 35$ und $50\,\mathrm{nm}$ nimmt der Einfluss der thermischen Anregung auf die Überwindung der Annihilationsenergiebarriere zu. Überraschenderweise kann die Vortex-Nukleation erheblich begünstigend beeinflusst werden, wenn ein zusätzliches, konstantes Bias-Feld angelegt wird, welches senkrecht zum Feld der Hystereseschleife, aber in der Schichtebene ausgerichtet ist. Drei unterschiedliche Erklärungen sind festzustellen, abhängig von Schichtdicke und Material: (1) Die Reduktion der magnetokristallinen Koerzitivität, (2) die Reduktion der Stabilität des Vorzustandes oder (3) die Erhöhung der Anzahl potentieller Nukleationskeime. Für $Co_{90}Fe_{10}$ ist bei einer Schichtdicke von 20 nm eine positive Verschiebung des Nukleationsfeldes um beinahe 14 % zu beobachten, wenn ein Bias-Feld mit 80 Oe Feldstärke angelegt wird. Bei $Co_{60}Fe_{20}B_{20}$ sind bei einer solchen Feldstärke im Mittel keine positiven Werte für $\mathit{\Delta} H_n$ zu beobachten, einzelne Strukturen zeigen jedoch ebenfalls positive Verschiebungen.

# Danksagung

Ohne die Unterstützung zahlreicher Personen wäre diese Arbeit niemals möglich gewesen. Ich möchte mich an dieser Stelle für diese Hilfe herzlichst bedanken. Dabei werde ich im Folgenden versuchen, möglichst alle Personen namentlich zu nennen, die mich auf vielfältige Art und Weise unterstützt, inspiriert und motiviert haben.

Anfangen möchte ich bei **Dr. Wolfgang Raberg** für die ausgezeichnete Betreuung. Er hatte immer ein offenes Ohr für Fragen oder Ideen, die gemeinsamen Diskussionen waren äußerst fruchtbar und seine Korrekturen stets hilfreich. Darüber hinaus hat er mich zu Beginn meiner Arbeit bei Messungen im Labor unterstützt und auch immer ein gutes Gefühl dafür gehabt, mich zu motivieren und, wenn nötig, weiter anzutreiben. Das Thema dieser Arbeit wäre so nicht zu Stande gekommen ohne die Vorarbeit von **PD Dr. Hubert Brückl** und **Ass.-Prof. PD Dr. Dieter Suess**. Ich möchte mich darüber hinaus bei **PD Dr. Hubert Brückl** für die erstklassige fachliche Betreuung bedanken sowie für die ausgiebige Zeit, die er aufgewendet hat für die gemeinsamen Diskussionen, den vielseitigen Input und die umfassenden Korrekturen von Manuskripten. **Prof. Dr. Günter Reiss** danke ich aufs herzlichste für die ebenfalls erstklassige fachliche Betreuung sowie seinem Lehrstuhl, der meinen fünfmonatigen Aufenthalt in Bielefeld zu etwas Besonderem gemacht hat.

Einen besonderen Dank möchte ich auch an **Dr. Sebastian Luber** aussprechen. Er hat mir meine Doktorandenstelle bei Infineon, in einem großartigen Team mit netten Kollegen, erst ermöglicht und war darüber hinaus auch immer ein exzellenter Ansprechpartner bei fachlichen Themen. Ohne die fachliche Expertise von **Dr. Klemens Prügl** wäre die Abscheidung der untersuchten TMR Strukturen nicht möglich gewesen. **Dr. Milan Agrawal** gebührt mein größter Dank für die Unterstützung im Labor, das Vorantreiben der Messmöglichkeiten und die Geduld beim Lösen von Problemen im Zusammenhang mit neuen Messroutinen. Beim verwendeten experimentellen Aufbau ist außerdem die Arbeit von **Markus Eckinger** nicht wegzudenken. **Dr. Jürgen Zimmer** hat mich zu Beginn meiner Arbeit in die mikromagnetischen Simulationen eingeführt und war immer ein äußerst kompetenter Ansprechpartner, wenn es um die Interpretation der Simulationen ging. Die zahlreichen Workshops, die von **Dr. Armin Satz** organisiert wurden, waren immer eine Inspiration. Es war äußerst motivierend, im Rahmen dieser Workshops einer interessierten Gruppe über den aktuellen Stand der Arbeit zu berichten sowie die unterschiedlichsten Aspekte und Themen auch noch am Abend beim gemeinsamen Essen mit den anderen Workshop-Teilnehmern zu diskutieren. Bei **Gerd Wetzig** möchte ich mich vielmals für sein handwerkliches Geschick und seine Unterstützung im Labor bedanken. Die Mitbetreuung der Masterarbeit von **Christoph Durner** hat mir immer sehr viel Spaß gemacht und die gemeinsamen Diskussionen haben mich auch bei meiner Arbeit weitergebracht. Mich freut insbesondere, dass der *Kraken* dank **Clemens Mühlenhoff** weiterleben wird. Außerdem konnte ich zum passenden Zeitpunkt, gegen Ende meiner Arbeit, einige Arbeitsthemen an ihn abgeben und danke ihm dafür vielmals. Die Gespräche mit **Dr. Thorsten Reichert** zur allgemeinen Planung meiner Doktorarbeit, bei einer Tasse Kaffee oder einer Joggingrunde durch den Perlacher Forst, haben mich immer wieder zusätzlich angetrieben. **Naciye Karakoc** war immer für einen da, zum Beispiel wenn es einen Konferenzbesuch zu planen galt oder der Umzug nach Bielefeld zu organisieren war.

**PD Dr. habil. Dmitry Berkov** hat mich bei besonderen Anliegen und Rückfragen zu MicroMagus unterstützt. **Dr. Anton Bachleitner-Hofmann** gilt mein Dank für die Zusammenarbeit und geteilte Expertise bei den mikromagnetischen Simulationen. Außerdem danke ich **Herbert Weitensfelder** für die fachliche Unterstützung und seine Gastfreundschaft während meiner Aufenthalte in Wiener Neustadt. Danke für die produktive und gleichzeitig schöne Zeit dort und in Wien. Die gezeigten SMRM und MFM Aufnahmen wurden an der Universität Augsburg durchgeführt. Für die entsprechenden Ressourcen möchte ich mich bei **Prof. Dr. Manfred Albrecht** bedanken, außerdem bei **Michael Heigl** für die Unterstützung bei den Messungen am SMRM. Mein besonderer Dank geht an **Dr. Dmitriy Mitin** für seinen Einsatz, seine Geduld bei den unzähligen Anläufen, seine Unterstützung bei der Interpretation der SMRM Daten und die gemeinsame Zeit nach getaner Arbeit.

Ohne die vielseitige Unterstützung von **Dr. Alexander Böhnke** wäre meine Zeit in Bielefeld bestimmt nicht so reibungslos verlaufen. **Dr. Torsten Hübner** danke ich ebenfalls für seine Hilfsbereitschaft beim Querlesen des Manuskripts. Des Weiteren war mir **Aggi Windmann** eine große Unterstützung bei der Planung des Rahmenprogramms der Verteidigung.

Während der Doktorandenzeit haben sich Freundschaften mit "Leidensgenossen" gebildet, die auch die ein oder andere Durststrecke erträglicher gemacht haben. Daher möchte ich mich bei **Katja Puschkarsky**, **Bernd Waschneck**, **Jonas Kammerer** und **Michael Ammer** bedanken. Für die gemütlichen Runden am Abend, die gemeinsamen Boulder-Sessions und die Beachvolleyball-Spiele.

Bei den Sprachkorrekturen haben mich neben **Saskia Tremmel** auch **Marlies Tremmel** und **Sylvester Tremmel** tatkräftig unterstützt. Danke für diesen Einsatz sowie für die Geduld und die Ausdauer. Meinen **Eltern** möchte ich danken für ihre allzeit offene Tür, für ihre unkomplizierte, liebevolle Art und natürlich auch für die finanzielle Unterstützung während des Studiums. Meiner **Schwester** danke ich schlicht dafür, dass sie da ist und mit mir immer genauso gerne Zeit verbringt, wie ich mit ihr. Mein abschließender Dank geht an **Saskia**, die mich immer unterstützt und motiviert hat. Selbst wenn die Arbeit wieder einmal kein Ende zu nehmen schien, hat sie mit mir zusammen bis in die Morgenstunden durchgehalten.

# Erklärung zur Verfassung der Arbeit

Hiermit erkläre ich, dass mir die geltende Promotionsordnung der Fakultät für Physik der Universität Bielefeld vom 10. Januar 2012 bekannt ist und dass ich die vorliegende Dissertation selbstständig verfasst habe. Ich habe keine Textabschnitte von Dritten oder eigener Prüfungsarbeiten ohne Kennzeichnung übernommen und alle benutzten Hilfsmittel und Quellen in der Arbeit angegeben. Dritte haben weder unmittelbar noch mittelbar geldwerte Leistungen von mir für Vermittlungstätigkeiten oder für Arbeiten erhalten, die im Zusammenhang mit dem Zustandekommen oder dem Inhalt dieser Dissertation stehen. Diese Dissertation oder wesentliche Teile davon wurden nicht als Prüfungsarbeit für eine staatliche oder andere wissenschaftliche Prüfung eingereicht. Außerdem wurde weder diese Arbeit, noch eine in wesentlichen Teilen ähnliche oder eine andere Abhandlung bei einer anderen Hochschule als Dissertation eingereicht.

München, 27.08.2018 Tobias Wurft

# Contents

# Symbols and Acronyms

| | |
|---|---|
| $A$ | Exchange stiffness constant |
| **AFM** | Antiferromagnet |
| **AMR** | Anisotropic magnetoresistance |
| **CL** | Coupling layer |
| $d$ | Disk diameter |
| $D_{\mathbf{grain}}$ | Average crystal grain size |
| **DUT** | Device under test |
| **DV** | Double vortex |
| $E_{\mathbf{aniso}}$ | Magneto-crystalline anisotropy energy |
| $E_{\mathbf{demag}}$ | Stray field energy |
| $E_{\mathbf{exch}}$ | Exchange stiffness energy |
| $E_{\mathbf{Zeeman}}$ | Zeeman energy |
| $E_{\mathbf{tot}}$ | Total energy of a magnetic body ($E_{\mathrm{aniso}}+E_{\mathrm{demag}}+E_{\mathrm{exch}}+E_{\mathrm{Zeeman}}$) |
| **FL** | Free layer |
| **FM** | Ferromagnet |
| **GMR** | Giant magnetoresistance |
| $H_0$ | $H_{\mathrm{ext}}$ below which the vortex state is energetically favorable |
| $H_{an}$ | Vortex annihilation field |
| $H_{an+}$ | Vortex annihilation field for $H_{\mathrm{ext}}= H_x > 0$ |
| $H_{an-}$ | Vortex annihilation field for $H_{\mathrm{ext}}= H_x < 0$ |
| $\varDelta H_{an}$ | Shift of $H_{an}$ |
| $H_{\mathbf{coll}}$ | $H_{\mathrm{ext}}$ below which the uniformly magnetized state becomes unstable |
| $H_{\mathbf{crit}}$ | Vortex critical fields $H_n$ and $H_{an}$ |

| | |
|---|---|
| $H_{\mathbf{demag}}$ | Stray or demagnetizing field |
| $H_{\mathbf{ext}}$ | External magnetic field |
| $H_{\mathbf{form}}$ | Formation field of an arbitrary magnetic state |
| $H_n$ | Vortex nucleation field |
| $H_{n+}$ | Vortex nucleation field subsequent $H_{an+}$ |
| $H_{n-}$ | Vortex nucleation field subsequent $H_{an-}$ |
| $\mathit{\Delta} H_n$ | Shift of $H_n$ |
| $H_x$ | $\hat{x}$-component of $H_{\text{ext}}$ |
| $H_y$ | $\hat{y}$-component of $H_{\text{ext}}$ |
| $H_z$ | $\hat{z}$-component (out-of-plane) of $H_{\text{ext}}$ |
| $K_1$ | Uniaxial magneto-crystalline anisotropy constant |
| $\vec{M}$ | Magnetization |
| $\vec{m}$ | Normalized magnetization: $\vec{m} = \frac{\vec{M}}{M_s}$ |
| **MFM** | Magnetic force microscopy |
| $M_s$ | Saturation magnetization |
| **MTJ** | Magnetic tunnel junction |
| $m_x$ | $\hat{x}$-component of $\vec{m}$ |
| $m_y$ | $\hat{y}$-component of $\vec{m}$ |
| $m_z$ | $\hat{z}$-component (out-of-plane) of $\vec{m}$ |
| $\hat{n}$ | Surface normal |
| $n^*$ | Undulation number of a buckling state |
| **RKKY** | Ruderman-Kittel-Kasuya-Yosida |
| **PL** | Pinned layer |
| $r$ | Aspect ratio ($\frac{d}{t}$) |
| **RL** | Reference layer |
| **RVM** | Rigid vortex model |
| **SAF** | Synthetic antiferromagnet |
| **SEM** | Scanning electron microscopy |

| | |
|---|---|
| **SMRM** | Scanning magnetoresistive microscopy |
| $t$ | Film thickness of the free layer (disk thickness) |
| $T$ | Temperature |
| **TB** | Tunnel barrier |
| $T_C$ | Curie temperature |
| **TEM** | Transmission electron microscopy |
| **TMR** | Tunneling magnetoresistance |

# 1 Introduction

In the automotive industry, magnetic sensors are widely used for various applications, such as angle, speed, position or current sensing [1–6]. Speed sensors, for example, are used to measure crankshaft speed, camshaft position, transmission speed, transfer case speed, and wheel speed. Until 2016, Infineon Technologies AG sold over two billion of integrated magnetic sensors [7], which are based on the Hall effect [8] or giant magnetoresistance (GMR) effect [9, 10]. At the same time, the magnetoresistive (MR) sensors achieve a better performance from generation to generation. The rapid development of magnetoresistive (MR) sensors started with the discovery of the GMR effect in 1988 [10]. Its fast implementation into hard disk drives gave the impulse for a new field of research: spintronics [11]. The GMR effect enabled much higher signals compared to the Hall sensor. First generations of automotive MR sensors also utilized the anisotropic magnetoresistance (AMR) effect [2, 6]. Today, AMR sensors are still important due to their stability over field[1]. GMR spin-valve sensors and AMR sensors exhibit signal ranges of typically a few percent (AMR) up to approximately 10 % (GMR spin-valve) at ambient temperature. The tunneling magnetoresistance (TMR) allows for resistance changes of several hundred percent [14]. In addition, TMR sensors have a low power consumption as well as wider air gap ranges as a result of the higher signal [15]. Currently (2018), several manufacturers have announced to enter or have already entered the market of automotive/industrial TMR sensors [16–19].

However, signal amplitude is not the only decisive parameter. Stability over field and performance of the sensing layer are just as important, where the term *performance* includes factors such as hysteresis, linearity and operating field range. The proposed magnetic vortex sensor concept [20] allows to adjust the operating field range and shows a large linear range with almost zero hysteresis at the same time. Thus, it provides superior properties for the next generation automotive sensing technology. The magnetic vortex is defined by an in-plane circular closed flux magnetization with a vortex core where the magnetization is pointing out-of-plane.

The next sections will give a brief introduction into the automotive applications of MR sensors based on the example of wheel speed sensing. Furthermore, the advantages of the magnetic vortex are presented as well as which requirements must be met to enable its application.

---

[1] The AMR effect is an intrinsic property of a bulk ferromagnetic material already discovered in 1856 [12], whereas the GMR and the TMR [13] are interfacial effects and occur, for example, in a layer stack.

## 1.1 Magnetoresistive Sensors in Automotive Applications - Example Wheel Speed Sensing

GMR and TMR sensors are typically implemented by using a so-called spin-valve structure. The characteristic feature of a spin-valve is its change of resistance with the changing angle/uniformity of the magnetization [21]. Spin-valve sensors can be used, for example, to sense current [22, 23], angle [24] or wheel speed [2–4].

The wheel speed sensing principle is illustrated in Figure 1.1a: The sensor consists of two spatially separated sensor cells (the distance between the sensor cells is typically in the range of a few millimeters) and is mounted at a fixed distance of only a few millimeters to a magnet wheel. Each sensor cell consists of two spin-valve resistors (green elements) arranged as a Wheatstone bridge (see also [2]), which allows to measure a field difference between the locations of the two sensor cells and suppresses external homogeneous magnetic disturbance fields. In the example, a constant current $I$ is supplied and the differential voltage $V$ is measured. All spin-valve resistors are sensitive to the $\hat{x}$-component of the magnetic field generated by the magnet wheel. Sensor cell 1 is exposed to a magnetic field pointing in $+\hat{x}$-direction and sensor cell 2 is exposed to a magnetic field pointing in $-\hat{x}$-direction which results in a non-zero voltage signal $V$. During a rotation of the magnet wheel, $V$ reverses its polarity with each pole segment, thus allowing to measure the rotation of the wheel and therefore its speed.

The application of such a speed sensor as a wheel speed sensor is illustrated in Figure 1.1b. The signal of the sensor is used, for example, for the anti-lock braking system (ABS) or for the electronic stability program (ESP). Such applications demand the highest reliability. For example, the presence of potential magnetic disturbance fields must not affect the sensor performance (e.g. by causing hysteresis).

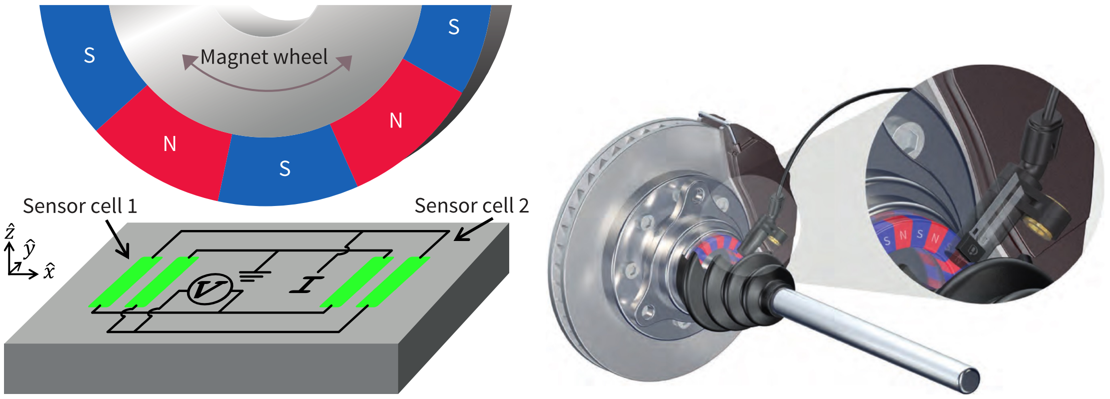

(a) (b)

**Figure 1.1.** (a) Speed sensor principle in combination with an encoder wheel (adapted from [7], 2016). Sensor is sensitive to the $\hat{x}$-component of the magnetic field. Drawing is not in scale, the sensor is shown magnified. (b) Application as wheel speed sensor (taken from [7], 2016).

## 1.2 Motivation and Outline

MR sensors typically use sensing elements - so-called *free layer* (FL) - with a thickness in the range of nanometers where the shape anisotropy of the FL is often utilized to adjust the sensitivity and linear range of the sensor [25, 26]. Further linearization techniques are possible, such as crossed anisotropies, perpendicular anisotropy, external bias fields or weakly pinned sensing layers [25]. The vortex sensor concept differs from all these concepts since any biasing or anisotropy of the FL is unwanted. A circular-shaped FL avoids any in-plane shape anisotropy and therefore facilitates vortex nucleation isotropically. A detailed introduction into the vortex state and its properties is given in the next chapter. In the following, a brief overview of the technologically interesting aspects is given.
Figure 1.2a shows the hysteresis loop of a vortex sensor in a field range in which the signal is almost perfectly linear: for small fields - compared to the saturation field - the magnetization is directly proportional to the applied field [27] and thus a technically attractive linear signal is observed.
Usually, one remaining drawback of MR sensors - compared to Hall sensors - is the inherent hysteresis of the sensing layer. When, for example, the shape anisotropy is used for the linearization of the signal two different, energetically equivalent ground states exist, if the element is mirror-symmetrical and no additional anisotropies are present. Consequently, magnetic switching is possible if magnetic disturbance fields are present, what in turn causes unwanted noise of the sensor [28]. A particularly interesting feature of the vortex state is the (theoretical) absence of hysteresis: as long as no annihilation of the vortex state occurs all remagnetization processes are in principle reversible[2], at least for amorphous materials. The term *annihilation* describes the irreversible transition from the vortex state to the saturated state. Furthermore, switching of the vortex state is only

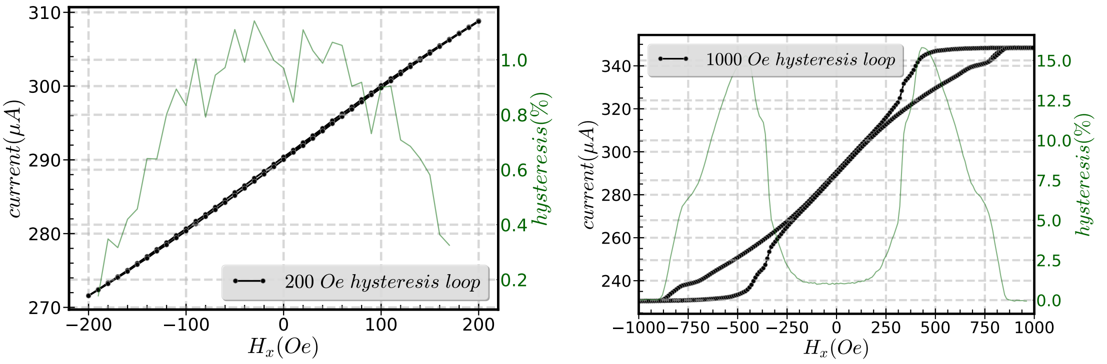

**(a)** **(b)**

**Figure 1.2.** (a) Hysteresis loop of a vortex sensor for ±200 Oe field range. The sensor consists of 1170 TMR spin-valves with circular-shaped CoFeB free layers (diameter 1.1 µm and thickness 50 nm). (b) Hysteresis loop of the same sensor up to saturation of the free layer.

---

[2] The remaining hysteresis observed in Figure 1.2a may also be caused by the core hysteresis of the measurement setup.

possible via annihilation. Under normal operating conditions an annihilation of the vortex state is not expected to occur. Figure 1.2b shows the hysteresis loop of the same vortex sensor, but now saturation and thus annihilation is reached. A further, highly interesting property of the vortex state is visible here: after vortex annihilation has been occurred the formation of the vortex state - also called *nucleation* - is already observed before field sign reversal and thus again almost zero hysteresis is measured around zero field in the linear range. In the example, almost all elements are expected to be in the vortex state when the hysteresis plateau has been reached (at approximately 100 Oe). Consequently, the vortex *nucleation field* $H_n$ is another key parameter when considering the vortex state in sensor application. Therefore, $H_n$ is the main subject of this work.

The magnetic vortex, its required conditions for nucleation, and its properties are explained in Chapter 2. In Chapter 3, an introduction into the vortex sensor concept is given and the experimental approach is introduced. Chapter 4 discusses how the intrinsic factors of the sensing element affect the vortex state, including the lateral dimension of the patterned disk structures, film thickness, free layer material and process influence. There are certain challenges regarding the automotive qualification of a sensor, especially the harsh extrinsic environment conditions in terms of temperature budget ($-40\,°\mathrm{C}$ up to $150\,°\mathrm{C}$) and magnetic field ranges (air-gap range up to 4.5 mm) [29]. The corresponding investigations of the influence of temperature and of applied magnetic bias fields are discussed in Chapter 5.

# 2 The Magnetic Vortex

In this work, the magnetic behavior of ferromagnetic right circular cylindrical elements - as illustrated in Figure 2.1a - was investigated. The dimensions of the experimentally investigated elements ranged from $d = 0.8\,\mu\text{m}$ to $4.1\,\mu\text{m}$ and $t = 10\,\text{nm}$ to $50\,\text{nm}$. Additional numerical micro-magnetic simulations covered an even larger range. Since $d \gg t$, the term *disk* is used to describe the elements. Within the specified dimension range the vortex state is the magnetic ground state. This state is characterized by its closed flux magnetization as shown in Figure 2.1b. Figure 2.1c shows how the center of the vortex is shifted when a magnetic in-plane field is applied: in the example the magnetic field

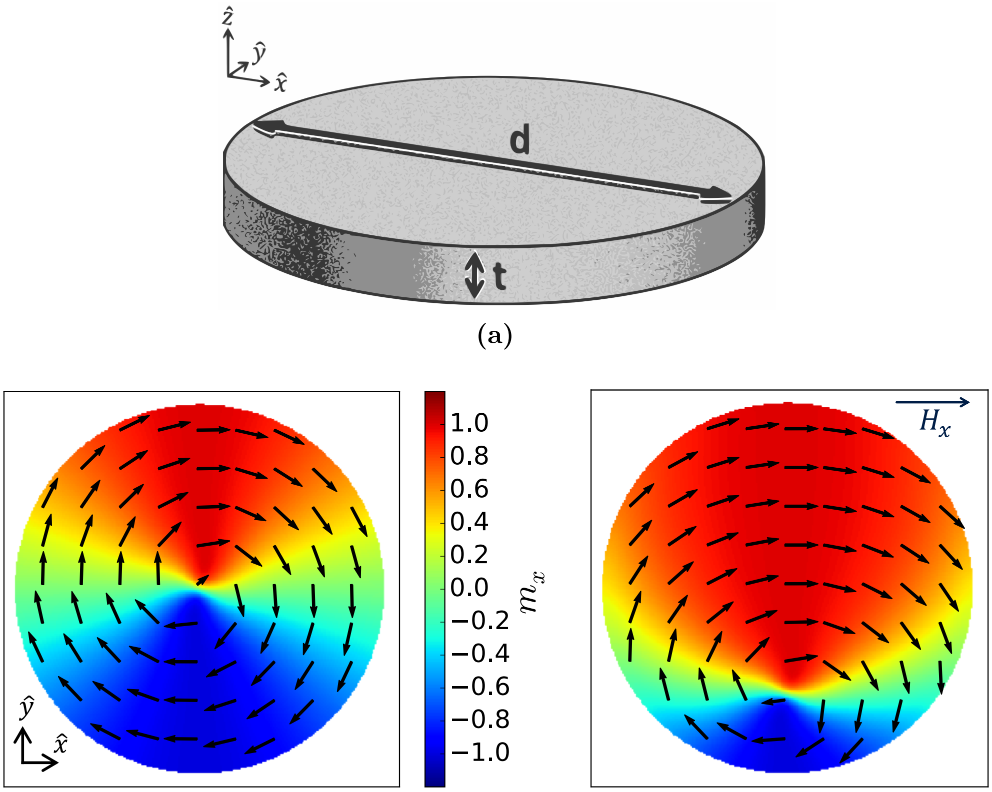

(a)

(b)

(c)

**Figure 2.1.** (a) Right circular cylinder with diameter $d$ and thickness $t$. (b) Simulated in-plane magnetization of the vortex state in such a cylindrical, disk-shaped element ($d = 400\,\text{nm}$ and $t = 50\,\text{nm}$), at zero field. (c) Simulated in-plane magnetization for an applied magnetic in-plane field in $\hat{x}$-direction ($H_x$). Standard simulation parameters for NiFe are given in Section 3.3.

($H_x$) is aligned parallel to the $\hat{x}$-axis. As a result, the portion of the red area - where the magnetization is pointing to the right side - increases and thus a shift of the center of the vortex in negative $\hat{y}$-direction is observed.

In this chapter, the properties of the magnetic vortex will be introduced. Furthermore, an overview of its various aspects and fields of research will be given. The energy analysis of the vortex state will set the base for the interpretation of the results of this work.

## 2.1 Properties of the Magnetic Vortex

In the introduction of this chapter the in-plane configuration of the vortex state was described. The questions that now arise are: why does the vortex state form and what happens in the center of this configuration? These two questions are interlinked. The reason for the formation of the vortex state (**nucleation**) is its negligibly small stray field: Figure 2.2a shows that at zero field the magnetization has an out-of-plane component only in the center of the disk. Furthermore, the parallel alignment at the edge/side surface of the disk leads to a circular magnetization. Consequently, only in the center of the disk the magnetization has a component that is perpendicular to the surface of the element and thus magnetic surface charges - which create the magnetic stray field of the element - are only present here. A detailed discussion of the energetics of a ferromagnetic body in general, and applied to disk-shaped elements, is given in Section 2.3.1.

A detail view of the vortex core, which is defined by its distinct out-of-plane magnetization, is shown in Figure 2.2b. In this illustration, the individual simulation grid cells, which have an in-plane dimension of approximately 1.7 nm × 1.7 nm, are visible. The area

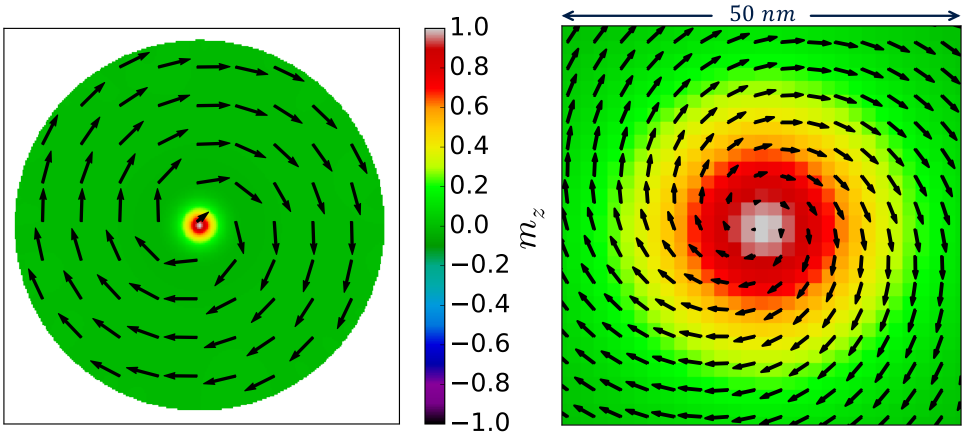

(a) (b)

**Figure 2.2.** (a) Simulated out-of-plane magnetization ($m_z$) - at the disk surface - of the vortex state shown in Figure 2.1b. (b) Square-shaped detail view of the vortex core. Disk dimensions and simulation parameters are given in the caption of Figure 2.1.

where mainly an out-of-plane magnetization is present ($m_z > 0.5$) has a diameter of approximately 20 nm and defines the vortex core. In the region of the vortex core the magnetization is not only rotating in-plane but also rotating out-of-plane, also visible by the plotted vectors, which represent the orientation and magnitude of $\vec{m}$, projected into the $\hat{x}$-$\hat{y}$ plane. The out-of-plane rotation of the magnetization extends across the whole thickness and is limited to one direction within one state. In general, the two equivalent vortex core polarities - up and down - together with two equivalent senses of rotation allow four possible vortex configurations.

Figure 2.3a shows simulated hysteresis loops of disk-shaped elements where the magnetic field ($H_x$) is gradually reduced from 800 to $-800$ Oe and subsequently gradually increased up to again 800 Oe as indicated by the arrows. A main characteristic of the vortex state is evident: the central part of the loops is free of hysteresis. This characteristic feature is also the driving factor for the investigation of the vortex state regarding its

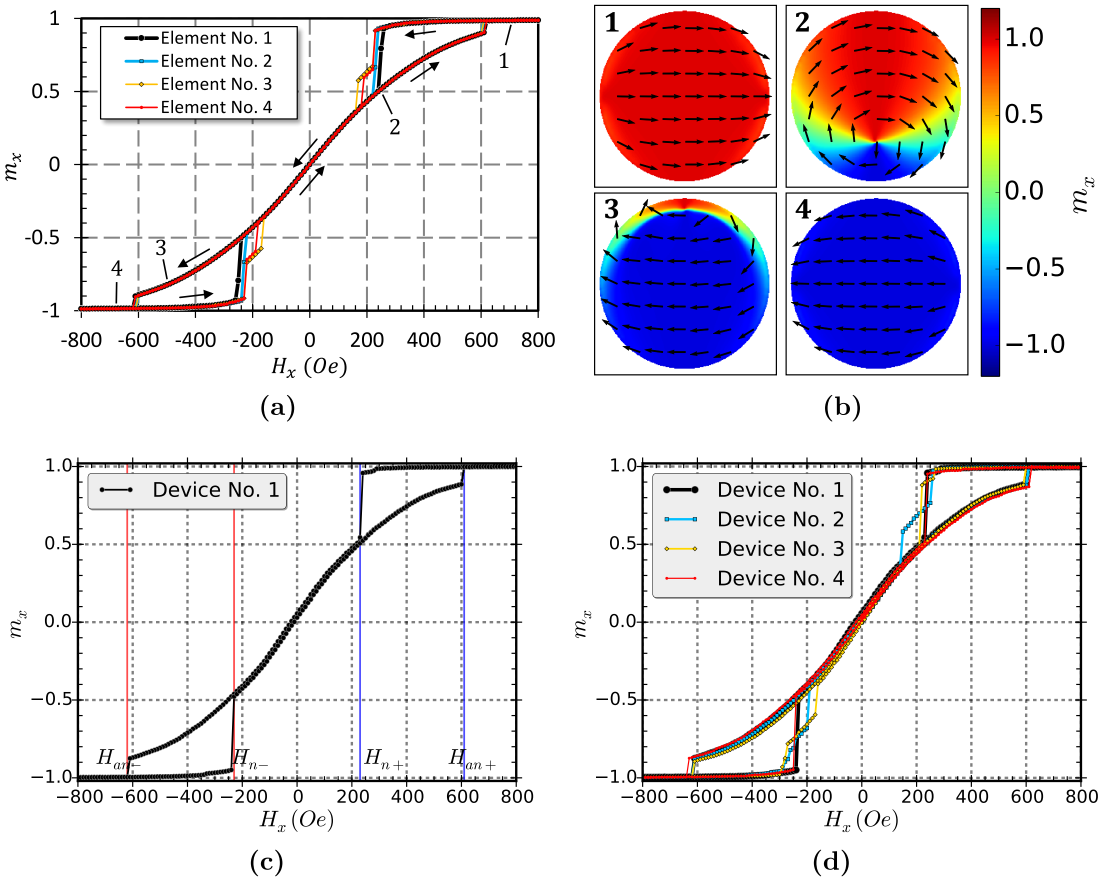

(a) (b)

(c) (d)

**Figure 2.3.** (a) Simulated hysteresis loops of disk-shaped elements ($d = 1.1$ µm and $t = 35$ nm). Only difference between the elements is the discretization of the edge of the disks. (b) Magnetic states of certain field steps as marked in (a). (c) Experimental hysteresis loop of a disk-shaped CoFeB element of the same dimensions. Marked are the vortex critical fields. (d) Experimental hysteresis loops of various elements, all from one wafer and with the same dimensions. Standard simulation parameters for CoFeB are given in Section 3.3.

usage in sensing applications. It can be explained by two facts: (1) the different vortex configurations - defined by sense of rotation and polarity - are in principle energetically equivalent. (2) The motion of the vortex core is not restricted by energy barriers. Fact (1) naturally only applies to perfectly circularly shaped disk elements and (2) only to amorphous materials where zero magneto-crystalline anisotropy is present.

In Figure 2.3b, magnetic states of half of the hysteresis loop are shown exemplarily: coming from positive saturation (inset No. 1) the saturated state collapses at a certain applied magnetic field and the nucleation of the vortex state (2) is observed. During the subsequent reduction and reversal of the external field, the vortex core is moved to the other side (3) where it finally annihilates and negative saturation (4) is reached. A closer look at Figure 2.3a reveals that the hysteresis and the vortex nucleation field depend on the individual elements, which only differ in the shape of the edge. A detailed analysis of such effects as well as the influence of different pre-vortex configurations is given in Chapter 4.

The vortex critical fields - nucleation field $H_n$ and annihilation field $H_{an}$ - are marked in the experimental hysteresis loop, shown in Figure 2.3c. In addition, it can be distinguished between positive ($H_{n+}$ and $H_{an+}$) and negative half branch ($H_{n-}$ and $H_{an-}$). The experimental hysteresis loops, especially $H_n$, also vary from device to device as shown in Figure 2.3d.

## 2.2 Theoretical Background and Fields of Research

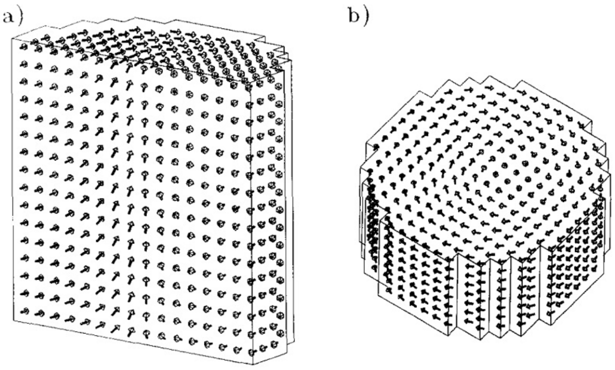

**Figure 2.4.** Magnetization of a soft magnetic quasi-cylindrical particle with a diameter and thickness of 80 nm, respectively. (a) The crosscut illustrates the out-of-plane component of the vortex core. (b) Complete element. Reprinted from *Journal of Magnetism and Magnetic Materials,* Vol. 118 Issue 3, N.A. Usov and S.E. Peschany, ©1993 [30], with permission from Elsevier.

When a ferromagnetic body is not exposed to a magnetic field a disintegration of the magnetization into a domain structure is observed. This observation was derived analytically first by Landau and Lifshitz and can be explained by the minimization of the exchange, anisotropy and magnetostatic energy [31]. As a consequence, the remanent magnetization at the boundary of a ferromagnetic body is usually aligned parallel to the surface, whereas in the bulk the magnetization is assumed to be parallel to any easy anisotropy axis [32]. Thus, for thin films, where the lateral extension is much larger than the thickness of the film, the remanent magnetization is parallel to the surface of the film [33]. On the basis of these facts the domain structure of various shaped thin film objects can be derived, assuming that the magnetization is solenoidal [34–36]. It must be noted that below a certain critical dimension, usually somewhere in the two-digit nanometer regime, the magnetization will always stay in a saturated single domain state [33].

On this basis, possible remanent magnetizations of a circular disk-shaped element can be assessed. With the requirement of a (1) solenoidal magnetization which is (2) parallel to the boundary of the element four possible magnetization patterns are obtained: a vortex with two possible senses of rotation and two possible types of core polarities. It has to be noted that the magnetization is not completely solenoidal due to the $\hat{z}$-component of the vortex core (see Figure 2.2 and 2.4). All modifications of the vortex configuration that are still solenoidal at the edge of the element and thus require a circular magnetization would increase the exchange energy and are therefore less favorable. Likewise, any other configuration which fulfills the criteria $m_x = 0$, $m_y = 0$ and $m_z \approx 0$ will require more extended domain walls - as the only domain wall of the vortex state is its core - which increase the exchange stiffness and stray field energy.

The nucleation field of the ’magnetization curling’ in an infinite cylinder was first treated theoretically by Frei et al. and Brown simultaneously [37, 38]: by calculating the energy of three different states - uniform, buckling and curling magnetization - nucleation fields were derived as a function of the cylinder radius [37]. The energetics of the magnetization curling state were intensively studied in the following decades by Aharoni[1] for different shapes [40–42] including cylindrical elements [39, 43]. Early simulation studies were carried out by Usov and Peschany in 1993 and they derived the magnetization of the vortex state at zero field analytically [30]. This way, they were able to study the influence of the cylinder size. Their original illustration of the magnetization pattern is shown in Figure 2.4.

The increase of experimental investigations of magnetic vortices was closely linked with the progressing development of miniaturization in semiconductor fabrication. In 1990, Rührig et al. reported the observation of magnetic vortices in large circular disk structures with 60 and 120 µm diameter [44]. The center of the vortex becomes a curved domain wall for these large and thick structures when magnetic in-plane fields are applied as shown in Figure 2.5. Progressing lithography techniques such as electron or ion beam lithography enabled the investigation of deep sub-micron ferromagnetic particles in the 90s [45] in a way that the observation of vortices was reported for elliptical [46–50] and rectangular shapes [47, 51]. The work of Wernsdorfer et al. published in 1996 has to be mentioned here [46]. Although they did not have an entirely correct picture of the vortex state since they thought of a stretched domain wall in the central part instead of a vortex core (see Figure 2.6a), their work included (among other things) the first vortex hysteresis loop which shows the typical hysteresis-free central part as well as an investigation of the nucleation and annihilation probability as a function of sweep rate and temperature. Figure 2.6b shows the actually expected, simulated magnetic configuration of an elliptical element with the corresponding dimensions. It should be noted that the vortex core moves to the left side, instead to the right side as shown in Figure 2.6a, which results from the reversed direction of rotation.

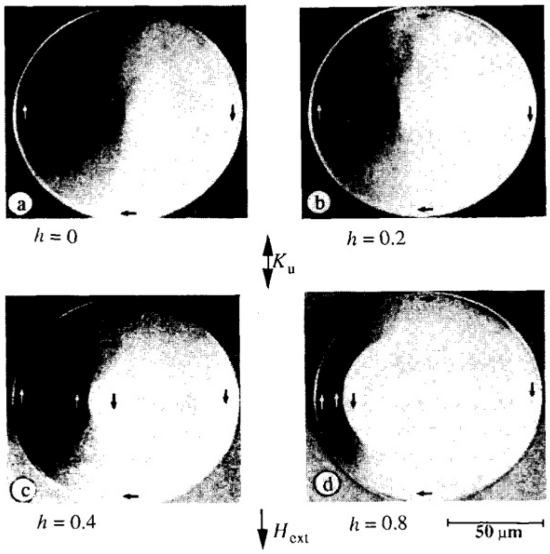

**Figure 2.5.** (a) Kerr image of the vortex state at zero field in a disk-shaped element with 120 µm diameter and 0.27 µm thickness. (b-d) An increasing external magnetic in-plane field (reduced field $h = H_{\text{ext}} \frac{d}{t \cdot M_s}$) leads to a shift and deformation of the vortex core. Reprinted from "Elementary magnetization processes in a low-anisotropy circular thin film disk," by M. Rührig et al., 1990, *IEEE Transactions on Magnetics.* ©1990 IEEE [44]. Reprinted with permission.

---

[1] His own sense of humor and his self-confidence is outstanding when starting with "Ishii and Sato could have saved a large part of the algebra that they did, had they started with the general expression for the magnetostatic energy in a cylinder" [39] and ending with "Results are not given, because the idea here is to outline the method of calculation, and not to study any particular physical model" [39].

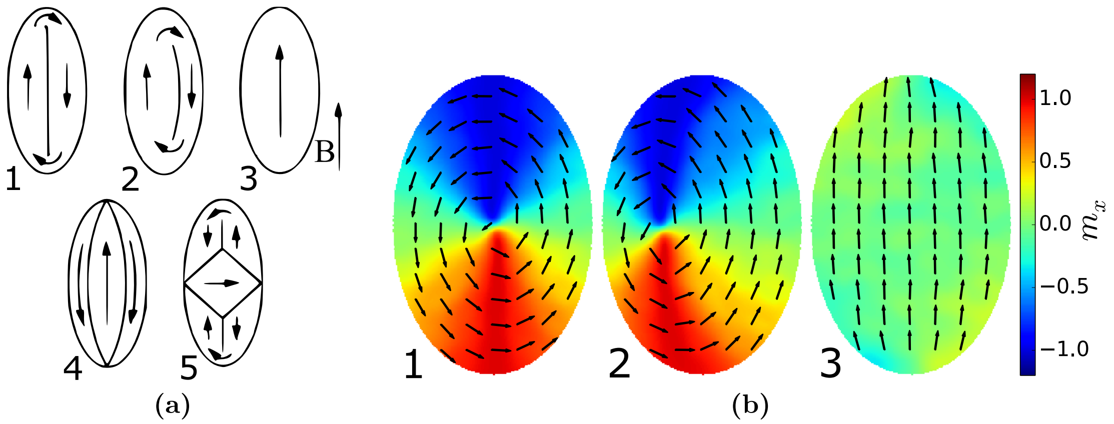

**Figure 2.6.** (a) Expected domain wall structure for an elliptical particle (300 x 200 x 30 nm) [46]. At zero field (1), intermediate field (2) and saturated (3). Alternative zero field configurations - which were excluded by Wernsdorfer et al. - are shown in (4) and (5). Reprinted figure with permission from W. Wernsdorfer et al., *Physical Review B*, 53, 3341-3347, 1996 [46]. ©1996 by the American Physical Society. (b) Simulated magnetic configuration. Simulation parameters for CoFe are given in Section 3.3.

The investigation of circular sub-micrometer nanomagnets by Cowburn et al. in 1999 brought the magnetic vortex into a broader focus [52]. They studied whether vortex nucleation occurs during magnetic reversal depending on the diameter (55 - 500 nm) and thickness (6 - 15 nm). Their work triggered a growing interest in the vortex state [53–66]. Guslienko and Metlov were the first to investigate the vortex state analytically under applied fields and they derived the annihilation field [67]. In another publication of Guslienko et al., the analytical expression of the size dependent nucleation field was derived [68]. The *rigid vortex model* of Guslienko et al. will be explained in more detail in Section 2.3.3.

The influence of the element shape and the question whether the vortex state nucleates are both complex topics. In principle, the vortex state is the energetic ground state for elements in the micrometer and sub-micrometer regime if their thickness is large enough and the element is not elongated [69]. A detailed analysis of different shapes, such as polygons, squares and triangles can be found elsewhere [69–73]. For elongated elements, such as rectangles or elliptical particles, the double vortex state is often observed [49, 51]. To be more precise, for a micrometer sized elliptical particle with the aspect ratio 1:2 the double vortex state is expected to be energetically favorable after exceeding 50 nm film thickness [2] [74]. For smaller elliptical elements even larger thicknesses have to be overcome [75].
It has been demonstrated that in asymmetric disk elements where a part of the disk is

---

[2] In the context of this work elliptical elements were also investigated (results are not shown). It was observed in simulation and experiment that for micrometer sized elliptical elements (1 µm × 2 µm × 50 nm) the formation of a stable double vortex state depends on the orientation of the applied in-plane field. If the easy axis of the ellipse is parallel to the applied field, then the double vortex state is favored due to its higher susceptibility. For a perpendicular alignment the transition into the single vortex state was finally observed in all experimental hysteresis loops.

cut off the sense of rotation of the vortex state can be controlled by the orientation of the prior saturation field, which in turn affects the annihilation field [76–79]. The sense of rotation of the vortex state can be controlled in a similar way by a step shape of the disk in out-of-plane direction, where one half of the disk has another thickness then the other half [80]. Other shapes with a vortex configuration have been investigated, such as overlapping disks [81] and different ring structures [75, 82–84]. Pacman-like disk elements show an increased nucleation field for certain orientations of the external magnetic field, due to the resulting stray field interaction within one element [85–87].
Other studies have investigated how the vortex state can be influenced by the exchange bias effect: field cooling leads to an anisotropy of the vortex critical fields [88–91], whereas zero-field cooling determines the direction of rotation of the vortex state and can cause an earlier vortex nucleation[3] [92, 93].

In this work, the focus is set on the quasi-static behavior of the vortex state. Nevertheless, it should be mentioned that when a magnetic in-plane field pulse is applied the vortex core describes a precession around the equilibrium position at zero field [94–96]. Consequently, the magnetic vortex shows resonance as a translational motion of the vortex core when an alternating field in the Megahertz-regime is applied [96, 97]. An electrical switching of the vortex core - based on current-driven resonance - is possible [98, 99] and has been implemented in tunneling magnetoresistance junctions [100, 101]. Other memory concepts that use rotating fields to switch the core have been reported [102]. In other geometries, where the double vortex state is energetically favorable, the dynamic interaction of vortex and anti-vortex can be utilized for an identification of the core configuration [103]. The polarity of a moving vortex core can be measured electrically [100, 104]. It was also demonstrated that a defined switching of the sense of rotation of the vortex state is possible, not only dynamically but also statically [105]. Logic operations based on stray field coupled vortices, monitoring the vortex gyrations, were experimentally demonstrated [106, 107] and high-frequency concepts with dipolar or exchanged coupled vortices were experimentally investigated [108].
Until today, there is a broad interest in the vortex state and its possible applications, be it for its possible implementation in spintronic storage media - by taking advantage of the vortex chirality and polarity - or be it for sensing applications because of its low hysteresis.

---

[3] Zero-field cooling exchange-biased disk structures were also investigated in the context of this work but the used spin valve structure complicated the manufacturing process since two antiferromagnetic layers with different blocking temperatures are needed (results are not shown).

## 2.3 Energy Analysis of the Vortex State

This section will discuss the different magnetic energy terms and their contribution to the total energy of a cylindrical ferromagnetic structure. The terms of exchange stiffness, external field, stray field and magneto-crystalline anisotropy energy are introduced in Section 2.3.1. For further details see, for example, Hubert and Schäfer, p. 100-144 [36]. These energy terms are then analyzed in Section 2.3.2 for a micrometer-sized ferromagnetic cylindrical structure and its different magnetic states. This way the nucleation of a magnetic vortex will be derived since it is the energetically favorable ground state for such a disk structure with sufficiently large layer thickness.

### 2.3.1 Energetics of a Ferromagnetic Structure

The basic characteristic of ferromagnetism is its near-order, the strive for a parallel alignment of magnetic moments. Therefore, different orientations of the neighboring spins will increase the energy of the system. Accordingly, the corresponding energy term is called exchange stiffness energy $E_{\text{exch}}$:

$$E_{\text{exch}} = \int\limits_V A(\vec{r})\{(\nabla m_x)^2 + (\nabla m_y)^2 + (\nabla m_z)^2\}\,\mathrm{d}V \tag{2.1}$$

The exchange stiffness constant $A(\vec{r})$ is a measure for the strength of the exchange interaction. In case of one ferromagnetic layer consisting of a homogeneous material it can be simplified to $A(\vec{r}) = A$. The exchange stiffness energy is always positive or zero for a completely saturated state. It can be compared with the energy stored in a system of springs, hence the quadratic dependence on the gradient of magnetization. A determination of $A$ is usually done via resonance experiments [109, 110].

In case of a given magnetization $\vec{M}(\vec{r})$, the energy in a uniform external magnetic field $\vec{H}_{\text{ext}}$ is given by the Zeeman energy:

$$E_{\text{Zeeman}} = -\int\limits_V \vec{H}_{\text{ext}} \cdot \vec{M}(\vec{r})\,\mathrm{d}V \tag{2.2}$$

$E_{\text{Zeeman}}$ is zero at zero field, typically decreasing with increasing field strength and it is always negative around and above the saturation field.

In addition to the external field, the stray field $\vec{H}_{\text{demag}}$ of a magnetic body itself induces a torque on the magnetization. For illustration, the sample magnetization can be divided into smaller magnetic dipoles that act as sink and sources for the stray field. In case of a saturated sample next neighboring dipoles will thus create a stray field opposed to the nearby magnetization. Consequently, the stray field energy will reach its maximum in case of saturation. Accordingly, the energy term is often also called demagnetization energy $E_{\mathrm{demag}}$, since it favors a reduction in magnetic polarization and it causes a decay into magnetic domains for large enough samples.

$$E_{\mathrm{demag}} = -\frac{1}{2}\int\limits_V \vec{H}_{\mathrm{demag}}(\vec{r}) \cdot \vec{M}(\vec{r})\,\mathrm{d}V \tag{2.3}$$

$E_{\mathrm{demag}}$ also includes the frequently mentioned term *shape anisotropy*. This term describes a preferred direction of magnetization - the so-called easy axis - that results from the stray field energy of the magnetic body. For reasons of symmetry, a disk-shaped element has no in-plane shape anisotropy. However, the cylindrical axis is the hard axis (if diameter > thickness) because an out-of-plane magnetization leads to a much larger $E_{\mathrm{demag}}$ compared to an in-plane magnetization.

The previously discussed terms are sufficient to treat the magnetic energy of an amorphous body. For crystalline materials there is an energy dependence on the orientation of the magnetization with respect to the crystalline structure which results from spin-orbit interactions [36]. In the case of a single uniaxial anisotropy:

$$E_{\mathrm{aniso}} = \int\limits_V K_1(\vec{r}) sin^2\theta(\vec{r})\,\mathrm{d}V \tag{2.4}$$

where $\theta(\vec{r})$ is the angle between magnetization direction and anisotropy axis and $K_1$ is the uniaxial anisotropy constant. If $K_1 > 0$, the anisotropy axis is an easy axis (energy minimum for $\theta = 0$), if $K_1 < 0$, an easy plane perpendicular to the anisotropy axis is present (energy minimum for $\theta = 90°$). Higher-order terms have been neglected in Equation 2.4. They are needed to determine the easy axis within the easy plane, if $K_1 < 0$ (see e.g. [36], p. 106). However, within this work, only positive values of $K_1$ are discussed.

The previously discussed energy terms contribute to the total magnetic energy $E_{\mathrm{tot}}$ of a magnetic body:

$$E_{\mathrm{tot}} = E_{\mathrm{exch}} + E_{\mathrm{Zeeman}} + E_{\mathrm{demag}} + E_{\mathrm{aniso}} + E_{\mathrm{me}} \tag{2.5}$$

A further energy contribution appears in Equation 2.5, the magneto-elastic energy $E_{\mathrm{me}}$ which is related to the deformation of a magnetic body under an applied magnetic field and, vice versa, the change in magnetization due to an applied mechanical stress results in a change of $E_{\mathrm{me}}$. Magneto-elastic interactions were neglected in this work since no defined additional mechanical stress was applied.

To determine a certain magnetic state by minimizing $E_{\mathrm{tot}}$ is the approach of micromagnetic simulations (see Section 3.3).

### 2.3.2 Energetics of a Micrometer-Sized Disk Structure

With the energy terms introduced in the previous section it will now be shown why the nucleation of a magnetic vortex is energetically favorable for a disk-shaped element. In this context, *disk-shaped* describes a right circular cylindrical structure. The choice of diameter and thickness may appear to be random here, but a sufficient large layer thickness of approximately 5-10 nm is mandatory to enable the formation of an out-of-plane magnetization and thus to allow the nucleation of a vortex core. A detailed discussion of the influence of thickness and diameter is given in Section 4.1.

Figure 2.7a shows the simulated hysteresis loop of a ferromagnetic disk structure with 1.1 µm diameter and 35 nm thickness. In Figure 2.7b the corresponding energies are plotted as a function of $H_x$ separately for the vortex state and the non-vortex states. For the saturated state (see inset No. 1 in Figure 2.7a), a maximum in $E_{\mathrm{demag}}$ and a minimum in $E_{\mathrm{exch}}$ are observed due to a maximum in polarization/uniform magnetization. Both terms are constant and $E_{\mathrm{Zeeman}}$ shows a linear behavior because of the constant magnetization. Consequently, a linear trend is observed for $E_{\mathrm{tot}}$.

For $H_x < H_{an}$ - below 600 Oe in this example - the saturated state starts to reduce its uniformity at some point which leads to a decrease of $E_{\mathrm{demag}}$, while an increase of $E_{\mathrm{Zeeman}}$

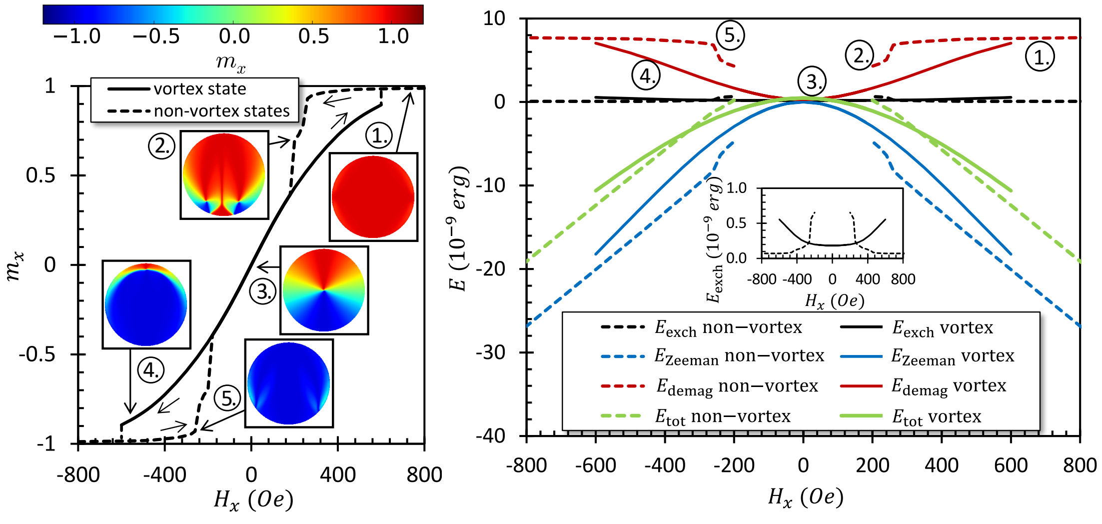

(a) (b)

**Figure 2.7.** (a) Simulated hysteresis loop of a ferromagnetic disk structure with 1.1 µm diameter and 35 nm thickness. The insets show the magnetization pattern of the structure for the marked field steps in plan view. (b) Energy levels of the different energy terms are plotted for the same hysteresis loop. Due to the smaller level of $E_{\mathrm{exch}}$ it is plotted additionally in the inset with a different scale. Marked are the stray field energies of the states shown by the insets in (a). *MicroMagus* was used for all micro-magnetic simulations shown. A brief introduction and the used simulation parameters (here CoFeB) are given in Section 3.3.

and $E_{\text{exch}}$ takes place at the same time. These two energy terms have a larger impact than $E_{\text{demag}}$. $E_{\text{Zeeman}}$ alone has more weight than $E_{\text{demag}}$ due to the factor $\frac{1}{2}$ of the stray field energy term (see Equation 2.3). For these reasons $H_n \neq H_{an}$ and thus hysteresis is observed.

The following observations can be made when comparing the energies of vortex and non-vortex state with each other:

- $\mathbf{E_{demag}}$ of the vortex state (No. 3 and 4 in Figure 2.7a) is always smaller in comparison with the non-vortex state. The non-vortex state summarizes in this example the saturated state (No. 1), double vortex state (No. 2), and C-state (No. 5). The smaller stray field energy can be explained by the closed flux of the vortex state. It is also observed that the double vortex state drastically decreases $E_{\text{demag}}$.
- In contrast, $\mathbf{E_{Zeeman}}$ of the vortex state is always larger than of the non-vortex state. This results from the non-uniformity of the vortex state. It has to be noted that in cases where vortex nucleation occurs after field reversal $E_{\text{Zeeman}}$ of the non-vortex state can actually become positive.
- For all non-vortex states, except the double vortex state, $\mathbf{E_{exch}}$ is smaller compared to the vortex state (see inset in Figure 2.7b). This results from the curling magnetization of the vortex core(s). In the example shown, the exchange stiffness energy is about one order of magnitude smaller than the stray field energy. For smaller diameters the relative influence of $E_{\text{exch}}$ will increase. It also has to be noted that the thickness has an influence on the out-of-plane magnetization of the saturated state in close proximity to the disk edge (see Section 4.1.4) and thus affects $E_{\text{exch}}$.
- The comparison of total energies $\mathbf{E_{tot}}$ of the vortex and non-vortex state indicates that the vortex state is energetically favorable below an external field of approximately 330 Oe (intersection point). But the actual nucleation and annihilation is delayed because energy barriers are present for the corresponding transitions: remagnetization only occurs if the total energy is decreasing during the whole remagnetization process. For example during vortex annihilation the complete reversal of magnetization leads to a decrease of $E_{\text{Zeeman}}$ but at the same time it causes an increase of $E_{\text{exch}}$ and $E_{\text{demag}}$. Consequently, only if the energy barrier becomes zero - as the increase of $E_{\text{exch}}$ and $E_{\text{demag}}$ is smaller than the decrease of $E_{\text{Zeeman}}$ - annihilation is observed (this applies to the simulation at zero Kelvin).

### 2.3.3 Analytical Vortex Models

The discussion of the energy terms in the previous section can be described mathematically with an analytical model. Well-known is the so-called *Rigid Vortex Model* (RVM) [27, 68]. In the RVM the total energy of the vortex state - as a function of the displacement of the vortex core - is analytically derived for cylindrical elements taking into account $E_{\text{demag}}$,

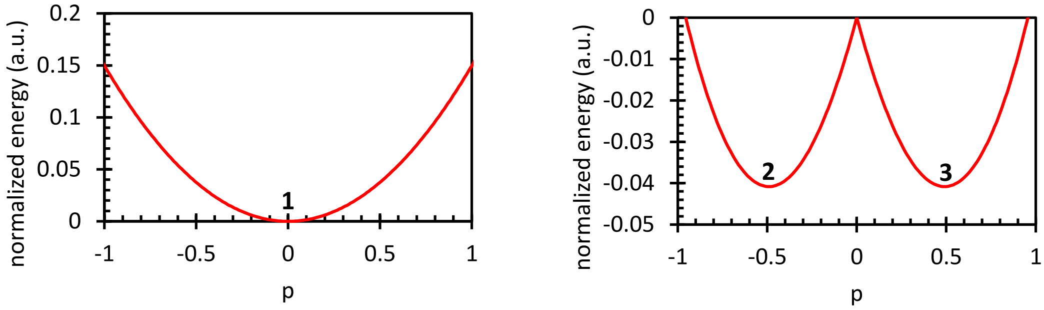

**(a)** RVM: $H_{\text{ext}} = 0$ **(b)** RVM: $H_x \approx H_{an}/2$

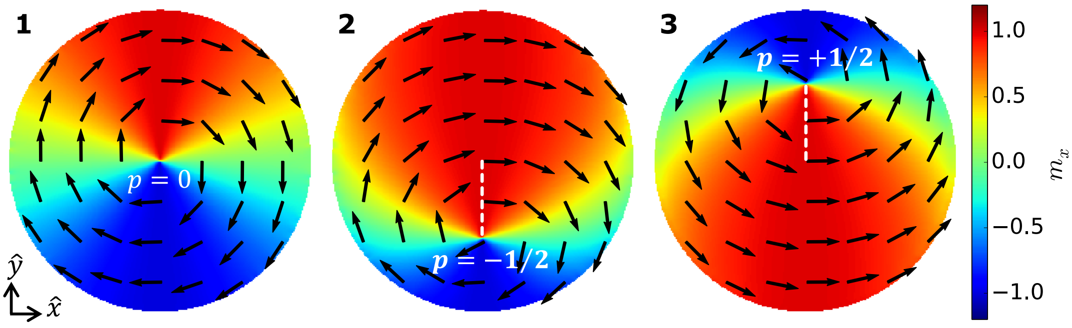

**(c)** Possibe vortex core positions for (a) and (b)

**Figure 2.8.** (a-b) Total energy of the vortex state as a function of the vortex core displacement $p$ obtained via the Rigid Vortex Model (RVM). The displacement $p$ is in-plane, perpendicular to the applied in-plane field $H_x$, and normalized to the disk radius. The energies are normalized to $E(p = 0)$. (a) At zero field $p = 0$ is the energetic ground state. (b) For an applied field $H_x < H_{an}$ two vortex core displacements are possible due to the two possible directions of rotation of the vortex state. (c) Corresponding magnetic states in top view obtained via micro-magnetic simulations. The formula for $E(p)$ was taken from Burgess et al. [111].

$E_{\text{Zeeman}}$, and $E_{\text{exch}}$. The name of the RVM is derived from the simplifying assumption that the rotationally symmetric spin structure of the vortex state at zero field does not change during a shift of the core, i.e. is *rigid*. Figure 2.8 shows the total energy of the vortex state, calculated with the RVM, as a function of vortex core displacement $p$ at zero field. As expected, the energy minimum is found at $p = 0$. The corresponding in-plane spin structure is shown in Figure 2.8c (No. 1). A reversed direction of rotation of the vortex state is also possible (not shown) but does not affect $p$. In Figure 2.8b, energy vs. $p$ is exemplarily plotted for a magnetic in-plane field below $H_{an}$. Two minima are observed which can be attributed to the two possible core displacements, for a clockwise or for an anti-clockwise direction of rotation, respectively, as illustrated by Figure 2.8c (No. 2 and 3).

The simulation results, shown in Figure 2.8c, indicate a known limitation of the RVM: at zero field (No. 1), color transitions - from red to green and from green to blue - form straight lines. This means that the spin structure of the curling mode is rotationally symmetric. However, this does not apply for state No. 2 and 3, where a bending of the color transitions is observed. This bending results from the fact that the magnetization strives to be parallel to the edge, which reduces the stray field created at the side surface of the disk. In other words, the RVM overestimates the stray field created by the side surface charges and accordingly the RVM should only be used for small $p$ [27]. Further developed models exists where the face surface charges of the disk are additionally taken into account [67]. There are also models which assume that no side surface charges exist [112], others that use two models separately for different sections of the disk [111] or where additional states are taken into account [113]. A more detailed overview and comparison between the different analytical models is given elsewhere [111, 114].

The RVM allows the determination of the vortex critical fields: $H_{an}$ is usually approximated via the condition $p \approx 1$ [68]. But the RVM can also be used to derive the energy barrier for vortex annihilation [115]. $H_n$ can be estimated by assuming that the saturated state can be described by the vortex state but with the vortex core located outside the disk. Then the magnetic field, below which this 'saturated state' becomes unstable - characterized by the fact that also the second derivative of the total magnetic energy becomes zero - represents the nucleation field [68].
There are certain limitations within the RVM: (1) in the RVM usually only two magnetic states are considered. (2) The deformation of the spin structure for displacements $p$ close to one is not reproduced. (3) Surface charges on the disk face are neglected. Nevertheless, the RVM is a powerful model which provides a good estimation of the critical fields and allows to understand the different effects and energetic contributions that define the magnetic behavior of micrometer-sized disk-shaped elements. Other models eliminate some of the mentioned weaknesses, but it will be shown in Section 4.1 that especially the disk thickness defines which type of surface charges appear and thus strongly affects $E_{\text{demag}}$. Consequently, all different models have their justified existence, depending on the dimensions of the disk. In this work, experimental data was only compared to micro-magnetic simulations. Even though micro-magnetic modeling is much more time consuming, it has the benefit of being accurate as well as flexible.

# 3 Methodology

In the context of this work, Tunnel Magnetoresistance (TMR) spin-valve structures with a disk-shaped free layer were investigated experimentally. The sensor concept is introduced in Section 3.1. The setup in which the sensors were electrically characterized - as a function of magnetic in-plane fields and under various temperature conditions - is explained in Section 3.2. Experimental results were analyzed in combination with micro-magnetic simulations, which are introduced in Section 3.3.

## 3.1 Implementation of the Vortex Sensor Concept

First concepts of a Magnetic Tunnel Junction (MTJ), which basically consists of two ferromagnetic electrodes separated by a thin tunnel barrier, utilizing the magnetic vortex were not very promising since the hysteresis loop did not look like a typical vortex transfer curve [55]. This was due to the fact that the TMR hysteresis loop shown by Pokhil et al. actually indicates that not the vortex state but the C-state was present[1]. MTJs were often used to investigate the dynamics of the vortex state [99–101, 105]. Also other sensor concepts were reported which used the GMR effect to investigate the vortex state [116–118].

This section provides the foundation for an understanding of the physics behind the investigated TMR spin-valve sensor concept. Furthermore, optical microscopy, scanning electron microscopy, and transmission electron microscopy images show results of the implemented sensor concept. Scanning magnetoresistive microscopy - in addition to the TMR measurements - proves that the vortex state is actually present in the investigated structures.

### 3.1.1 Tunnel Magnetoresistance

The TMR effect - discovered by Julliere [13] - is a spin-dependent tunneling effect that takes place between two ferromagnetic electrodes which are separated by a tunneling barrier. The effect was explained by Julliere with the simplified phenomenological model with spin-resolved Density Of States (DOS). This model is illustrated in Figure 3.1. A

---

[1] Compare Figure 2 in [55] with the hysteresis loop of the C-state shown in Figure 5.14b in Section 5.3. In addition, it has to be noted that the presence of the double vortex state proposed by Pokhil et al. is unlikely for the investigated thickness of 10 nm (see Section 4.1.5).

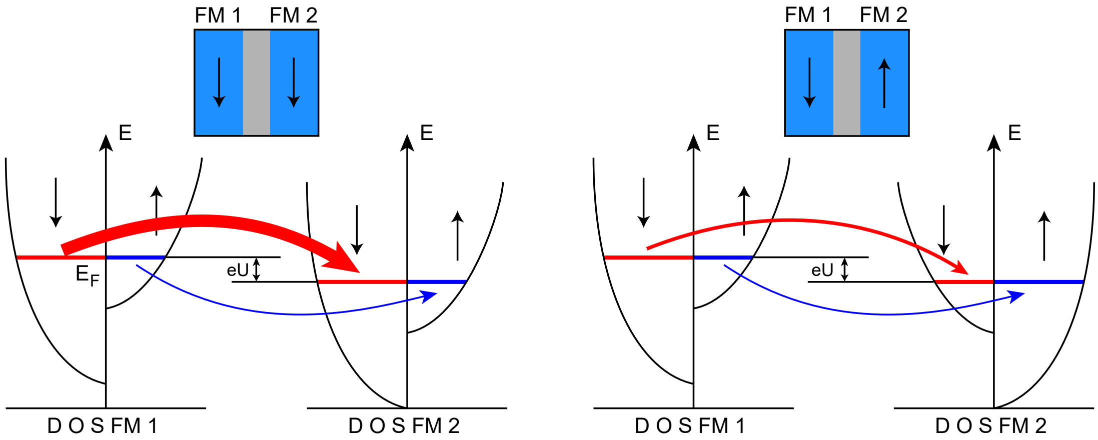

(a) (b)

**Figure 3.1.** Simplified schema for the TMR effect illustrating (a) high conductivity for a parallel orientation of the magnetizations and (b) low conductivity for an anti-parallel alignment (adapted from [119], 2014). DOS at the Fermi energy $E_F$ are plotted separately for spin down (left) and spin up (right), respectively for both ferromagnetic layers, FM1 and FM2. The ferromagnetic layers are separated by a tunnel barrier, represented by the grey layer.

parallel alignment of the magnetizations (see Figure 3.1a) leads to a high DOS for spin down (majority charge carriers) on both interfaces of the tunnel barrier. In contrast, spin up DOS is low on both sides (minority charge carriers). When a voltage $U$ is applied it is assumed that tunneling only occurs without spin flipping (regarding the spin diffusion length see e.g. [120]). Consequently, the tunneling probability - and therefore conductivity - is proportional to the sum of the tunneling probabilities of the two 'spin channels'. This leads to an overall high conductivity because of the high conductivity of the spin down channel, which is illustrated by the thick red arrow. In the case of an anti-parallel alignment (see Figure 3.1b) tunneling occurs from majority to minority charge carriers or minority to majority charge carriers, respectively, which leads to a low conductivity.

This model explains well the tunneling process through amorphous aluminum oxide tunnel barriers where TMR ratios (change of resistance, usually normalized to the resistance minimum [121]) of tens of percents are observed [122, 123]. It was predicted in 2001 that higher TMR ratios are possible when crystalline MgO tunnel barriers are used [124]. There are several reasons for this: among other things, the tunneling probability depends on the symmetry of both the Bloch states of the ferromagnetic layer and the evanescent states of the tunnel barrier. Moreover, the different states have different decay rates within the tunnel barrier. Detailed background information about the symmetry filtering effect of the crystalline MgO barrier is given elsewhere [124–127]. The predicted high TMR ratios were experimentally proven [121]. In 2008, a TMR ratio of 604 % at room temperature was reported [14].

It has been demonstrated that a minimum of five monoatomic MgO layers - in combination with $Co_{60}Fe_{20}B_{20}$ as ferromagnet - is required in order to achieve a crystallization of the

tunnel barrier and thus to reach high TMR ratios [128]. The MTJs investigated in this work have a tunnel barrier thickness of 1.0 nm, which corresponds quite accurately to five monoatomic MgO layers since the lattice constant of MgO(0 0 1) is 2.1 Å [126]).
It needs to be emphasized that the TMR effect is a conductivity effect despite its name. Consequently, not the resistance but the conductivity is directly proportional to the magnetization. This is of great relevance to be able to interpret the experimental results (see also [129]) and to allow a correct comparison with simulations (see Section 3.3).

### 3.1.2 Tunneling Magnetoresistance Spin-Valve

The term *spin-valve* was originally introduced for a GMR[2] structure consisting of basically four layers: a trilayer structure that is similar to the MTJ (only the tunnel barrier (TB) is substituted by a nonmagnetic metallic layer) and supplemented by an antiferromagnetic layer (AFM) at the interface of one of the ferromagnetic layers (FM) [21]. The term spin-valve is also used in combination with the TMR effect [126]. A simple TMR spin-valve structure is shown in Figure 3.2a. The AFM allows the pinning of the magnetization of the FM located at the interface of the AFM. Accordingly, this layer is usually called pinned layer (PL). The pinning is done by utilizing the exchange bias effect [130, 131], which is an interface effect between AFM and FM. In the presence of a magnetic field, the AFM-FM hetero-structure is cooled down from above the blocking temperature which is required to be below the Curie temperature of the FM, and, as a result, a unidirectional alignment of

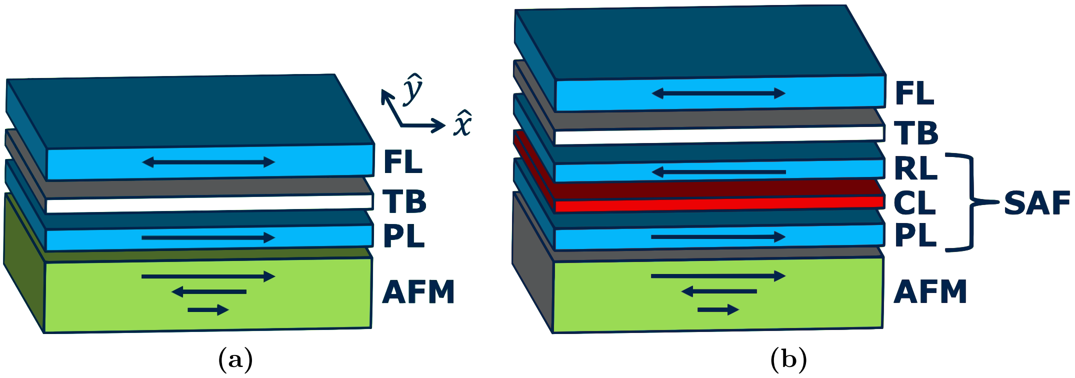

**Figure 3.2.** Exploded-view drawing of spin-valves. (a) Spin-valve with a simple Pinned Layer (PL). (b) Spin-valve with a Synthetic Antiferromagnet (SAF). Remaining acronyms: Free Layer (FL), Tunnel Barrier (TB), Reference Layer (RL), Coupling Layer (CL) and Antiferromagnet (AFM). The layers are oriented in the $\hat{x}$-$\hat{y}$-plane. The spin-valves shown are sensitive to the $\hat{x}$-component of the FL magnetization ($m_x$).

---

[2] The GMR effect [9, 10] is observed in trilayer structures consisting of basically two ferromagnetic layers (FM) which are separated by an ultrathin nonmagnetic metallic layer. The GMR effect has a different origin than the TMR effect - a spin-dependent scattering of electrons - but the phenomenological observation is similar to the TMR effect: low resistance for parallel magnetization and high resistance for antiparallel magnetization.

the magnetic moments at the AFM interface is obtained. Due to the exchange interaction between AFM and FM, a unidirectional exchange anisotropy of the FM results from the exchange biasing which leads to a shift of the hysteresis loop, or in other words to a pinning of the PL. Accordingly, the other FM is called free layer (FL), describing its capability of following the external magnetic field 'freely'. Simple MTJs without pinning are sometimes also referred to as pseudo-spin-valves [132].
The stability of a simple spin-valve - with a PL only, as shown in Figure 3.2a - is limited as a result of the net moment of the PL and its resulting stray field. In addition, the stray field of the PL affects the magnetization of the FL. For these reasons, a simple spin-valve is technologically unattractive. Spin-valves with a synthetic antiferromagnet (SAF) are therefore usually used [24, 133, 134]. In the SAF, the PL is supplemented by two additional layers (see Figure 3.2b): a metallic coupling layer (CL) and an additional FM called reference layer (RL). The interlayer thickness is chosen in order to achieve an anti-parallel Ruderman-Kittel-Kasuya-Yosida (RKKY) coupling between both FMs [135–137]. Such an anti-parallel alignment is favorable because the total moment and the stray field of the SAF sandwich are minimized. Consequently, the SAF spin-valve is very robust in terms of stability versus the external magnetic field, as will be shown in the next section. Further types of spin-valves are discussed elsewhere [138].

The special aspects of the investigated TMR vortex spin-valves are the circular cylindrical shape of the FL and its dimensions. Figure 3.3a shows an illustration of the vortex spin-valve. MgO was used as TB. The top contact - the electrical contact on top of the FL - is required to be laterally smaller or equal than the FL to ensure highly reliable functional spin-valves. Film thicknesses and materials of the investigated stacks are discussed in the following section. Due to the small dimensions of the FL, commercial automotive sensors are supposed to use many spin-valves connected in series to increase

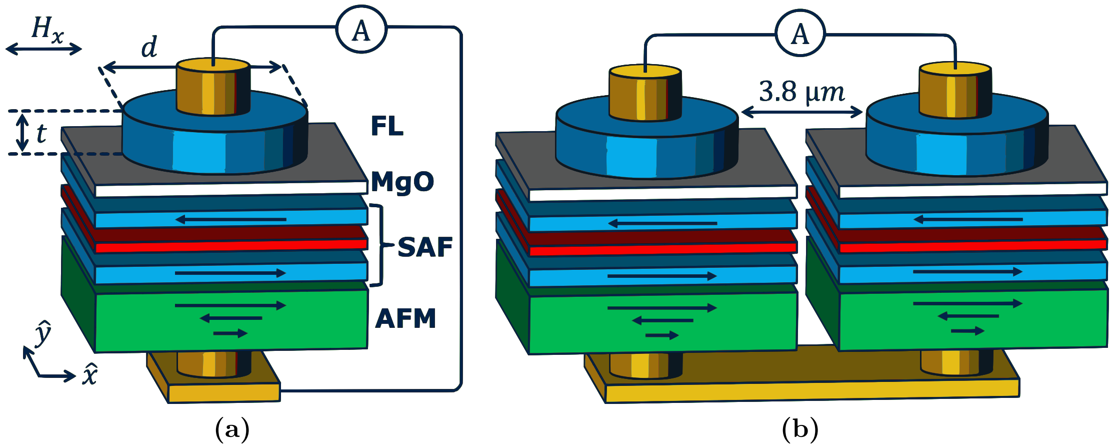

(a) (b)

**Figure 3.3.** Exploded-view drawing of TMR vortex spin-valves. (a) Single disk device with FL thickness $t$ and diameter $d$. MgO is used as tunnel barrier. The spin-valve is sensitive to $H_x$. (b) Dual disk device with bottom metal interconnection (golden layer) between tow MTJs.

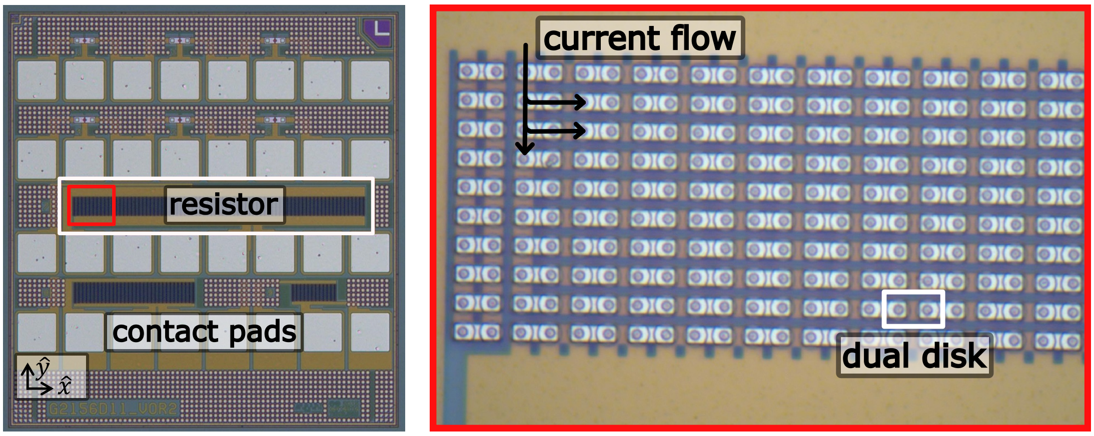

(a) (b)

**Figure 3.4.** (a) Optical microscopy image of a test chip with four rows of contact pads. In the middle a device is framed (resistor) which is built up of 585 electrically active dual disk spin-valve structures. (b) The detail section of the resistor - see red frame in (a) - allows to identify the dual disk elements. (The resistor is framed by one row of dummy structures which are electrically inactive.)

the signal-to-noise ratio as well as the dielectric strength. The corresponding unit cell of such a sensor is shown in Figure 3.3b. A dual disk device like this can be connected via a top metal interconnection with the next dual disk device, and this way a sensing element is built up. The spacing between the disks is chosen large enough in order to avoid any stray field coupling between the disks [52, 61].
Both types - single and dual disk devices - were investigated in this work. Devices consisting of up to 1170 spin-valves were additionally characterized. An optical microscopy image of a test chip with such a device is shown in Figure 3.4a. The image shows four rows of contact pads which belong to different test structures. In the third row, from top to bottom, contact pads are placed which allow to measure a resistor with 1170 spin-valves. A detail section of the left part of the resistor is shown in Figure 3.4b. In this image, the individual dual disk elements are clearly visible. Bottom metal interconnections appear golden in the optical image and top metal interconnections appear white. The top and bottom metal contacts are barely visible because the same metal as for the interconnections was used. The free layer is visible as the small circular bluish elements. The larger circular elements reflect the bottom electrode of the spin-valve, which primarily consists of the SAF and AFM.

Figure 3.5 shows an experimental spin-valve structure in side view. A thin section in the center position of the FL was prepared by using focused ion beam, and subsequently Transmission Electron Microscopy (TEM) images were taken. The overview in Figure 3.5a shows the complete FL with the aluminum top contact and tungsten bottom contacts. The edge of the spin-valve stack is shown with a higher resolution in Figure 3.5b. Here, the tunnel barrier is clearly visible as a small layer with bright contrast. The polycrystalline structure of the CoFe-part of the FL is also apparent. In the stack shown,

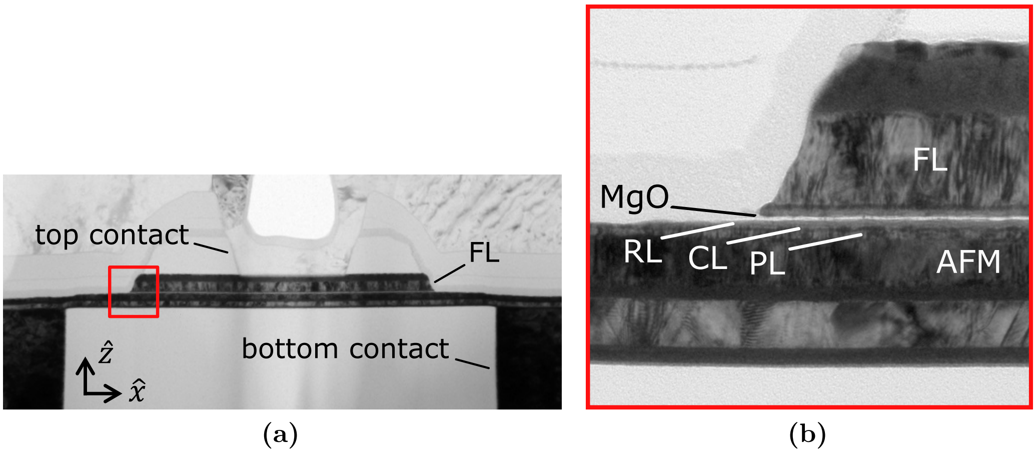

**Figure 3.5.** (a) TEM image of a thin section of an individual spin-valve. (b) The TEM detail section, as framed in red in (a), shows a trilayer FL structure with CoFeB at the interface to the TB, followed by a Ru-CL (dark contrast) and on top CoFe.

a Ru coupling layer was used both in the SAF and in the FL. As the image shows, the Ru-thickness is larger in the FL (parallel RKKY-coupling) than in the SAF (anti-parallel coupling).

A Scanning Electron Microscopy (SEM) image of a disk-shaped FL is shown in Figure 3.6a. SEM samples were prepared by mechanical grinding to remove the layers above the FL. However, remaining parts of the top contact are still visible. SEM images were of particular interest regarding the rounding of the corners when non-circular elements were patterned (see Figure 3.6b). This rounding results from the used lithography tool in the manufacturing process. The lithography process is also the limiting factor regarding the minimum FL diameter that can be implemented for functional spin-valves. Thus, the smallest elements had a layout FL diameter of 700 nm.

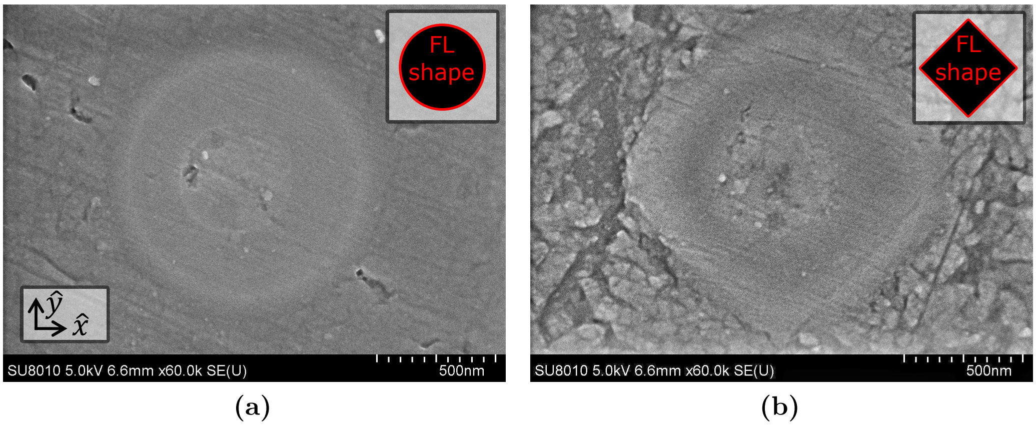

**Figure 3.6.** (a) SEM image of a circular-shaped FL element. In the center of the FL, the top contact is additionally visible. (b) SEM image of a square-shaped FL element.

TEM and SEM images were also used to estimate the actual FL diameter of the processed spin-valves. The actual disk diameter was approximately 0.1 µm larger in comparison with the layout of the lithography masks at nominal 1.0 µm. This difference was taken into account when experimental data was compared to micro-magnetic simulations.

### 3.1.3 Stack and Layout Variants

TMR stacks were deposited using physical vapour deposition. The stack in order of deposition was as follows: seed/ PtMn/ CoFe/ Ru/ CoFe/ CoFeB/ MgO/ FL(t)/ cap. As FL material $Co_{60}Fe_{20}B_{20}$ - further referred to as CoFeB - and $Co_{90}Fe_{10}$ - further referred to as CoFe - were deposited with a thickness of 10, 20, 35, and 50 nm. Patterning was done using photolithography in combination with ion beam etching. Annealing of the stack was carried out at 280 °C for one hour.

For the deposited CoFeB, a nano-crystalline cubic phase begins to form at approximately 250 °C which is visible by the increase of $M_s$ vs. temperature in Figure 3.7 [139]. Wang et al. also determined the corresponding cubic anisotropy constant ($K_c$) at various temperatures: below 300 °C, $K_c$ does not exceed $1 \times 10^3\,\mathrm{erg/cm^3}$ [139]. It is therefore a reasonable assumption to treat the investigated CoFeB disk elements as amorphous. A detailed investigation of the poly-crystalline CoFe and its magneto-crystalline anisotropy is given in Section 4.2.3.

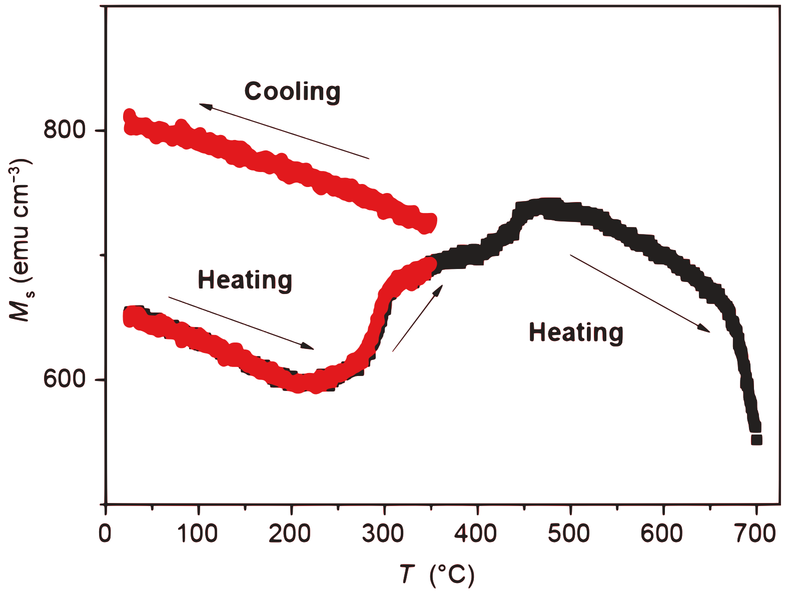

**Figure 3.7.** $M_s$ vs. temperature ($T$) of a 50 nm thick $Co_{60}Fe_{20}B_{20}$ film (Ta (9 nm)/$Co_{60}Fe_{20}B_{20}$/MgO (1.8 nm)), measured with a heating rate of 25 °C/ min in a magnetic field of 1000 Oe. Black curve from room temperature (RT) to 700 °C, red curve from RT to 350 °C and subsequently cooling back to RT. Reprinted by permission from Springer Nature *Science China Materials* "Magnetic, thermal, electrical properties and crystallization kinetics of $Co_{60}Fe_{20}B_{20}$ alloy films," Ke Wang, Zhan Xu, Ya Huang et al, ©2016 [139].

FL disk diameters between 0.8 and 4.1 µm were patterned. Other shapes (squares and polygons) were also patterned, but as a result of the limitations in the resolution of the lithography process, the resulting geometries only slightly varied from the circular shape (see e.g. Figure 3.6b). Consequently, also the magnetic behavior was only slightly different from the disk shape.

### 3.1.4 Device Characteristics

Figure 3.8 shows typical transfer curves of resistor elements. Resistors were chosen here because certain, rare hysteretic effects of individual spin-valve structures average out this way. Hysteresis loops with different maximum field amplitude are shown. The extracted, relative hysteresis is normalized to the current range of the corresponding data set. This means that in Figure 3.8a the absolute maximum hysteresis increases with increasing field amplitude. However, a hysteresis of approximately 1 % at zero field - independent of the maximum applied field - indicates a high stability of the SAF and that all disks are in the vortex state. Remaining hysteresis is expected to result from the core hysteresis of the quadrupole setup, the hysteresis of the reference system, and also FL hysteresis: it has occasionally been observed that a few elements have a noticeably large and constant hysteresis (see e.g. Figure 4.35a in Section 4.2.3).

The stability of the reference system is even more clearly visible in Figure 3.8b: all disks are annihilated above $|H_x| > 700\,\mathrm{Oe}$ but a change in conductivity is not observed.

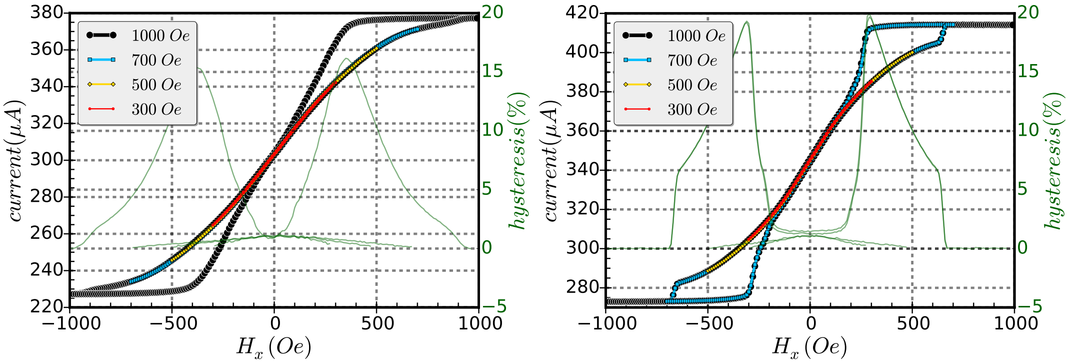

**(a)** CoFe **(b)** CoFeB

**Figure 3.8.** Hysteresis loops of resistor elements with 1170 spin-valves ($d = 1.1\,\mu\mathrm{m}$ and $t = 35\,\mathrm{nm}$, connected in series and in parallel) for different field ranges.

## 3.2 Experimental Methods

### 3.2.1 Electrical Characterization of Spin-Valve Structures

Spin-valve structures were characterized in a quadrupole magnet setup which is shown in Figure 3.9. The setup is capable of applying magnetic fields up to approximately 2000 Oe. The maximum applied field was typically between 1000 and 1200 Oe, depending on the annihilation field of the investigated structures. Sweep rates were in the range of 50 to 100 Oe/s. Measurements were performed either at 35 °C (standard setting) or at 150 °C by heating the chuck on which the wafer was placed. The quadrupole magnet was used in combination with a UF-200 prober from TSK. A needle card, which is required to contact the device under test (DUT), was installed at the DUT position (not shown). Functional testing and calibration were periodically done by using Hall sensors. The difference between the actual and the set value of the magnetic field was below 1 % (Milan Agrawal, personal communication, June 1, 2018).
Single and dual disk structures were measured at a bias voltage of 100 mV while resistor elements (30 MTJs connected in series) were measured at a bias voltage of 1.0 V. Consequently, the voltage drop across one MTJ was between 30 and 100 mV.

Analysis of the data was done with a self-written, object-oriented Python program with a graphical user interface (GUI) - the *xMR Kraken*. Its GUI is shown in Figure 3.10. The *Kraken* allows the grouping and sorting of experimental data sets by different attributes, such as module, maximum applied field, or temperature. This is done by using a table based widget (green frame in Figure 3.10). Selected data sets are plotted

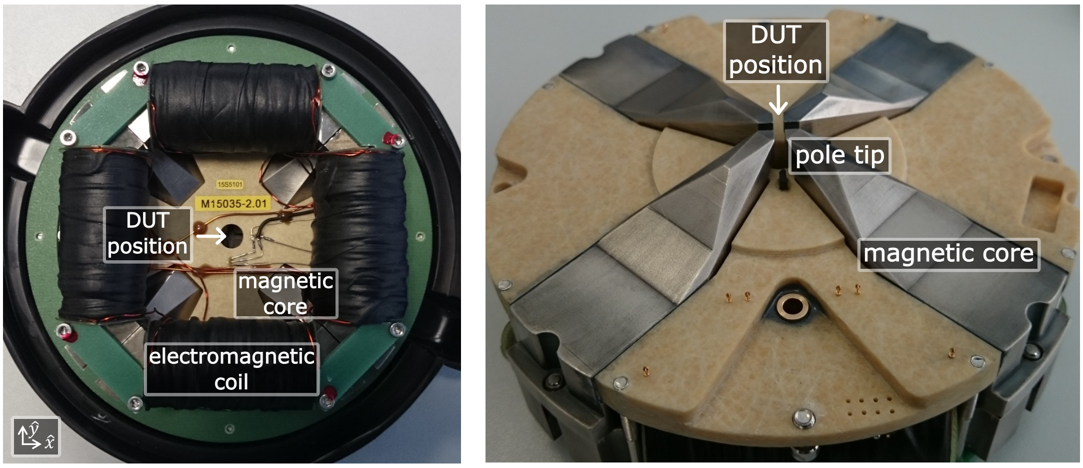

**(a)** **(b)**

**Figure 3.9.** (a) Quadrupole magnet setup in top view. The four electromagnetic coils in combination with the magnetic cores allow to apply any angle of magnetic in-plane field ($\hat{x}$-$\hat{y}$-plane) at the position of the device under test (DUT). (b) The bottom view of the quadrupole magnet setup shows the shape of the cores and the DUT position in more detail.

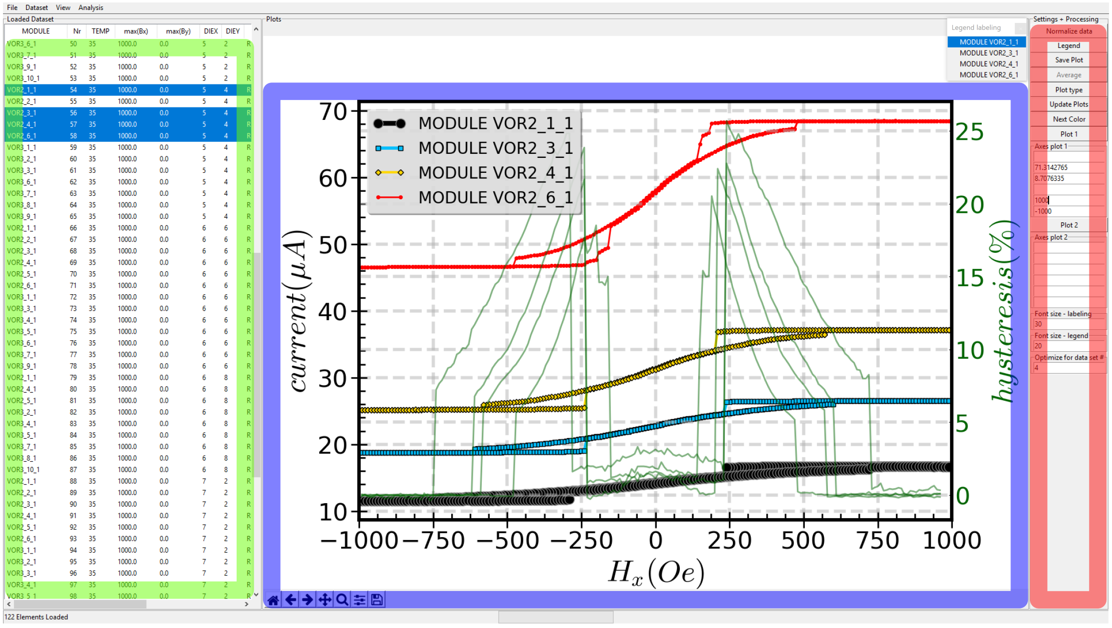

| MODULE | Nr | TEMP | max(Bx) | max(By) | DIEX | DIEY | |
|---|---|---|---|---|---|---|---|
| VOR3_6_1 | 50 | 35 | 1000.0 | 0.0 | 5 | 2 | R |
| VOR3_7_1 | 51 | 35 | 1000.0 | 0.0 | 5 | 2 | R |
| VOR3_9_1 | 52 | 35 | 1000.0 | 0.0 | 5 | 2 | R |
| VOR3_10_1 | 53 | 35 | 1000.0 | 0.0 | 5 | 2 | R |
| VOR2_1_1 | 54 | 35 | 1000.0 | 0.0 | 5 | 4 | R |
| VOR2_2_1 | 55 | 35 | 1000.0 | 0.0 | 5 | 4 | R |
| VOR2_3_1 | 56 | 35 | 1000.0 | 0.0 | 5 | 4 | R |
| VOR2_4_1 | 57 | 35 | 1000.0 | 0.0 | 5 | 4 | R |
| VOR2_6_1 | 58 | 35 | 1000.0 | 0.0 | 5 | 4 | R |
| VOR3_1_1 | 59 | 35 | 1000.0 | 0.0 | 5 | 4 | R |
| VOR3_2_1 | 60 | 35 | 1000.0 | 0.0 | 5 | 4 | R |
| VOR3_3_1 | 61 | 35 | 1000.0 | 0.0 | 5 | 4 | R |
| VOR3_6_1 | 62 | 35 | 1000.0 | 0.0 | 5 | 4 | R |
| VOR3_7_1 | 63 | 35 | 1000.0 | 0.0 | 5 | 4 | R |
| VOR3_8_1 | 64 | 35 | 1000.0 | 0.0 | 5 | 4 | R |
| VOR3_9_1 | 65 | 35 | 1000.0 | 0.0 | 5 | 4 | R |
| VOR2_1_1 | 66 | 35 | 1000.0 | 0.0 | 6 | 6 | R |
| VOR2_2_1 | 67 | 35 | 1000.0 | 0.0 | 6 | 6 | R |
| VOR2_3_1 | 68 | 35 | 1000.0 | 0.0 | 6 | 6 | R |
| VOR2_4_1 | 69 | 35 | 1000.0 | 0.0 | 6 | 6 | R |
| VOR2_5_1 | 70 | 35 | 1000.0 | 0.0 | 6 | 6 | R |
| VOR2_6_1 | 71 | 35 | 1000.0 | 0.0 | 6 | 6 | R |
| VOR3_1_1 | 72 | 35 | 1000.0 | 0.0 | 6 | 6 | R |
| VOR3_3_1 | 73 | 35 | 1000.0 | 0.0 | 6 | 6 | R |
| VOR3_4_1 | 74 | 35 | 1000.0 | 0.0 | 6 | 6 | R |
| VOR3_5_1 | 75 | 35 | 1000.0 | 0.0 | 6 | 6 | R |
| VOR3_6_1 | 76 | 35 | 1000.0 | 0.0 | 6 | 6 | R |
| VOR3_7_1 | 77 | 35 | 1000.0 | 0.0 | 6 | 6 | R |
| VOR3_9_1 | 78 | 35 | 1000.0 | 0.0 | 6 | 6 | R |
| VOR2_1_1 | 79 | 35 | 1000.0 | 0.0 | 6 | 8 | R |
| VOR2_4_1 | 80 | 35 | 1000.0 | 0.0 | 6 | 8 | R |
| VOR2_5_1 | 81 | 35 | 1000.0 | 0.0 | 6 | 8 | R |
| VOR3_2_1 | 82 | 35 | 1000.0 | 0.0 | 6 | 8 | R |
| VOR3_4_1 | 83 | 35 | 1000.0 | 0.0 | 6 | 8 | R |
| VOR3_5_1 | 84 | 35 | 1000.0 | 0.0 | 6 | 8 | R |
| VOR3_7_1 | 85 | 35 | 1000.0 | 0.0 | 6 | 8 | R |
| VOR3_8_1 | 86 | 35 | 1000.0 | 0.0 | 6 | 8 | R |
| VOR3_10_1 | 87 | 35 | 1000.0 | 0.0 | 6 | 8 | R |
| VOR2_1_1 | 88 | 35 | 1000.0 | 0.0 | 7 | 2 | R |
| VOR2_2_1 | 89 | 35 | 1000.0 | 0.0 | 7 | 2 | R |
| VOR2_3_1 | 90 | 35 | 1000.0 | 0.0 | 7 | 2 | R |
| VOR2_4_1 | 91 | 35 | 1000.0 | 0.0 | 7 | 2 | R |
| VOR2_5_1 | 92 | 35 | 1000.0 | 0.0 | 7 | 2 | R |
| VOR2_6_1 | 93 | 35 | 1000.0 | 0.0 | 7 | 2 | R |
| VOR3_1_1 | 94 | 35 | 1000.0 | 0.0 | 7 | 2 | R |
| VOR3_2_1 | 95 | 35 | 1000.0 | 0.0 | 7 | 2 | R |
| VOR3_3_1 | 96 | 35 | 1000.0 | 0.0 | 7 | 2 | R |
| VOR3_4_1 | 97 | 35 | 1000.0 | 0.0 | 7 | 2 | R |
| VOR3_5_1 | 98 | 35 | 1000.0 | 0.0 | 7 | 2 | R |

122 Elements Loaded

Axes plot 1: 71.3142765, 8.7076335, 1000, -1000

Font size - labeling: 30

Font size - legend: 20

Optimize for data set #: 4

**Figure 3.10.** Graphical user interface of the *xMR Kraken* which was used to evaluate and plot the experimental data. The three main widgets are marked: table with loaded data sets (green frame), plot (blue frame), and settings (red frame).

in the central widget (blue frame) and can be adjusted and analyzed (red frame). In Figure 3.10, the hysteresis is additionally plotted and the attribute 'module' is chosen for the generation of the legend. The disk diameter increases from "`MODULE VOR2_1_1`" (black) to "`MODULE VOR2_6_1`" (red), which is why $H_{an}$ and $H_n$ decrease and the current increases (constant bias voltage of 100 mV).

For the typical presentation of the experimental data, full hysteresis loops were normalized to [-1,1]. This allows a direct comparison between experimental data (conductivity) and simulated data ($m_x$) [129]. The vortex critical fields - $H_n$ and $H_{an}$ - were also extracted via the *Kraken*. The algorithm was optimized to detect the jumps in signal into the saturated state ($H_{an}$) and into the vortex state ($H_n$). Consequently, the *Kraken* was used to evaluate the data of single or dual disk spin-valve structures. In case of resistor elements, such jumps do not occur due to the distribution of the critical fields and an analysis of the hysteresis is expected to be the appropriate approach. The extracted critical field values were checked manually before further processing.

### 3.2.2 Imaging of the Vortex State

The vortex state can be directly depicted with techniques, such as scanning magnetoresistive microscopy (SMRM) [141, 142] and magnetic force microscopy (MFM). SMRM utilizes a hard disk drive read/write head (RWH) to perform a raster scan in direct contact with the sample surface allowing a lateral resolution of the out-of-plane (stray) field of about 50 nm [143]. In Figure 3.11a, the SMRM image of a CoFeB disk shows in

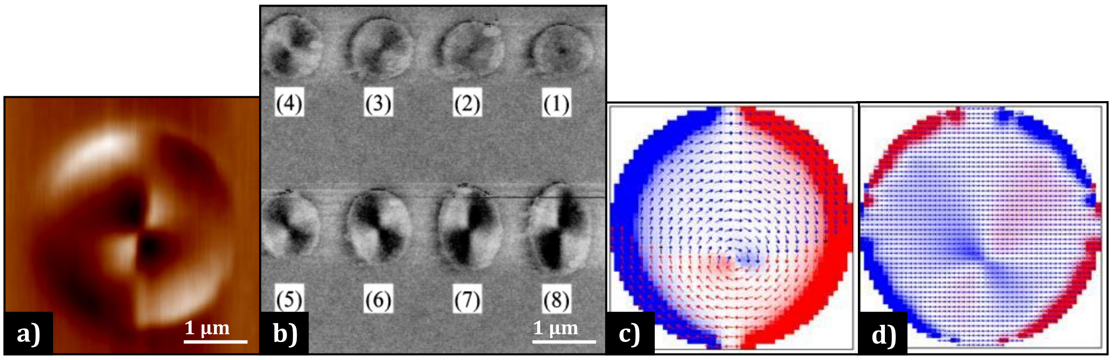

**Figure 3.11.** (a) Zero field SMRM image of a TMR spin-valve with a CoFeB FL disk ($d = 3.1\,\mu\mathrm{m}$ and $t = 50\,\mathrm{nm}$). (b) MFM image of circular (1) and elliptical (2-8) permalloy dots ($t = 50\,\mathrm{nm}$ and short axis $1\,\mu\mathrm{m}$). Reprinted from *Journal of Magnetism and Magnetic Materials,* Vol. 240 Issue 1-3, T. Okuno et al., ©2002 [140], with permission from Elsevier. (c-d) The simulated stray field (at $H_x \neq 0$) of a disk structure, together with the underlying SAF of the spin-valve, is forming dipoles with the out-of-plane component (c) and quadrupoles with the in-plane component (d). (c-d) From Hubert Brückl (unpublished).

the center a pattern which is typically obtained for a Bloch point (see e.g. [143]). This pattern may contradict the initial expectation that only the $\hat{z}$-component of the vortex core itself is visible. Nevertheless, the image shows a symmetric pattern, which allows to locate the position of the vortex core in the center of the disk. Similar vortex images were reported for MFM measurements of slightly elliptical disk shapes by Okuno et al. [140]. They demonstrated that the vortex core itself only shows a high contrast in a circular-shaped disk element (see (1) in Figure 3.11b), but when a small shape anisotropy is introduced a drastic change of the stray field pattern is observed (see (2-8) in Figure 3.11b). Such quadrupole patterns of vortices were also observed in rectangular-, square-, or triangular-shaped elements [144–146]. In Figure 3.11a, the pictured structure has a circular shape but it was observed that the SAF introduces a small anisotropy: simulations of the full stack (including the SAF) showed that the stray field of the SAF (approximately 10 - 15 Oe on average) induces a small biasing of the free layer magnetization, which is consistent with the experimentally observed shift of the hysteresis loops. Such a small anisotropy may thus explain the observed quadrupole pattern in the center. Furthermore, the stray field of the reference system may explain the reversed quadrupole pattern at the edge of the disk. Finally, it should be noted that a tilting of the RWH (the SMRM sensor becomes sensitive to in-plane fields) cannot be fully excluded. Stray fields of a disk structure on top of a reference system are plotted in Figure 3.11c and d, showing a quadrupole pattern for the in-plane component.

## 3.3 Simulations Methodology

The static package of the software *MicroMagus* was used to perform micro-magnetic simulations. Its code is based on the finite difference method (FDM) and takes into account $E_{\text{Zeeman}}$, $E_{\text{exch}}$, $E_{\text{aniso}}$, and $E_{\text{demag}}$ to minimize $E_{\text{tot}}$ of a static magnetic state [147, 148]. The basic task of micro-magnetic simulations is to find the minimum of $E_{\text{tot}}$ numerically, coming from a certain magnetic configuration. The minimum may be the global minimum, but it is also possible that a local minimum is found, which is separated from the global minimum by an energy barrier. A variational principle is applied to find the minimum of $E_{\text{tot}}$ [31, 36], which means that the magnetization is changed iteratively until no further decrease of $E_{\text{tot}}$ is observed. More insight into numerical micro-magnetism is given elsewhere [149–152].

A comparison with micro-magnetic simulations based on the finite element method (FEM, see e.g. [153]) generally showed the same results. However, especially vortex nucleation as well as the formation of intermediate states is sensitive to edge roughness, which is intrinsically existent in FDM micro-magnetic simulations due to the discretization of the grid. If no additional edge roughness is applied in FEM simulations, edge related pinning effects may be underestimated for circular shapes, and thus vortex nucleation occurs much earlier compared to FDM and to the experiment.

All performed simulations started with the saturated state. The applied magnetic in-plane field was rotated by 1° with respect to the $\hat{x}-$direction. It has been shown that such a small modification of the field axis affects the magnetic behavior drastically if there are element borders which are parallel to the simulation grid [154]. Unless otherwise stated, the discrete element unit cell was $\leqslant 5 \times 5 \times 5\,\text{nm}^3$. Standard simulation parameters for the investigated materials are given in Table 3.1. A more precise material specific adaption of the exchange stiffness constant $A$ was not required due to the relatively large diameter of the investigated disk structures and the consequently small effect of $E_{\text{exch}}$ (see Figure 2.7b in Section 2.3.2). A detailed analysis of the different material parameters and their impact on the vortex state is given in Section 4.2.

**Table 3.1.** Standard simulation parameter sets. Acronyms as follows: Saturation magnetization ($M_s$), exchange stiffness constant ($A$), uniaxial magneto-crystalline anisotropy constant ($K_1$), and average crystal grain size ($D_{\text{grain}}$).

| **material** | $M_s$ (emu/cm$^3$) | $A$ (µerg/cm) | $K_1$ (erg/cm$^3$) | $D_{grain}$ (nm) | disturbed edge (nm) |
|---|---|---|---|---|---|
| **CoFeB** | 1038 | 1.53 | - | - | 15 |
| **CoFe** | 1240 | 1.53 | $5 \times 10^5$ | 20 | - |
| **NiFe** | 770 | 1.53 | - | - | - |

# 4 Experimental Results - Intrinsic Factors

In this chapter, intrinsic factors such as disk diameter, thickness, material and process influence (e.g. roughness) will be discussed. It is investigated how the critical fields $H_n$ and $H_{an}$ are affected by these factors as well as how intermediate pre-vortex states are influenced. Some of these factors additionally affect the hysteresis loop of individual disk structures. The magneto-crystalline anisotropy of CoFe, for example, can lead to negative hysteresis.

## 4.1 Disk Dimensions - Diameter and Thickness

The influence of the dimensions of the disk-shaped free layer on the vortex state, and especially on its formation, is investigated in this section. The focus here is on micrometer sized elements. The smallest processed elements were roughly about 700 to 800 nm in diameter ($d$), the largest 4 µm. The thickness ($t$) was varied between 10 and 50 nm. Thus, all of the investigated structures favor the vortex state as magnetic ground state. CoFeB was used as free layer material.

In Section 4.1.2, a high correlation between the aspect ratio $d/t$ and the critical fields $H_n$ and $H_{an}$ is reported for a free layer thickness of 35 and 50 nm. The correlation is linked to the scaling of stray field of the saturated disk (see Section 4.1.3). For $t = 20\,\text{nm}$ such a correlation of the vortex nucleation field is not observed. This nonlinear behavior of the nucleation field as a function of $t$ is investigated in Section 4.1.4. In Section 4.1.5, different nucleation modes with different pre-states are extracted from micro-magnetic simulations. The obtained results agree well with the experimental measurements (see Section 4.1.6). It is shown that the modes are mainly dependent on thickness. Through the differentiation into the different nucleation modes it is shown statistically which intermediate configurations have an increased stability and thus cause a delay of vortex nucleation. In addition, thickness-dependent effects of the shape and symmetry of the vortex core are investigated in Section 4.1.7.

### 4.1.1 Fields of Research

There are already many publications investigating the influence of the disk dimensions on the vortex state. For the subsequent investigation, the different aspects of the influence of the disk dimensions will be divided into three categories: **phase diagrams**, **critical fields** and **nucleation modes**. The new aspects of this work will be highlighted at the end of this section.

**Phase diagrams** as a function of $t$ and $d$ were obtained experimentally [52, 61, 155] and analytically or via micro-magnetic simulations [74, 75, 156–159]. Below a lateral size of about 40 nm a permalloy disk element will definitely be in a uniformly magnetized single-domain state, either in-plane or out-of-plane, depending on the thickness [155]. For larger diameters, the vortex state will be present as a remanent state for a sufficiently large thickness: a thickness of approximately 30 nm is required for $d = 40$ nm [155, 157]. With increasing disk diameter the required minimum thickness to favor vortex nucleation decreases, for example, it is around 10 to 20 nm for $d = 300$ nm [52, 61], depending on the material, and further decreasing with increasing diameter. This trend results from the increasing influence of the stray field energy ($E_{\mathrm{demag}}$): an out-of-plane rotation of the magnetization leads to a local increase of the exchange stiffness energy ($E_{\mathrm{exch}}$) mainly in the area of the vortex core. Thus, $E_{\mathrm{exch}}$ of the vortex core is independent of the lateral size by first approximation. Moreover, the stray field generated by the remanent vortex state is mainly caused by the vortex core and consequently is also nearly constant. In contrast, $E_{\mathrm{demag}}$ of the single domain state increases both with lateral size and with thickness. As a result, smaller elements require a larger thickness in order to increase $E_{\mathrm{demag}}$ of the single domain state and thus favor vortex nucleation.

For thickness values smaller than the required minimum to favor vortex nucleation the presence of a single domain state is just an approximation: diameters in the range of hundreds of nanometers up to micrometers favor as remanent magnetization, for example, the leaf state (also called onion state [158]) or C-state. These states will perform a (coherent) rotation during field reversal, similar to a single domain particle [61]. Micro-magnetic simulations showed that for a disk structure of 100 nm diameter and thickness a lateral vortex may be present at zero field[1] [158].

So far, the requirements regarding thickness and minimum diameter were addressed. Regarding the maximum diameter a well-founded limitation cannot be given. The vortex state has been observed in disk structures with 120 µm diameter [44].

Schneider et al. were one of the first to investigate experimentally the vortex **critical fields** in a systematic manner [57, 64]. They studied $H_n$ and $H_{an}$ of permalloy nanodisks with diameters between 150 and 1000 nm. The film thickness was varied between 3 and 20 nm [64]. It was shown in experiment and simulation that there is a correlation between the critical fields and the aspect ratio (diameter divided by thickness) but the film thickness causes deviations in the correlation which was attributed to the fact that $E_{\mathrm{demag}}$ and $E_{\mathrm{exch}}$ scale differently. Further investigations of the critical fields were done on permalloy [59, 60, 160] and cobalt [53, 60] disk structures covering altogether

---

[1] These results could not be reproduced when another computer code was used but the vortex state will definitely have a significant $\hat{z}$-component for aspect ratios (diameter divided by thickness) around 1 [74]

a thickness range from 3 to 100 nm and a diameter range from 55 to 2000 nm. The behavior of the critical fields was studied analytically by Guslienko et al. [67, 68, 114]. The so-called *rigid vortex model* and modifications of it were already discussed in Section 2.3.2.

The description of intermediate, metastable states, which is referred to as **nucleation modes**, was done for disk structures mostly by combining experimental techniques with micro-magnetic simulations [61, 64, 66, 160–163]. It was observed that the double vortex state needs a certain minimum thickness [66] and minimum diameter [61] to nucleate in a disk structure. With micro-magnetic simulations it has also been shown that magnetic buckling occurs only after exceeding a diameter of 200 nm [164]. Ha et al. put a lot of effort in a phase diagram of the remanent states but only for diameters equal or below 500 nm [158]. No publication was found which describes in depth the different phases of intermediate, metastable states, such as C-, S-, and double vortex state, as a function of disk diameter and thickness. On the contrary, only statements about the gap in knowledge were found: "The theoretical expression of the size-dependent transition between different nucleation modes still remains to be deduced." [68] "Apart from the double-vortex state, which only occurred in larger disks with a minimum thickness of 40 nm, we found in experiment no clear correlation between the disk size and a specific nucleation mode." [66]

The new aspects of this work are the following: in Section 4.1.5, it is shown how the different intermediate states prior to vortex nucleation are affected mainly by the thickness but the trend versus diameter is given as well. It is also shown how the different metastable states affect $H_n$. The analysis of $E_{\mathrm{demag}}$ of the saturated disk as a function of $t$, given in Section 4.1.4, is providing further insights into the mechanisms that are driving vortex nucleation. The obtained results - a shift from side surface charges to face surface charges with increasing thickness - can explain why for $t = 20\,\mathrm{nm}$ no correlation of $H_n$ as a function of $d$ is observed. Furthermore, these results are also expected to help to further develop analytical vortex models.

### 4.1.2 Lateral Size and Aspect Ratio

Figure 4.1 summarizes the extracted $H_n$ and $H_{an}$ values for three different thicknesses (20, 35 and 50 nm) and disk diameters between 700 nm and 4.1 µm. Simulations were additionally performed for the complete diameter series with $t = 35\,\mathrm{nm}$. The results are in good agreement with the experimental data. Only for $d = 2.5\,\mu\mathrm{m}$ a significantly delayed vortex nucleation is observed in the simulation, which is caused by an unusually stable double vortex state. Such stable double vortices were observed in the experiment only for CoFe (see Figure 4.32 in Section 4.2.3). Consequently, the discrepancy observed here is attributed to the missing thermal excitation in the simulations.
The shown simulation results were tested through additional cross check simulations, in

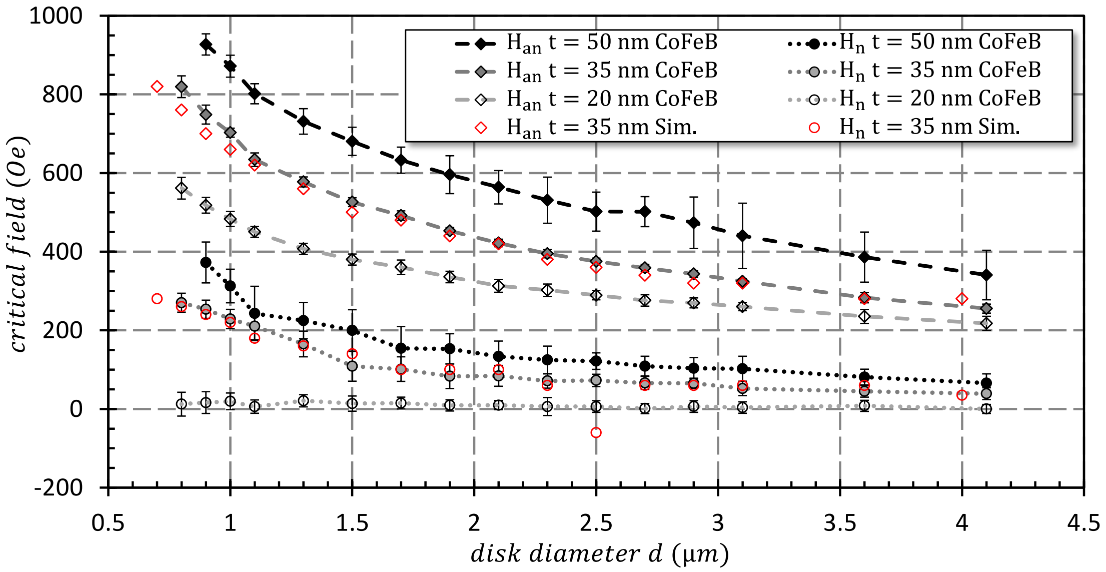

**Figure 4.1.** Critical fields $H_n$ and $H_{an}$, extracted from three CoFeB diameter-series, each with a different free layer thickness $t$. One experimental data point represents between six and 25 individually measured dual-disk devices at different positions on the wafer. Simulations were performed with 20 Oe field steps in the range of the expected critical fields. Standard simulation parameters for CoFeB are given in Section 3.3. For 2.7 - 3.6 µm diameter the discrete element unit cell was $\leqslant 7.4 \times 7.4 \times 5\,\mathrm{nm}^3$ to limit the increasing computing time with increasing diameter.

total for seven different diameters with different grids and grid-resolution. (Regarding the influence of discretization and edge roughness see Section 4.2.11.) In this process, an average deviation of the critical field values of 24 Oe was obtained which is in the same range as the simulation field step size of 20 Oe. The maximum shift of $H_n$ was observed for the 2.5 µm disk with the initially delayed vortex nucleation: $H_n$ was shifted in the cross check by 120 Oe and thus achieving congruence with the experimental average value. It is referred to Section 4.2 regarding the approach how the material parameters for the simulations were obtained.

In order to illustrate the scaling of the critical fields the same data set as shown in Figure 4.1 is plotted as a function of the inverse aspect ratio $t/d$ in Figure 4.2. It has to be noted that the critical fields are often plotted vs. the aspect ratio $r = d/t$ [57, 59, 60, 64, 68] but this type of display has the drawback that no linear trends are observed. Figure 4.2 clearly shows that $H_{an}$ universally scales with the aspect ratio. This scaling applies also to $H_n$, but only for 35 and 50 nm film thickness. $H_n$ of 20 nm thick elements is discussed in Section 4.1.5. An additional parameter is introduced in Figure 4.2: $H_0$ reflects the field value where the corresponding vortex state and non-vortex state (after annihilation) are energetically equivalent. $H_0$ was extracted from simulations and has the same $1/r$ trend as shown in Figure 4.2. The reason why vortex nucleation does not occur at $H_0$ is because the two states are separated by an energy barrier: the required reversal of magnetization of half of the disk leads to an increase of $E_{\mathrm{Zeeman}}$, but at the same time causes an almost negligible decrease of $E_{\mathrm{demag}}$ (at the beginning of the rotation). The

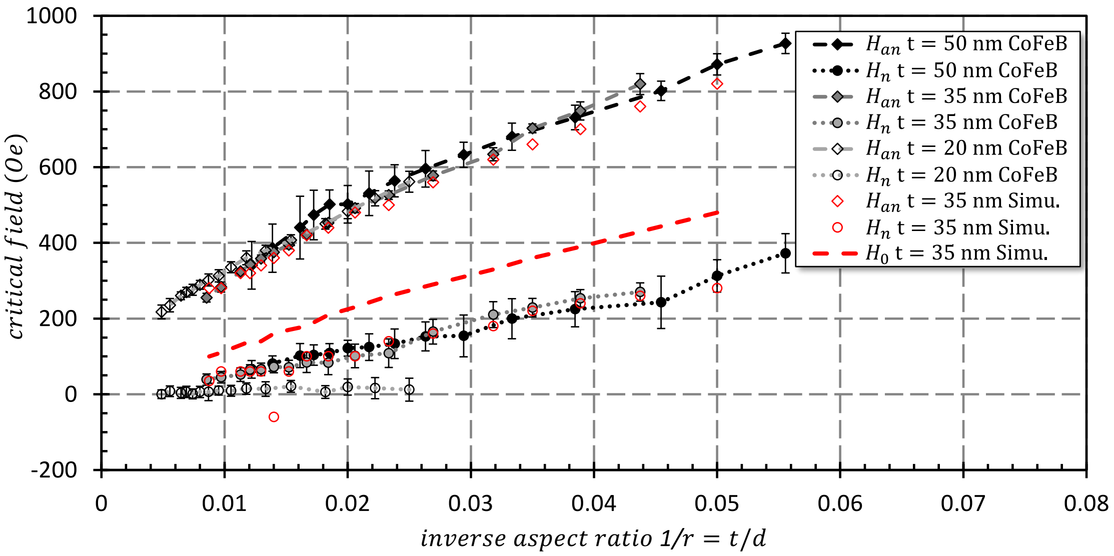

**Figure 4.2.** Critical fields $H_n$ and $H_{an}$ as a function of the inverse aspect ratio. Plotted is the same data set which was shown in Figure 4.1. In addition $H_0$, the field value where the vortex state becomes equally favorable as the pre-nucleation magnetization pattern, is plotted. Simulation parameters are given in the caption of Figure 4.1.

resulting energy barrier is thus decreasing with decreasing field until it vanishes at $H_n$ facilitating vortex nucleation.

The observed correlation of $H_{an}$ - a universal scaling as a function of the aspect ratio and in particular independent on absolute thickness - is in contrast to the observation of Schneider et al. for the same aspect ratio range (see Figure 6 in [64]). This is due to the fact that Schneider et al. investigated disks with a thicknesses $t \leq 20\,\mathrm{nm}$.

Finally, it has to be noted that experimental data measured at 308 K was compared to simulations performed at 0 K. The small difference between both data sets indicates that the influence of thermally assisted barrier jumps is comparatively low. A more detailed investigation of the temperature influence is given in Section 5.2.

To summarize, it was shown that $H_{an}$ is scaling with the aspect ratio $\frac{t}{d}$ (disk thickness $t$ and disk diameter $d$). $H_n$ shows the same scaling for 35 and 50 nm thick disk elements but for 20 nm it is not observed. In the next sections, it will be shown that the observed scaling of the critical fields is caused by the scaling of $E_{\text{demag}}$ of the saturated disk structure. In Section 4.1.5 and 4.1.6, it will be demonstrated that the formation of certain thickness-dependent pre-vortex states affects the trend of $H_n$ additionally.

### 4.1.3 Collapse and Estimated Stray Field of the Saturated State

On the next pages, a derivation is presented which estimates the magnetic field at which the magnetization of a saturated disk is expected to collapse with a further reduction of the applied magnetic field. This explains why $H_n$ is proportional to $t/d$. It is known that the critical fields - $H_n$ and $H_{an}$ - are directly correlated with the stray field

[49, 53]. The following assumptions were made to estimate the collapse of the saturated state:

- The starting point is a saturated ferromagnetic disk element.
- The saturated state is also present for an external field $|H_{\mathrm{ext}}| < |H_{an}|$.
- With decreasing $|H_{\mathrm{ext}}|$ the vortex nucleation is completed at zero field at the latest, if at all.
- The previous assumption allows the conclusion that at zero field, not only $E_{\mathrm{Zeeman}}$ is zero but also $E_{\mathrm{demag}}$ (neglecting the magnetization of the core).
- In Section 2.3.1, it was shown that for a disk with $d = 1.1\,\mu\mathrm{m}$ and $t = 35\,\mathrm{nm}$ the exchange stiffness energy $E_{\mathrm{exch}}$ is about one order of magnitude smaller than the stray field energy $E_{\mathrm{demag}}$. It is therefore a reasonable simplification to neglect $E_{\mathrm{exch}}$.
- $E_{\mathrm{demag}}$ of a saturated disk structure is by first approximation constant when changing the external field.

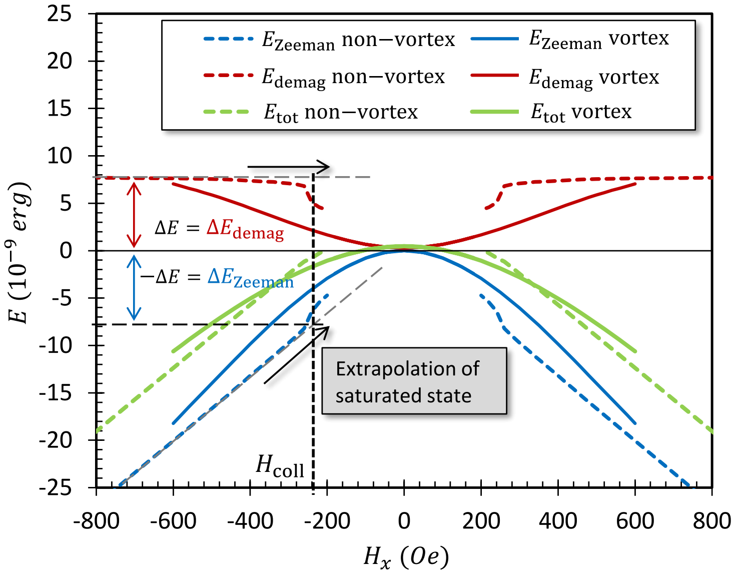

**Figure 4.3.** The energy levels of the different energy terms for a simulated hysteresis loop of a ferromagnetic disk structure with 1.1 µm diameter and 35 nm thickness (see also Figure 2.7). In the extrapolation of the saturated state the crossing of $E_{\mathrm{Zeeman}}$ with $-\Delta E$ determines $H_{\mathrm{coll}}$. If it is assumed that (1) the vortex state is present at zero field - meaning that $E_{\mathrm{demag}}(H_x = 0) \approx E_{\mathrm{Zeeman}}(H_x = 0) = 0$ - and that (2) the saturated state is still present at $H_{\mathrm{coll}}$, it can be concluded that for $|H_x| < |H_{\mathrm{coll}}|$: $\left|\frac{\partial E_{\mathrm{demag}}}{\partial H_x}\right| > \left|\frac{\partial E_{\mathrm{Zeeman}}}{\partial H_x}\right|$. This fact is driving vortex nucleation as the possible total decrease of $E_{\mathrm{demag}}$ as well as its average gradient are larger than the increase and gradient of $E_{\mathrm{Zeeman}}$. Simulation parameters are given in the caption of Figure 4.1.

If $H_{\text{ext}}$ is reduced, a critical field value is reached where the saturated state is expected to collapse for reasons of energy minimization. This field value - $H_{\text{coll}}$ - is defined by the following relation:

$$-E_{\text{Zeeman}} = E_{\text{demag}} \Rightarrow H_{\text{coll}} = \frac{H_{\text{demag}}}{2} \tag{4.1}$$

For all values below $H_{\text{coll}}$, the total possible reduction of $E_{\text{demag}}$ is larger than the possible increase of $E_{\text{Zeeman}}$ and thus a collapse of the (nearly) saturated state should occur. This fact is illustrated in Figure 4.3. The grey dashed lines represent the energy extrapolation of the saturated state. The intersection of the extrapolated $E_{\text{Zeeman}}$ energy with $-\Delta E$ represents $H_{\text{coll}}$ and explains well the collapse of the buckling pattern, which is observed in the simulation.

This simple model does not take into account additional intermediate states which form before or after reaching $H_{\text{coll}}$. However, since the vortex state is expected to have the smallest stray field energy, $H_{\text{coll}}$ seems to be a good measure of $H_n$, as illustrated in Figure 4.3. Nevertheless, it must be emphasized that this model does not take into account energy barriers which may result from the formation of intermediate states. Accordingly, it is observed in Figure 4.3 that $H_n < H_{\text{coll}}$, in this particular case due to the formation of the double vortex state.

Furthermore, it was demonstrated in Figure 4.2 that the critical fields, $H_{an}$ and $H_n$, scale with the aspect ratio in the same manner as $H_0$ does[2]. Since $H_0$ is also derived from energetic considerations it is assumed that $H_{\text{coll}}$ has to show the same scaling. Fernandez and Cerjan already demonstrated a linear correlation for elliptical elements with different lateral size and thickness between the (modeled) stray field (of the uniformly magnetized ellipsoids) and $H_n$ and $H_{an}$, respectively [53]. Consequently, an investigation of the scaling of $H_{\text{demag}}$ explains the scaling of $H_n$ and $H_{an}$. The exchange stiffness energy is neglected in this simple model and therefore, it is only valid for large enough elements.

For an estimation of $H_{\text{coll}}$, one possibility is to look up the demagnetizing factor for an elliptical particle (see e.g. [36] p. 118-121) but at this point, a derivation of the stray field leads to a deeper understanding and thus enables a better interpretation for further discussions of different magnetic states.

For reasons of simplification, the stray field of a saturated disk structure at $H_{\text{ext}} \approx H_{an}$ is investigated. It has to be noted that transferring this magnetization pattern to $H_{\text{coll}}$ may not be valid for all aspect ratios and thicknesses. However, the trend of the stray field energy below $H_{an}$ (see Figure 4.3) demonstrates that this approximation is reasonable.

Figure 4.4a shows the magnetization of a saturated disk structure. The in-plane ($\hat{x}$-$\hat{y}$-plane) magnetization of this state is shown in top view. Note that in this illustration,

---

[2] This applies to the investigated aspect ratio range. For smaller values deviations are expected, as the comparison between the $1/r$ trend and the trend of $H_0$ is indicating (see Figure 4.2).

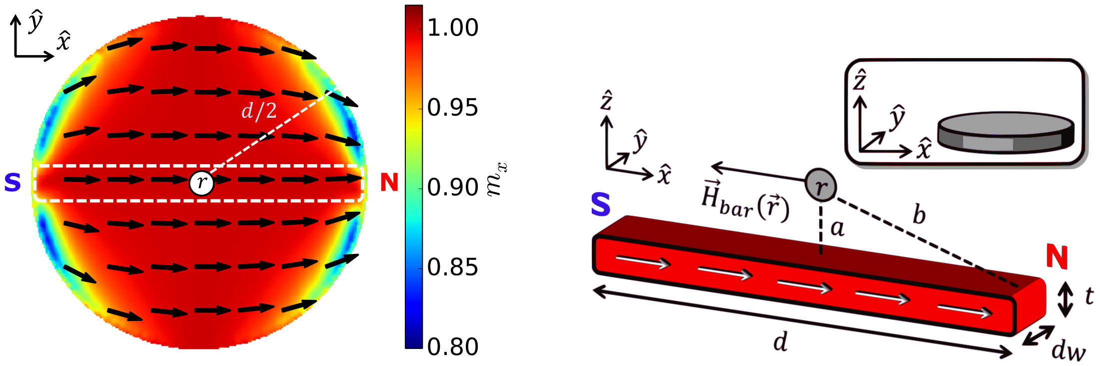

**(a)** Top view **(b)** Side View

**Figure 4.4.** (a) Saturated disk structure at $H_{\text{ext}} \approx H_{an}$ ($H_x = 600\,\text{Oe}$). Disk dimensions: 35 nm thickness $t$ and 1.1 µm diameter $d$. (b) Detail section of a small part of the disk element, which can be treated in first approximation as a bar magnet. The section is marked in (a) by the central dashed box. Simulation parameters are given in the caption of Figure 4.1.

$m_x$ is restricted to the interval $[\,0.8, 1.0\,]$, which allows a more detailed display of the deviation from a completely saturated element. It is observed here that $m_x \geqslant 0.85$ at the edge of the element. Thus, the assumption of a saturated element ($m_x = 1$) is a reasonable approximation. At the position $r$ (in the center of the disk, see Figure 4.4) the potential of the stray field of the saturated disk is given by the following equation [36]:

$$\Phi_{\text{demag}}(\vec{r}) = M_s \Big[ \int \frac{\lambda_s(\vec{r}\,')}{|\vec{r} - \vec{r}\,'|}\, \mathrm{d}V' + \int \frac{\sigma_s(\vec{r}\,')}{|\vec{r} - \vec{r}\,'|}\, \mathrm{d}S' \Big] = M_s \int \frac{\sigma_s(\vec{r}\,')}{|\vec{r} - \vec{r}\,'|}\, \mathrm{d}S' \tag{4.2}$$

with the volume charge density $\lambda_s = \nabla \cdot \vec{m}$, which is zero for the completely saturated state, and the surface charge density $\sigma_s = \vec{m} \cdot \hat{n}$. Since the small $m_z$-component is neglected an integration over the lateral surface yields the stray field $H_{\text{demag}}(\vec{r})$ of the disk.

For reasons of simplification, the disk can be seen as an array of bar magnets. The two regions of a bar magnet, where the magnetization is pointing in (S) and out (N), can be treated separately. Following relation is obtained for the surface charge density of one pole of the bar magnet: $\sigma_s = \vec{m} \cdot \hat{n} = t\,\mathrm{d}w$, where $t$ is the thickness of the disk and $\mathrm{d}w$ the width of the bar magnet in $\hat{y}$-direction (see Figure 4.4b). With the assumption $a \ll d$ and $t \ll d$ the potential of the stray field of such a bar magnet becomes:

$$\Phi_{\text{bar}}(\vec{r}) \approx 2M_s \int \frac{t}{b}\, \mathrm{d}w \tag{4.3}$$

where both poles of the bar magnet are taken into account and $b$ is the equal distance to the poles (see Figure 4.4b).

The resulting stray field of the bar magnet is given by:

$$\vec{H}_{\mathrm{bar}}(\vec{r}) = \nabla \varPhi_{\mathrm{bar}}(\vec{r}) = -\vec{e_x} 2M_s \int \frac{t}{b^2}\,\mathrm{d}w \tag{4.4}$$

An advantage of this treatment is the fact that $H_{\mathrm{bar}}$ depends only on $M_s$, $t$, and $\mathrm{d}w$, whereas the angle of the lateral surface has in this approximation no impact on $H_{\mathrm{bar}}$. Nevertheless, it must be noted that this equation is only valid for the central position $\vec{r}$ with respect to the disk. For reasons of symmetry, the $\hat{y}$- and $\hat{z}$-component of the stray field are zero at this position. By integrating over the whole disk, one gets:

$$H_{\mathrm{demag},x}(\vec{r}) = -2M_s \int_0^d \frac{t}{b^2}\,\mathrm{d}w = -2M_s \frac{t}{b^2} \cdot d \approx -8M_s \frac{t}{d} \tag{4.5}$$

This equation is valid for $M_s$ in emu/cm$^3$. For the exemplary CoFeB disk ($t = 35\,\mathrm{nm}$ and $d = 1.1\,\mathrm{\mu m}$), a stray field of $H_{\mathrm{demag}} = 8 \cdot 1038 \cdot \frac{35}{1100}\mathrm{Oe} \approx 264\,\mathrm{Oe}$ is obtained. Accordingly, $H_{\mathrm{coll}} = \frac{H_{\mathrm{demag}}}{2} = 132\,\mathrm{Oe}$ is obtained with Equation 4.1, which is approximately half as much as the graphically extracted value in Figure 4.4. The $H_{\mathrm{demag}}$ value obtained by Equation 4.5 is in very good agreement with simulations, as illustrated in Figure 4.5a and 4.5b: for the central point close to the disk center (20 nm above the surface) a value of approximately 270 Oe results from the micro-magnetic simulations.

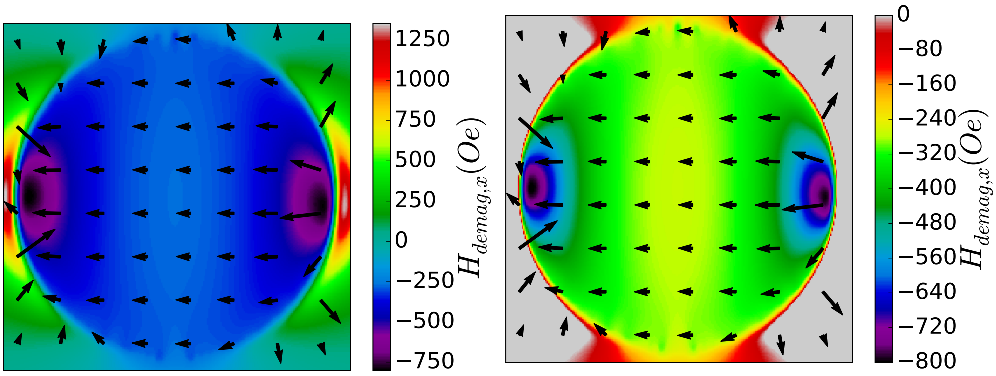

**(a)** full $H_{\mathrm{demag},x}$ range **(b)** $H_{\mathrm{demag},x} < 0$

**Figure 4.5.** (a) $\hat{x}$-component of $H_{\mathrm{demag}}$ of the leaf state (see Figure 4.4a) at $H_{\mathrm{ext}} = H_{an}$ (620 Oe) in 20 nm distance to the disk surface ($d = 1.1\,\mathrm{\mu m}$ and $t = 35\,\mathrm{nm}$). Vectors represent the orientation and magnitude of $\vec{H}_{\mathrm{demag}}$ projected into the $\hat{x}$-$\hat{y}$ plane. (b) Clipping of the positive $H_{\mathrm{demag},x}$ values. Simulation parameters are given in the caption of Figure 4.1. The discrete element unit cell was in-plane $\leqslant 5 \times 5\,\mathrm{nm}^2$ and out-of-plane 7 nm (5 cells in $\hat{z}$-direction) due to limitations in the calculation of the stray field. Reference simulations with 5 nm out-of-plane unit cell size were in good agreement regarding $\vec{m}$.

The difference to the graphically extracted $H_{\mathrm{coll}}$ (see Figure 4.3) originates from various factors: (1) The average stray field is larger than the stray field above the center of the disk as it can be observed in Figure 4.5b. This results from the $\frac{1}{b^2}$ dependence (where b is the distance to the surface charges, see Figure 4.4a). Thus, the larger $H_{\mathrm{demag}}$ at the 'pole regions' cannot be neglected when an exact value of $H_{\mathrm{coll}}$ is determined. (2) The approximation of $\vec{H}_{\mathrm{demag}}$ in 20 nm distance to the disk surface leads to a small mismatch, especially at the edge where maximum fields are observed and thus a maximum in stray field energy density is expected. (3) An increase of surface charges takes place with increasing thickness, which will be discussed in the next section. The resulting increased out-of-plane magnetization at disk edge leads not only to an increase of the surface charge density (see Equation 4.2) but also to an increase of the volume charge density, which was neglected in Equation 4.5.

To summarize, the magnetic field $H_{\mathrm{coll}}$, where the saturated state is expected to collapse, was estimated based on the Zeeman and stray field energy term. The resulting $H_{\mathrm{coll}}$ reproduces $H_n$ very well. Furthermore, an analytical derivation of $H_{\mathrm{demag}}$ above the center of the disk was done for the saturated state and is in very good agreement with the simulated stray field.

### 4.1.4 Stray Field Energy of the Saturated State

Figure 4.6 shows the stray field energy of a saturated disk vs. its thickness. After exceeding a thickness of approximately 30 nm, the trend of $E_{\mathrm{demag}}$ becomes linear as illustrated by the red line which is fitted to the selected values (red dots). For thinner elements, especially below $t = 20$ nm, the behavior of the stray field energy may explain why in the investigation of Schneider et al. $H_{an}$ did not scale with the aspect ratio [64]. Furthermore, small values of $E_{\mathrm{demag}}$ lead to a (relatively) increased influence of $E_{\mathrm{exch}}$ which makes the

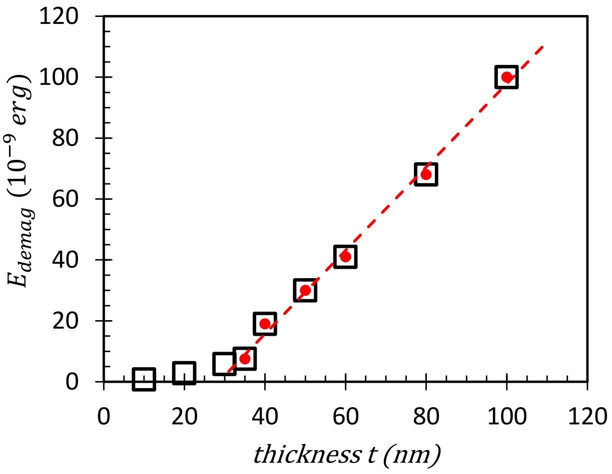

**Figure 4.6.** Stray field energy of simulated saturated disk elements ($d = 1.1\,\mu$m) in an external field $|H_{\mathrm{ext}}| \approx |H_{an}|$. Standard simulation parameters for CoFeB are given in Section 3.3.

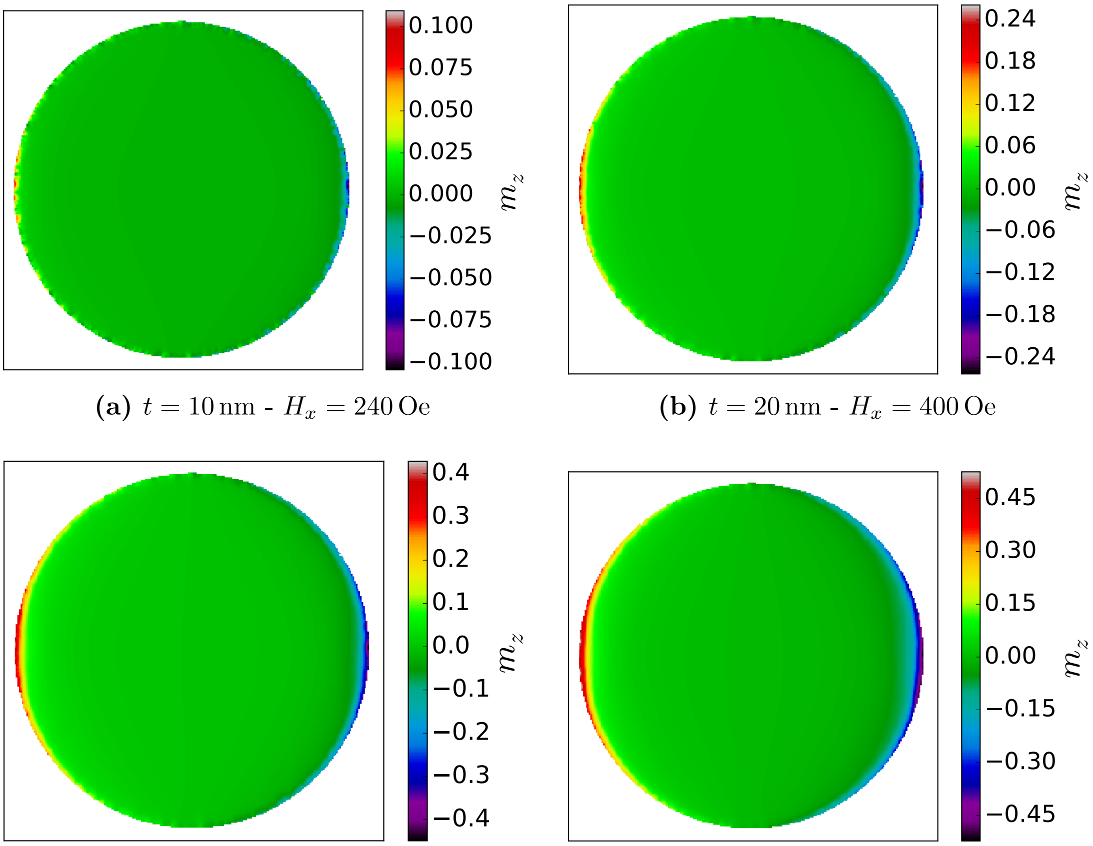

**(a)** $t = 10\,\text{nm}$ - $H_x = 240\,\text{Oe}$ **(b)** $t = 20\,\text{nm}$ - $H_x = 400\,\text{Oe}$

**(c)** $t = 35\,\text{nm}$ - $H_x = 620\,\text{Oe}$ **(d)** $t = 50\,\text{nm}$ - $H_x = 800\,\text{Oe}$

**Figure 4.7.** Out-of-plane magnetization - at the disk surface - of the leaf state (see Figure 4.4a) at $H_{\text{ext}} \approx H_{an}$ for various thicknesses. Note the different color ranges adjusted to minimum and maximum values. All disks have a diameter of 1.1 µm. Standard simulation parameters for CoFeB are given in Section 3.3.

vortex state energetically less favorable and also fits to the data of Schneider et al. In the following, it will be shown that the non-linear trend of $E_{\text{demag}}$ vs. thickness is linked to an increase of $m_z$ at the edge of the disk, which increases the face surface charge density as well as the volume charge density of the saturated state.

Figure 4.7 shows $m_z$ of saturated disk elements in the leaf state (see Figure 4.4a) for a thickness between 10 and 50 nm. For 10 nm (Figure 4.7a), the out-of-plane component of the magnetization is vanishingly small at the edge, too. Furthermore, $|m_z| < 0.12$ for all (static) simulation steps prior to vortex nucleation (not shown because the exact value depends on the step size before nucleation). For 20 nm (Figure 4.7b), $m_z$ is larger at the edge ($|m_z| < 0.26$). Only in the last steps before vortex nucleation, when the externally applied magnetic field is reversed, the out-of-plane magnetization increases: $|m_z| < 0.36$ (not shown). In Figure 4.7c ($t = 35\,\text{nm}$), $m_z$ of the leaf state is further increased: $|m_z| < 0.45$. During the subsequent field steps, $m_z$ is always below 0.5 prior to the double vortex nucleation (not shown). For 50 nm (Figure 4.7d), $m_z$ is only slightly larger at the edge ($|m_z| < 0.52$), but during the subsequent reduction of the external

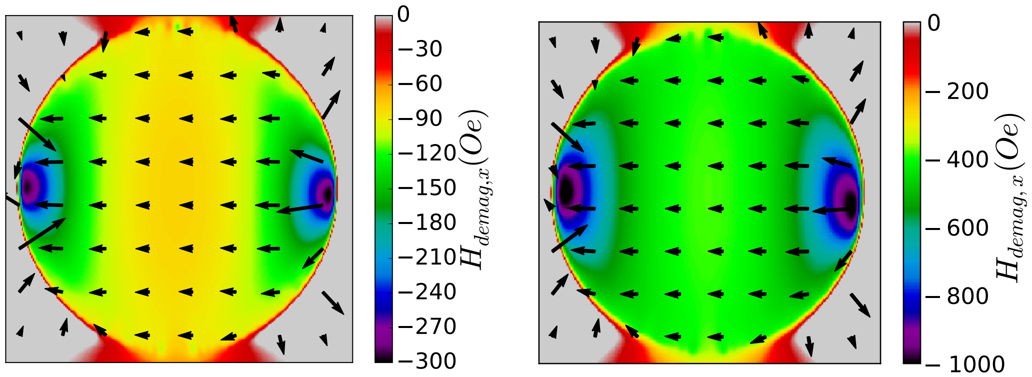

**(a)** $t = 10\,\text{nm}$ **(b)** $t = 50\,\text{nm}$

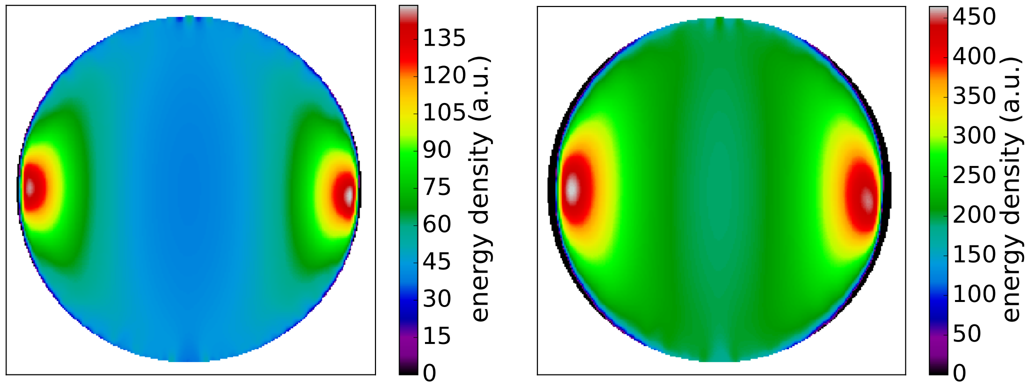

**(c)** $t = 10\,\text{nm}$ **(d)** $t = 50\,\text{nm}$

**Figure 4.8.** (a-b) $\hat{x}$-component of $H_{\text{demag}}$ of the leaf state at $H_{\text{ext}} = H_{an}$ in 20 nm distance to the disk surface. Vectors represent the orientation and magnitude of $\vec{H}_{\text{demag}}$ projected into the $\hat{x}$-$\hat{y}$ plane. (c-d) Corresponding approximated stray field energy density (normalized to $M_s$) at the disk surface: $-\frac{1}{2}\vec{H}_{\text{demag}} \cdot \vec{m}$. Negative values - only observed at the edge mainly due to the approximation ($\vec{H}_{\text{demag}}$ in 20 nm distance) - are clipped. Note the different value ranges adjusted to the according data set. Disk diameter $d = 1.1\,\mu\text{m}$. Standard simulation parameters for CoFeB are given in Section 3.3. The discrete element unit cell was in-plane $\leqslant 5 \times 5\,\text{nm}^2$ and out-of-plane $\leqslant 10\,\text{nm}$ (5 cells in $\hat{z}$-direction), due to limitations in the calculation of the stray field. Reference simulations with 5 nm out-of-plane unit cell size were in good agreement regarding $\vec{m}$.

field $m_z$ gradually increases up to 1.0 (not shown), allowing a steady formation of the double vortex state. In summary, $m_z$ of the leaf state gradually increases at the edge of the disk with thickness of up to approximately 35 nm. This effect explains why for 20 nm thickness, $H_n$ seems to be independent of the aspect ratio (see Section 4.1.2): the formation of an out-of-plane magnetization at the edge is significantly suppressed for 'thin' disk structures which can be seen as an energy barrier for vortex nucleation.
It has to be noted that the trend of $m_z$ vs. thickness at the edge of the disk is not limited to the saturated state: the same trend is observed for the vortex state near $H_{an}$ (not shown) which is why the scaling of $H_{an}$ is independent of the thickness.

The question that now arises is how the increasing $m_z$-component affect $H_{\text{demag}}$ and

$E_{\mathrm{demag}}$. Figure 4.8a and 4.8b show that above the center of the disk, $H_{\mathrm{demag}}$ is scaling nicely with thickness: for $t = 10\,\mathrm{nm}$, $H_{\mathrm{demag}}$ is 80 Oe, and for $t = 50\,\mathrm{nm}$ it is 385 Oe. This is an increase of almost exactly factor five as expected from the disk thickness. Accordingly, the stray field energy density at the surface of the disk is also scaling with thickness in a similar way (see Figure 4.8c and 4.8d). In addition, it can be observed that the difference between maximum energy density (close to the pole region) and average energy density decreases with increasing disk thickness. This fact is attributed to the decrease of the surface charge density on the disk sides as well as a more broadly distributed increase of surface charge density at the disk faces and volume charge density, which is also visible in the stray field plots. The results of Figure 4.8 do not show any unusual increase of $H_{\mathrm{demag}}$ with increasing thickness. It is therefore reasonable to conclude that the observed trend of $E_{\mathrm{demag}}$ vs. $t$ originates from the interaction of the volume magnetization with the stray field. Especially the volume charge density term of the stray field potential (see Equation 4.2), which appears to be negligible when estimating the average stray field, is expected to increase $E_{\mathrm{demag}}$ for larger thicknesses due to the out-of-plane rotation of the magnetization over a large portion of the edge volume of the disk. Further investigations are needed to establish a detailed picture of $H_{\mathrm{demag}}$ and $E_{\mathrm{demag}}$ over the whole volume of the disk.

In summary, it was shown that $E_{\mathrm{demag}}$ of the saturated disk structure shows a non-linear trend for a CoFeB thickness that is smaller than 35 nm. This non-linearity is caused by an increase of $m_z$ at the edge of the disk with increasing thickness. For 20 nm thickness, a low gradient of $E_{\mathrm{demag}}$ vs. thickness is observed that offers an explanation for the question why no scaling of $H_n$ vs. $d$ was observed for this thickness in Section 4.1.2. The observed non-linearity of $m_z$ vs. $t$ may help to improve existing analytical vortex models.

### 4.1.5 Thickness-Dependent Nucleation Modes - Simulations

In this section, the influence of the different thickness-dependent metastable pre-vortex states is investigated and different slopes of trend are derived for $H_n$ vs. $t$. Until now, there has not been a substantiated theory that explains why $H_n$ as a function of disk thickness has sections with different slopes. Different types of vortex nucleation modes - such as C-, S-, and double vortex state - have been reported, but no general correlation with the thickness could be shown for all states, mainly due to the limitations of the investigated systems [55, 61, 64, 66, 68, 113, 160, 162, 163].

In Section 4.1.3, it was shown that an increase of thickness is expected to increase $H_n$ and $H_{an}$ due to an increase of the stray field (see Equation 4.5). Also in analytical models, such as the rigid vortex model (see Section 2.3.2), $H_n$ is expected to scale universally as a function of the aspect ratio and therefore linear with thickness [68]. This universal scaling is based on the assumption that the general type of pre-vortex magnetization does not change. It has already been disproved in the experiment by the non-existent

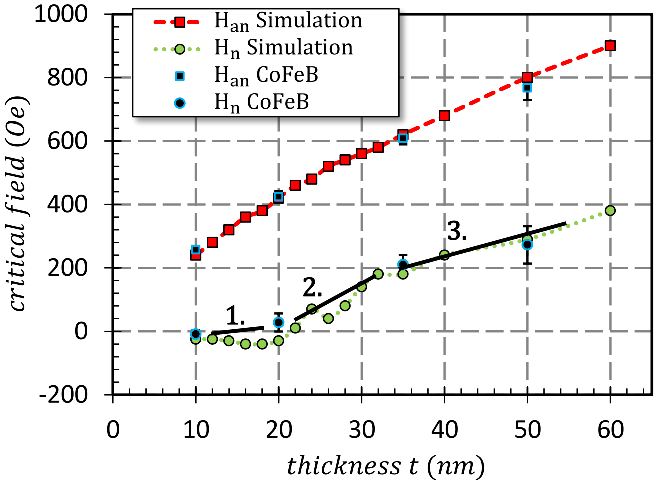

**Figure 4.9.** Critical fields of the vortex state extracted from micro-magnetic simulations and measurements (CoFeB) at individual, disk-shaped TMR structures with 1.1 µm diameter. Simulation parameters for CoFeB are given in Section 3.3.

scaling for 20 nm thickness (see Figure 4.2). Only for $t = 35$ and 50 nm, $H_n$ and $H_{an}$ scale very well with $H_0$, the energy crossing point of the vortex and non-vortex state. It was demonstrated in the previous section that the trend of $E_{\text{demag}}$ vs. $t$ is non-linear up to 35 nm thickness. But $E_{\text{demag}}$ alone cannot explain the different trends of $H_n$ vs. disk thickness as shown in Figure 4.9: critical fields were extracted from simulations and experimental hysteresis loops of single disk CoFeB TMR structures. There is good agreement between the experiment and simulation as $H_{an}$ shows an almost linear trend vs. $t$. Only a small kink is observed around approximately 30 nm. In contrast, the trend of $H_n$ vs. $t$ can be separated into three different sectors, each with a different slope: In section No. 1 (up to 20 nm thickness), $H_n$ stays nearly constant and is only lightly affected by $t$. $H_n$ increases in section No. 2 with approximately the same slope as $H_{an}$. The slope is reduced again above 35 nm (section No. 3).

The observed $H_n$ trend can be attributed to three factors: (1) Below a thickness of approximately 35 nm, the out-of-plane magnetization at the disk edge - which is required to enable vortex nucleation [165] - increases with increasing thickness as shown in the previous section. (2) It has also been demonstrated that this trend of $m_z$ leads to an increase of $E_{\text{demag}}$ with increasing thickness which facilitates vortex nucleation. (3) The occurrence of thickness-dependent pre-vortex states can cause a delay of vortex nucleation, as will be shown in the next section. Factor (1) and (2) explain the strong increase of $H_n$ from 20 to 35 nm thickness (see Figure 4.9). Furthermore, it is expected that the kink of the trend of $H_{an}$, observed at approximately 30 nm, in Figure 4.9 is also related to the trend of $m_z$ vs. $t$. Factor (3) explains the sections where the slope of the $H_n$ trend is decreased in Figure 4.9.

The phase diagram shown in Figure 4.10 was extracted from micro-magnetic simulations. Formation fields $H_{\text{form}}$ of the different magnetic states, normalized to $H_{an}$, are plotted as a function of disk thickness. (In the context of this work, the term *nucleation field* is

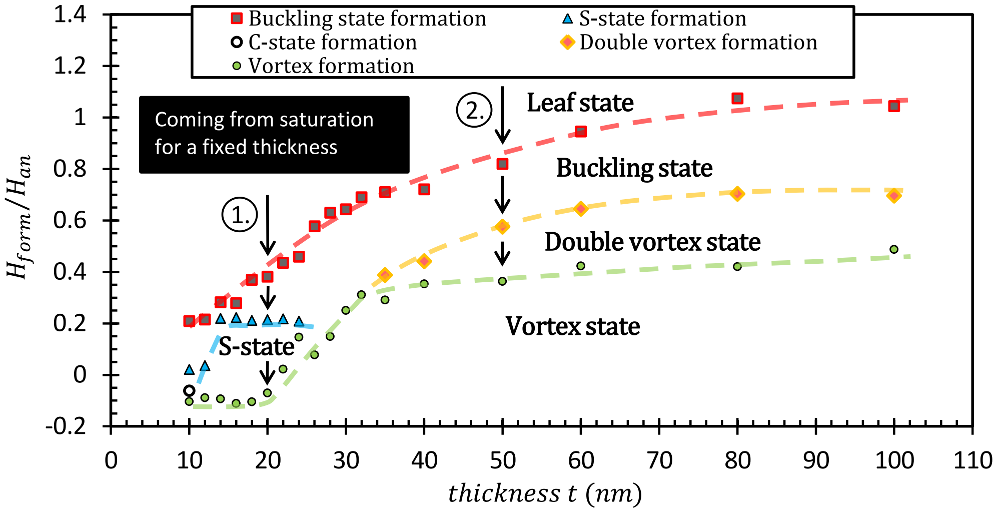

**Figure 4.10.** Phase diagram of the magnetic states of disk-shaped elements with $d = 1.1\,\mu\text{m}$ extracted from simulations. It has to be stressed that the phase diagram is only valid for a unidirectional reduction of an applied magnetic in-plane field coming from saturated state, and no additional orthogonal components are applied. Simulation parameters for CoFeB are given in Section 3.3. The different magnetic states are illustrated in Figure 4.11.

reserved for the single vortex nucleation, even though the formation of other magnetic states may include nucleation processes.) This way, formation fields of thin and thick elements can be easily compared.

The phase diagram has to be read the following way: for a certain thickness, for example 20 nm (No. 1), the starting point is the saturated state ($H_{\text{ext}} > H_{an}$). Via a reduction of $H_{\text{ext}}$ (without changing its orientation) one obtains the formation fields that are plotted here. For $H_{\text{ext}} < H_{an}$ (below 1 in the phase diagram), the **leaf state** [157] is observed first (see Figure 4.11a): the disk structure is nearly saturated, but at the edge of the disk the magnetization tends to be parallel to the outer contour. This state is sometimes also called 'onion state' [113, 158].

During a further reduction of the external magnetic field, a buckling of the magnetization is observed, as it is shown exemplarily in Figure 4.11b and 4.11c. For the 20 nm thick structure, the buckling starts at roughly 40 % of $H_{an}$. Savel'ev and Nori stated that "this [..] buckling instability is an example of spontaneous symmetry breaking" [113] and thus its orientation is more or less unpredictable. $H_{\text{form}}$ of the **buckling state** is defined here as the field value where the buckling is present on both halves of the disk. The type of buckling can be differentiated with the undulation number $n^*$ which represents the total number of wave crests and troughs [113]. According to this definition, Figure 4.11b shows buckling $n^* = 3$ and Figure 4.11c buckling $n^* = 4$, respectively. The correlation between thickness, diameter, and mode of the buckling state is discussed in Section 4.1.7 (see Figure 4.15).

The buckling state is stable until approximately 20 % of $H_{an}$ is reached. In this context stable means that no principally changes of the pattern are observed. In other words, the undulation number $n^*$ of the buckling mode stays unchanged, whereas minor changes in

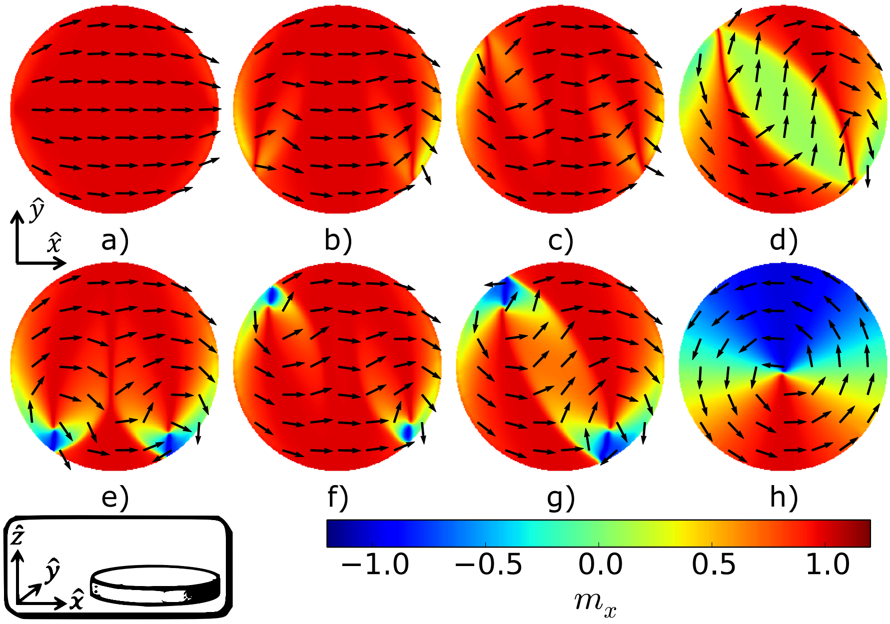

**Figure 4.11.** Overview of the different magnetic states of a disk-shaped ferromagnetic element with 1.1 µm diameter and a thickness between 20 and 50 nm. a) Leaf state, b) buckling state with undulation number $n^* = 3$, c) buckling state ($n^* = 4$), d) S-state (buckling state $n^* = 2$), e)-g) double vortex with $n^* = 3, 4, 2$ and h) vortex. For a detailed three-dimensional description of the magnetization pattern of leaf, buckling and S-state see Ha et al. [158]. Simulation parameters are given in the caption of Figure 4.9.

$m_x$ and $m_y$ (which only affect the undulation amplitude) are observed with a changing external field. When $H_{\text{ext}}$ goes below $0.2\,H_{an}$ an abrupt change of the buckling mode from $n^* = 4$ to $n^* = 2$ is observed. This state is also known as **S-state**. In the context of this work, the S-state is treated separately from the buckling state. This separation is reasonable since the S-state is only observed for thinner structures, as it can be seen in Figure 4.10. The S-state has been confirmed experimentally for disk structures with similar diameter and thickness [64, 66].

Vortex nucleation is observed shortly after reversing the external field (see Figure 4.11h). In example No. 2 in Figure 4.10 (50 nm thickness), the vortex nucleates via leaf, buckling, and double vortex state. A closer look at the phase diagram reveals that the S-state is only observed for disk structures with a thickness below approximately 25 nm. In contrast, the nucleation of a **double vortex** is observed for larger thicknesses. Different configurations of the double vortex state are illustrated in Figure 4.11e-g. The type of observed double vortex configuration depends on the previous buckling pattern. This explains the similarities between the double vortex states and the buckling patterns: b) vs. e), c) vs. f), and d) vs. g), respectively. The window of stability of the double vortex state significantly opens above 35 nm thickness. The experimental observation of a double vortex state in similarly sized disk-shaped ferromagnetic elements has been reported in literature [61, 66, 160, 163].

The nucleation of a double vortex state via S-state was only observed in one simulation (see Figure 4.14, $t = 20\,\text{nm}$, $d = 1.7\,\mu\text{m}$). Accordingly, it is stated that there is a 'triple

point' of pre-vortex states at around $t = 30\,\mathrm{nm}$ where buckling, S-, and double vortex state coexist (for the investigated CoFeB system with $d = 1.1\,\mu\mathrm{m}$).
The C-state ($n^* = 1$) is observed for thin systems ($\leq 10\,\mathrm{nm}$). Below 10 nm, a rotation of the C-state without vortex nucleation was observed in the simulations. This observation is in qualitative agreement with literature [113] but vortex nucleation has also been observed in the experiment (at room temperature) for thinner systems with the aspect ratio in the same range (see e.g. [52, 64]).
It has to be noted that the clear separation of the different pre-vortex states, observed in Figure 4.10, results from the 'ideal' conditions in the simulations: there is no thermal excitation (see Section 5.2), all elements have an identical edge (see Section 4.2.11), and the orientation of the external field shows no deviations (see Section 5.3). Thus, it is expected that the experimental elements will show the same general trend but without such a clear separation of the states. Furthermore, Figure 4.10 shows a stagnating value of $\frac{H_n}{H_{an}}$ after exceeding 32 nm thickness. This observation is attributed to the fact that the scaling of $E_{\mathrm{demag}}$ vs. $t$ becomes linear after exceeding approximately 35 nm (see inset of Figure 4.2). Therefore, it can be concluded that the delayed vortex nucleation, observed for $t = 20\,\mathrm{nm}$, can be attributed to both the non-linear scaling of $E_{\mathrm{demag}}$ and the presence of the S-state.

The different trends of $H_n$, observed in Figure 4.9, can now be explained by the different metastable pre-vortex states: up to 20 - 25 nm, the S-state has a large window of stability delaying vortex nucleation due to the so-called *configurational stability* [164]. The main reason for the stability of the intermediate states is their non-uniform magnetization distribution which leads to a small stray field. Ultimately, the vortex state is the magnetic state with the highest non-uniform magnetization distribution (at zero field $m_x = 0$, $m_y = 0$ and $m_z \approx 0$) and, as a result, the state which delays magnetization reversal the most. Above 35 nm, the double vortex state causes a delay of the vortex nucleation similar to the S-state. Between 25 and 35 nm thicknesses, neither the S- nor the double vortex state seem to be particularly stable. Consequently, vortex nucleation occurs via buckling $n^* > 2$. It is apparent from Figure 4.11 that these high order buckling states have a strong pronounced uniform magnetization and are therefore less stable with decreasing magnetic field, compared to the S- or the double vortex state. As a result, a significant increase of the vortex nucleation field parallel to the buckling formation field trend is observed in Figure 4.10.

The observed magnetic states fit the existing literature very well: Schneider et al. showed the S- and the buckling state ($n^* = 3$) for $d = 800\,\mathrm{nm}$ and $t = 15\,\mathrm{nm}$ permalloy disk structures measured with Lorentz microscopy [64]. Aharoni and Shtrikman demonstrated analytically in 1958 that the nucleation of the curling mode occurs for infinite cylinders via buckling mode [43]. Rahm et al. reported the formation of the S-state for 500 nm diameter permalloy disk structures with a thickness of up to 40 nm [66]. This thickness is larger compared to that of the phase diagram. Therefore, smaller elements with 400 nm diameter were simulated. It can be concluded from these results that due to the smaller lateral size the S-state is preferable up to 35 nm thickness (see Figure 4.15). Thus, a shift of the phase diagram is observed which is expected to be linked to the increased energy contribution of $E_{\text{exch}}$. As a result, the double vortex state is less favorable. For 30 nm thick permalloy disk structures ($d = 1.0\,\mu\text{m}$), vortex nucleation was reported to occur via buckling only [162]. Davis et al. reported that in their investigation of 42 nm thick, 1.0 µm diameter permalloy disks, vortex nucleation occurred via buckling [166]. They did not further investigate which mode of buckling occurred since it was not crucial for their study. The observation of a transition via buckling fits the results of this work well since a smaller $M_s$ (permalloy instead of CoFeB) shifts the double vortex mode to larger thicknesses (see Section 4.2.1). The nucleation of a double vortex in a micrometer-sized disk structure has been observed in the experiment. A minimum thickness of 30 nm was needed for Co to observe its nucleation [61], as was for permalloy a minimum of 40 nm [66, 163].

To summarize, the investigation of the nucleation modes showed that vortex nucleation can occur via the S-state for a CoFeB thickness below approximately 30 nm. For larger thicknesses, the formation of the double vortex state is observed. Both pre-vortex states delay vortex nucleation, which will be proven experimentally in the next section.

### 4.1.6 Thickness-Dependent Nucleation Modes - Experiment

Different nucleation modes and phases were extracted from the experimental TMR curves in addition to the simulation phase diagram of the previous section, which allows to quantify the probability of the different nucleation modes at room temperature. Furthermore, it will be shown that the S- and the double vortex state clearly delay vortex nucleation. The differentiation between the various magnetic states through the comparison of single device hysteresis loops with simulations has been done by Rahm et al. [66] in a similar way, but they concluded due to the limitation of sample variations and maybe also due to computation power: "Apart from the double-vortex state, which only occurred in larger disks with a minimum thickness of 40 nm, we found in experiment no clear correlation between the disk size and a specific nucleation mode." [66] In contrast, experimental results on the following pages confirm the previously discussed simulation phase diagram.

First of all, it can be distinguished between two types of phase transitions: first- and second-order phase transitions. These terms are used here in analogy to the Ehrenfest classification of phase transitions [167]. The only difference is that instead of the Gibbs free energy the free energy of the magnetic system is treated. Accordingly, the first and second derivative with respect to the applied field are the magnetization and susceptibility [168]. First-order phase transitions are defined by the discontinuity of the first derivative of the free energy; second-order (or rather higher-order) phase transitions are defined by the discontinuity of the second derivative [169]. As a result, **jumps** in the magnetization

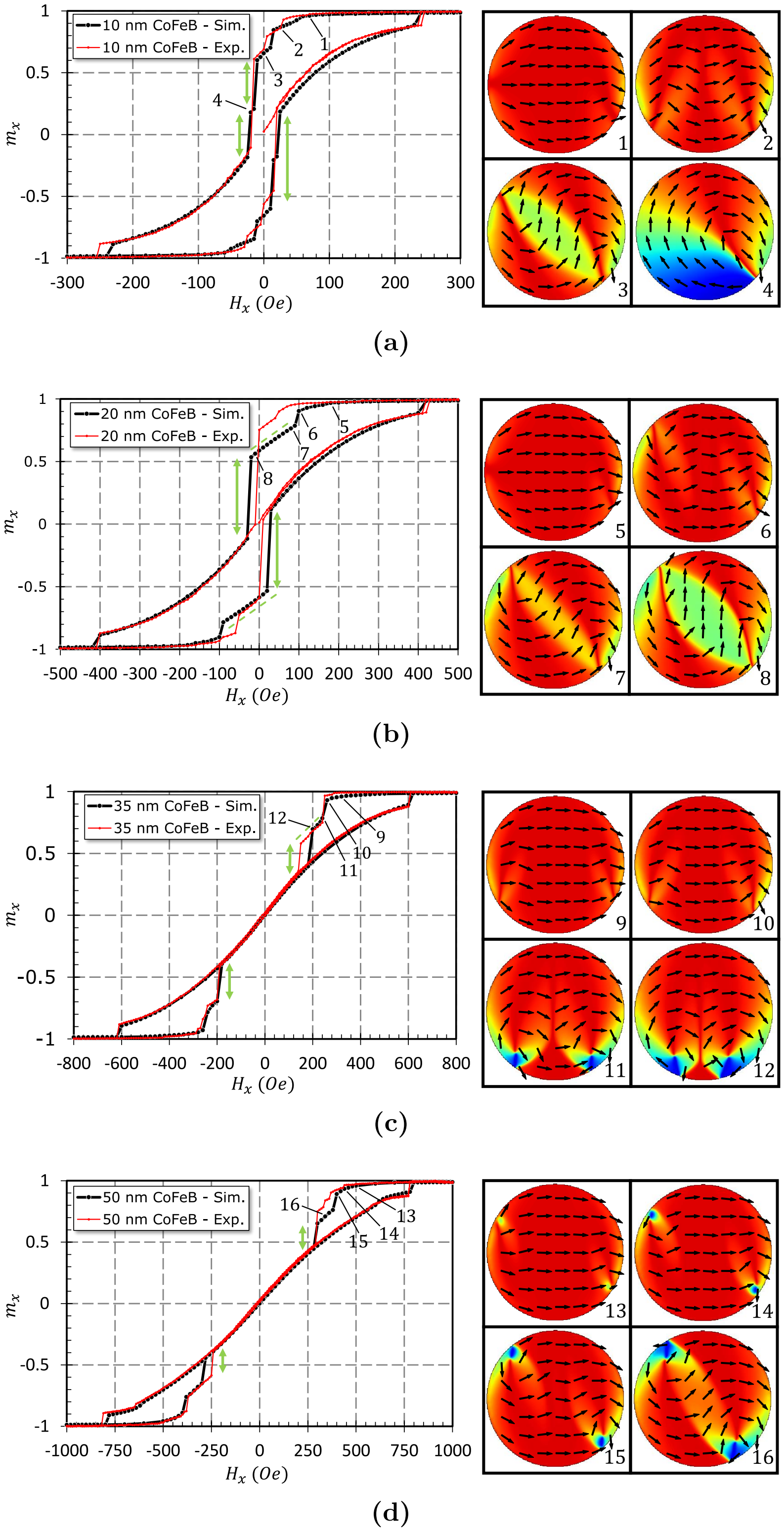

**Figure 4.12.** Example hysteresis loops of 1.1 µm diameter CoFeB single disk devices (Exp.) plotted together with the simulation data (Sim.) for 10 (a), 20 (b), 35 (c), and 50 nm thickness (d). Additionally, four different pre-vortex magnetization configurations are plotted for each thickness. Intermediate leaf-buckling state: 1, 5. Buckling state: 2, 6, 9-10, and 13. S-state: 3 and 7-8. C-state: 4. Double vortex state: 11-12 and 14-16. Simulation parameters are given in the caption of Figure 4.9.

of the quasi-static hysteresis loop can be assigned to **first-order** phase transitions and **kinks** to **second-order** phase transitions. This allows to narrow down the observable features of phase transitions.
As a next step the observed magnetic states need to be classified in: buckling ($n^* > 2$), S-state ($n^* = 2$), C-state ($n^* = 1$), double vortex, and vortex state. Figure 4.12 shows experimental and simulated data for disk structures with 10 (a), 20 (b), 35 (c), and 50 nm (d) thickness, which will be discussed in the following classification.

The formation of the **buckling** pattern, coming from the leaf state, is a second-order phase transition. The "kink has been correlated with the buckling of the parallel-spin state to the C-state" [166]. (In literature, buckling $n^* = 4$ is sometimes named C-state [66].) For 10 and 20 nm thickness, the kink is clearly visible in the simulations: it can be observed in Figure 4.12a between 1 and 2 and in Figure 4.12b between 5 and 6. The intermediate leaf-buckling state in the illustrations 1 and 5 shows the start of the buckling in one half of the disk structure. Only after the buckling is present in the full structure (illustration 2 and 6), a pronounced reduction in $m_x$ and thus a kink is observed. Kinks are often difficult to assign in the experiment, thus giving rise to the assumption that edge pinning is more pronounced here. Therefore, kinks were not assigned to all experimental hysteresis loops, which are summarized in Table 4.1. For larger thicknesses ($> 25$ nm), the assignment of a kink to the formation of a buckling pattern is less practical. For 35 nm, the kink was observed in simulations when the two domain walls of the buckling pattern are fixed with respect to the edge. For 50 nm, the largest kink at approximately 460 Oe is actually due to a second-order phase transition of the buckling pattern into a double vortex state.

The formation of the **S-state**, originating from buckling state, is observed as a first-order phase transition. The S-state nucleates in Figure 4.12 in between Illustration 2 and 3 and in between 6 and 7. A relatively small jump in the transfer curve, a smaller slope of the curve compared to the vortex state, and a subsequent large jump into the vortex state can all be linked to the S-state. In the experiment, S-state features are often observed but not for every device (see Table 4.1). It has to be pointed out that the formation of the S-state is not necessarily a first-order phase transition: for smaller structures (400 nm diameter NiFe disks), the formation of the S-state as second-order phase transition was observed directly out of the leaf state (not shown). The formation of a **C-state** was observed in simulations only for 10 nm thickness and below (1.1 µm diameter). In the experiment, only seven events (out of 60) looked similar to the nucleation of a C-state (for $t = 10$ nm). The formation of a **double vortex** can either occur via first or second-order phase transition, which is expected to be linked to the previous $m_z$-component at the disk edge (see Section 4.7). For 35 nm, a first-order phase transition is observed (see transition from 10 to 11 and the corresponding jump in signal in Figure 4.12c). A second-order phase transition with corresponding kink is observed for 50 nm (Figure 4.12d, Illustration 13 to 14). A jump in signal is also observed but it is related to the first-order phase transition of the buckling pattern of the double vortex state from $n^* = 4$ to the S-shaped

$n^* = 2$ (see Illustration 15 to 16). The characteristics of the stabilized double vortex state are a slightly increased slope compared to the vortex state as well as a relatively small change in $m_x$ when the double vortex transforms to the single vortex. The change in $m_x$ can even occur with reversed sign if the double vortex is still present after field reversal (only observed for CoFe elements - see Figure 4.32 in Section 4.2.5).

**Vortex** nucleation is a first-order phase transition regardless of the pre-state: Its nucleation is always linked to a rapid change of the magnetization in out-of-plane direction (either zero or more than one vortex cores are present before its formation) and in-plane direction as a consequence of the change in quantity of the vortex cores and the associated change of the in-plane magnetization pattern.

The annihilation of the vortex is also a first-order phase transition. However, there is a big difference between vortex nucleation and annihilation. Nucleation occurs via spontaneous symmetry breaking because two types of sense of rotation and two types of polarities generate an energy landscape with equivalent energy minima. In contrast, annihilation does not occur via symmetry breaking since there is only one possible direction of polarization. It has been shown by Davis et al. that, as a consequence of this, vortex annihilation is only thermally activated, but the nucleation of a vortex core additionally involves magnetic supercooling [166]. Consequently, the influence of magnetic

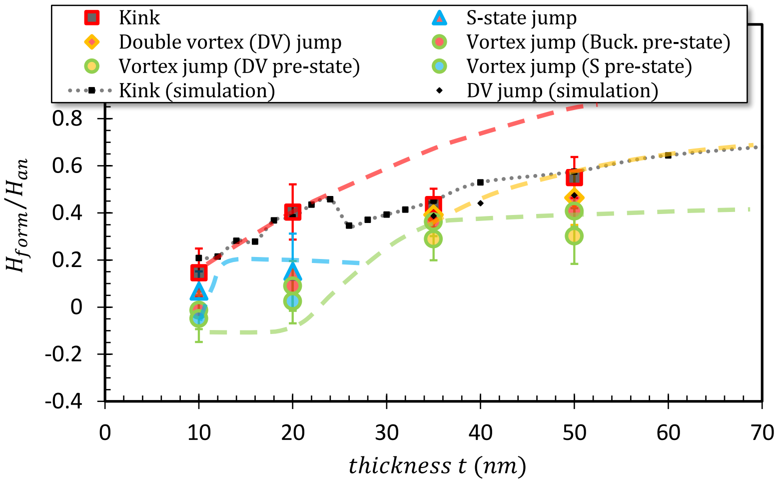

**Figure 4.13.** Experimentally determined values for the nucleation fields of the different magnetic phases. For each thickness, roughly 30-40 CoFeB single disk structures with 1.1 µm diameter were characterized. The trend lines of the phase boundaries are those from the simulation results shown in Figure 4.10. The color code of the experimental data points is as follows: the color edge reflects the state that nucleates and the inner color represents the pre-state. Red for buckling, blue for S-state, yellow for double vortex and green for vortex state.

supercooling is expected to differ depending on the pre-state[3].

The resulting phase diagram of the experimental data, plotted together with the trend lines of phase transitions extracted from simulations, is shown in Figure 4.13. The formation fields of the simulation are reproduced very well: The observed **kinks** match the simulations. For 10 and 20 nm thickness, they are in accordance with the start of the complete buckling pattern. For 35 nm, the experimental kink fits the fixation of the buckling domain walls observed in simulations, and for 50 nm it matches the formation of the double vortex. S-state characteristic jumps are mainly observed for 10 and 20 nm thickness in the experiment. For 10 nm, the S-state nucleation is observed earlier in the experiment, which is expected to be a result of temperature activated nucleation. Transitions into states that can be assigned to double vortices were only observed for 35 and 50 nm thickness. For 35 nm, the average double vortex nucleation field is in close proximity to the single vortex nucleation field, but this gap increases with increasing thickness, as expected from the simulations. Moreover, less jumps into the double vortex state were observed for 35 nm thickness (see Table 4.1).
$H_n$ fits the simulations quite well, but for the thinner systems nucleation occurs earlier in the experiment. This observation is attributed to temperature activated nucleation due to smaller energy barriers of thinner systems, which are documented in Section 5.2. The results also show a reduced influence of a temperature elevation on $H_n$ if the thickness is increased. Furthermore, the vortex nucleation events were subdivided into three classes in Figure 4.13: nucleation via buckling only, via S-state, or via double vortex state. It has

**Table 4.1.** Statistics of the 1.1 µm diameter CoFeB disks phase analysis. Between 30 and 40 devices were measured for each thickness. For 20 - 50 nm, each device was measured up to three times, for 10 nm only once. It is indicated how often the formation of a certain phase could be assigned to an event ($DV$ stands for double vortex). The 'Kink' (second-order phase transition) represents the formation of the buckling pattern for 10 and 20 nm, but also double vortex formation for 50 nm thickness (see Figure 4.12d).

| t (nm) | No. of loops | Kink (%) | S-state (%) | C-state (%) | DV (%) | unclear jumps (%) |
|---|---|---|---|---|---|---|
| 10 | 30 | 100 | 58 | 12 | 0 | 0 |
| 20 | 105 | 100 | 38 | 1 | 0 | 7 |
| 35 | 88 | 38 | 10 | 0 | 22 | 3 |
| 50 | 118 | 89 | 0 | 0 | 49 | 4 |

---

[3] Davis et al. observed a bimodal nucleation field distribution but expected vortex nucleation to occur via buckling only [166]. The educated guess is made that the bimodal distribution is caused by two possible vortex nucleation paths: either via buckling formation only (93 % [166]) or via the nucleation of a double vortex first (7 %). This assumption is based on the fact that 7 % of the vortex nucleation events did not show any sweep rate dependency and thus cannot be associated with magnetic supercooling. Furthermore, they rotated the external bias field by 2°, which moved the vortex creation site along approximately 17 nm at the edge, due to the the alternating field component of the setup. This removed the supercooling effect of the 93 %. They assigned this observation to 'smoothening' of the edge roughness. However, the rotation did not affect the 7 % at all. The presence of a double vortex state may explain this behavior since it prevents the nucleation of further curling modes. Davis et al. were aware of the double vortex state. They excluded the possibility of its nucleation since they expected it to be stable even at zero field, which stood in contrast to their data [166].

to be noted that for 50 nm thickness it cannot be stated clearly whether double vortex formation occurs if no typical double vortex jump is observed (simulations and the small value of $H_n$ for 50 nm compared to 35 nm, indicate the presence of a double vortex state even for elements without the characteristic double vortex jump).
Nevertheless, the significance of the experimental results is clear: if a first-order phase transition into an intermediate magnetic state is observed, then the nucleation of the single vortex state is delayed.

### 4.1.7 Nucleation Modes and the Influence of the Diameter

So far, the disk diameter of the investigated structures was kept constant (1.1 µm). Figure 4.14 extends the phase analysis to different diameters between 400 nm and 4 µm. The observed shift of the S-state window to larger thicknesses for smaller diameters is consistent with literature [66]. Similarly, Figure 4.14 shows a shift of the window where only buckling states with higher undulation number are observed. This shift can be derived from the fact that the double vortex state needs a larger thickness for smaller diameters. Only for $d = 400$ nm, $t = 50$ nm vortex nucleation was observed directly via the leaf state.

More detailed information about the different pre-states is given by Figure 4.15. This phase diagram shows all the different non-leaf pre-vortex states. Figure 4.14 shows in contrast only one state prior to vortex nucleation. Regarding the maximum undulation number of the buckling states, certain lower limits, which are mainly defined by the diameter, seem to exist (grey dashed lines). In the phase diagram shown, almost all elements in the blue colored segment go through the S-state. Based on the experimental results, it can

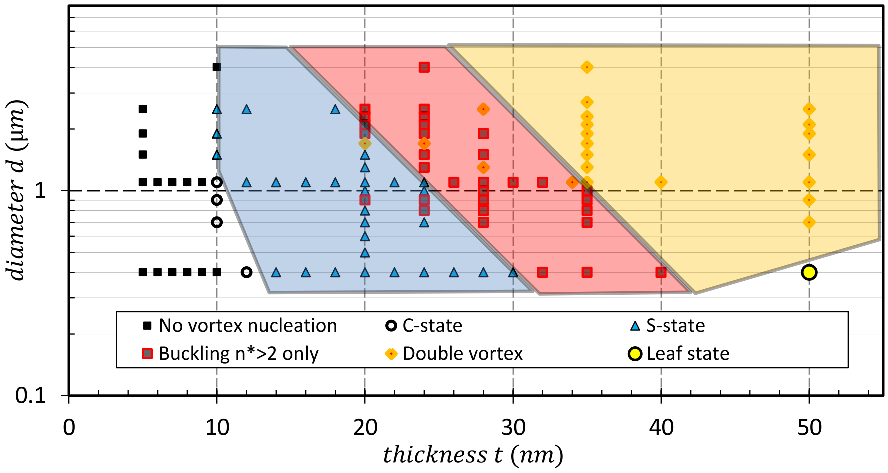

**Figure 4.14.** Phase diagram of the magnetic states that are present in the last step before vortex nucleation, extracted from simulations. Different colored segments are guides for the eyes: on the left side (blue) vortex nucleation occurs mainly via the S-state, in the central part (red) mainly via the buckling states $n^* = 3$ and $n^* = 4$, and on the right (orange) via the double vortex state. Simulation parameters (CoFeB) are given in the caption of Figure 4.9.

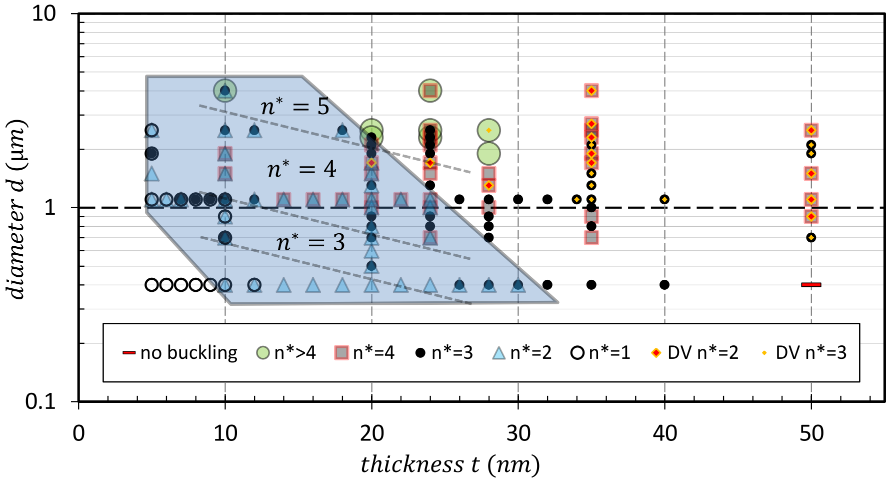

**Figure 4.15.** Phase diagram of the different buckling states that are present during a full hysteresis loop. The blue colored segment is a guide for the eyes, illustrating that all structures inside go through the S-state ($n^* = 2$), with three exceptions. For higher order buckling states such sectors do not exist, but apparently there are certain limits under which they do not form, indicated by the dashed lines. In addition, the double vortex (DV) buckling patterns are plotted. Simulation parameters (CoFeB) are given in the caption of Figure 4.9.

be stated that this observation cannot be generally valid. Figure 4.15 also shows that a simple rule exists for the buckling pattern of the double vortex state: all buckling patterns with an even undulation number will result in a double vortex buckling pattern with an even undulation number. Accordingly, uneven undulation numbers remain uneven (mirror symmetry stays mirror symmetry and point symmetry stays point symmetry). This rule cannot be applied to the non-double vortex buckling patterns. Furthermore, all $n^* = 4$ double vortices undergo $n^* = 2$ (not shown).

### 4.1.8 Symmetry Breaking of the Vortex Core

At last, further thickness-dependent observations will be mentioned. For thicker systems, a deformation of the vortex core has been observed in simulations and in experimental investigations when external fields close to but below $H_{an}$ are applied [163, 170, 171]. It will be shown here that this deformation of the vortex core (see Figure 4.16b No. 4) can occur discontinuously and is thus detectable in the TMR measurement in form of a small jump in signal: in Figure 4.16a for a 50 nm free layer thickness, a small jump in the signal is visible at around −620 Oe. For 35 nm thickness, such a jump does not occur within the vortex state. For both thicknesses, experimental results are in accordance with the simulation results. This enables the attribution of the signal jump to a discontinuity in the vortex core trajectory, which only happens here for 50 nm free layer thickness. In Figure 4.16b the vortex core trajectories are illustrated within the out-of-plane magnetization figures. It can be seen that for 50 nm thickness the vortex core jumps to the right side from 3 to 4, causing the small jump in the TMR signal.

It needs to be mentioned that the jump occurs to the other side on the opposing surface

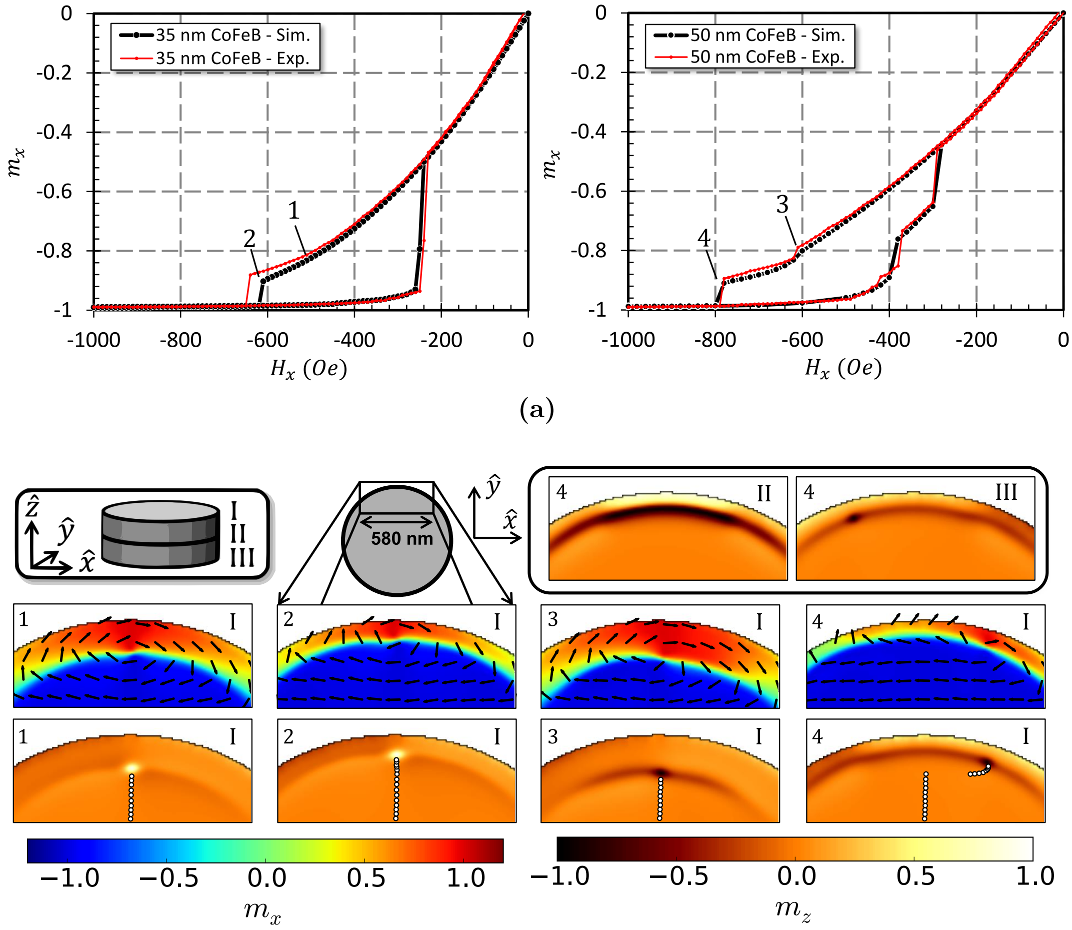

**(a)**

**(b)** $m_x$ and $m_z$ for the marked field values in (a).

**Figure 4.16.** (a) Negative branch of experimental (Exp.) and simulated (Sim.) hysteresis loops for $d = 1.1\,\mu\text{m}$. The 35 nm thick disks show no jumps within the vortex state near $H_{an}$ (see 1 and 2). For 50 nm, a jump is observed around −620 Oe (see 3 and 4). This jump is caused by an erratic change of the vortex core trajectory, which is illustrated in (b): for every previous 20 Oe field step the vortex core positions were marked additionally with white circles in the $m_z$-plots. The actual core positions at the respective fields are the white dots (up polarity) for 35 nm and the black dots (down polarity) for 50 nm. For 35 nm, the vortex core trajectory is a nearly straight line, whereas for 50 nm, the core jumps to the right side at −620 Oe causing the jump in the transfer curve. For the $t = 50\,\text{nm}$, $m_z$ of field step No. 4 is also plotted for the bottom surface (III) and in the $\hat{z}$-center of the disk structure (II), additionally to the top surface plot (I). Simulation parameters are given in the caption of Figure 4.9.

of the disk (see inset, right side in Figure 4.16b), thus maintaining symmetry with respect to the applied field. The vortex core broadens in the central part of the disk structure, reaching from the left to the right side and thus connecting top and bottom surface core positions.

Figure 4.17a shows measurements at ten different devices for each thickness (35 and 50 nm), all of them with 1.1 µm diameter. For 35 nm, all devices show no jump within the vortex state. The 50 nm thick devices show the jump in all cases, apart from two. In these two cases, vortex annihilation occurs at smaller external magnetic fields. This

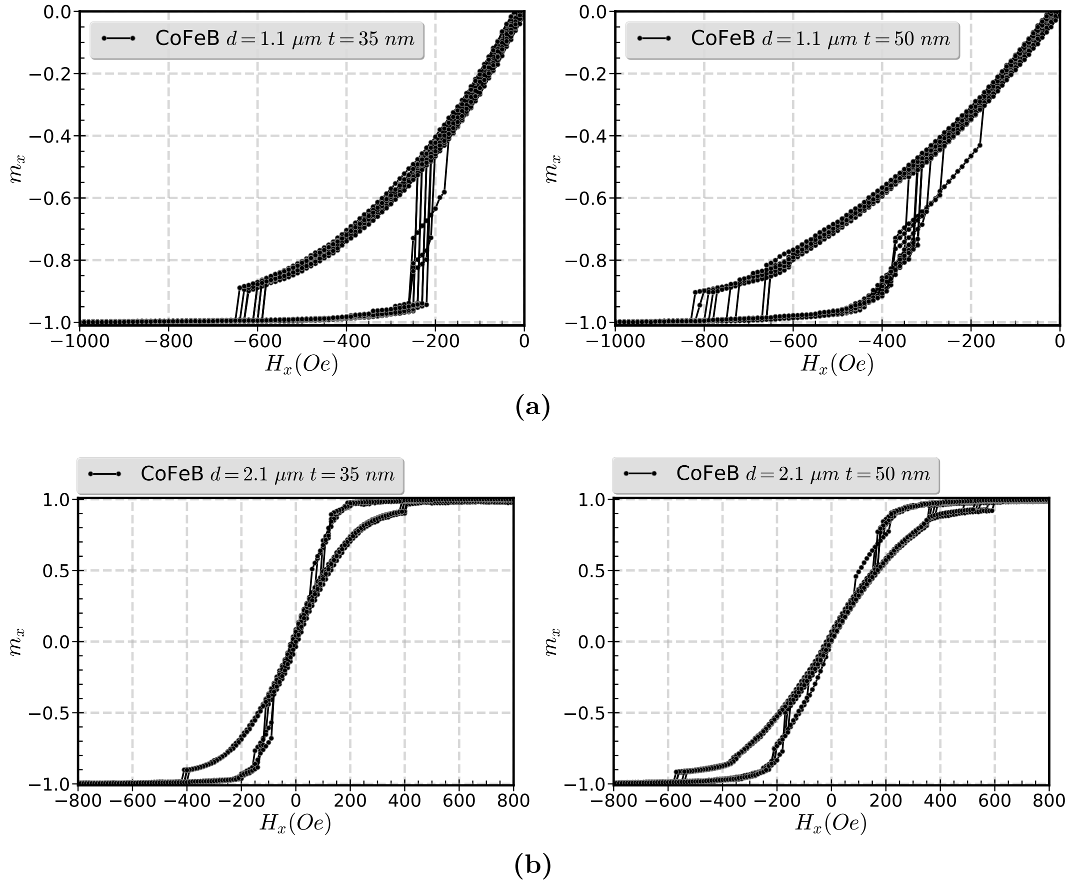

(a)

(b)

**Figure 4.17.** (a) Ten hysteresis loops of ten different single disk devices (for each thickness). For $t = 50\,\mathrm{nm}$, 8 of 10 measurements show a jump at around $-600\,\mathrm{Oe}$. The remaining two devices without such a jump show a reduced $H_{an}$ value which leads to an increased $H_{an}$ distribution. (b) For devices with $d = 2.1\,\mu\mathrm{m}$, the impact of the thickness on the $H_{an}$ distribution is even larger. For $t = 35\,\mathrm{nm}$, measurements of four different disks are plotted and for 50 nm of five, respectively.

observation is in line with the fact that the vortex core trajectory is expected to describe a straight line here, which seems to result in an earlier annihilation than in the case of a curved path. Furthermore, it was observed that the occurrence of the vortex core deformation is not mandatory for all structures with the same dimensions and not even necessarily reproducible for a single device. When the measurement is repeated on devices with 50 nm CoFeB thickness, sometimes both types of core trajectories - with and without jump in the vortex state - were observed in the experiment (not shown).

In addition, it was found that an increase in diameter leads to a larger difference in the two $H_{an}$ distributions (with and without deformation of the vortex core): Figure 4.17b shows exemplary TMR measurements at single disk cells with 2.1 µm diameter and 35 or 50 nm thickness. For 35 nm, again no jumps within the vortex state appear, and thus a small $H_{an}$ distribution is observed. For 50 nm, huge differences in $H_{an}$ are apparent: in some measurements annihilation occurs in close proximity to the jump/kink at an absolute value of about 370 Oe. As for the rest, $H_{an}$ has an average absolute value of approximately 550 Oe. This finding explains now why the $H_{an}$ error bars in Figure 4.1

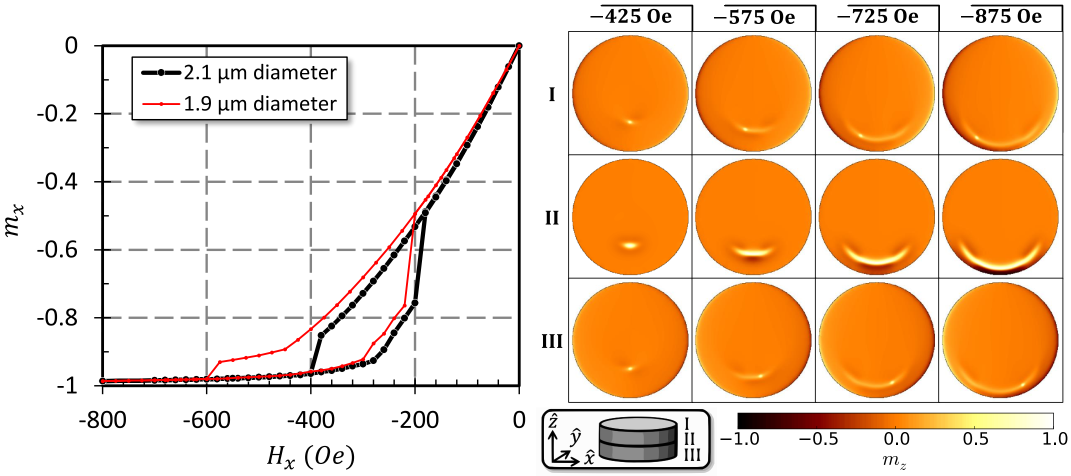

**(a)** $t = 50\,\text{nm}$

**(b)** $t = 80\,\text{nm}$ $d = 1.1\,\mu\text{m}$

**Figure 4.18.** (a) Simulated hysteresis loops with drastic change of $H_{an}$: only for $d = 1.9\,\mu\text{m}$ a deformation of the vortex core near $H_{an}$ occurs (see Figure 4.16) which increases $H_{an}$. (b) For $t = 80\,\text{nm}$, the deformation and broadening of the vortex core becomes continuous with increasing field amplitude. Simulation parameters are given in the caption of Figure 4.9.

increase with increasing diameter only for 50 nm thick structures.

How close the two possibilities - deformation of the vortex core or direct annihilation - are becomes apparent when the simulation results of a 1.9 µm and a 2.1 µm disk structure are compared. Figure 4.18a shows a 50 % increased $H_{an}$ for 1.9 µm, although the diameter is only increased by 10 %. This is due to the fact that only for 1.9 µm a vortex core deformation is observed.

The observed jumps within the vortex state only seem to occur in a small thickness range. For 40 nm CoFeB thickness, the core still describes the straight line, whereas for 60 nm and more the drift to the side becomes continuous, which is illustrated in Figure 4.18b for 80 nm thickness. Thus, it can be assumed that for a thickness larger than 50 nm the experimental $H_{an}$ distribution will become smaller again.

In this work, the focus was on disk thicknesses between 10 and 50 nm. Nevertheless, an outlook regarding the magnetic phases has already been given in Figure 4.10. It is therefore important to mention that the double vortex state transforms with increasing thickness to double-vortex-similar patterns. Figure 4.19 shows that for 50 nm two vortices are present and expand over the whole thickness. Such a structure was also observed in all CoFeB simulations with smaller thicknesses if a double vortex was formed. For 80 nm, two vortices are present in a similar pattern at the top surface (I). In the middle of the disk (II), the cores are blurred. At the bottom surface (III), domain walls are observed instead of a symmetrical curling. Such a domain wall is observed for 100 nm in the upper right part of the top surface while a vortex is observed in the lower left part. This pattern is mirrored at the bottom surface. Accordingly, it is important to know that similar but slightly different magnetic configurations are summarized with the term *double vortex* in Figure 4.10.

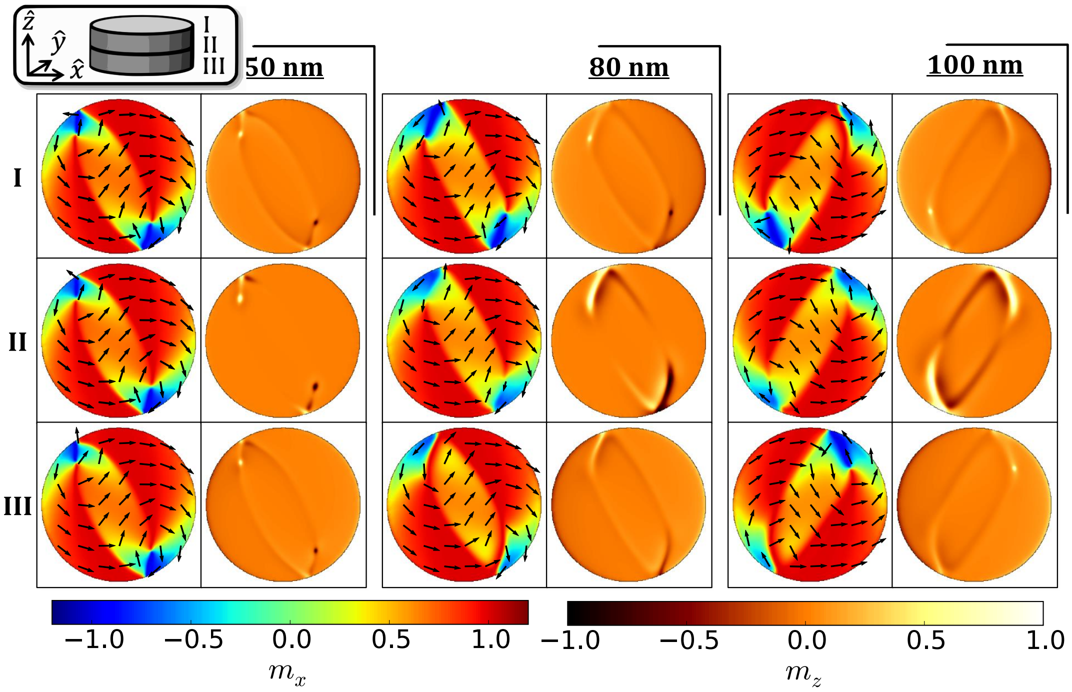

**Figure 4.19.** Change of the double vortex configurations with increasing thickness, starting with 50 nm (left at 300 Oe), covering 80 nm (middle at 460 Oe) and up to 100 nm (right at 580 Oe). The in-plane magnetization patterns (blue-red) and out-of-plane patterns (orange) are shown for the top surface of the disk structure (I), bottom surface (III), and $\hat{z}$-center (II). The field values are chosen in a way that the single vortex state has nucleated after a subsequent field reduction of 20 Oe. Simulation parameters are given in the caption of Figure 4.9. The diameter of all structures is 1.1 µm.

To summarize, it was shown that the deformation of the vortex core close to $H_{an}$, observed for 50 nm disk thickness, has a large impact on $H_{an}$ and its distribution. An outlook was given about the way the double vortex state can change when a thickness of 50 nm is exceeded.

## 4.2 Material and Process

This section gives a basic understanding of the influence of the material/simulation parameters on the one hand and, on the other hand, allows the reproduction and interpretation of various effects, observed in the experiment. In principle, it can be distinguished between bulk material properties - such as saturation magnetization, exchange length and magneto-crystalline anisotropy - and process influence, which mainly affects the edge and microstructure of the elements and cannot be neglected in larger disk structures: because vortex nucleation and annihilation "occur at the film edge, the edge properties play an important role in the reversal." [154]
The investigation of the various factors enabled a fairly accurate determination of the properties of the CoFeB and CoFe disk structures. These findings were used for the interpretation of the experimental results in all other chapters.

### 4.2.1 Saturation Magnetization

Figure 4.20 shows the critical fields of simulated disk structures with different $M_s$ values in comparison with experimental data of CoFe, CoFeB, and NiFe structures. It becomes apparent that $H_{an}$ scales with $M_s$ as a constant factor for all thickness values (with the exception of the kink around 35 - 40 nm which will be discussed at the end of this section). This scaling was attributed to the scaling of the stray field energy $H_{\mathrm{demag}}$, which is directly proportional to $M_s$ (see Equation 4.5), and the driving force behind vortex nucleation and annihilation.
The scaling of $H_{\mathrm{demag}}$ with $M_s$ is also evident in the simulations by the fact that for the

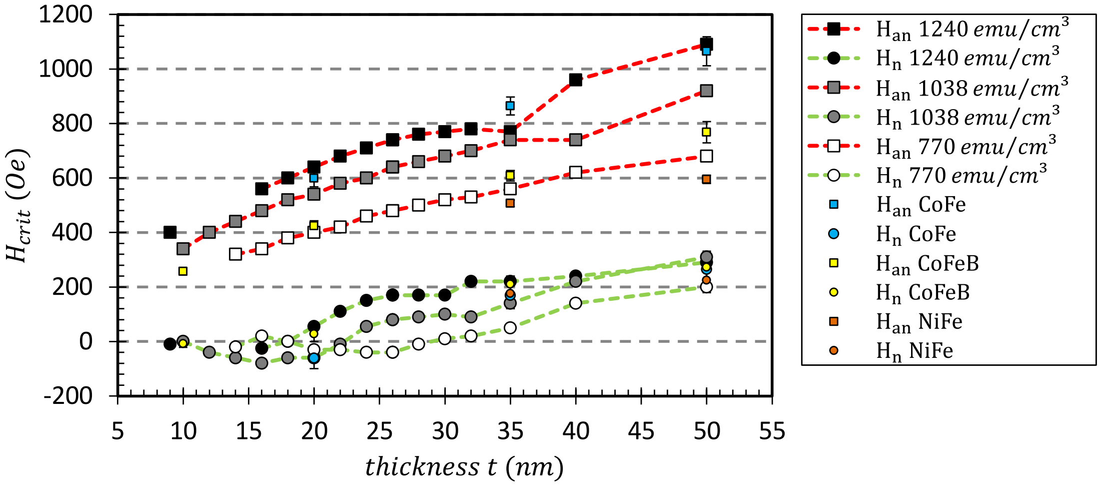

**Figure 4.20.** Critical fields $H_n$ and $H_{an}$ as a function of disk thickness for three saturation magnetization ($M_s$) values (simulations) and three different materials: CoFe, CoFeB, and NiFe (experiment). All disk structures have a disk diameter of 1.1 µm. In simulations, an exchange stiffness constant of $A = 1.53$ µerg/cm, zero magneto-crystalline anisotropy and no magnetically disturbed edge were applied.

smallest $M_s$ value vortex nucleation is not observed below 14 nm thickness, whereas for a larger $M_s$, vortex nucleation is also favored for thinner structures.
The picture becomes more complicated in the examination of $H_n$. For one thing, there is the non-linearity of $H_n$ as a function of thickness (see Section 4.1.4), mainly visible by the threshold thickness that is needed to increase $H_n$ as a function of thickness. Furthermore, the experimental data shows a delayed vortex nucleation for thinner CoFe elements compared to CoFeB. This characteristic is attributed in Section 4.2.3 to the magneto-crystalline anisotropy ($K_1$) of CoFe.

To highlight the scaling behavior of the critical fields as a function of $M_s$, Figure 4.21a shows $H_n$ and $H_{an}$ (obtained via simulation) from Figure 4.20 which are here normalized to $M_s$. For $H_{an}$ a good correlation is observed, except for the thickness range from 35 - 40 nm, which can be addressed to the deformation of the vortex core and will be discussed in detail at the end of this section. Regarding $H_n$, deviations are observed in the normalized plot. These differences can be attributed to a shift of the thickness-dependent vortex pre-states, caused by a change in $M_s$. This connection is exemplarily illustrated in Figure 4.21b for the 26 nm thick free layer structures with three different $M_s$ values. The transfer curves show that for the smallest saturation magnetization value (770 emu/cm$^3$) the disk structure is in the regime where vortex nucleation occurs via the S-state. In this regime, nucleation occurs typically around zero field. For the middle value (1038 emu/cm$^3$) vortex nucleation occurs only via buckling $n^* > 2$, identifiable in the transfer curve by the lack of a jump into an intermediate state before vortex nucleation. Furthermore, this regime is characterized by the sharp increase of $H_n$ as a function of thickness. For the largest $M_s$ value, nucleation occurs for one half-branch via the double vortex state. The double vortex state delays single vortex nucleation and is thus decreasing the slope of the $H_n$ trend when plotted versus thickness. Thus, it is not surprising that in Figure 4.21a the normalized $H_n$ values are almost congruent for 50 nm thickness because here

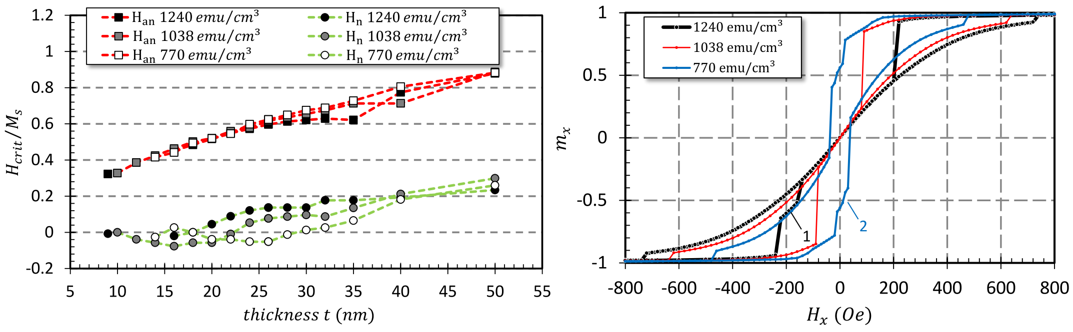

**(a)** $d = 1.1\,\mu\mathrm{m}$ **(b)** $d = 1.1\,\mu\mathrm{m}$ $t = 26\,\mathrm{nm}$

**Figure 4.21.** (a) Normalized simulation values of the critical fields, taken from Figure 4.20. (b) Hysteresis loops for 26 nm thickness. For 1240 emu/cm$^3$ the double vortex (1) is observed previous to vortex nucleation, whereas for 1038 emu/cm$^3$ only buckling $n^* = 4$ occurs and thus no jumps into transition states are observed. For 770 emu/cm$^3$ the S-state (2) delays vortex nucleation. Simulation parameters are given in the caption of Figure 4.20.

the double vortex is observed for all three $M_s$ values.

It has been found out that a possible way to determine $M_s$ was to fit simulated transfer curves iteratively to the experimental data sets [172]. A comparison with experimental determined $M_s$ would be desirable but is still pending. Exemplary simulated transfer curves, in comparison with experimental CoFeB data, are given in Figure 4.22. For the 35 nm thick free layer element congruent transfer curves are achieved for $M_s = 1038\,\mathrm{emu/cm^3}$. If $M_s$ is reduced to achieve a good matching of $H_{an}$ - shown for $M_s = 860\,\mathrm{emu/cm^3}$ - the feature of a congruent course is lost. No factor was detected to compensate this type of mismatch. However, it has been found out that it is possible to reduce $H_{an}$ massively by introducing a magnetically disturbed edge or a sloped edge (see Section 4.2.7) [172]. This way congruent transfer curves and matching critical fields were obtained for $M_s = 1038\,\mathrm{emu/cm^3}$.
It is shown in Figure 4.22b that the small increase of $M_s$ from 950 to 960 $\mathrm{emu/cm^3}$ causes a massive increase of $H_{an}$. This effect is related to the deformation of the vortex core near the edge of the disk structure (see in in detail Figure 4.16 in Section 4.1.5). Vortex core deformation needs a certain minimum thickness to occur, thus it is not observed for the 35 nm CoFeB device. Due to this effect it was not possible to fit $H_{an}$ by only adjusting $M_s$. The significant increase of $H_{an}$ for a very small change of $M_s$ fits the enormous $H_{an}$ distribution for certain disk dimensions (see Figure 4.17). It can be assumed in both cases that minor changes in total moment or layout, which also affects the total moment, lead to two possible vortex configurations close to $H_{an}$: a deformation of the vortex core resulting in a curved vortex core trajectory (delayed annihilation) or the vortex core trajectory describing a straight line (early annihilation). It is also apparent

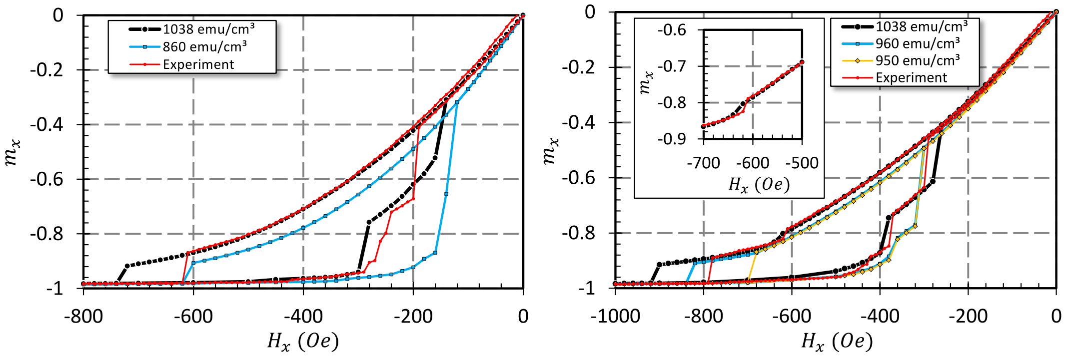

**(a)** CoFeB $d = 1.1\,\mu\mathrm{m}$ $t = 35\,\mathrm{nm}$ **(b)** CoFeB $d = 1.1\,\mu\mathrm{m}$ $t = 50\,\mathrm{nm}$

**Figure 4.22.** (a) Transfer curves of two simulated disk structures with two different $M_s$ values. (b) Influence of $M_s$ on $H_{an}$: The increased stability of the vortex state for 960 and 1038 $\mathrm{emu/cm^3}$ is caused by a deformation of the vortex core near the edge (see Figure 4.16). The discontinuous deformation can be identified in the transfer curve by a small jump (see inset). TMR measurements of the corresponding CoFeB single disk devices are plotted for comparison. Simulation parameters are given in the caption of Figure 4.20. The discrete element unit cell was $\leqslant 5 \times 5 \times 5\,\mathrm{nm^3}$ for $t = 35\,\mathrm{nm}$ and for $t = 50\,\mathrm{nm}$ slightly larger in $\hat{z}-$direction (7.1 nm) due to limitations in the memory of the graphics processing unit.

in Figure 4.22b that for $M_s = 1038\,\mathrm{emu/cm^3}$ the simulated course of hysteresis shows the best agreement with the experiment. Furthermore, the jump around $-600\,\mathrm{Oe}$ (see inset) is only visible for this $M_s$ value. Although the vortex core deformation takes place for $960\,\mathrm{emu/cm^3}$, it is only visible in the transfer curve by the reduction of the slope at around $-700\,\mathrm{Oe}$.

In summary, fitting the shape of the hysteresis loop is a good way to determine $M_s$. In contrast, adjusting $M_s$ by only fitting the critical fields does not allow an exact determination of the material properties. The room temperature (RT) $M_s$ for $\mathrm{Co_{60}Fe_{20}B_{20}}$ reported by Helmer et al. - between approximately $1010\,\mathrm{emu/cm^3}$ and $1110\,\mathrm{emu/cm^3}$ [173] - is in good agreement with the best fit value of this work of approximately $1040\,\mathrm{emu/cm^3}$. In contrast, Wang et al. reported RT values of only $800\,\mathrm{emu/cm^3}$ (see Figure 3.7). The comparison with experimental determined $M_s$ of the investigated system is still pending. For $\mathrm{Co_{90}Fe_{10}}$ a RT value of $M_s = 1302\,\mathrm{emu/cm^3}$ was reported [174]. This value matches the $M_s$ determined in this work ($1240\,\mathrm{emu/cm^3}$).

### 4.2.2 Exchange Stiffness

Figure 4.23 illustrates how the exchange stiffness constant $A$ affects the behavior of the vortex state. Two different values, $A = 1.0\,\mathrm{\mu erg/cm}$ and $1.53\,\mathrm{\mu erg/cm}$, were applied to two thickness series from 5 to 50 nm. $H_{an}$ is nearly unaffected, whereas $H_n$ is on average slightly increased for the smaller $A$. The chosen exchange stiffness constant values are in the typical range for $\mathrm{Co_{60}Fe_{20}B_{20}}$ [173]. Values of $A = 1.8\,\mathrm{\mu erg/cm}$ for cobalt [175] and $A = 1.0\,\mathrm{\mu erg/cm}$ for iron [37] were reported. Accordingly, $\mathrm{Co_{90}Fe_{10}}$ is expected to have the approximately same exchange stiffness constant as $\mathrm{Co_{60}Fe_{20}B_{20}}$.
A smaller exchange stiffness constant two relevant consequences has in this context: first, the material becomes magnetically softer, and second, the exchange length is reduced (which is a consequence of the former). The soft magnetic aspect can be explained

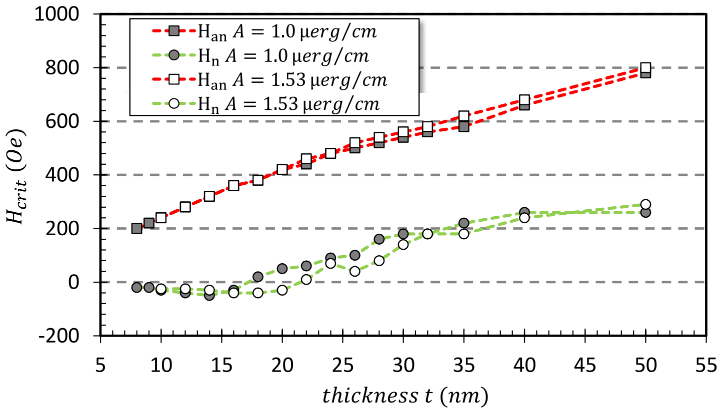

**Figure 4.23.** Critical fields $H_n$ and $H_{an}$ as a function of disk thickness ($d = 1.1\,\mathrm{\mu m}$) for two exchange stiffness constants $A$. A saturation magnetization of $M_s = 1038\,\mathrm{emu/cm^3}$, no magneto-crystalline anisotropy and no magnetically disturbed edge were applied.

by the fact that different magnetic states are usually separated by an energy barrier. These energy barriers are partly caused by the field independent term $E_{\text{exch}}$ and can consequently be reduced by reducing $A$. Thus, $H_{an}$ is smaller and $H_n$ is larger for a smaller $A$.
The second aspect, a reduced exchange length, also allows thinner systems to form an out-of-plane magnetization, which is mandatory for vortex nucleation. Consequently, vortex nucleation already occurs at 8 nm thickness for $A = 1.0\,\mu\text{erg/cm}$, instead of 10 nm for $A = 1.53\,\mu\text{erg/cm}$ (see Figure 4.23).

A reduction of $A$ can also be treated as if the dimensions of the structure are scaled up (for a fixed aspect ratio and $M_s$) since it reduces the energetic contribution of $E_{\text{exch}}$. It has been shown in Section 4.1.3 that the critical fields $H_n$ and $H_{an}$ scale with the stray field of the structure, which is proportional to $M_s \cdot \frac{t}{d}$. Accordingly, no large changes of $H_n$ and $H_{an}$ are expected, which has already been shown in Figure 4.23. At this point, it will be proven that it is only possible to reproduce the magnetic behavior of a disk structure up to a certain degree by changing $A$ and adapting the volume of the disk accordingly. However, a complete reproduction, especially of $H_n$, is not possible due to the thickness dependence of the pre-vortex states.
A scaling of the structure where the aspect ratio is kept constant can be described in the following way: $x' = a \cdot x$, $y' = a \cdot y$ and $z' = a \cdot z$. Within this formulation $x$, $y$ and $z$ are the space coordinates and $a$ is the scaling factor. This results in the following energy terms for $E'_{\text{Zeeman}}$, $E'_{\text{demag}}$, and $E'_{\text{exch}}$:

$$\begin{aligned}
E'_{\text{Zeeman}} &= \int\limits_{V'} \vec{H}_{\text{ext}} \cdot \vec{M}(\vec{r})\,\mathrm{d}V' = \int\limits_{V'} \vec{H}_{\text{ext}} \cdot \vec{M}(\vec{r})\,\mathrm{d}x'\,\mathrm{d}y'\,\mathrm{d}z' \\
&= \int\limits_{V} \vec{H}_{ext} \cdot \vec{M}(\vec{r}) a^3\,\mathrm{d}x\,\mathrm{d}y\,\mathrm{d}z \\
&= a^3 E_{\text{Zeeman}} \\
E'_{\text{demag}} &= -\frac{1}{2}\int\limits_{V'} \vec{H}_{\text{demag}}(\vec{r}) \cdot \vec{M}(\vec{r})\,\mathrm{d}V' = -\frac{a^3}{2}\int\limits_{V} \vec{H}_{\text{demag}}(\vec{r}) \cdot \vec{M}(\vec{r})\,\mathrm{d}V \\
&= a^3 E_{\text{demag}} \\
E'_{\text{exch}} &= \int\limits_{V'} A(\vec{r})\left(\left(\frac{\partial m_x}{\partial x'}\right)^2 + \left(\frac{\partial m_y}{\partial y'}\right)^2 + \left(\frac{\partial m_z}{\partial z'}\right)^2\right)\mathrm{d}x'\,\mathrm{d}y'\,\mathrm{d}z' \\
&= \int\limits_{V} A(\vec{r})\frac{1}{a^2}\left(\left(\frac{\partial m_x}{\partial x}\right)^2 + \left(\frac{\partial m_y}{\partial y}\right)^2 + \left(\frac{\partial m_z}{\partial z}\right)^2\right)a^3\,\mathrm{d}x\,\mathrm{d}y\,\mathrm{d}z \\
&= aE_{\text{exch}}
\end{aligned} \tag{4.6}$$

In this equation the exchange stiffness constant was assumed to be equal in both systems ($A'(\vec{r}) = A(\vec{r})$).

To achieve the same balance of energy in the scaled system as in the initial system, the exchange stiffness constant is adjusted the following way:

$$aA'(\vec{r}) = a^3 A(\vec{r}) \Longrightarrow a = \sqrt{\frac{A'(\vec{r})}{A(\vec{r})}} \tag{4.7}$$

Accordingly, a scaling of the structure with the exchange length [176] has to be carried out ($M_s$ is not changed here). Such a scaling, where the relative energy contributions are kept constant, is illustrated in Figure 4.24a: two 35 nm thick disk structures are plotted with 1.1 µm diameter and $A = 1.0\,\mu\text{erg/cm}$ or $1.53\,\mu\text{erg/cm}$. Corresponding structures with dimension matching to the changed value of $A$ are plotted additionally. For instance, structure IV with 1.36 µm ($= 1.1\,\mu\text{m} \cdot \sqrt{1.53}$) diameter and 43.3 nm ($= 35\,\text{nm} \cdot \sqrt{1.53}$) thickness pairs with structure I since $A$ is larger by a factor of 1.53 for IV. In contrast, the volume and exchange stiffness constant were scaled down for structure III compared to II and therefore these two disks pair up. The following similarities can be observed within the pairs allowing a differentiation between them:

First, the type of transition (kink or jump) into the double vortex state and the corresponding field values are similar. These transitions are marked in Figure 4.24a. No. 1 marks the continuous double vortex formation out of the buckling state and No. 2 the erratic collapse of the buckling state.

Second, the profiles of the vortex core, when approaching the edge of the structure, are similar within each pair. It is shown in Figure 4.24b that I and IV have a much more pronounced $\hat{z}$-component of the domain wall next to the vortex core compared to II and

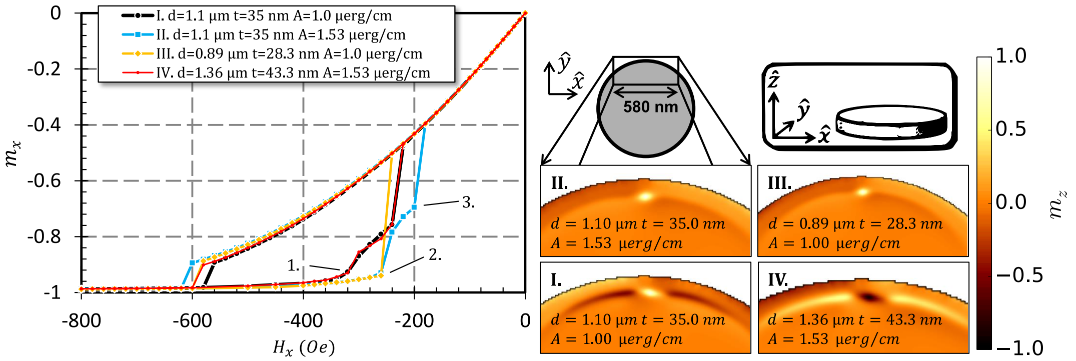

(a) (b)

**Figure 4.24.** (a) Hysteresis loops of two disks with $d = 1.1\,\mu\text{m}$, $t = 35\,\text{nm}$ and two different exchange stiffness constants ($A$). Furthermore, one disk structure (III) where the volume and exchange stiffness constant were scaled down (originating from II) and one where volume and $A$ were scaled up (IV, originating from I) are plotted. The aspect ratio $\frac{d}{t}$ is identical for all disks. (b) Illustration of the differences and similarities in the vortex core profile for the last simulation step before annihilation. Simulation parameters are given in the caption of Figure 4.23.

III. The figure also shows that the vortex core gains size with increasing disk thickness. However, the reference structures do not show exactly the same $H_n$ and $H_{an}$ values. The reason for this appears to be complex. One reason could be that there are deviations in volume or, for example, edge roughness due to the discretization. A real limitation of the scaling is the fact that the pre-states are mainly determined by the thickness of the structure (see Section 4.1.5), which is scaling linearly with the scaling factor $a$, whereas $A$ is scaling quadratically with $a$. This fact is demonstrated by the thinnest structure III, where vortex nucleation occurs only via buckling $n^* > 2$, whereas the thicker reference structure II intermediately forms the double vortex state (see No. 3 in Figure 4.24a). These observations fit the phase diagram (see Figure 4.14) presented Section 4.1.7.

In summary, it has been demonstrated that variations of the exchange stiffness constant $A$ in a reasonable range have only a small impact on the vortex characteristics of a micrometer-sized disk structure. For this reason, $A$ was kept constant (1.53 µerg/cm) for all other investigations within this work. Furthermore, a different $A$ can be treated like a scaling of the volume in a first approximation. However, deviations regarding $H_n$ are observed then due to the thickness dependence of the pre-vortex states.

### 4.2.3 Magneto-Crystalline Anisotropy

So far the magneto-crystalline anisotropy was neglected in the simulations. It has already been noted in Section 4.2.1 that an explanation is missing for the delayed vortex nucleation in 20 nm thick CoFe disk structures. This missing link will be given in this section and further related effects will be discussed in the subsequent sections, such as the visibility of a change in sense of rotation of the vortex state, extremely stable double vortex states and crossed hysteresis.

Figure 4.25a shows the comparison of an experimental transfer curve of a CoFe disk with the simulation of such an element without any magneto-crystalline anisotropy applied. It is immediately noticeable that the experimental transfer curve shows certain 'mini-hysteretic' effects (term proposed by Hubert Brückl, 2015): Small jumps are observed in the hysteresis loop of the vortex state. The observed 'mini-hysteretic' effects have already been described and explained in literature [111, 177]: the polycrystalline grain texture can be considered as an energy landscape for the vortex core causing a non-linear and non-steady movement of the core which leads to the step-shaped hysteresis loop. The analytical model by Burgess, Losby and Freeman [111] reproduces those 'mini-hysteretic' effects very well.
If simulating an amorphous structure, the effect is not observed in simulations, as was to be expected. By introducing a polycrystalline grain structure with a medium magneto-crystalline anisotropy the 'mini-hysteretic' effects can be reproduced as it is shown in Figure 4.25b. Furthermore, $H_n$ is also reduced when a magneto-crystalline anisotropy is

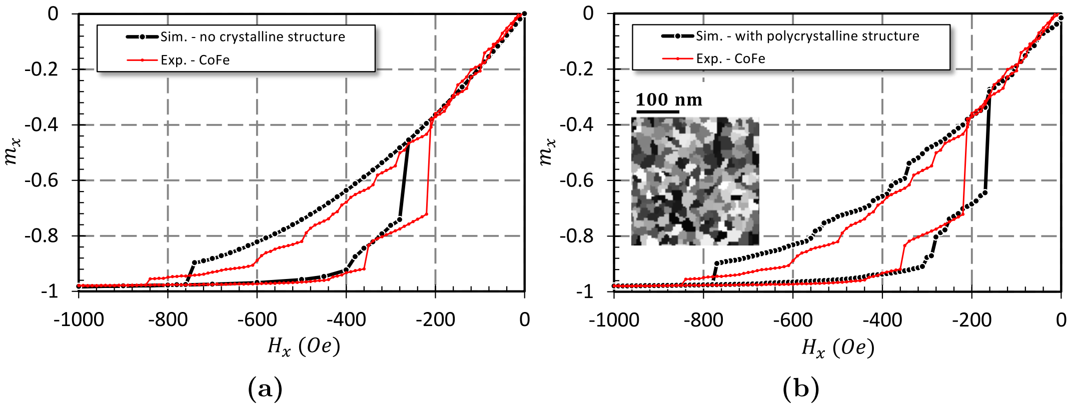

**Figure 4.25.** Half of the quasi-symmetric hysteresis loop of a 35 nm thick CoFe disk structure (Exp.) with 1.1 µm diameter. (a) The simulation (Sim.) of a structure with the same dimensions but without any crystalline structure shows a smooth transfer curve. (b) If applying a polycrystalline structure, the step shape of the experimental (Exp.) transfer curve is reproduced by the simulation very well. An average crystallite size of 20 nm (in-plane) with randomly distributed uniaxial in-plane magneto-crystalline anisotropy axes was applied for the shown simulation. The polycrystalline structure is illustrated in plan view in the inset in (b). The color code, ranging from black to white, represents the 360° orientation of the anisotropy axes. The crystal growth is assumed to be columnar, so the texture does not change in $\hat{z}-$direction. An anisotropy constant of $K_1 = 5 \times 10^5\,\mathrm{erg/cm^3}$ was applied. Remaining simulation parameters for CoFe are given in Section 3.3.

applied. This explains why in Section 4.2.1 in Figure 4.20 for 20 and 35 nm thickness the average nucleation field values are inverted for CoFe and CoFeB, despite the larger $M_s$ of CoFe.

The influence of the magneto-crystalline anisotropy on the vortex state can also be made visible with magnetic imaging techniques. Figure 4.26 shows measurement results obtained via scanning magnetoresistive microscopy (SMRM)[4] [141, 142] and magnetic force microscopy (MFM) [178]. A localization of the vortex core is not possible due to the stray field that results from the magneto-crystalline grain structure of the material. Also when changing the externally applied magnetic field (1-4 in Figure 4.26a), the position of the vortex core cannot be localized. The MFM image, shown in Figure 4.26b, shows a similar stray field landscape as the SMRM images but with a reduced resolution. The localization of a vortex core is again not possible.
Simulations of the stray field of a disk element with medium magneto-crystalline anisotropy are shown in Figure 4.27 for a distance of 50 nm to the disk surface. In the experiment, the distance between the TMR sensor of the hard disk drive read/write head (RWH) and the sample surface was about 30 nm [143]. Together with the thickness of the encapsulation of the disk element - remaining hard mask and passivation layer were expected to be in the range of 20 nm - the spacing between SMRM sensor and disk surface was estimated to be about 50 nm. The in-plane stray field, shown in Figure 4.27a, does not allow the localization of the vortex core, but the out-of-plane stray field does (see Figure 4.27b).

---

[4] The SMRM technique is briefly introduced in Section 3.2.2.

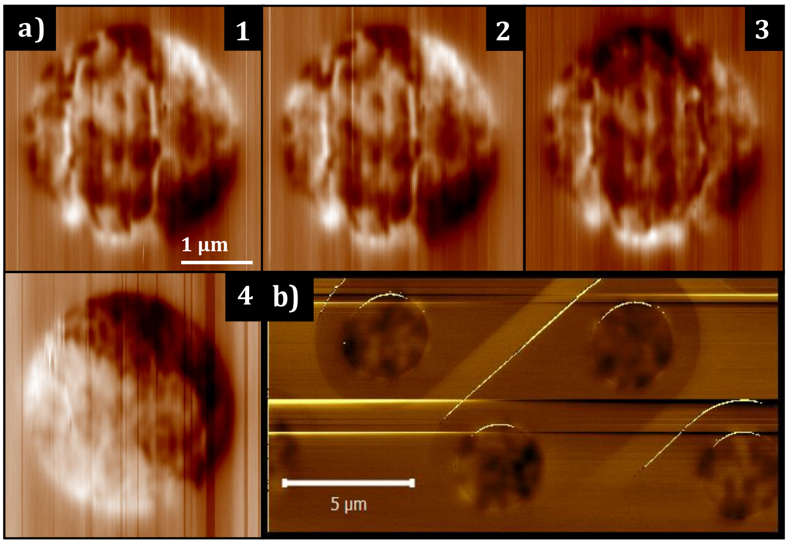

**Figure 4.26.** (a) SMRM images of a TMR spin-valve with a CoFe free layer disk ($d = 3.1\,\mu\mathrm{m}$ and $t = 50\,\mathrm{nm}$). A coil current (arbitrary units) of 0 (1), 10 (2), 20 (3) and 50 (4) was applied. (b) MFM image of several CoFe disk structures (same dimensions) at zero field. The topology was not completely removed for all line scans in this image and therefore the bottom metal connection of the TMR cells is also visible.

Assuming that the RWH sensor is in saturation at approximately 80 Oe [141], the image drastically changes (see Figure 4.27c) and a localization of the vortex core is no longer clearly possible. Thus, the clipping of the sensor can explain why the localization of the vortex core is not possible in the SMRM images. Note that the simulated disk has a diameter of 1.1 µm, whereas the experimentally obtained images in Figure 4.26 show disks with a diameter of 3.1 µm. Consequently, the dark and bright spots seem to appear larger in the simulation.

In Figure 4.27d $m_z$ is plotted for a reduced color range allowing to conclude that the depicted stray field results from an out-of-plane magnetization between plus and minus 3 %.

Figure 4.28a and 4.28b show experimental transfer curves of CoFe disk elements with 1.1 µm diameter. The grouping in early $H_n$ (4.28a) and delayed $H_n$ (4.28b) was done because of the broad nucleation field distribution. The chosen devices were picked randomly. A connection between $H_n$ and the step shape was not observed in the experiment. Furthermore, a general connection between the type of kink, when coming from saturation, and $H_n$ could also not be established.

On the following pages, different factors such as grain texture, average grain size ($D_{\mathrm{grain}}$), spatial orientation and magnitude of the uniaxial magneto-crystalline anisotropy are investigated to allow a more detailed interpretation of the experimental data. A rough estimation of $D_{\mathrm{grain}} \approx 20\,\mathrm{nm}$ is possible by the TEM thin section of the free layer, shown in Section 3.1.2. A CoFe thickness of 20 nm was chosen to study the factors since a continuous columnar crystal growth is most likely here compared to thicker systems.

Figure 4.28c shows the influence of the grain texture. The different textures stand for

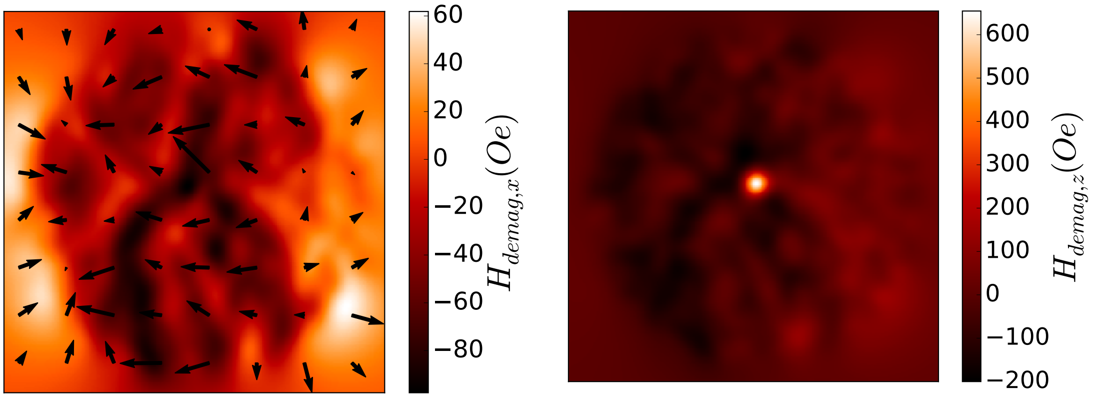

**(a)** in-plane stray field **(b)** out-of-plane stray field

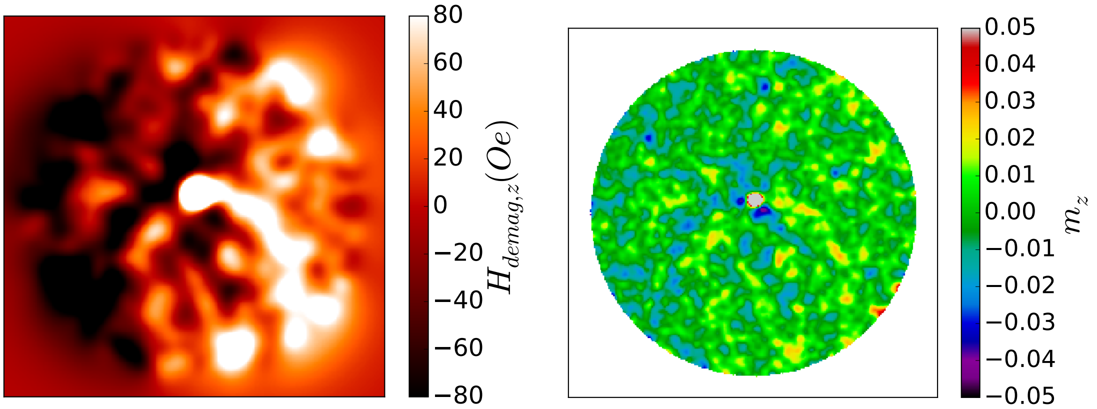

**(c)** clipping: $|H_{\mathrm{demag},z}| \leqslant 80\,\mathrm{Oe}$ **(d)** clipping: $|m_z| \leqslant 0.05$

**Figure 4.27.** Simulated in-plane (a) and out-of-plane (b) stray field component in a distance of 50 nm above the surface of the disk. Shown is the vortex state at $H_{ext} = 20\,\mathrm{Oe}$ for a polycrystalline disk with 1.1 µm diameter and 50 nm thickness. (a) Vectors represent the orientation and magnitude of $\vec{H}_{\mathrm{demag}}$, projected into the x-y plane. (c) Out-of-plane stray field with applied clipping of the color range. (d) Corresponding out-of-plane magnetization with applied clipping of the color range. Simulation parameters are given in the caption of Figure 4.25. Additionally, a sloped edge with $\alpha = 59°$ was applied (see Figure 4.38 in Section 4.2.7) and the discrete element unit cell was $\leqslant 5 \times 5\,\mathrm{nm}^2$ in-plane, but out-of plane 10 nm due to limitations in the calculation of the stray field. A reference simulation with 5 nm out-of-plane unit cell was in good agreement regarding $\vec{m}$.

different random arrangements of the randomly shaped grains ($D_{\mathrm{grain}}$ constant), each grain with a random in-plane orientation of the constant $K_1$. An example of a grain texture is shown in the inset in Figure 4.25b. A relatively large change of $H_n$ and also of the nucleation paths (intermediate states) can be observed. The size of the steps seems to be unchanged. Small changes in annihilation field can also be observed. The general curve characteristics of the annihilated state, e.g. the position and shape of the kink seem to be unchanged if the edge of the structure stays unchanged (Texture No. 1 - 3). When the edge of the structure is additionally changed (Texture No. 4), the part of the curve of the annihilated state is slightly changed. These effects will be discussed in more detail in Section 4.2.11. It seems reasonable to conclude that the grain texture has a large effect

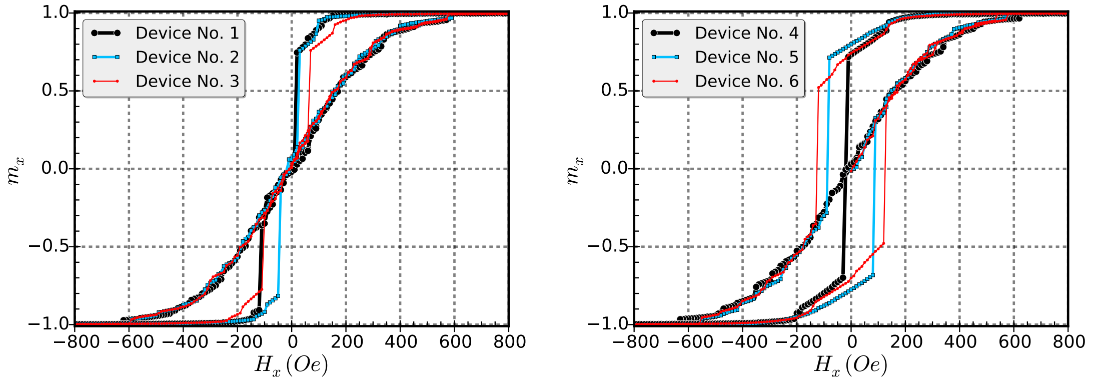

**(a)** Exp. - early nucleation **(b)** Exp. - delayed nucleation

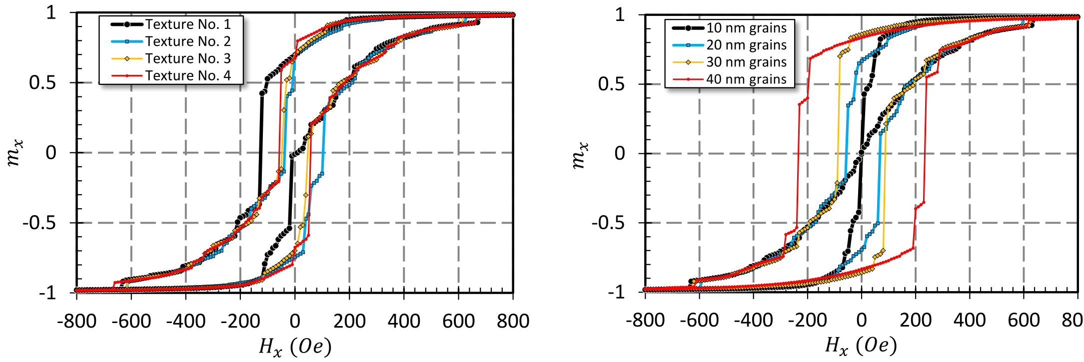

**(c)** Sim. - grain texture **(d)** Sim. - average grain size

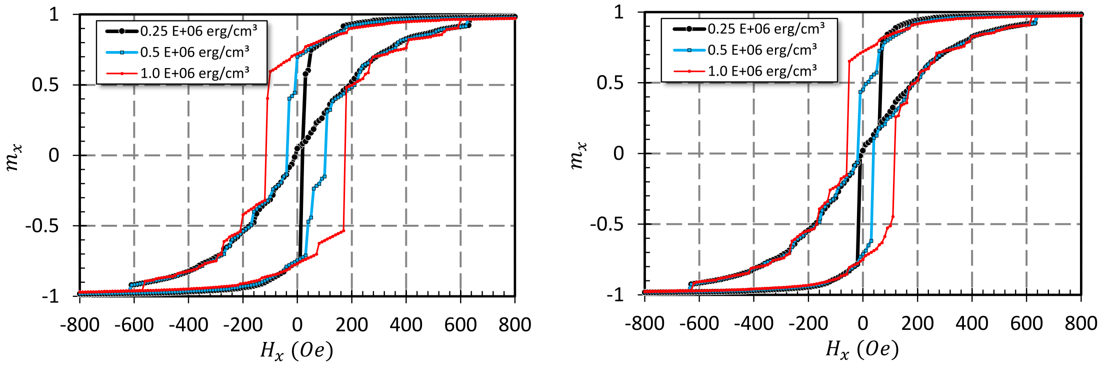

**(e)** Sim. - in-plane $K_1$ **(f)** Sim. - three-dimensional $K_1$

**Figure 4.28.** (a-b) Spectrum of measured transfer curves of different single disk devices with 1.1 µm diameter, all from one wafer with 20 nm CoFe free layer thickness. A part of the elements shows an early vortex nucleation (a), others a delayed nucleation (b). (c-e) Simulations of disk structures with the same dimensions show how the hysteresis loops are affected by the polycrystalline structure, including its grain texture (c), average grain size ($D_{\text{grain}}$) (d) and magnitude of the uniaxial magneto-crystalline anisotropy constant $K_1$ for random in-plane (e) or three-dimensional (f) orientation. For (c) $D_{\text{grain}}$ was 20 nm and $K_1 = 5 \times 10^5\ \text{erg/cm}^3$, in addition the geometry of the edge has been changed for texture No. 4 by applying a small random roughness with an amplitude of 1.2 nm. For (d) $K_1$ was $5 \times 10^5\ \text{erg/cm}^3$ and every structure had a slightly different edge. For (e) and (f) $D_{\text{grain}}$ was 20 nm and the grain texture and shape of the edge were kept constant. Unspecified simulation parameters for (c) - (f) are given in the caption of Figure 4.25.

on $H_n$ but the full spectrum of magnetic behavior of the experimental devices cannot be reproduced by changing only the grain texture.

The influence of $D_{\text{grain}}$ is illustrated in Figure 4.28d, where the transfer curves of four disk elements with different $D_{\text{grain}}$ are plotted. Naturally, the grain texture of each element was different as a result of the change in grain size. By applying a small random roughness with an amplitude of 1.2 nm, the edge of each structure was slightly different. Nevertheless, a clear trend with increasing $D_{\text{grain}}$ is immediately apparent: a widening of the hysteresis. Thus, $H_n$ is becoming increasingly delayed for larger $D_{\text{grain}}$. Such an increase of the coercivity field $H_C$ with increasing $D_{\text{grain}}$ has also been reported in literature [179]. Since $D_{\text{grain}}$ is affecting $H_n$ massively as well as the course of hysteresis, it seems to be likely that the grain size distribution of one wafer is broader compared to that of one simulation parameter set[5]. This would explain the broad $H_n$ distribution observed in the experiment.

At a close look, one can observe that the change of $m_x$ during a step in the vortex state is also increased for a larger $D_{\text{grain}}$. That is expected since the energy landscape, which affects the path of the vortex core, is getting coarser. With $D_{\text{grain}} = 20\,\text{nm}$ a good matching between experiment and simulation is observed. This value is consistent with literature [45, 92] and confirms the results of the TEM analysis. Larger values, such as the shown 30 and 40 nm, cause a much larger hysteresis (compared to the experiment) in connection with the chosen $K_1$. However, they cannot absolutely be excluded since the grain size distribution was fix in MicroMagus.

Figure 4.28e and 4.28f give an insight into the influence of the magnitude of the uniaxial magneto-crystalline anisotropy constant $K_1$ and the influence of its spatial orientation.

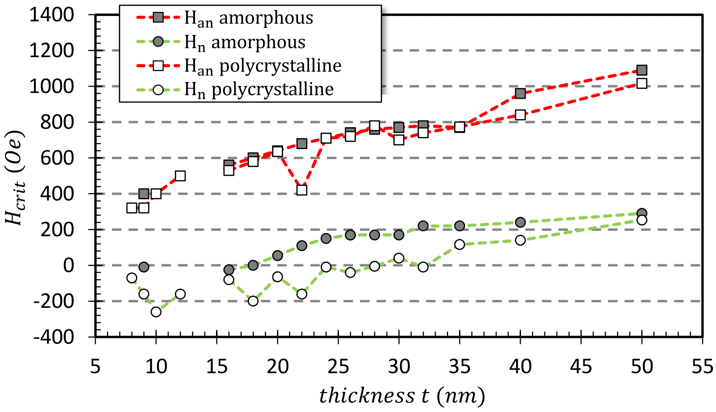

**Figure 4.29.** Critical fields $H_n$ and $H_{an}$ (simulation) as a function of disk thickness for elements without and with polycrystalline structure. All disk elements have a diameter of 1.1 µm. For $t = 20$, 35 and 50 nm, the shown $H_{crit}$ values are the average values from three structures with different grain texture. For all other thicknesses only one device was simulated, but each with a different texture. The discrete element unit cell was $\leqslant 5 \times 5 \times 5\,\text{nm}^3$ for all elements with a thickness $\leqslant 35\,\text{nm}$. For $t = 40$ and 50 nm, the cell size in $\hat{z}-$direction was increased to 5.7 nm and 7.1 nm due to limitations in the memory of the graphics processing unit. Remaining simulation parameters are given in the caption of Figure 4.25.

---

[5] An adaption of the grain size distribution within MicroMagus was not possible.

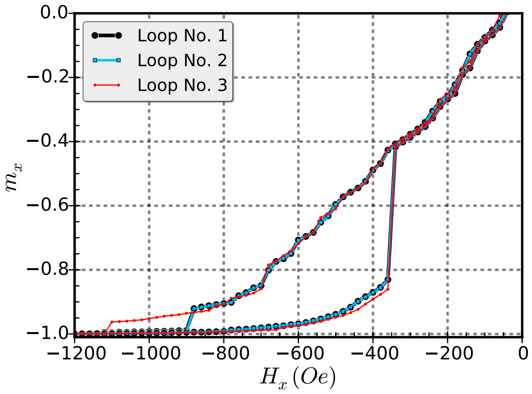

**Figure 4.30.** Half of three complete hysteresis loops of one CoFe single disk device with $d = 1.1\,\mu\text{m}$ and $t = 50\,\text{nm}$. A large variation of the annihilation field can be observed.

For both figures, grain texture and shape of edge were kept constant to allow a conclusion to be drawn. The main results can be summarized as follows: an increase in $K_1$ increases the hysteresis and thus delays vortex nucleation. The pinning of the vortex core to certain grains is also increased, which is visible by the more pronounced step shape of the transfer curve. The picture does not change in principle if the anisotropy axes are distributed randomly in all three spatial dimensions (Figure 4.28f), instead of only in-plane (Figure 4.28e). However, a larger $K_1$ is needed to observe a similar magnitude of hysteresis and step shape. Due to the large $H_n$ distribution in the experiment the exact value and type of magneto-crystalline anisotropy cannot be defined without further experimental research of the exact magneto-crystalline properties of $\text{Co}_{90}\text{Fe}_{10}$, especially if the material is considered to be used in a productive vortex sensor. Nevertheless, it can be stated that an average $K_1$ of approximately $5 \times 10^5\,\text{erg/cm}^3$ is a reasonable value which allows a good reproduction of the mini-hysteretic effects and is consistent with literature values: Liu et al. reported for pure cobalt $K_1$ values of around 5 to $6 \times 10^5\,\text{erg/cm}^3$ [109].

An overview of different layer thicknesses and how the critical fields are affected if a magneto-crystalline anisotropy is introduced is given by Figure 4.29. It becomes apparent once again that individual devices may differ drastically in their nucleation field, which leads to a 'noisy' trend of the critical fields. However, it can be observed that all polycrystalline structures have a smaller nucleation field compared to the amorphous equivalent. Differences in $H_n$ between amorphous and polycrystalline structure appear to decrease with increasing thickness, which is consistent with the experimental data (see Table 5.1 in Section 5.2.2). For $H_{an}$, the differences are usually smaller and the polycrystalline structure does not necessarily need to cause a reduced $H_{an}$.

Figure 4.30 illustrates that a large variation of the critical fields is not only observed from device to device but also if one device is measured several times. Although the transfer curve seems to be highly reproducible, a large difference in $H_{an}$ can be observed here. Thermal activation into different states can explain this.

To summarize, it was shown that the magneto-crystalline anisotropy of CoFe is causing already known mini-hysteretic effects and leads to a reduction of $H_n$. SMRM and MFM images of the investigated elements did not allow to localize the vortex core primarily because of the stray field generated by the grain texture. An estimation of the crystalline properties was done by comparison with micro-magnetic simulations, but an exact determination of the properties requires further experimental investigations.

### 4.2.4 Magneto-Crystalline Anisotropy and Direction of Rotation of the Vortex State

The complex influence of the magneto-crystalline anisotropy on the magnetic behavior of CoFe disk structures is illustrated in detail in Figure 4.31. A good repeatability of the mini-hysteretic effects for one single disk device is shown in Figure 4.31a. The graph shows two types of measurements: full hysteresis loops with $|H_x| > |H_{an}|$ for the positive and negative branch and partial loops which only reach saturation in the positive branch (see inset in Figure 4.31a). Both types of loops were performed two times. It is clearly visible that all curves are almost perfectly congruent and independent of the measurement type or of the fact that a measurement was repeated.

This observation does not apply for every measured disk structure. The measurement in Figure 4.31b demonstrates this exemplarily: the full loop and the partial loop differ considerably from each other regarding the step shape. Furthermore, both types of curves are highly reproducible when the measurement is repeated.

Highly reproducible mini-hysteretic effects - which are independent of the orientation of the previous saturation field or which depend on the previous saturation direction - are not the only observed possibilities but the most common ones. In some cases, the mini-hysteretic effects did vary within one loop type which results from thermal activation. However, it is important to note that in the vortex state more than two clearly distinguishable courses of hysteresis were never observed even if more than four loops were performed. This suggests that the observation can be explained by the two different directions of rotation of the vortex state. The shown simulation results demonstrate this clearly. For nearly identical transfer curves (Figure 4.31c), the directions of rotation are identical (Figure 4.31d). For different courses (Figure 4.31e), the direction of rotation of the loop with field reversal is anticlockwise (No. 3 in Figure 4.31f), whereas the direction of rotation of the full loop is clockwise (No. 4 in Figure 4.31f).

Different polarities seem to have only a minor impact: for the shown states with equal sense of rotation (Figure 4.31d), the core with the negative polarity is slightly shifted to the right side at 370 Oe causing a negligibly small difference in $m_x$, which is hardly visible in Figure 4.31c. This is expected because the applied uniaxial magneto-crystalline anisotropy has an in-plane orientation. Such small differences in signal can also be observed in Figure 4.31a. Whether they are due to different core polarities or due to the small hysteresis of the measurement setup could not be clarified in this context. But the very small differences may be an indication that an *in-plane* magneto-crystalline

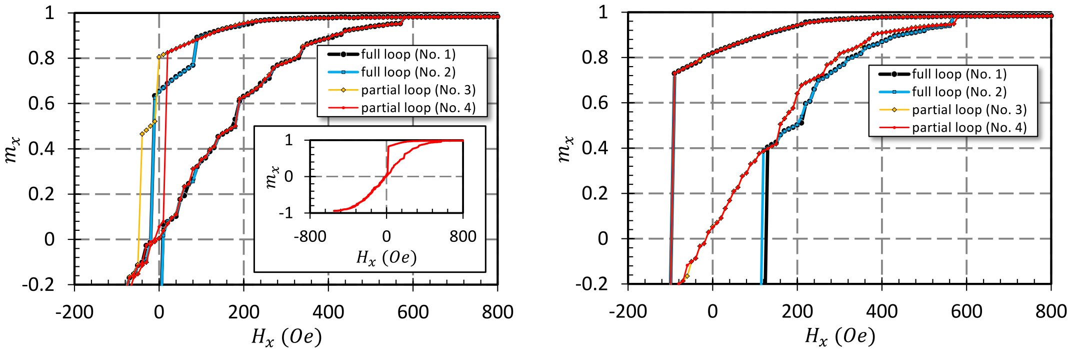

**(a)** Exp. - congruent curves **(b)** Exp. - unequal curves

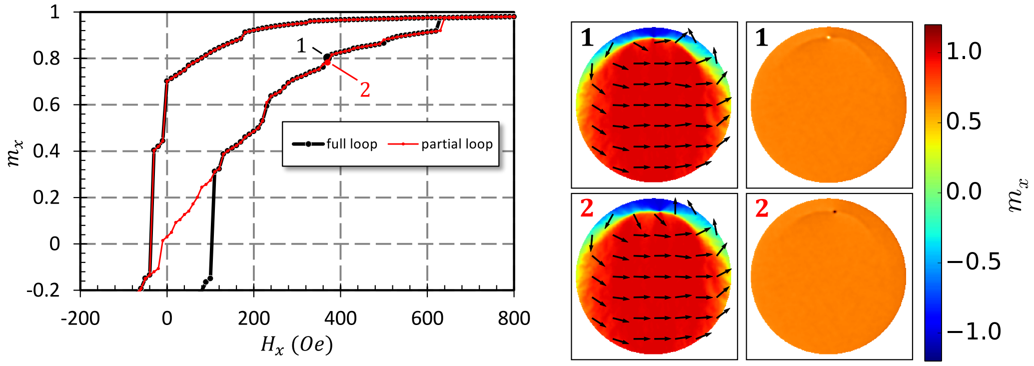

**(c)** Sim. - congruent curves **(d)** Equal direction of rotation

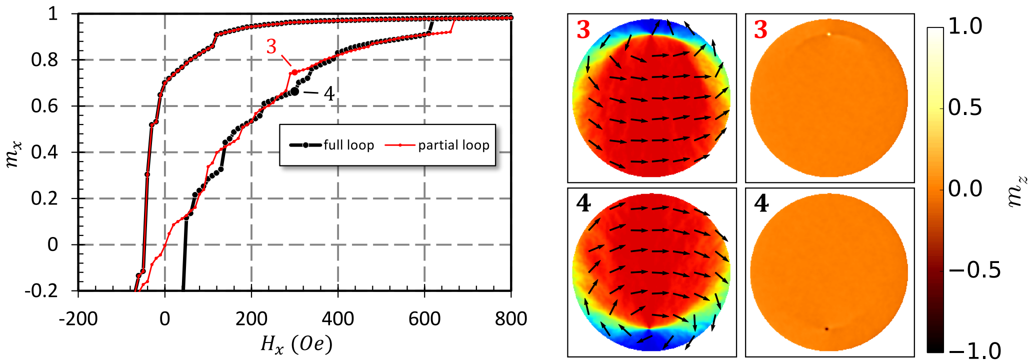

**(e)** Sim. - unequal curves **(f)** Opposed direction of rotation

**Figure 4.31.** (a) Some CoFe TMR single disk devices show a good reproducibility of the mini-hysteretic effects independent of the previous saturation direction. Full hysteresis loops are plotted together with partial loops where the field was reversed before $H_{an-}$ as shown in the inset. (b) Other devices exhibit two slightly different transfer curves. These two types of curves are also highly reproducible as the repeated measurements demonstrate (No. 1 and 2 vs. No. 3 and 4). When in simulations a partial loop is performed, additionally to the full hysteresis loop, in some cases a good reproducibility of the mini-hysteretic effects is observed (c) and it is not observed in other cases (e). The reason for this lies in the sense of rotation of the vortex state. For equal sense of rotation (d) the mini-hysteresis is reproducible, whereas for unequal sense of rotation (f) it is not. Simulation parameters for (c) - (f) are given in the caption of Figure 4.25. All structures have a disk diameter of 1.1 µm and a thickness of 20 nm.

anisotropy is actually present for the investigated CoFe.

It has been shown statistically by Pike and Fernandez that a field reversal after vortex nucleation decreases the annihilation field which they explained with the preferred location of vortex nucleation equally facilitating vortex annihilation [50]. This observation could not be confirmed in the experiment and the opposite observation can be made in Figure 4.31e. One reason for this could be that Pike and Fernandez investigated elliptical cobalt dots with a thickness of 30 nm and a lateral size of only 450 nm × 260 nm, thus the number of grains in their system is expected to be much smaller and as a result the individual grains will have a larger impact on the magnetic behavior. Furthermore, the 20 nm thick CoFe disk structures investigated here favor vortex nucleation around zero magnetic field applied. During such a delayed nucleation process, nearly half of the structure changes is magnetization. Therefore, it is difficult to imagine that the annihilation of the vortex core occurs at exactly the same position at the edge as the nucleation occurred (via buckling, S- or double vortex state).

In this section, it was shown that mini-hysteretic effects allow to identify whether the direction of rotation of the vortex state has changed.

### 4.2.5 Magneto-Crystalline Anisotropy and Increased Stability of the Double Vortex State

Some of the TMR cells with 50 nm thick CoFe showed an increased slope in the central part of the hysteresis loop. An exemplary measurement curve is shown in Figure 4.32a. The zoom view in Figure 4.32b shows the central part in more detail for a better comparison with the simulation data set which is shown in Figure 4.32c. The curve characteristics of the state with increased slope, such as its nucleation, annihilation and the slope itself, are very similar. The magnetization plots of the simulation (Figure 4.32d) reveal the presence of a double vortex state. Its large stability may be caused by the complex domain wall pattern visible in the $m_z$-plots: the crystalline structure causes an alternating polarity of the domain wall and even more than two cores appear in a small field range (see No. 2 in Figure 4.32d). On the other surface of the disk, only two cores with negative polarity are visible (not shown here). It has to be noted that it appears as if the domain wall is pinned to the edge of the disk.

For the simulation results shown, the crystal texture was different at the top and bottom of the disk. When assuming a continuous columnar growth with only one grain texture, double vortices with such a stability were not observed (four devices with different grain textures were simulated: $H_n \geq 220\,\mathrm{Oe}$). However, when a second grain texture was introduced for two of the already applied textures in both cases an increased stability of the double vortex state and thus delayed single vortex nucleation was observed. One of these structures is shown here, the field range of the double vortex state for the other structure was increased by 80 Oe for one branch ($H_n = 160\,\mathrm{Oe}$). Thus, it is assumed that a change in texture in $\hat{z}-$direction introduces an additional energy barrier for the transition from double to single vortex state. A change in texture seems reasonable for

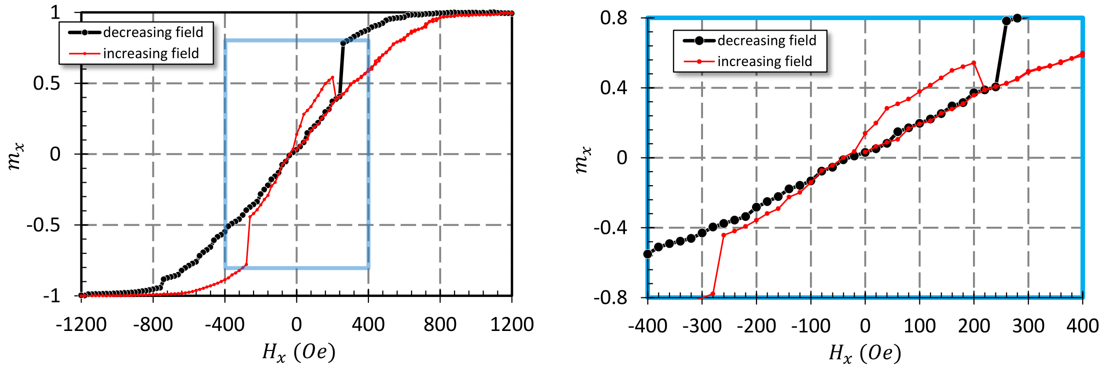

**(a)** Experiment **(b)** Experiment - Zoom

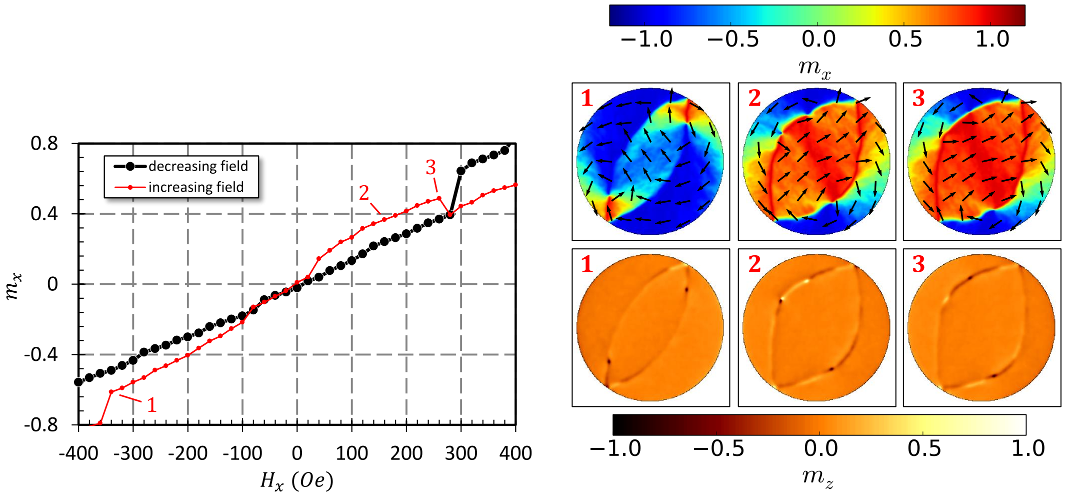

**(c)** Simulation - Zoom **(d)** Simulation

**Figure 4.32.** (a) Occasionally very stable double vortex states were observed for the 50 nm thick CoFe free layer system (single disk spin-valve with $d = 1.1\,\mu\text{m}$). (b-c) The zoom into the experimental data shows a very good agreement with the simulated data (same disk dimensions). (d) The magnetic states in the corresponding simulation show the formation of a $n^* = 2$ double vortex state at $-340$ Oe which is stable up to 260 Oe. Simulation parameters are given in the caption of Figure 4.25. In $\hat{z}-$direction the cell size was increased to 7.1 nm due to limitations in the memory of the graphics processing unit. Furthermore, the columnar crystal growth was not continuous: the texture does change approximately in the middle of the disk with respect to the $\hat{z}-$extension. The signal shown in (c) - extracted from simulation - is calculated with an electrically inactive edge (see Section 4.2.10) of about 33 nm. The magnetization patterns (d) show the states at one surface of the structure.

50 nm thickness since the average grain size is assumed to be approximately 20 nm. Such stable double vortex states as shown in Figure 4.32 were not observed for 35 nm CoFe free layer thickness. Relatively stable double vortices were also observed, but single vortex nucleation was always finished before field reversal.

In summary, an increased stability of double vortices was demonstrated in experiment and simulation for CoFe only. The characteristic feature of such a stable double vortex - which is present after field reversal - is the resulting crossed hysteresis with different susceptibility.

### 4.2.6 Magneto-Crystalline Anisotropy and Crossed Hysteresis

In a few cases, a different type of crossed hysteresis has been observed in the TMR measurements at CoFe disk structures. A typical case of such a crossed hysteresis is shown in Figure 4.33a. The zoom in on the same data set (Figure 4.33b) shows that it is caused by the increasing field part. Starting from −90 Oe, a crossing of the decreasing branch causes a negative hysteresis. At −20 Oe, a jump in signal can be observed which further increases the negative hysteresis. The curves are largely congruent from 60 Oe on, indicating that a single vortex state is present from now on.

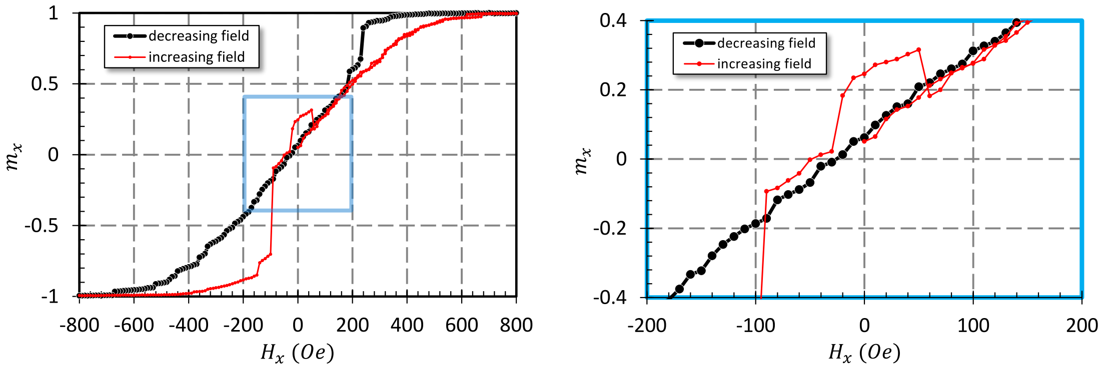

**(a)** Experiment **(b)** Experiment - Zoom

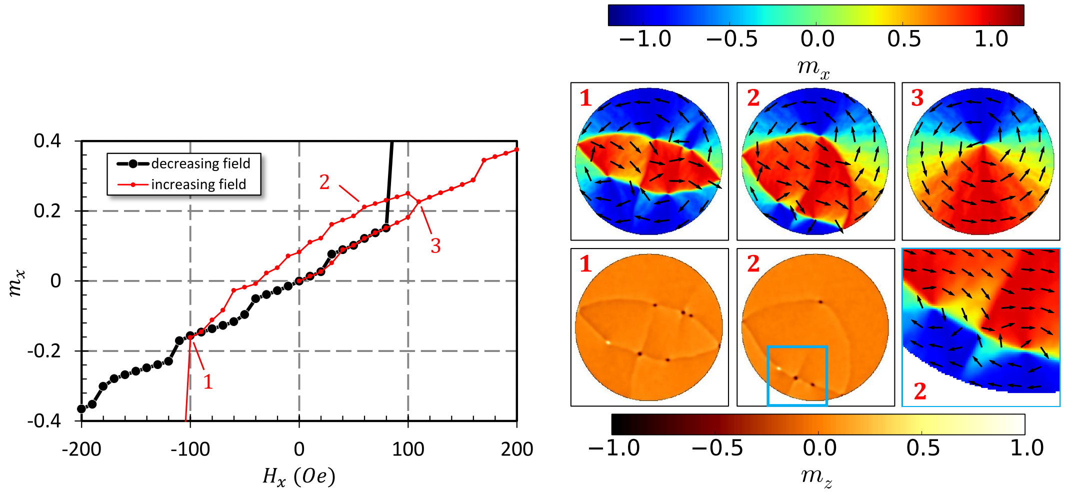

**(c)** Simulation - Zoom **(d)** Simulation

**Figure 4.33.** (a) In some cases the CoFe devices showed a crossed hysteresis (TMR measurement of a single disk device with $d = 1.5\,\mu\text{m}$ and $t = 35\,\text{nm}$). The measurement started at zero field, then $H_x$ was increased until positive saturation of $m_x$ was reached. Subsequently, a full hysteresis loop was performed. (b) The zoom into the central part of the hysteresis loop shows the crossed hysteresis in more detail. (c) Such phenomenon was also observed in micro-magnetic simulations ($d = 1.1\,\mu\text{m}$ and $t = 35\,\text{nm}$). (d) It is caused by an intermediate multiple vortex state. Simulation parameters are given in the caption of Figure 4.25. The shown signal in (c) - extracted from simulations - is calculated with an electrically inactive edge (see Section 4.2.10) of about 33 nm.

It is apparent that the slopes of decreasing branch (vortex state) and the increasing branch are very similar for the crossed hysteresis. This distinguishes such an event from the occurrence of an extremely stable double vortex state as it was shown in Figure 4.32, which has an increased slope. In micro-magnetic simulations, a crossed hysteresis was also observed sometimes. Results are shown in Figure 4.33c and demonstrate that such an effect can be caused by the presence of a complex multiple vortex state as shown in Figure 4.33d. What seems to appear the single vortex nucleation (No. 1 in Figure 4.33c) at −100 Oe is revealed as a complex multiple vortex pattern with six cores. This pattern decays subsequently (No. 2 with four cores in Figure 4.33d) while causing a crossed hysteresis until finally, at 110 Oe, the single vortex state is present (No. 3) and the crossed hysteresis has disappeared.

It should be noted that in the previous discussion vortex and antivortex were summarized under the term vortex: a closer look at No. 1 in Figure 4.33c shows the presence of six cores in the $m_z$-plot but only four of them show the circular rotation of $m_x$. The cores in the middle of the two domain walls turn out to be antivortices. The zoom view (No. 2 in Figure 4.33d) shows this state in detail: the in-plane magnetization can be divided into four quadrants where each quadrant has an antiparallel magnetization with respect to the opposing quadrant in first instance and neighboring quadrants are perpendicular oriented.

The nucleation of such vortex-antivortex-vortex triplets is known for elliptical shapes [161] as well as rectangular shapes [72, 103] and it has also been observed in a slightly different pattern for 100 nm thick circular permalloy disk structures [163].

Crossed hystereses were also observed for 50 nm thick disk structures. The stability of the state with a negative hysteresis can widely differ from device to device as shown in Figure 4.34 but also from measurement to measurement (not shown here).

Most frequently, multiple vortex states were observed in the simulations of the 20 nm CoFe disks even if their presences usually does not lead to a crossed hysteresis, but rather to a small positive hysteresis. In the experiment - with 20 nm CoFe - a crossed hysteresis was observed only in one case (not shown).

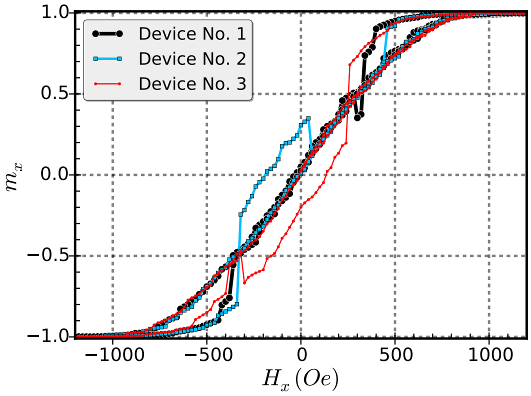

**Figure 4.34.** Crossed hysteresis of various 50 nm thick CoFe single disk TMR cells with 1.1 µm free layer diameter.

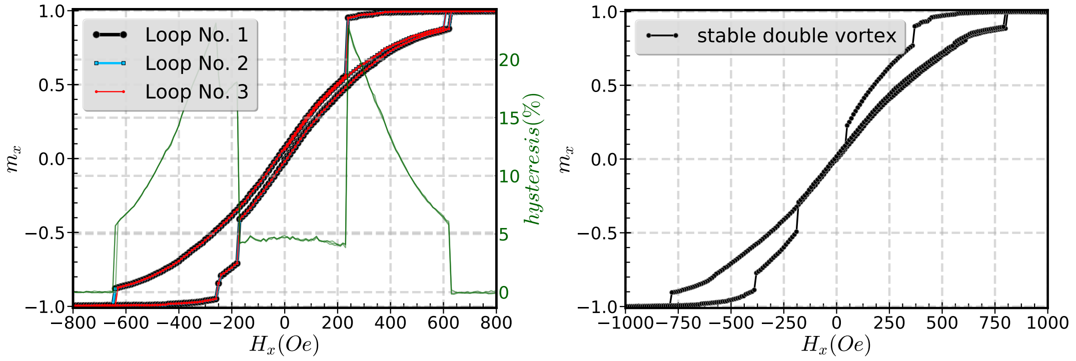

**(a)** $d = 1.1\,\mu\text{m}$ $t = 35\,\text{nm}$ **(b)** $d = 1.1\,\mu\text{m}$ $t = 50\,\text{nm}$

**Figure 4.35.** (a) Slight differences in the transfer curves depending on the orientation of the previous saturation field were observed for some CoFeB single disk devices. These differences cause a small hysteresis and are reproducible as shown by the three hysteresis loops. (b) A relatively stable double vortex state is shown for another CoFeB single disk device. The measurements started at 0 Oe with increasing $H_x$ up to 1000 Oe. Subsequently, a full hysteresis loop was performed.

The question which now arises is whether the observed effects - such as a measurable impact of the direction of rotation of the vortex state, extremely stable double vortices or crossed hysteresis - are unique features that are only present in materials with a medium or large magneto-crystalline anisotropy. Figure 4.35 shows measurements at CoFeB devices for comparison. In some cases, a slightly pronounced, constant hysteresis can be observed as shown in Figure 4.35a. Additionally, two different annihilation field values are observed for $H_{an+}$ here. The presence of both senses of rotation depending on the previous saturation field orientation may explain these two values as well as the observed, reproducible hysteresis in the vortex state. The resulting difference in $m_x$ may then be caused by e.g. shape imperfections. Still, a confirmation of this assumption is pending.
The most stable double vortex state observed in the context of this work is shown for CoFeB (50 nm thickness) in Figure 4.35b. A double vortex which was still present after zero crossing as shown for CoFe in Figure 4.32, was not observed for CoFeB. Unsurprisingly, crossed hysteresis caused by various 'trapped' vortices seems to be a unique feature of CoFe and was not observed for the amorphous CoFeB.

Wang et al. reported a uniaxial magnetic anisotropy of $\sim 2 \times 10^4\,\text{erg/cm}^3$ for a 50 nm $Co_{60}Fe_{20}B_{20}$ film, measured directly after deposition [139]. The introduction of a grain texture with an in-plane uniaxial magnetic anisotropy in the order of $\sim 1 \times 10^4\,\text{erg/cm}^3$ has no visible impact on the vortex transfer curve as to be expected: $H_n$ was delayed by only one 10 Oe field step for the $d = 1.1\,\mu\text{m}$ and $t = 20\,\text{nm}$ disk structure (not shown here). In conclusion, it is evident that even polycrystalline CoFeB can be treated as if the magneto-crystalline anisotropy is zero, in other words as if it is amorphous. Consequently, a difference between amorphous and polycrystalline CoFeB is expected to be almost invisible in the vortex transfer curve.

To summarize, it was shown that the magneto-crystalline anisotropy of CoFe can cause a negative hysteresis with unchanged susceptibility. The effect was observed in experiment and simulation and can be explained by a multiple vortex state. The observation of different types of increased and negative hysteresis (see also previous section) speak against the use of CoFe in a vortex sensor concept. Further investigations are required to assess whether these effects disappear with further increasing disk thickness.

### 4.2.7 Magnetically Disturbed Edge

Figure 4.36a illustrates - as has already been pointed out in Section 4.2.1 - that it was not possible to achieve congruent transfer curves and identical critical fields for CoFeB by only adjusting $M_s$ in the simulations. For 860 emu/cm$^3$, $H_{an}$ fits the experiment, but only for 1038 emu/cm$^3$ both the slope of the vortex state and the course of hysteresis

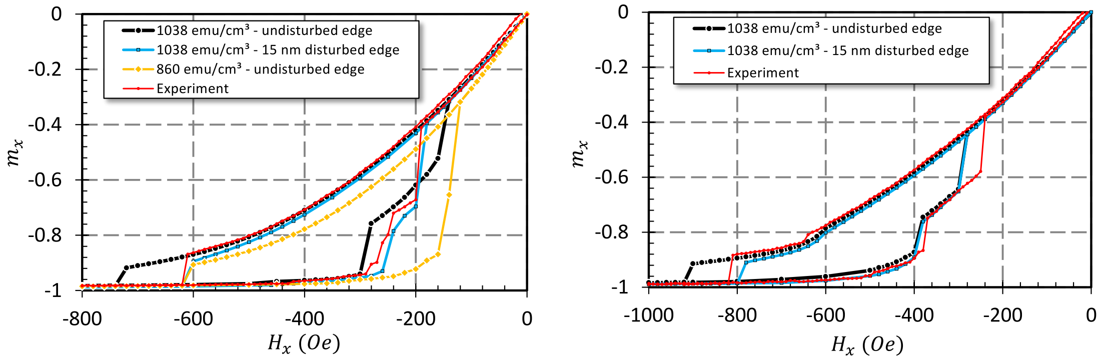

**(a)** $t = 35\,\mathrm{nm}$ **(b)** $t = 50\,\mathrm{nm}$

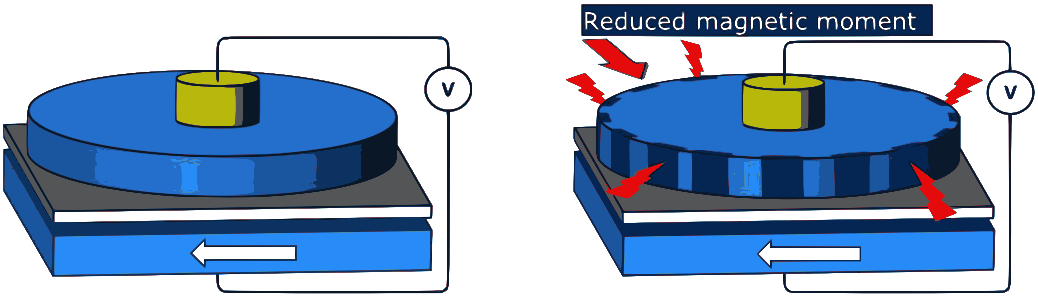

**(c)** undisturbed edge **(d)** disturbed edge

**Figure 4.36.** (a-b) Half of the quasi-symmetric hysteresis loops for 35 (a) and 50 nm (b) thick CoFeB ($d = 1.1\,\mu\mathrm{m}$). The simulations demonstrate that a magnetically disturbed edge of 15 nm width enables a detailed reproduction of the experimental data by reducing $H_{an}$ without changing the general characteristics of the transfer curve, such as the susceptibility or $H_n$. (c-d) Illustration of an undisturbed and a magnetically disturbed edge. An exchange stiffness constant of $A = 1.53\,\mu\mathrm{erg/cm}$ and zero magneto-crystalline anisotropy were applied in the simulations.

fit. A reasonable reduction of the exchange stiffness constant - shown in Section 4.2.2 - has an small influence on $H_{an}$ which is much too small to achieve a fitting for the investigated micrometer-sized disk structures. Likewise, by introducing an uniaxial magneto-crystalline anisotropy (see previous section), $H_{an}$ remains virtually unchanged. In summary, it was not possible to reproduce in detail the CoFeB data with the previously discussed bulk material parameters: saturation magnetization, exchange stiffness constant and magneto-crystalline anisotropy. Consequently, further factors need to be taken into account.

As shown in Figure 4.36a and 4.36b, good agreement between simulation and experiment is achieved by applying a magnetically disturbed edge of 15 nm. In this context, a magnetically disturbed edge means a weakening of the magnetization over a certain width of the element edge as illustrated in Figure 4.36d which is implemented via a random reduction of the local magnetic moment of each cell. On average, the reduction is larger if the cells are closer to the edge [148]. Such a magnetically disturbed edge can arise, for example, from the patterning process by doping with the gas ions [154]. The disturbed edge causes a magnetic softening of the edge. Consequently, the general curve progression of the vortex state is nearly unaffected except near $H_{an}$. The influence is illustrated by Figure 4.37a for various disk thicknesses. $H_{an}$ is reduced drastically for all elements. In other words, the stability of the vortex state, when approaching the edge of the structure, is reduced. The illustration in Figure 4.37b shows the positions of the vortex cores, at the last simulation step before annihilation. It is clearly visible that without a disturbed edge the core can approach the edge much closer. With the disturbed edge of 15 nm, the center of the core is approximately 4 cells further away from the edge. This corresponds almost exactly to the disturbed edge region since the in-plane length and width of the

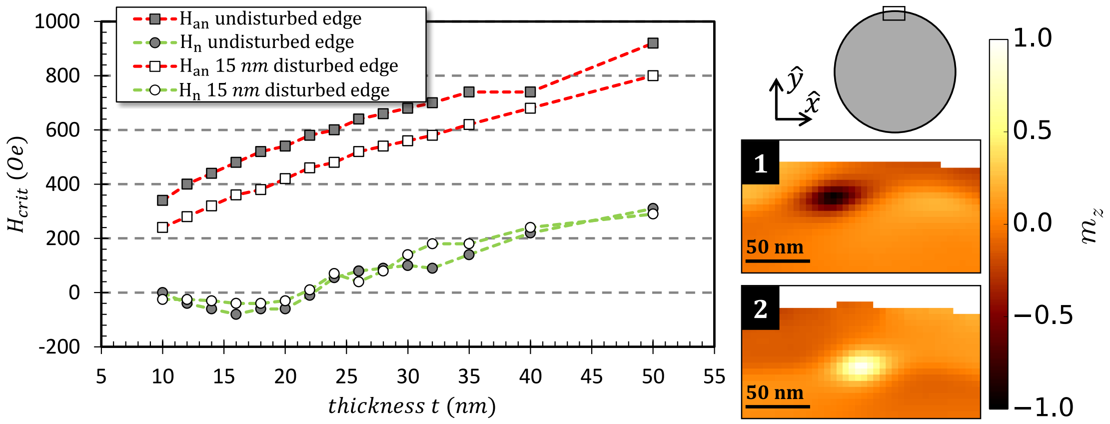

**(a)** $d = 1.1\,\mu\text{m}$ **(b)** $d = 1.1\,\mu\text{m}$ $t = 35\,\text{nm}$

**Figure 4.37.** (a) Critical fields $H_n$ and $H_{an}$ as a function of disk thickness for structures without and with magnetically disturbed edge. (b) The detail section shows the vortex core position in the last simulation step before annihilation without (No. 1) and with 15 nm disturbed edge (No. 2). A saturation magnetization of $M_s = 1038\,\text{emu/cm}^3$ was applied. Further simulation parameters are given in the caption of Figure 4.36.

cells are 4.6 nm. In contrast, the reduction of the total moment of the structure amounts to less than 5.5 % due to the magnetic weakening of the edge, even if a moment of zero is assumed for the disturbed edge area (15 nm disturbed edge and $d = 1.1\,\mu\text{m}$). Thus, the reduction of $H_{an}$ (approximately 15 %) can only be explained sufficiently by the introduced local instability of the vortex core.
The influence on $H_n$ is considerably smaller but on average $H_n$ is slightly increased as it is shown in Figure 4.37a. This effect may be explained by a reduced strength of magnetic pinning sites at the edge. Pinning sites may be caused by imperfections of the edge after the patterning process. In finite difference simulations pinning sites may also be present due to the discretization of the structure. The finite difference simulation usually employs a regular grid, which is rectangular in case of the used software MicroMagus [148]. Therefore, even if no additional roughness is applied, the edge will show a certain roughness that can affect the magnetization. Furthermore, perfectly smooth edges can also delay magnetization reversal. Perfectly smooth edges are avoided through the use of such a random weakening of the moment of individual cells. Edge effects that are related to the finite element discretization are discussed in more detail in Section 4.2.11.

It was demonstrated in simulations that a magnetic weakening of the edge has a drastic impact on $H_{an}$: The vortex core is destabilized when approaching the edge and thus an earlier annihilation is observed. The effect may explain why for CoFeB an earlier annihilation is observed in the experiment. $H_n$ is nearly unaffected by the magnetically disturbed edge. Further experimental investigations are required to prove or disprove the proposed effect.

### 4.2.8 Sloped Edge

The previous section showed that a weakening of the magnetization at the edge can reduce $H_{an}$ significantly. In the following, it is demonstrated that a modification of the slope of the edge can lead to similar results. The inset in Figure 4.38a shows a schematic detail section of the simulated disk element with a sloped edge applied. Such an edge shape is present due to the ion beam etch process (see TEM image in Figure 3.5b): the wafer is tilted with respect to the ion beam while, at the same time, the chuck where the wafer is attached to rotates. This measure is intended to avoid redeposition during the patterning of the TMR elements. Redepostion can cause, for example, a short of the elements [180]. Results for varying edges with $\alpha = 90°$ (vertical), 74° ($s = 10\,\text{nm}$), and 60° ($s = 20\,\text{nm}$) are shown in Figure 4.38a. The results are clear: a sloped edge leads to a decrease of $H_{an}$ and an increase of $H_n$, similar as if a disturbed edge was applied. Accordingly, both factors - disturbed and sloped edge - can explain the observed reduced $H_{an}$ values. In case of the sloped edge, the stability of the vortex state is limited by the smaller disk diameter of one surface. Figure 4.38b shows that the vortex core itself does not become tilted shortly before $H_{an}$. It approaches the edge of the smaller top surface as close as in

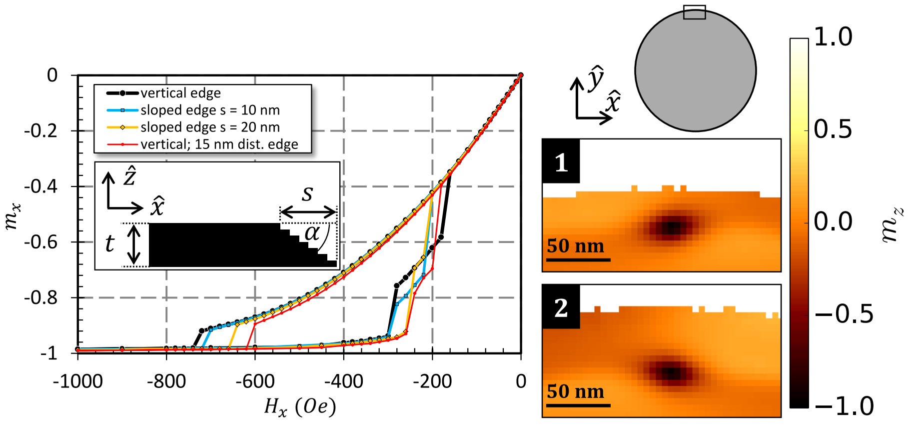

(a) (b)

**Figure 4.38.** (a) Half of the simulated, quasi-symmetric hysteresis loops for a varying degree of the sloped edge and zero magneto-crystalline anisotropy. All structures have a diameter of 1.1 µm at the bottom and a thickness of $t = 35$ nm. The implementation of the sloped edge is illustrated in the inset in (a) which shows a detail section of the disk edge in side view. The step shape arises from the discretization. The parameter $s$ reflects the difference of the disk radii, bottom layer compared to top layer. For comparison, an additional simulation shows the result for a magnetically disturbed edge of 15 nm (for a vertical edge, which corresponds to $s = 0$). All other simulations are without magnetically disturbed edge. (b) The detail section shows the vortex core position for $s = 20$ nm in the last simulation step before annihilation for the top (No. 1) and bottom surface (No. 2). $M_s = 1038\,\mathrm{emu/cm^3}$. Remaining simulation parameters are given in the caption of Figure 4.36. In all simulations a random edge roughness with an amplitude in the range of the unit cell size was applied, also in $\hat{z}-$direction. The aim was to reduce partial smooth edges as a result of the discretization (see Section 4.2.11).

the case of the vertical edge. As a result, annihilation occurs earlier due to the smaller diameter of the top surface.

It is beyond the scope of this work to decide whether a magnetically disturbed edge is present additionally to the sloped edge. Nevertheless, it must be pointed out that good agreement between experiment and simulation was obtained for a constant width of a magnetically disturbed edge, independent of the thickness of the structure. For a sloped edge with a constant angle this is not to be expected. Factors such as the penetration depth of an ion beam mainly depend on the acceleration energy, which could explain a thickness-independent magnetically disturbed edge. Furthermore, it has to be noted that the experimentally observed slope of the edge is steeper than 60° (see Figure 3.5b).
On the basis of these considerations it is assumed that both effects, sloped edge and magnetically disturbed edge, are present. Since the overall effects are similar, mainly all CoFeB simulations were performed with magnetically disturbed edge, which was much easier to implement.

### 4.2.9 Edge Effects in Combination with Magneto-Crystalline Anisotropy

In the previous two sections, edge effects such as magnetically disturbed edge and sloped edge were chosen to fit CoFeB best. At this point, the question arises whether the obtained results can be transferred to CoFe. The patterning process and the subsequent temperature annealing were identical which gives rise to the assumption that edge related effects may be identical, too. However, it also needs to be noted that a reduction of $H_{an}$ in the simulations is not required to achieve a better fitting with CoFe (see e.g. Figure 4.25 in the last section).

The main difference of CoFe, besides its larger $M_s$, is the magneto-crystalline anisotropy (see Section 4.2.3). Simulation results are shown in Figure 4.39a where a magneto-crystalline anisotropy was applied additionally to the magnetically disturbed edge or sloped edge. It is obvious that $H_{an}$ is significantly less affected by the different edge effects. Thus, it seems that the polycrystalline structure stabilizes the vortex core or, in other words, introduces an additional energy barrier. For $s = 10$ and 15 nm, even an increase in $H_{an}$ was observed (not shown here). Furthermore, a large delay of $H_n$ is evident for 35 nm thick simulated disk elements if a sloped edge or a disturbed edge is applied. Such a delayed nucleation was sometimes also observed in the experiment as illustrated by the experimental data set. In addition, it has to be noted that the bias field-induced $H_n$ shifts, reported in Section 5.3.1, are better reproduced in simulations when applying a sloped edge compared to a vertical edge.

It needs to be stressed that the shown simulation results are based on one random grain texture. It is therefore not expected that such a large reduction of $H_n$ can be

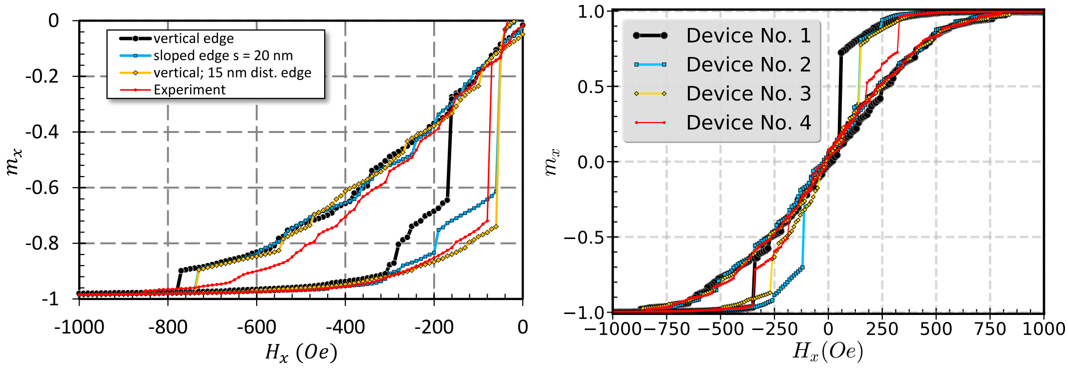

**(a)** **(b)**

**Figure 4.39.** (a) Half of the quasi-symmetric hysteresis loops with sloped edge or magnetically disturbed edge in combination with a uniaxial in-plane magneto-crystalline anisotropy. All of the simulated disk structures have a diameter of $d = 1.1$ µm at the bottom of the disk element and a thickness of $t = 35$ nm. An illustration of the sloped edge and its parameter $s$ is given in Figure 4.38a. The transfer curve of an experimental CoFe single disk device with the same dimensions shows a nucleation path that is similar as if one of these two edge effect is present. (b) Further experimental data sets, all from one wafer, demonstrate the variety of nucleation paths and $H_n$ distribution. Standard simulation parameters for CoFe are given in Section 3.3. All simulated structures had identical grain textures.

observed for every grain texture when one of the proposed edge effects is introduced. The variety of different experimental nucleation paths in Figure 4.39b is meant to illustrate this.

In conclusion, the different edge effects allow a better fitting of simulation and experiment for CoFeB with respect to a large reduction of $H_{an}$. Such a reduction of $H_{an}$ is not desired to fit CoFe and it also does not occur in the simulations due to the influence of the magneto-crystalline anisotropy. Moreover, sloped and magnetically disturbed edge in combination with such a polycrystalline structure can lead to a massive reduction of $H_n$, which is also sometimes observed in the experiment. Thus, the investigated edge effects appear to be present in both material systems. Such a detailed analysis of the NiFe spin-valve structures was not possible due to (1) the used coupled free layer system there, (2) a different etch process, and (3) a different reference system. These factors are expected to cause the high hysteresis which was observed for NiFe (not shown).

### 4.2.10 Electrically Inactive Edge

In some cases CoFe TMR transfer curves reveal a small but fundamental difference between experiment and simulation: in the vortex state close to $H_{an}$, $m_x$ is much closer to the saturated state in the experiment compared to the simulation, i.e. the jump threshold is small or non-existent. This fact is illustrated in Figure 4.40: in case of the experimental TMR measurement the change in signal during annihilation is very small (Figure 4.40a) or barely visible (Figure 4.40b). In contrast, the change in signal is much more pronounced if the full disk structure is assumed to be electrically active. This is the common assumption and all the previous $m_x$ plots were generated this way unless otherwise stated. This means that the magnetization of the full disk structure is simulated and subsequently the average $m_x$ component of the full element - as illustrated in Figure 4.41a - is extracted and plotted for comparison with the experimental TMR signal.

To address the reduced change in $m_x$ during annihilation, an electrically inactive edge area was introduced for the evaluation of the simulation results. It was implemented by masking the edge of the disk structure as illustrated in Figure 4.41b [172]. The consequences of this approach are illustrated in Figure 4.40c: once again the magnetization of the entire disk element is simulated as a first step (No. 1 and 3). Then, the average $m_x$ signal of a smaller subarea, where an edge region with defined thickness is neglected, is calculated (No. 2 and 4). This way, the whole element is magnetically active, but only part of it contributes to the measured signal. Thus, it becomes immediately evident that the vortex core can actually approach the new introduced edge of the structure (see No. 4). Consequently, a reduced change in $m_x$ is observed during annihilation.

In the examples shown in Figure 4.40, it may look like the effect of an electrically inactive edge region increases with increasing free layer thickness. Further comparisons, also for 20 nm free layer thickness, showed that the width of the inactive edge region seems

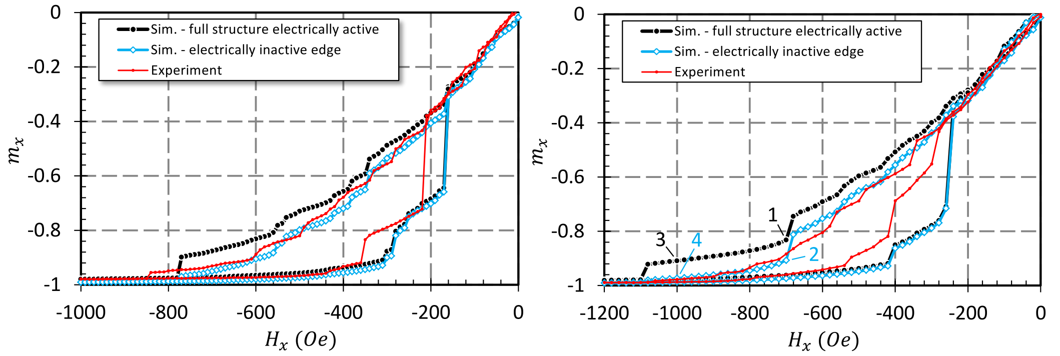

**(a)** $t = 35\,\mathrm{nm}$ **(b)** $t = 50\,\mathrm{nm}$

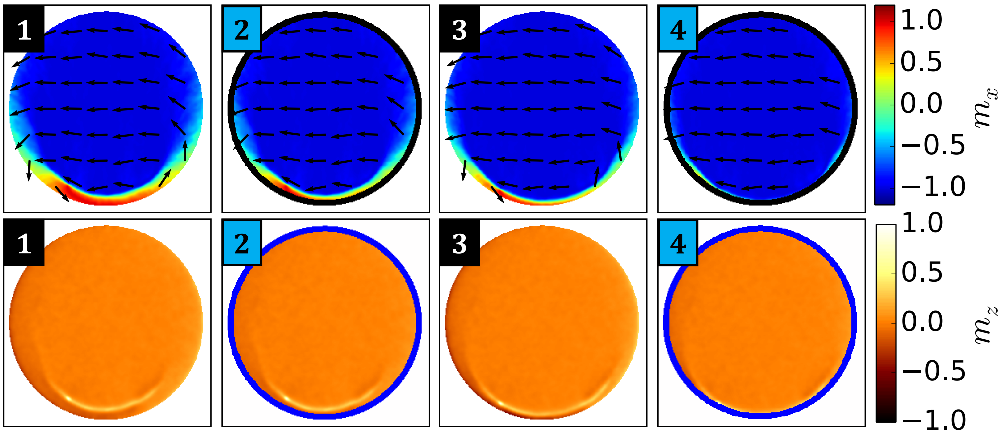

**(c)** $t = 50\,\mathrm{nm}$ - Implementation of the electrically inactive edge

**Figure 4.40.** (a-b) Negative branch of the transfer curves of two CoFe single disk devices ($d = 1.1\,\mu\mathrm{m}$) in comparison with simulations. For both thicknesses, the experimental signal of the vortex state gets significantly closer to the saturated state before annihilation compared to the simulated average $m_x$ component of the full structure. If during calculation of the average $m_x$ component a defined part of the edge region is neglected - in this case with a width of approximately 33 nm - the experimental course of hysteresis can be reproduced very well (see electrically inactive edge). (c) Illustration of the procedure for the 50 nm thick disk shown in (b): magnetic states are plotted for fully electrically active structures (No. 1 and 3) and for an applied electrically inactive edge region (No. 2 and 4). The electrically inactive edges are marked as black ($m_x$) or blue areas ($m_z$). $m_x$ (upper row) and $m_z$ components (lower row) are shown for $-700\,\mathrm{Oe}$ (No. 1 and 2) and $-1000\,\mathrm{Oe}$ (No. 3 and 4) as marked in (b). Standard simulation parameters for CoFe are given in Section 3.3. The discrete element unit cell was $\leqslant 5 \times 5 \times 5\,\mathrm{nm}^3$ for $t = 20\,\mathrm{nm}$ and for $t = 50\,\mathrm{nm}$ slightly larger in $\hat{z}-$direction (7.1 nm) due to limitations in the memory of the graphics processing unit.

to be independent of the film thickness (not shown). This fact allows to narrow down the possibilities of an explanation: it is less likely to find the root cause in the sloped edge (see Section 4.2.7) since it depends on the film thickness. Furthermore, a local magnetic weakening of the reference system is also considered to be rather unlikely since the effect was not observed for CoFeB. Both free layer materials were deposited on identical reference systems and were patterned the same way. The measured TMR curves also show stable conductivity plateaus after the saturation of the free layer has been reached. Since the electrically inactive edge is not observed for the amorphous CoFeB, it

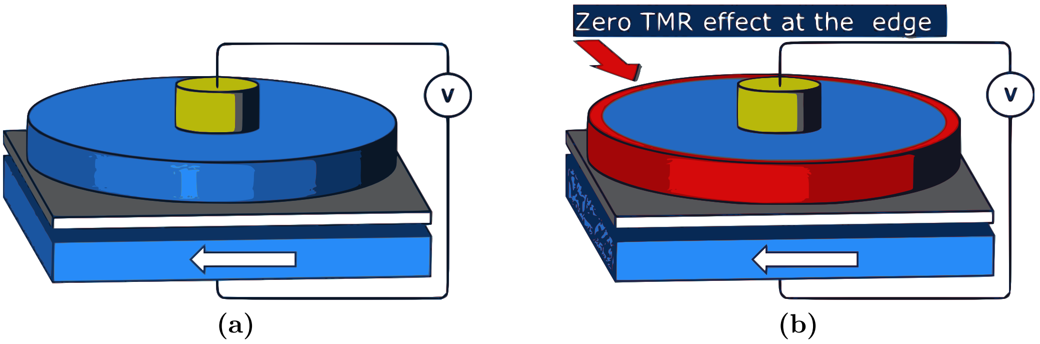

**Figure 4.41.** (a) Complete free layer disk contributes to the TMR signal. (b) The edge of the element is electrically inactive.

is expected to be linked to the polycrystalline structure of the investigated CoFe as all other parts of the stack are identical and were processed the same way, at the same time and directly following each other. In conclusion, the tunnel barrier itself can therefore be excluded as an explanation. Three possible scenarios are proposed: (1) an oxidation process that only affects the outer layer of crystal grains. In this scenario, the amorphous CoFeB ($D_{\text{grain}}$ of CoFeB is expected to be in the nanometer/subnanometer range [139]) is oxidized noticeably weaker. The oxidation in turn increases the resistance and thus for CoFe a significant loss of signal from the edge is observed. (2) The ion beam etch process damages the crystal structure of the CoFe permanently, e.g. by doping. Consequently, the resistance at the edge is increased even after annealing/crystallization. (3) Single grains have an anisotropic resistance which is smaller in the direction of growth and larger perpendicular to it. This leads to a reduced potential at the tunnel barrier in the edge region as a result of the columnar crystal growth in combination with sloped edge (see TEM image in Figure 3.5b). Unfortunately, a proof or disproof of the proposed explanations is beyond the investigation possibilities of this work.

Finally, it has to be mentioned that the effect does not seem to be equally strong for every single element as illustrated by Figure 4.42. This observation also indicates that

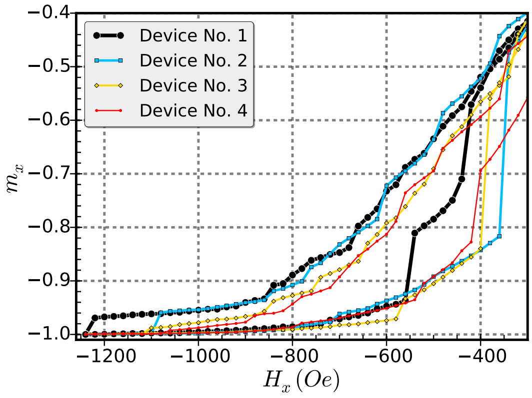

**Figure 4.42.** Different courses of hysteresis prior to vortex annihilation for various 50 nm thick CoFe single disk TMR cells with 1.1 µm free layer diameter.

the effect may be related to the polycrystalline structure of CoFe.

To summarize, the experimental analysis of the vortex annihilation jump, observed for CoFe, suggests that a small part of the edge of the free layer does not contribute to the TMR signal. The origin of this effect is unclear and requires further experimental study.

### 4.2.11 Edge Shape - Discretization and Roughness

In this section, it is investigated how the discretization and resulting roughness of the edge affects the critical fields. The investigation is limited to edge roughness with amplitudes in the range of the cell size. Surface roughness is not studied because TEM images showed that it is in the range of approximately 1 nm (see Figure 3.5b) and therefore significantly smaller than film thicknesses. Furthermore, the effects discussed within the previous sections - magneto-crystalline anisotropy, magnetically disturbed edge, and sloped edge - already enabled a reproduction of the experimental observations in simulations. Accordingly, edge roughness and discretization of the edge were only investigated to a degree that allows a better interpretation of the simulations. It will be shown that different edges introduce a distribution of the critical fields, also for amorphous materials such as CoFeB.

A detailed experimental investigation of the influence of edge roughness on the vortex nucleation was done by Lau et al. [181]. They investigated 250 nm wide and 30 nm thick teardrop-shaped permalloy elements. The teardrop shape was chosen to avoid stable double vortex states. Different roughness amplitudes - between approximately 3.3 and 4.4 nm - were achieved by changing the writing dose of the electron beam patterning process. They reported that an increased edge roughness leads to an earlier vortex

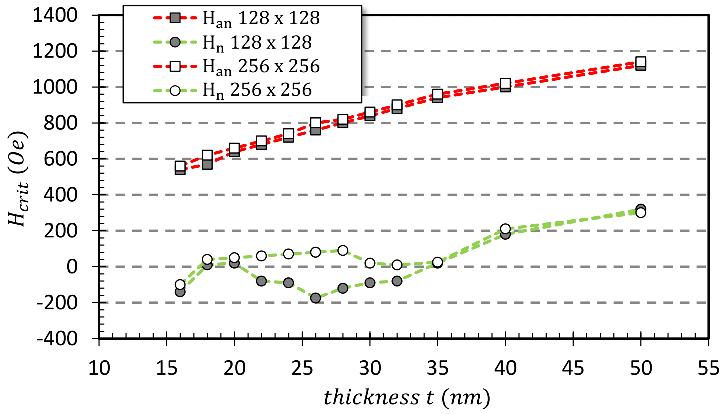

**Figure 4.43.** Critical fields $H_n$ and $H_{an}$ as a function of disk thickness $t$ for two different in-plane grids which result in a gradation with an edge length of approximately 1.7 nm (256x256) or 3.4 nm (128x128). All disks have a diameter 0.4 µm. The shape of the edge is identical within one type of grid. Standard simulation parameters for NiFe are given in Section 3.3.

nucleation (mean value shift of about 60 Oe) while, at the same time, it also increases the nucleation field distribution (about 70 Oe). Another work showed that edge roughness increases the magnetostatic energy in the vortex state which leads to a larger range of stability of the uniform state, especially for thin systems [182].

In the first part of this section, the influence of the grid cell size is investigated. Different grid sizes with an edge length of 1.7 nm and 3.4 nm were applied to 400 nm diameter disk structures. The resulting trends of the critical fields are shown in Figure 4.43. For structures with a thickness of up to 32 nm, a delay in vortex nucleation is observed for the 128x128 grid. For larger thicknesses, the grid resolution seems to have no additional impact on $H_n$. It has been reported for permalloy stripe structures that edge sensitive parameters - such as the field dependence of the edge mode resonance frequency and the edge saturation field - do not further change after exceeding a similar thickness [183]. This thickness coincides with the thickness from where $E_{\text{demag}}$ of the saturated state starts to scale linearly with thickness (see Section 4.1.4).
Figure 4.44a shows the response of the two 28 nm thick structures, where a delay occurs for the coarser grid. Coming from saturation, the transfer curves are nearly congruent. After the kink, which represents the formation of the S-state (see No. 1 in Figure 4.44a), the 256x256 disk structure shows a softer response (No. 2), which is not as linear as the response of the 128x128 disk structure (No. 3). The reason for this different behavior can be found in Figure 4.44b, where the S-state is plotted for the marked field steps.

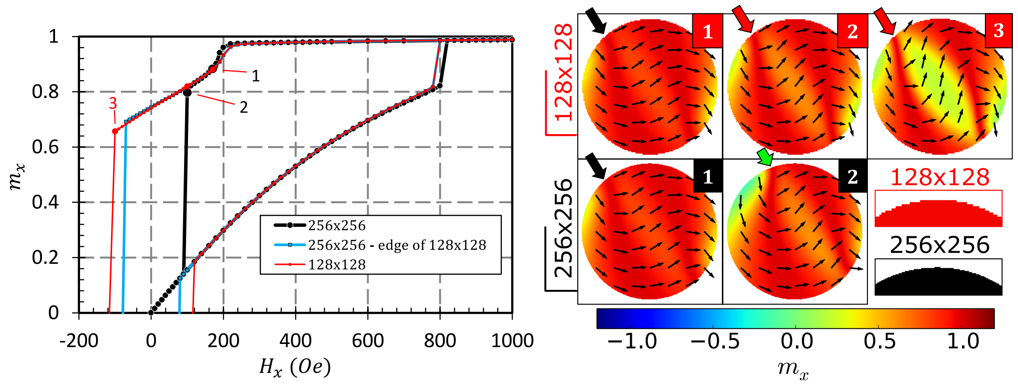

(a) (b)

**Figure 4.44.** (a) Parts of the quasi-symmetric hysteresis loops ($d = 0.4\,\mu\text{m}$ and $t = 28\,\text{nm}$) for two different in-plane grids which result in a gradation with an edge length of approximately 1.7 nm (256x256) or 3.4 nm (128x128). The delayed vortex nucleation for the 128x128 grid is caused by an extremely stable S-state. For comparison, the fine grid with the same coarse edge reveals that the effect is indeed mainly caused by the edge. (b) The illustration shows that at 170 Oe (No. 1) the S-states are nearly identical especially at the left upper edge (black arrows). For the 256x256 grid, a shift of the state is observed, indicated by the green arrow (No. 2) which results in an asymmetry of the S-state and leads to vortex nucleation at 90 Oe. For the 128x128 grid, such a shift is not observed (red arrows in No. 2 and 3). Detail sections of the 'north poles' of the disks (bottom right in (b)) show that the 128x128 grid has a smoother edge at the 'polar cap' compared to the 256x256 grid. Standard simulation parameters for NiFe are given in Section 3.3.

It becomes apparent from this illustration that for the 128x128 structure the S-state is stable over a large field range: both ends of the S-shape are virtually fixed. In contrast, such a stability is not observed for the 256x256 grid, which results in an asymmetric S-state that facilitates vortex nucleation.
It has been shown that surface effects - in this case at the element edge - drastically influence the amount of supercooling - in other words the vortex nucleation delay - which occurs during such a first-order phase transition from S-state to vortex state [166, 184]. Furthermore, an increased pinning as a result of an increasing roughness has been reported by Meyners et al., which causes a delayed magnetization reversal [185]. In the case shown here, it may therefore be possible that some sort of pinning results from the coarser step shape of the edge of the 128x128 structure. It is also likely that the nucleation delay of the 128x128 structures is caused by perfectly smooth edge regions. In the performed simulations, smooth edges are present in regions where the disk edge is parallel to the two in-plane axes of the grid, i.e. in the four directions of the compass. It has been shown for simulated rectangular nanostructures with perfectly smooth borders that an edge roughness reduces the switching field (via formation of magnetic vortices) [186]. This illustrates why large, straight element edges which are parallel to the simulation grid should be avoided. Accordingly, it has been reported that an increasing edge roughness amplitude - ranging from 1.25 nm to 5 nm - leads to an earlier magnetization switching in rectangular submicrometer structures because it increases both exchange and stray field energy [187].

For this reason, further simulations were performed where an artificial random edge roughness with varying degree and appearance was applied. Figure 4.45a shows the

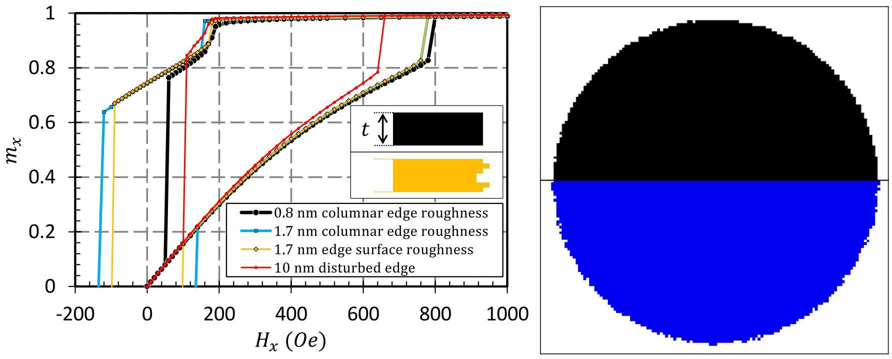

**(a)** $d = 0.4\,\mu\text{m}$ $t = 28\,\text{nm}$ **(b)** Roughness

**Figure 4.45.** (a) Parts of the quasi-symmetric hysteresis loops with different types of edge roughness (128x128 grid). The inset shows the edge in side view for a slice through the disk illustrating the difference between columnar (black) and edge surface roughness (golden). For the purpose of comparison, the same structure was simulated with 10 nm magnetically disturbed edge and without artificial roughness. (b) Illustration of the difference between 0.8 nm (upper half) and 1.7 nm (lower half) edge roughness amplitude. Standard simulation parameters for NiFe are given in Section 3.3. The in-plane edge length of the cells was 3.4 nm and out-of-plane 4 nm. No magnetically disturbed edge was applied for the disks with artificial roughness.

corresponding transfer curves. Results for two roughness amplitudes - 0.8 and 1.7 nm - are shown. These amplitude values are below the cell size, but due to the rounding within the discretization process the resulting roughness tends to be larger. For both amplitudes, resulting shapes of the edges are illustrated in Figure 4.45b. The resulting roughness for an amplitude of 1.7 nm may seem exaggerated, especially regarding the separated magnetic cells and the cavities. However, it will be demonstrated later in this section that for thicker disk structures, even if such a roughness is applied, hardly any effect is observed in the hysteresis loop.

The hysteresis loops in Figure 4.45a show that $H_n$ is very sensitive regarding the roughness of the edge. In contrast to $H_n$, $H_{an}$ reveals almost no changes as was to be expected. It should be emphasized that all elements shown in Figure 4.45a have a 128x128 grid. The change of the shape of the edge for the 0.8 nm edge roughness is minimal compared to the structure without artificial edge roughness. Nevertheless, the change in $H_n$ is enormous (160 Oe) when it is compared to the 128x128 device shown in Figure 4.44a, where no artificial roughness was applied. For the larger roughness amplitude of 1.7 nm, the smooth edge regions are drastically reduced (see Figure 4.45b). Nevertheless, vortex nucleation stays significantly delayed. This indicates that potential pinning sites affect the magnetization reversal at least as strong as smooth edge regions.

The first two hysteresis curves in Figure 4.45a show disk structures with a columnar edge roughness. In this case, no edge roughness is present in $\hat{z}-$direction (see Figure 4.45a in the upper part of the inset). A roughness is also introduced in $\hat{z}-$direction (lower part of the inset) by applying different random edge shapes for each layer separately. The effect of this measure is a slightly earlier vortex nucleation compared to the disk with a columnar edge and the same roughness amplitude. The same behavior was observed in several other simulations. The effect can be explained by a reduced pinning strength of prominent pinning sites: due to the edge surface roughness it is very likely that their extension in $\hat{z}-$direction is reduced, causing their overall pinning strength to reduce as well.

Figure 4.45a also shows that the effect of domain wall pinning of the S-state - caused by different fine discretization, roughness, and/or smooth edges - is drastically reduced if a magnetically disturbed edge is applied: vortex nucleation occurs for the 128x128 structure in this case even 10 Oe earlier compared to the 256x256 structure without magnetically disturbed edge (compare with Figure 4.44a). The change of $H_{an}$ has already been discussed in Section 4.2.7. The slightly increased slope of the curve in the vortex state results from the reduction of the total moment of the structure due to the magnetic weakening of the edge.

The previous discussion focused on relatively small disk structures with 400 nm diameter where the shape of the edge should play a decisive role. Figure 4.46 shows the results for disk structures with larger in-plane dimensions ($d = 1.1\,\mu\mathrm{m}$). Despite the magnetically disturbed edge (see Section 4.2.7), which was present in the CoFeB simulations shown in Figure 4.46a, quite a large nucleation field distribution can be observed for a constant

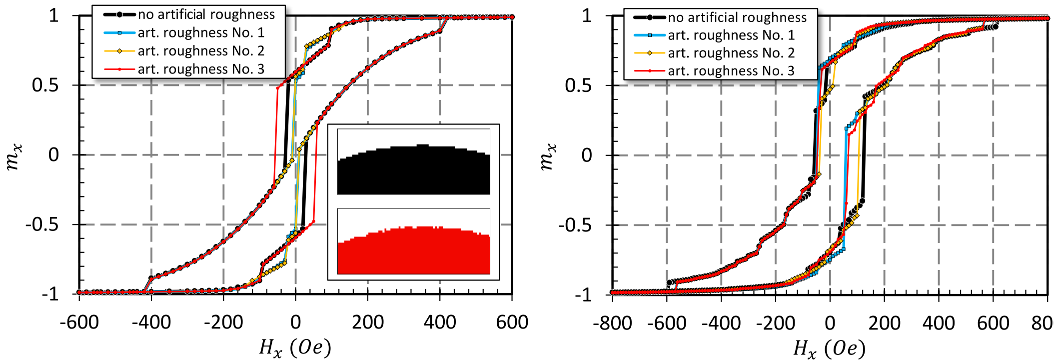

**(a)** CoFeB - Simulations **(b)** CoFe - Simulations

**Figure 4.46.** Simulated hysteresis loops of disk structures ($d$ = 1.1 µm and $t$ = 20 nm) without and with artificial edge roughness. The influence of the roughness is illustrated in top-view by the inset in (a) with no artificial roughness shown in black and artificial roughness shown in red. Edge roughness is also present in $\hat{z}-$direction (edge surface roughness). Different random edges were applied (No. 1 - 3), all of them with a roughness amplitude of 2.3 nm. (a) Standard simulation parameters for CoFeB are given in Section 3.3. The cell size is 4.6 nm in both in-plane directions and 4 nm in out-of-plane direction. (b) Standard simulation parameters for CoFe are also given in Section 3.3. All CoFe structures have the same grain texture.

roughness amplitude. Therefore, the influence of the edge can explain the $H_n$ distribution observed for CoFeB in the experiment. An influence on $H_{an}$ is not observed for the results shown, which was to be expected due the magnetically disturbed edge: it was demonstrated in Section 4.2.7 that the point of annihilation is shifted by almost exactly the width of the applied magnetically disturbed edge. Since this value is larger compared to the roughness no changes in $H_{an}$ are observed.
The polycrystalline CoFe shows a similar edge dependence regarding $H_n$ as shown in Figure 4.46b. However, no magnetically disturbed edge was applied in the simulations shown, and thus it seems that the influence of the magneto-crystalline anisotropy is stronger compared to the element edge. In contrast to the simulated CoFeB elements, $H_{an}$ shows a variation when the shape of the edge is changed. This may be due to the fact that the edge roughness affects the grain texture at the edge. However, in the case of CoFe the vortex core can approach the edge more closely due to the magnetically undisturbed edge. As a consequence, $H_{an}$ is more sensitive to modifications of the edge. Moreover, it can be observed in Figure 4.46b that for the positive half branch a different course of hysteresis is present for artificial roughness No. 3. This difference in the 'mini-hysteresis' results from a different sense of rotation of the vortex state (not shown), which has already been discussed in Section 4.2.3 (see Figure 4.31).

In order to conclude the discussion of the larger disk structures with 1.1 µm diameter, also with respect to the grid size, further observations need to be mentioned: even a small delay in vortex nucleation was observed when the cell edge length was decreased from 4.6 nm to 2.3 nm for the 20 nm thick CoFeB disks (not shown). Furthermore, the simulations indicate that edge roughness affects the nucleation of the vortex state less if

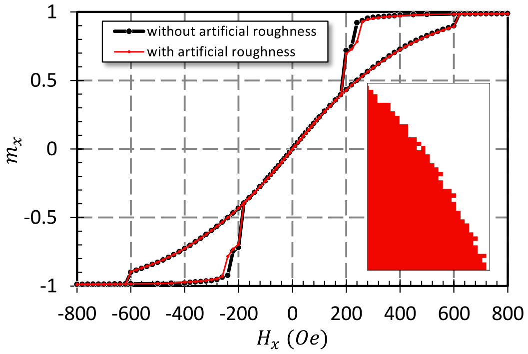

**Figure 4.47.** Negligible small effect of an artificial edge surface roughness for a 35 nm thick, simulated CoFeB disk structure with 1.1 µm diameter. Applied edge roughness amplitude: 2.3 nm, same as for Figure 4.46, but the discretization resolution of the distribution function was reduced which results in a coarser roughness. The inset shows in top-view a detail section of the edge with artificial edge roughness. Standard simulation parameters for CoFeB are given in Section 3.3.

the thickness is increased. It has been shown in Figure 4.43 that differences in $H_n$ for different grid sizes become insignificant after exceeding a certain threshold value of about 30 to 35 nm. Accordingly, an additional artificial edge roughness has a small impact on the magnetic behavior of a 1.1 µm diameter disk structure with 35 nm thickness which is demonstrated in Figure 4.47. The inset shows some potential pinning sites which do not have any impact on the hysteresis curve.

In summary, vortex nucleation is influenced by edge roughness positively as well as negatively, which explains the $H_n$ distribution observed for CoFeB in the experiment. The reason for a nucleation delay can be found in a pinning of the domain walls to the edge of the disk. Such pinning effects are more pronounced for smaller and thinner structures. Moreover, the findings suggest that the influence of the edge on the nucleation of the vortex state is drastically reduced for thicknesses of approximately 35 nm and more. Further investigations of the impact of edge roughness on the formation and stability of the double vortex state are required, especially when disk elements with a thickness above 50 nm are investigated.

# 5 Experimental Results - Extrinsic Factors

In this chapter, extrinsic factors such as changes in temperature and additionally applied magnetic bias fields are discussed; in particular, how the critical fields $H_n$ and $H_{an}$ are affected by them.

## 5.1 Processing of Changes of Critical Fields

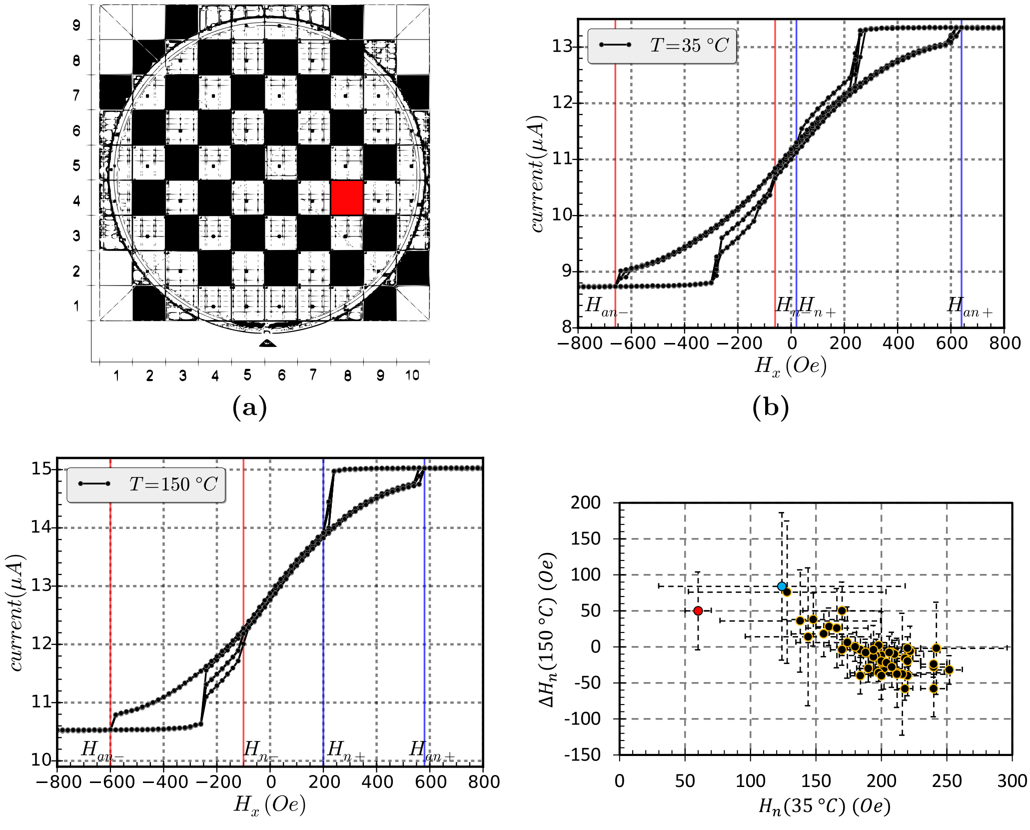

**(a)** **(b)**

**(c)** **(d)**

**Figure 5.1.** (a) Wafer map with checkerboard pattern of the measured 1.1 µm dual disk devices. The position of device 8x4 is marked in red. (b-c) For both 35 °C and 150 °C, ten complete hysteresis loops of device 8x4 from the wafer with 35 nm thick CoFeB free layer are plotted as an example. $H_n$ and $H_{an}$ are exemplary marked for one of the loops in each plot. (d) Average shifts of $H_n$ ($\Delta H_n$) plotted vs. $H_n$ at 35 °C. The red and blue marked data points represent the shifts of $H_{n-}$ and $H_{n+}$ of device 8x4.

To get a deeper understanding of the underlying processes, experiments were carried out at double spin-valve structures consisting of two TMR cells connected in series. These structures were not the smallest available test structure unit (single disk) but they have the advantage of a much better signal to noise ratio, especially regarding the mini hysteretic effects of CoFe (see Section 4.2.3), and thus the data analysis was significantly better to implement in the algorithm. Structures with a free layer diameter of 1.1 µm were characterized. Each device was measured ten times at different temperatures or bias field conditions. This way, the average shifts in $H_n$ and $H_{an}$ were extracted for each device individually. In order to obtain some statistics, 25 devices were measured on each wafer in a checkerboard pattern.

Figure 5.1 shows the exemplary results for one 35 nm CoFeB device in detail. The device position is marked in red in Figure 5.1a. Measured hysteresis loops for device 8x4 are shown for 35 °C (Figure 5.1b) and 150 °C (Figure 5.1c). The vortex critical fields of one of the loops are marked in each plot. The chosen device shows a significantly delayed vortex nucleation at 35 °C which is unusual for CoFeB but it emphasizes the observation that due to an increase in temperature certain energy barriers can be overcome and thus earlier vortex nucleation can be observed. The detailed relations are discussed in Section 5.2.2.

For the subsequent analysis each branch of the loop was treated separately so that for each device two $H_n$ values and two $H_{an}$ values were extracted. The values of $H_n$ and $H_{an}$ were adapted after the following convention:

$$\begin{aligned} H_n &= H_{n+} = -H_{n-} \\ H_{an} &= H_{an+} = -H_{an-} \end{aligned} \tag{5.1}$$

Shifts were calculated in the following way:

$$\begin{aligned} \Delta H_n(150\,^\circ\mathrm{C}) &= H_n(150\,^\circ\mathrm{C}) - H_n(35\,^\circ\mathrm{C}) \\ \Delta H_{an}(150\,^\circ\mathrm{C}) &= H_{an}(150\,^\circ\mathrm{C}) - H_{an}(35\,^\circ\mathrm{C}) \end{aligned} \tag{5.2}$$

Figure 5.1d shows the resulting ten times averaged shifts $\Delta H_n$ for 25 elements of 35 nm CoFeB on the wafer. The two values of device 8x4 are marked in red and blue, respectively. The extracted field values always refer to the second event of the two spin-valve structures neglecting the fact that the vortex of the other disk could already have been annihilated or nucleated. It should be noted that at 35 °C (Figure 5.1b) only five of the ten measured loops show a large nucleation delay for the positive branch ($H_{n+}$). Consequently, the average value of $H_{n+}$ is larger than $H_{n-}$ (see Figure 5.1d), even though it does not look like it at first glance in Figure 5.1b.

According to the previous definition, shifts of the biasing experiments were calculated in the following way:

$$\begin{aligned} \mathit{\Delta} H_n(H_y = 80\,\mathrm{Oe}) &= H_n(H_y = 80\,\mathrm{Oe}) - H_n(H_y = 0) \\ \mathit{\Delta} H_{an}(H_y = 80\,\mathrm{Oe}) &= H_{an}(H_y = 80\,\mathrm{Oe}) - H_{an}(H_y = 0) \end{aligned} \tag{5.3}$$

## 5.2 Temperature

In this section, the influence of an elevation of temperature on the vortex characteristics is investigated. In particular, how the critical fields $H_n$ and $H_{an}$ of individual disk structures are affected. The motivation of this investigation is to study the limitations of the magnetic vortex state regarding its sensor application. In the automotive sector, there are specific conditions under which sensors must work highly reliable. Regarding temperature, there is the requirement of a working range from $T = -40$ to 150 °C [29]. Parameters of a magnetoresistive sensor, such as resistance or sensitivity normally do not stay constant in this range. For a vortex sensor, it is additionally important how the vortex nucleation field changes over temperature because $H_n$ is a limiting factor regarding the magnetic field working range.
Section 5.2.1 gives an introduction into the theoretical expectations of temperature influence and a short overview over literature. In Section 5.2.2, positive and negative nucleation field shifts are described and discussed. The influence of thickness on $\Delta H_n$ is investigated in Section 5.2.3 as well as the influence of magneto-crystalline anisotropy in Section 5.2.4. Temperature-induced annihilation field shifts are discussed separately in Section 5.2.5. In Section 5.2.6, the material- and thickness-dependent ratios between temperature-induced reduction of $M_s$ and thermally assisted barrier jumps are estimated. Finally, the results are summarized in Section 5.2.7.

### 5.2.1 Initial Expectations

An increase in temperature is expected to affect the magnetic behavior of a disk structure in two ways. On the one hand it will reduce the saturation magnetization due to thermal excitation ($M_s(T)$) which in turn reduces the critical fields. On the other hand, the elevated temperature in combination with the slow sweep rate of the external applied field - slow compared to the spin dynamics - will affect thermally assisted barrier jumps [161]. Consequently, $H_n$ is expected to increase, whereas $H_{an}$ is expected to decrease due to thermal excitation. Dittrich et al. calculated the temperature-induced shift of the vortex nucleation probability for rectangular elements. They also showed that the energetic saddle point during vortex nucleation is reached when exactly the center of the vortex core has entered the element [165]. One can easily imagine that thermal excitation can by chance lead to a vortex-like curling of the magnetization at the element border which may then result in vortex nucleation.

The change of $M_s$ vs. temperature is expected to differ for the different investigated materials. For $Co_{60}Fe_{20}B_{20}$, an analysis of $M_s$ vs. temperature was done by Wang et al. (see Figure 3.7) [139]. Unfortunately, such a detailed analysis was not found for $Co_{90}Fe_{10}$. Therefore, a rough estimation of $\Delta M_s$ via the Curie temperatures ($T_C$) will be a sufficient alternative. The $T_C$ of CoFe is approximately 1120 °C [188], almost $T_C$ of cobalt. A reported $T_C$ for CoFeB was not found. Curie temperatures of the investigated alloy metals remain as reference points: Cobalt $T_C = 1125\,°\mathrm{C}$, iron $T_C = 771\,°\mathrm{C}$, and nickel $T_C = 354\,°\mathrm{C}$ [189, 190]. $T_C = 587\,°\mathrm{C}$ of permalloy [191] reveals that $T_C$ cannot be extracted one-to-one from the stoichiometry. However, it can be assumed that $T_C$ of CoFeB is smaller than $T_C$ of CoFe. A graphical extrapolation of the data from Wang et al. (measured up to 700 °C) indicates that $T_C$ is between 800 and 900 °C. Consequently, the relative reduction of $M_s$ as a function of $T$ is expected to be highest for NiFe, followed by CoFeB and the lowest for CoFe. A varying temperature dependence for different film thicknesses is not to be expected [192].

Early investigations regarding the question how temperature affects vortex nucleation and annihilation were done by Wernsdorfer et al. for amorphous, sub micrometer-sized, elliptical cobalt particles [46]. Both temperature and sweep rate dependence of the critical fields at low temperatures (below 6 K) showed that $H_n$ is increasing and $H_{an}$ increases with increasing temperature. As was to be expected, an increase in sweep rate led to an inverse behavior: a decrease of $H_n$ and an increase of $H_{an}$. Subsequent room temperature investigations of the sweep rate dependence reproduced these results for permalloy disk structures with $d = 1\,\mu\mathrm{m}$; $t = 42\,\mathrm{nm}$ [166] and $d = 2\,\mu\mathrm{m}; t = 32\,\mathrm{nm}$ ($H_{an}$ only) [115]. The results of the temperature dependencies of the critical fields were confirmed by Mihajlovic et al. and extended up to room temperature [193]: a decrease of $H_n$ with increasing temperature above 100 K was observed for 50 nm thick permalloy sub micrometer disk structures indicating that the temperature dependence of the saturation magnetization dominates the shift of the nucleation field here. Machado et al. showed in their simulations an increase of $H_n$ with increasing temperature ($d = 300\,\mathrm{nm}$; $t = 20\,\mathrm{nm}$), even above room temperature [194], which is contradictory to the results of Mihajlovic et al. It will be shown in Section 5.2.3 and 5.2.6 that the contradiction can be attributed to the difference in disk thickness.
In addition, it has been demonstrated that the process of thermally assisted barrier jumps has an influence on a long time scale: when a constant external magnetic field near $H_n$ is applied at elevated temperatures, hours can pass until vortex nucleation occurs [195].

What all of the publications mentioned above have in common is that in each of them only one type of material and one type of structure was investigated. In the next section, it will be shown that $H_n$ and even $H_{an}$ of individual elements can be shifted in both ways by elevation of temperature (above room temperature), depending on the material and film thickness. Furthermore, an assessment of the $M_s(T)$ dependence provides insight into the material and thickness-dependent ratio between $M_s(T)$ and thermally assisted barrier jumps.

### 5.2.2 Types of Temperature-Induced Nucleation Field Shifts

For the following studies, double spin-valve structures with 1.1 µm disk diameter were characterized. Each device was measured ten times at 35 °C and ten times at 150 °C. This way, the average shifts of $H_n$ and $H_{an}$ over temperature have been extracted for individual devices (see Section 5.1 for detailed description). Additionally, the change of the initial susceptibility (around zero field) of the vortex state was extracted in order to assess the $M_s(T)$ dependence only. A maximum of 25 dual disk devices was measured on each wafer. Additional measurements on single disk devices and on devices with 1170 disks in total were performed to complete the picture.

Figure 5.2 illustrates exemplarily the differing and complex influence an increase in temperature can have. It is important to note that the data shown is from two different materials - CoFeB and CoFe - but positive and negative $H_n$ shifts are not limited to one type of material, as will be demonstrated later in this section.
Focusing first on the nucleation fields, the example of a CoFeB device (Figure 5.2a) shows reproducible $H_n$ values at 35 °C. An increase in temperature (1) reduces $H_n$ in this case and (2) increases its distribution. Observation (1) is in line with the fact that $M_s$ is reduced with increasing $T$ which leads to a decrease of $H_n$. However, the elevated temperature also increases the chances to form other metastable magnetization configurations prior to $H_n$: a closer look at the measurements at 35 °C reveals that especially for the negative half branch the conclusion can be drawn that vortex nucleation occurs via buckling only (see Section 4.1.5). In contrast, at 150 °C, in many cases jumps into pre-states are observed, which can mainly be assigned to double vortex states. These states delay vortex nucleation additionally. Thus, it can be concluded that in this example not only $M_s(T)$ causes a reduction of $H_n$. The elevation in temperature also seems to increase the probability of simultaneous vortex nucleation at both ends of the buckling pattern. In this example, the thermally reduced vortex nucleation energy barrier consequently delays

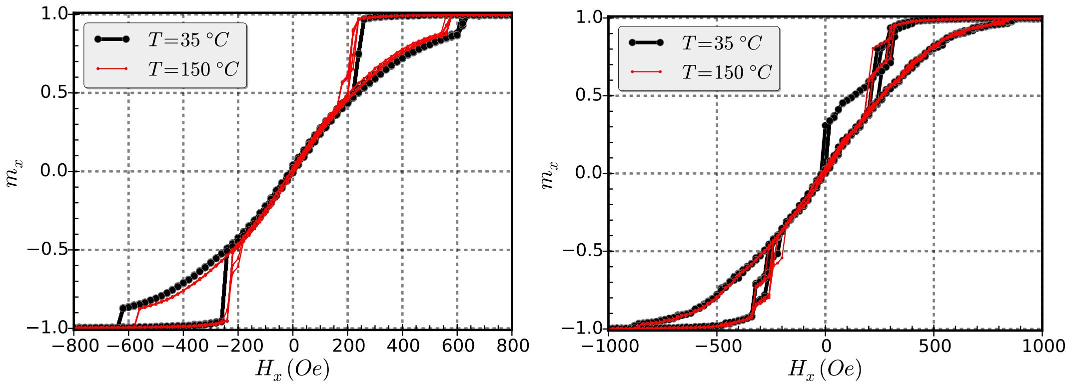

**(a)** CoFeB **(b)** CoFe

**Figure 5.2.** Normalized TMR transfer curves of dual disk devices ($d = 1.1$ µm and $t = 35$ nm), each measured ten times at 35 °C and ten times at 150 °C.

single vortex nucleation.

In contrast, the CoFe device in Figure 5.2b shows a large variation of $H_n$ and in the positive branch vortex nucleation is strongly delayed in some measurements. An increase in temperature leads to a significantly earlier vortex nucleation for this device. This observation fits into the framework that energy barriers can be overcome more easily at higher temperatures which in turn can lead to an earlier vortex nucleation. In case of CoFe additional energy barriers are present due to the magneto-crystalline anisotropy (see Section 4.2.3).

Two different nucleation field shifts at elevated temperatures were observed in Figure 5.2. Which type of shift occurs depends on which factor outweighs: reduction of vortex nucleation energy barrier or temperature-induced reduction of $M_s$. Furthermore, an elevation of temperature can facilitate the formation of intermediate metastable states which additionally delay vortex nucleation. It will be shown later in this section that the thickness of the elements has a large influence on the type of shift as a result of the different thickness-dependent pre-states. The hysteresis loops shown in Figure 5.2 also reveal a visible increase in slope around zero field for CoFeB at 150 °C, whereas for CoFe it is nearly unchanged. This suggests that the relative change in $M_s$ is larger for CoFeB compared to CoFe. The $M_s(T)$ dependencies are discussed in more detail in Section 5.2.6, where it will be demonstrated that the magneto-crystalline anisotropy affects the change of the slope.

As expected, $H_{an}$ decreases in Figure 5.2 with increasing temperature for both materials (barely visible for CoFe): both factors - overcoming of energy barriers and $M_s(T)$ - are expected to reduce the annihilation field (see Section 5.2.5).

The following pages will show that which type of shift dominates depends on the choice of material and free layer thickness and furthermore, on the individual ’performance’ of a device. Figure 5.3 shows the average $\Delta H_n$ for individual devices with 20, 35, and 50 nm thick CoFeB disks. For 35 nm, the coefficient of determination ($R^2 = 0.61$) of the regression line underlines that there is a strong correlation between $H_n(35\,°\mathrm{C})$ and $\Delta H_n$. The strong correlation substantiates the observation made in Figure 5.2: an increase in temperature can shift $H_n$ in both directions. It is shown here that the individual type of shift is independent of the choice of material. Devices with a comparable small nucleation field - at the lower end of the nucleation field distribution - usually show a positive shift, whereas for devices with a comparable large $H_n$ a negative shift is usually observed. These two observations can be explained as follows:

- A delayed vortex nucleation gives rise to the assumption that the energy barrier is increased to be overcome during vortex nucleation. This can be explained, for example, by deviations from a smooth disk structure, such as edge pinning sites, which then affect $H_n$ negatively (see Section 4.2.11). By increasing the temperature, it is more likely to overcome such pinning effects (at larger fields) and thus a positive $\Delta H_n$ is observed.

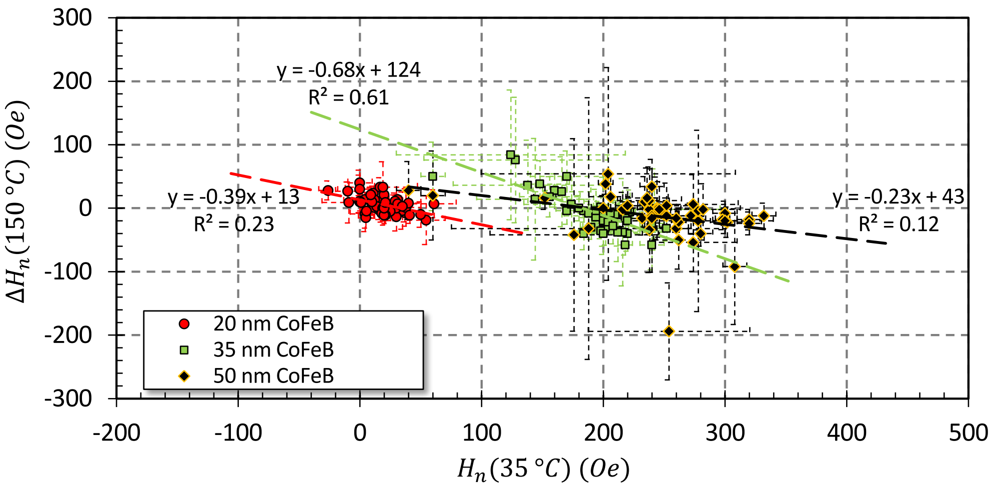

**Figure 5.3.** Shift of $H_n$ at 150 °C with respect to the $H_n$ value at 35 °C for three CoFeB thicknesses. Each data point represents the shift of either $H_{n+}$ or $H_{n-}$ of only one dual disk device ($d = 1.1\,\mu\text{m}$). A detailed explanation of $\mathit{\Delta} H_n$ is given in Section 5.1.

- An early vortex nucleation indicates that there are less deviations/defects compared to other devices with identical free layer dimension and material. Thus, the energy barrier is not increased additionally. The structure is closer to an ideal cylindrical free layer element or has certain nanoscopic features that facilitate vortex nucleation [181]. As a consequence, bulk material properties play an important role and a reduction of the total moment at higher temperatures will thus reduce $H_n$, which results in a negative $\mathit{\Delta} H_n$. Moreover, a temperature-induced nucleation of intermediate states can also affect $H_n$ negatively.

Consequently, an increase in temperature should have a balancing effect on the $H_n$ distribution (with a high correlation of $\mathit{\Delta} H_n$ vs. $H_n$). Balancing effect refers to the distribution that should become narrower due to the two possible shift types. In Figure 5.3, the 20 nm CoFeB shows a drastically reduced correlation compared to 35 nm. The slope and the coefficient of determination are significantly smaller. For 50 nm CoFeB, the correlation is even more reduced indicating that the change in temperature has almost no impact on $H_n$. These differences in correlation and slope of the trend are linked to the nucleation modes of the different disk thicknesses (see Section 4.1.5) and the $m_z$ component prior to vortex nucleation at the element edge (see Section 4.1.4) as will be shown in the next section. Table 5.1 summarizes the average critical fields of the investigated systems and will be used in the upcoming section. A detailed discussion of Table 5.1 will follow later on in the corresponding section.

### 5.2.3 Nucleation Modes and Temperature-Induced Nucleation Field Shifts

It was shown in Section 4.1.5 that for 20 nm thickness, vortex nucleation often occurs via the S-state and for 50 nm via the double vortex state, respectively. In contrast, vortex

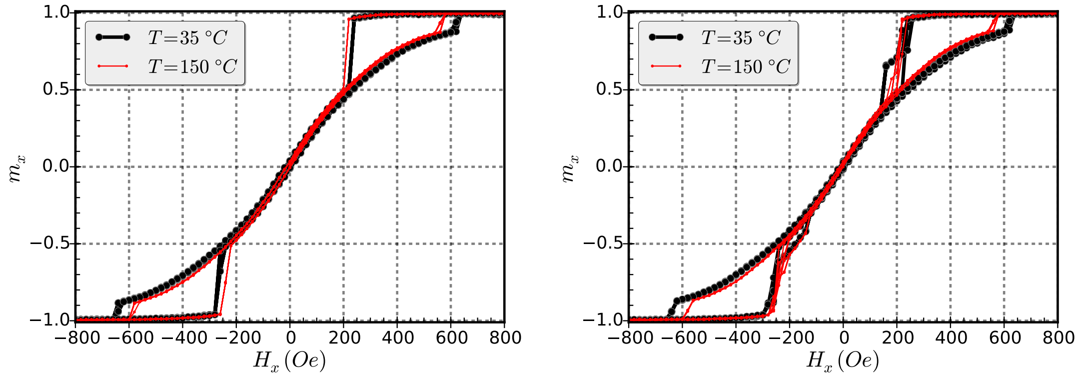

**(a)** $t = 35\,\text{nm}$ **(b)** $t = 35\,\text{nm}$

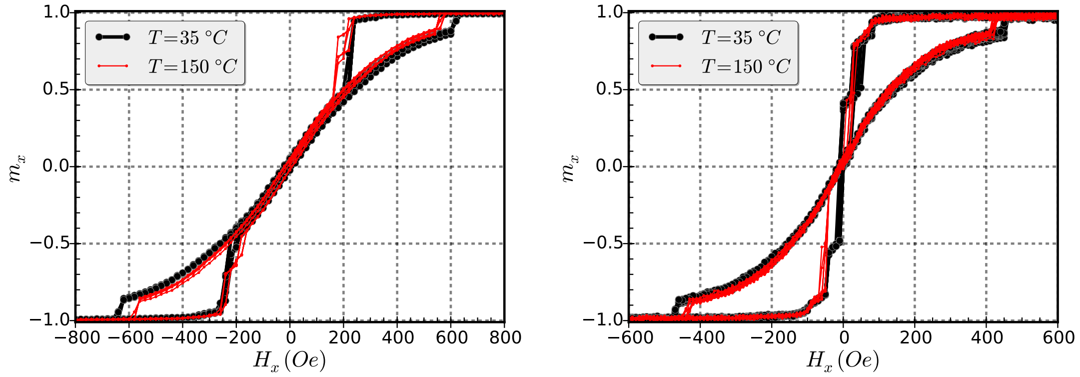

**(c)** $t = 35\,\text{nm}$ **(d)** $t = 20\,\text{nm}$

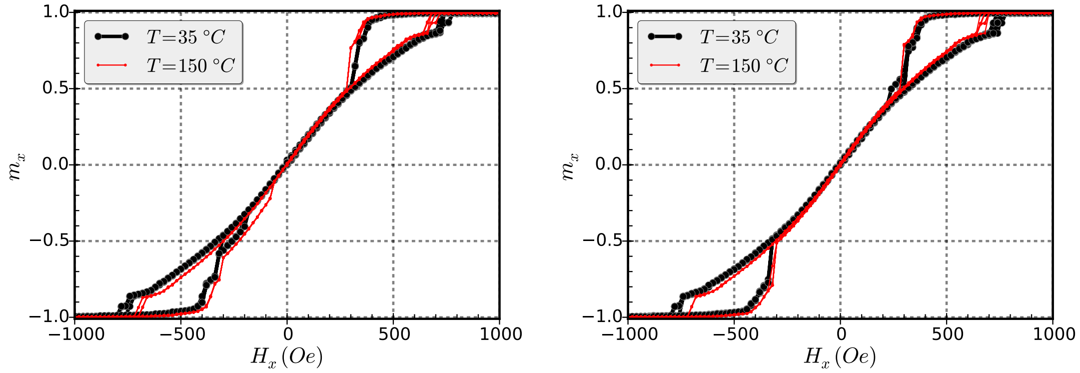

**(e)** $t = 50\,\text{nm}$ **(f)** $t = 50\,\text{nm}$

**Figure 5.4.** Normalized TMR transfer curves CoFeB dual disk devices ($d = 1.1\,\mu\text{m}$) for various thicknesses. Each plot shows ten hysteresis loops of the same device at 35 °C and ten at 150 °C.

nucleation occurs mainly via only buckling for the 35 nm thick structures. It has been demonstrated that such a first-order phase transition via buckling only has a signature of supercooling and consequently the influence of temperature is lowered [166]. This fact is demonstrated by Figure 5.4a. The hysteresis loops show that vortex nucleation occurs via buckling only for both disk elements. As a result $H_n$ is shifted similar as $H_{an}$, which explains the in average negative value of $\varDelta H_n$ (see Table 5.1).

Since not only vortex nucleation but also double vortex nucleation is a first-order phase transition (at least for 35 and 50 nm thickness), the double vortex state should also show a small temperature dependence. Indeed, it has been demonstrated that the nucleation field of the double vortex state is nearly unaffected by temperature above 200 K [193]. Thus, a general relation between temperature and the stability of pre-states could not be established in this investigation. Figure 5.4b illustrates that the S-state can become less stable at 150 °C, but this behavior is not valid in general as illustrated by Figure 5.4c. In this example, the increase in temperature induces the formation of S- and double vortex state.

In the following, the pre-states of Figure 5.4b are discussed in order to understand the argumentation. At 35 °C, mainly two different intermediate states are observed. For the negative branch, the intermediate state is close to the vortex path and has a larger slope than the vortex state. The intermediate state of the positive half branch is more far away and has a smaller slope. Since the measured elements are dual disk devices, factors such as the change in signal during jumps are not a clear indicator of the state, whereas the slope is. Therefore, it can be concluded that in Figure 5.4b at 35 °C a double vortex is sometimes observed prior to $H_{n-}$ and an S-state prior to $H_{n+}$. At 150 °C, the double vortex state is still present over the same field range in some measurements, but the S-state does not form anymore. Consequently, $\Delta H_n$ is positive for this device due to the fact that the S-state is skipped.

It can be concluded that for 35 nm thickness the formation of pre-states lowers the correlation of $\Delta H_n$ but not significantly due to their low formation rate. In general, the increase in temperature reduces $H_n$ by shifting the buckling-to-vortex-transition or inducing metastable pre-states, especially the double vortex state, which is more stable at smaller fields compared to the buckling state.

For the 20 nm thick structures, the S-state still frequently forms at the elevated temperature. The frequent formation of the S-state explains why the slope of the trend line and its correlation is decreased (see Figure 5.3) compared to that of 35 nm thickness. An average positive shift is observed (see Table 5.1) due to the fact that in some cases S-state formation is skipped at 150 °C as illustrated by Figure 5.4d. This is an example of the thermally assisted vortex nucleation described in Section 5.2.1. Moreover, it is expected that thermal excitation can cause an increased $m_z$ component at the element edge - which is suppressed for $t = 20\,\mathrm{nm}$ (see Section 4.1.4) - and therefore facilitates vortex nucleation.

For 50 nm in Figure 5.3, slope and correlation are further reduced, leading to the assumption that the transition from double vortex state to single vortex state is unaffected by temperature. Figure 5.4e illustrates that in some cases the stability of the double vortex state is increased for the elevated temperature. In other structures (Figure 5.4f), its formation is prevented by increasing the temperature. This leads to the observed large nucleation field distribution and to the virtually non-existent correlation of $\Delta H_n$.

The fact that two TMR elements in series were measured in this investigation also affects the correlation of $\varDelta H_n$. For structures where other pre-states (20 and 50 nm) than the buckling state were observed more frequently, a negative impact on the correlation has to be expected in consequence and is observed in Figure 5.3.

In summary, the thickness of the disk elements determines if a high correlation between $\varDelta H_n$ and $H_n$ is observed. The reason for this lies mainly in the thickness-dependent metastable pre-states. For 35 nm thick structures, vortex nucleation occurs most frequently via the buckling state only, whereas for 20 and 50 nm more often additional intermediate states, such as S- or double vortex, form. Additional states can be seen as a bifurcation by adding further energy levels and consequently reducing the correlation between $\varDelta H_n$ and $H_n$.

### 5.2.4 Magneto-Crystalline Anisotropy and Temperature-Induced Nucleation Field Shifts

Figure 5.5 shows the $\varDelta H_n$ values for the three investigated CoFe free layer thicknesses. At first, the broader nucleation field distributions - especially for 20 nm - and the larger error bars attract attention. These effects were discussed in Section 4.2.3. In this section, focus is set on the correlation and trend of $\varDelta H_n$. For CoFe, all three thicknesses show a clear trend. The regression lines of all three CoFe thicknesses have a slope in the range of the trend line of 35 nm CoFeB. Compared to CoFeB, the 35 nm $R^2$ is slightly smaller, but correlation is increased for the other thicknesses. The thickness independent correlation can be explained by the magneto-crystalline anisotropy which causes a vortex nucleation delay (see Section 4.2.3). Furthermore, since the average grain size is expected to be less or equal to the free layer thickness, the height of the energy barriers caused by the magneto-crystalline anisotropy should be more or less constant for all thicknesses. As a consequence, if the vortex nucleation is strongly influenced by the magneto-crystalline

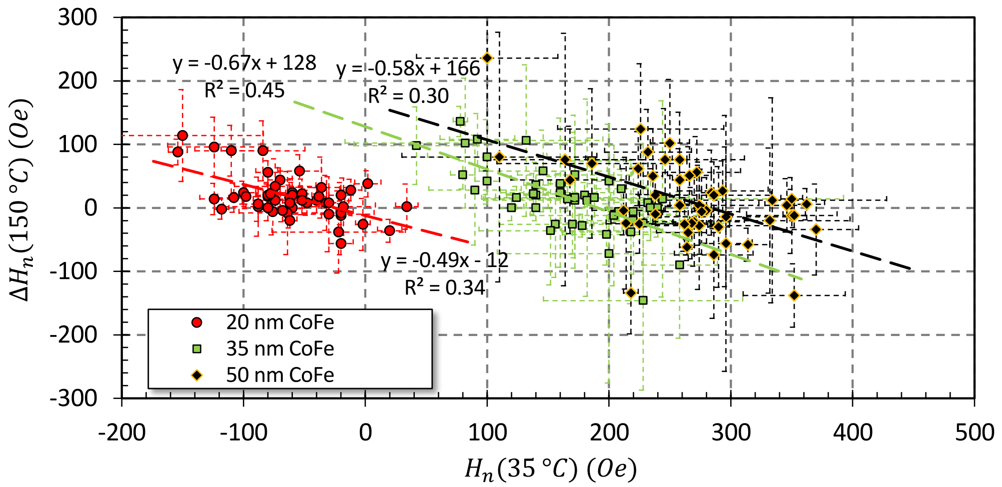

**Figure 5.5.** Shift of $H_n$ at 150 °C with respect to the $H_n$ value at 35 °C for three CoFe thicknesses. Each data point represents the shift of either $H_{n+}$ or $H_{n-}$ of only one dual disk device ($d = 1.1\,\mu\mathrm{m}$).

anisotropy, a thickness independent correlation of $\Delta H_n$ is expected to be observed, which explains the similar slopes and coefficients of determination.

It has to be noted that again the 35 nm thick devices have the largest trend line slope and coefficient of determination. This finding suggests that the observations made for CoFeB in the previous section - on how the thickness-dependent metastable pre-states affect the temperature characteristics - can be transferred to CoFe and are superimposed by its magneto-crystalline properties. The crystalline texture introduces additional energy barriers which on the one hand cause a broadening of the nucleation field distribution, and on the other hand increase the influence of thermally assisted barrier jumps. In addition, a reduction of the magneto-crystalline anisotropy as a function of temperature must also be taken into account (see Getzlaff, p. 98 [196]), but further research of the investigated $Co_{90}Fe_{10}$ is needed.

### 5.2.5 Temperature-Induced Annihilation Field Shifts

So far, the influence of temperature on the nucleation field were discussed and two types of shifts, positive and negative $\Delta H_n$, were observed. Initially, both types of shift were not expected for the annihilation field. Negative shifts should be observed since both effects, decrease in $M_s$ and decrease of energy barriers, should reduce the annihilation field with increasing temperature. Figure 5.6 shows the extracted $\Delta H_{an}$ scatter plots for all uncoupled free layer systems that were investigated. All CoFeB free layer show the expected behavior: a negative $\Delta H_{an}$ for every individual device. Furthermore, the absolute value of $\Delta H_{an}$ increases with increasing free layer thickness due to the increasing $H_{an}$. This trend is also observed for CoFe, but in this case the negative shift is less pronounced and there are even some devices that show a positive $\Delta H_{an}$. Such positive

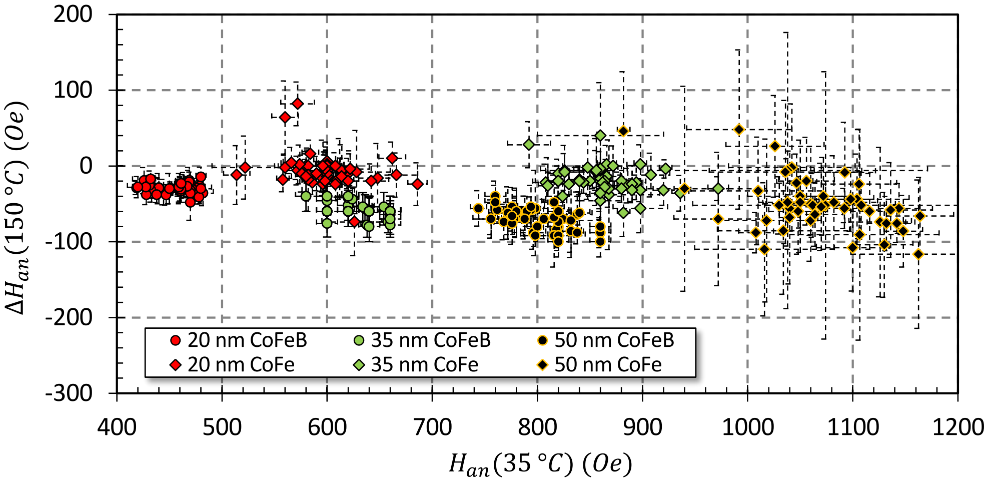

**Figure 5.6.** Shift of $H_{an}$ at 150 °C with respect to the $H_{an}$ value at 35 °C for CoFe and CoFeB. Each data point represents the shift of either $H_{an+}$ or $H_{an-}$ of only one dual disk device ($d = 1.1\,\mu m$).

shifts can be explained by a change of the sense of rotation of the vortex state, which influences $H_{an}$ due to the magneto-crystalline anisotropy of CoFe (see Section 4.2.3, Figure 4.31). In some cases, such a reversal of the sense of rotation is increasing $H_{an}$ at 150 °C, as will be demonstrated in the next section in Figure 5.8d.

The typical correlation of $\Delta H_{an}$ with a negative slope, which was clearly observed for $\Delta H_n$, can be hardly recognized for 35 nm thick CoFeB and 50 nm thick CoFeB and CoFe. Hypothetically, the $H_{an}$ distribution could be caused by a variation of the film thickness, even tough the width of the $H_{an}$ distribution contradicts this assumption. Furthermore, both factors thickness and $M_s$ have a linear relation to $H_{an}$ (see Section 4.1.3). Consequently, if one assumes that the $H_{an}$ distribution is caused by a variation of the total magnetic moment of the individual elements and an elevation in temperature only affects $M_s$, then the imaginary correlation trend line of $\Delta H_{an}$ is expected to cross zero (which seems to be the case for 20 nm thick CoFeB). Since the slope of the imaginary correlation trend line is larger for thicker elements it can be concluded that $H_{an}$ is not only affected by the $M_s(T)$ dependence. Therefore, edge effects and the grain texture of CoFe are mainly assumed to cause the observed $H_{an}$ distributions (see Section 4.2.11 and 4.2.3). Edge related effects have approximately the same or smaller dimensions than individual crystal grains of CoFe. As a consequence, an elevation in temperature should allow to overcome certain edge related energy barriers and facilitate vortex annihilation at smaller fields than a reduction in $M_s$ could explain.

To summarize, the increasing tilt of the scatter plots allows the conclusion that the influence of thermally assisted barrier jumps during annihilation increases with increasing disk thickness.

Table 5.1 summarizes the average critical field values for CoFe and CoFeB. In addition, ruthenium (Ru) coupled[1] $Ni_{81}Fe_{19}$ (NiFe) free layers were also characterized. For 20 nm

**Table 5.1.** Summary of average critical field values $H_n$ and $H_{an}$ at 35 °C and 150 °C of dual disk devices ($d = 1.1\,\mu m$).

| Material | t (nm) | $H_{n,35\,°C}(Oe)$ | $H_{n,150\,°C}(Oe)$ | $H_{an,35\,°C}(Oe)$ | $H_{an,150\,°C}(Oe)$ |
|---|---|---|---|---|---|
| **CoFeB** | **20** | $19 \pm 15$ | $25 \pm 14$ | $453 \pm 17$ | $424 \pm 18$ |
| **CoFeB** | **35** | $195 \pm 34$ | $187 \pm 20$ | $630 \pm 22$ | $571 \pm 19$ |
| **CoFeB** | **50** | $244 \pm 56$ | $232 \pm 55$ | $798 \pm 26$ | $728 \pm 20$ |
| **CoFe** | **20** | $-61 \pm 39$ | $-43 \pm 34$ | $599 \pm 31$ | $593 \pm 32$ |
| **CoFe** | **35** | $169 \pm 49$ | $184 \pm 42$ | $864 \pm 33$ | $845 \pm 33$ |
| **CoFe Ru-coupled** | **35** | $191 \pm 77$ | $212 \pm 55$ | $859 \pm 35$ | $808 \pm 30$ |
| **CoFe** | **50** | $265 \pm 60$ | $274 \pm 58$ | $1065 \pm 53$ | $1016 \pm 46$ |
| **NiFe Ru-coupled** | **35** | $176 \pm 28$ | $171 \pm 25$ | $507 \pm 12$ | $423 \pm 20$ |
| **NiFe Ru-coupled** | **50** | $225 \pm 46$ | $200 \pm 51$ | $595 \pm 15$ | $522 \pm 40$ |

---

[1] To achieve a large TMR effect, the NiFe free layers consist of three different layers with CoFeB at the MgO interface: CoFeB(5 nm)/Ru(1.2 nm)/NiFe(t). The Ru thickness is chosen in order to achieve a parallel Ruderman-Kittel-Kasuya-Yosida (RKKY) coupling between NiFe and CoFeB [135–137].

thickness, both materials - CoFe and CoFeB - have the higher value for $H_{n,150\,°\mathrm{C}}$ compared to $H_{n,35\,°\mathrm{C}}$. This indicates that the 20 nm system is dominated by a reduction of vortex nucleation energy barriers at elevated temperatures. This relationship is reversed for thicker CoFeB systems. Thus, $H_n$ is slightly dominated by the $M_s(T)$ dependence. On the other hand, CoFe shows for all three thicknesses a larger $H_{n,150\,°\mathrm{C}}$. Consequently, the energy barriers of the magneto-crystalline structure seem to be dominant here. The magneto-crystallinity also becomes evident when comparing $H_{n,35\,°\mathrm{C}}$ of CoFe with $H_{n,35\,°\mathrm{C}}$ of CoFeB for 20 and 35 nm thickness. In both cases, CoFeB shows a larger $H_n$ despite the smaller $M_s$.

Similar to the CoFeB, the NiFe free layers show a reduction of $H_n$ at 150 °C. This was to be expected since NiFe is the most soft magnetic material of the investigated materials, and thus the general influence of nucleation energy barriers should be reduced. Furthermore, the NiFe systems have the largest relative decrease of $H_{an}$ over temperature, which is expected to be linked to the fact that NiFe has the lowest Curie temperature (see Section 5.2.1). The much higher error bars result from the coupled (hysteretic) free layer system. Nevertheless, it should be pointed out that the Ru-coupled CoFe system also has a larger $\Delta H_{an}$ compared to the uncoupled system.

On average, a balancing effect on the $H_n$ distribution due to the temperature elevation is observed as it was already assumed in the discussion of $\Delta H_n$ of the individual devices. Free layers that show a large coefficient of determination in their temperature shift correlation (e.g. 35 nm CoFeB or 35 nm CoFe) show a clear decrease of the standard deviation from $H_{n,35\,°\mathrm{C}}$ to $H_{n,150\,°\mathrm{C}}$. A similar decrease of the nucleation field distribution was observed for temperatures between 0.1 K and 6 K [46].

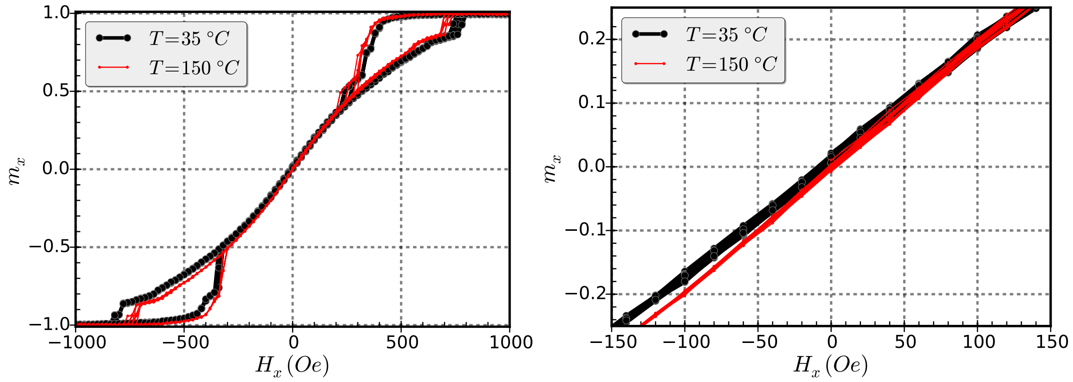

**(a)** Full loops **(b)** Zoom

**Figure 5.7.** Normalized TMR transfer curves - full hysteresis loops (a) and zoom into the central part of the same full loops (b) - measured at a CoFeB dual disk device ($d = 1.1\,\mu\mathrm{m}$ and $t = 50\,\mathrm{nm}$). For both temperatures, ten complete hysteresis loops are plotted.

### 5.2.6 Estimation of the Temperature-Induced Reduction of the Saturation Magnetization and Thermally Assisted Barrier Jumps

For the subsequent discussion, a quantitative estimation of $\Delta M_s(\Delta T)$ is required in order to estimate the ratio between the influence of $M_s$ and thermally assisted barrier jumps. For this purpose, the average slope around zero field - in other words the normalized initial susceptibility - was extracted from each single device measurement with 35 and 50 nm thickness at 35 °C and at 150 °C. The change in susceptibility is expected to be directly proportional to $\Delta M_s$ (see Section 4.2.1). This only seems to be valid for the amorphous CoFeB as will be shown later. Figure 5.7 illustrates the change in slope for a 50 nm thick CoFeB device: the full hysteresis loop is shown in Figure 5.7a while the zoom into their central part ($\pm 0.25\ m_x$) in Figure 5.7b illustrates the linear trend and the change of slope as a function of temperature.

Values of $\Delta M_s$ together with the relative changes of $H_n$ and $H_{an}$ are given in Table 5.2. The fitted $\Delta M_s$ of CoFeB also exhibits minimal deviations for the two thicknesses with small standard deviations. In addition, the $\Delta M_s$ of 6.2 % fits very well to the $\Delta H_{an}$ values since they are always larger and $\Delta M_s$ is in good agreement with literature: Wang et al. measured $M_s$ vs. temperature (between room temperature and 700 °C) of 50 nm thick CoFeB films [139]. Their data (see Figure 3.7) shows a $\Delta M_s$ of approximately 5 % between 35 °C and 150 °C for the amorphous phase. The small discrepancy between their result and the $\Delta M_s$ determined within this work may be due to the smaller absolute value of $M_s$ of Wang et al.

Fits for the 20 nm thick dual disk devices could not be carried out successfully due to a delayed vortex nucleation (CoFe) and a low signal to noise ratio (CoFeB)[2]. Since $\Delta M_s$ does not change over thickness for CoFeB, the same value is assumed for 20 nm. In this case it can be concluded that $\Delta H_{an}$ is almost exclusively caused by the reduction of $M_s$

**Table 5.2.** Summary of average critical field shifts and fitted $M_s$ shifts. The given values refer to an increase in temperature from 35 °C to 150 °C. $H_n$ and $H_{an}$ are normalized to $H_{an,35\,^\circ\mathrm{C}}$. $\Delta M_s$ is normalized to $M_{s,35\,^\circ\mathrm{C}}$. For 'Fit 1' measurements on dual disk devices (two TMR cells) were processed, for 'Fit 2' measurements on resistors (1170 TMR cells) all with $d = 1.1\,\mu\mathrm{m}$.

| Material | t (nm) | $\Delta H_n$ (%) | $\Delta H_{an}$ (%) | *Fit* 1 $\Delta M_s$ (%) | *Fit* 2 $\Delta M_s$ (%) |
|---|---|---|---|---|---|
| **CoFeB** | **20** | $1.3 \pm 3.0$ | $-6.4 \pm 1.3$ | – | – |
| **CoFeB** | **35** | $-1.3 \pm 4.9$ | $-9.3 \pm 1.5$ | $-6.2 \pm 0.8$ | – |
| **CoFeB** | **50** | $-1.6 \pm 4.2$ | $-8.8 \pm 1.7$ | $-6.2 \pm 0.9$ | – |
| **CoFe** | **20** | $2.9 \pm 5.5$ | $-1.0 \pm 3.5$ | – | – |
| **CoFe** | **35** | $1.7 \pm 5.6$ | $-2.2 \pm 2.0$ | $-3.0 \pm 2.5$ | $-2.3 \pm 0.3$ |
| **CoFe** | **50** | $0.8 \pm 6.0$ | $-4.6 \pm 3.4$ | $-5.6 \pm 2.5$ | – |

---

[2] An extended hysteresis loop is proposed for future investigations: A minor loop ($|H_x| < |H_{an}|$) inside a full hysteresis loop ($|H_x| > |H_{an}|$) is required in order to (1) allow correct normalization of the TMR signal (where saturation is needed) and (2) obtain the susceptibility at zero field.

for 20 nm CoFeB thickness (see also discussion of Figure 5.6) because $\Delta H_{an}$ and $\Delta M_s$ are nearly identical. For the thicker disk elements, the vortex annihilation energy barrier can be overcome more easily by the additional thermal excitation since $\Delta H_{an}$ is larger than $\Delta M_s$. This result may be linked to the change of the vortex core trajectory for the thicker disk structures. Especially for $t = 50\,\mathrm{nm}$, a bending of the vortex core with a reduction of the susceptibility is observed when the core approaches the edge (see Section 4.1.8, Figure 4.16). Furthermore, the susceptibility is generally reduced for thicker elements. Consequently, fluctuations of the magnetization, which are caused by thermal excitation, will have a larger impact on $H_{an}$ for thicker disks. It is assumed here that for large enough elements thermal excitation will cause thickness-independent local fluctuations of the magnetization.

In summary, for CoFeB, thermally assisted barrier jumps affect $H_{an}$ maximum half as much ($-9.3\,\% \pm 1.5\,\% + 6.2\,\% \pm 0.8\,\% = -3.1\,\% \pm 2.3\,\%$ for 35 nm) as $M_s(T)$ ($-6.2\,\% \pm 0.8\,\%$). For 20 nm thickness, thermally assisted annihilation seems to be almost negligible, but further investigations are required in order to prove or disprove the previous conclusion based on the assumption of extrapolating $\Delta M_s$. Of particular interest will be in future investigations: (1) simulations of the annihilation process in thin disk structures performed at elevated temperatures and (2) the investigation of uncoupled NiFe free layers since NiFe shows a much higher reduction of $M_s$ over temperature.

The results of $\Delta H_{an}$ can now be transferred to $\Delta H_n$. For 35 nm thickness, it can be assumed that the reduction of $M_s$ is approximately directly proportional to $H_n$, similar to $H_{an}$. This leads to an estimation of $4.9\,\% \pm 5.7\,\%$ relative nucleation field shift as a result of only thermally assisted nucleation barrier jumps. $\Delta H_n$ of the 50 nm thick elements is similar to that of 35 nm.

For 20 nm, it has been shown in Figure 4.20 in Section 4.2.1 that a proportionality between $H_n$ and $M_s$ is barely present: a reduction of $M_s$ by approximately 26 % even causes a small increase of $H_n$. Consequently, an increase in temperature is expected to lead to an earlier, thermally assisted vortex nucleation, which explains why a positive $\Delta H_n$ is observed for 20 nm thickness. Such a behavior was also reported for laterally smaller (300 nm diameter) permalloy disk structures with the same thickness [194].

In summary, for CoFeB thermally assisted barrier jumps affect $H_n$ slightly more than $H_{an}$. A more precise quantitative assessment was not possible due to the large standard deviation of $\Delta H_n$. Subsequent investigations may address a reduction of the standard deviation by measuring elements with many TMR cells, but it should be kept in mind that the $H_n$ shift of individual disk structures cannot be extracted then. For 20 nm thickness, a positive $\Delta H_n$ is observed, which can be explained by the almost non-existent correlation between $M_s$ and $H_n$ in this thickness range enabling thermally assisted barrier jumps to dominate.

An exact determination of $\Delta M_s$ for CoFe was not possible by extracting the change of the susceptibility from the dual device measurements (Fit 1 in Table 5.2). There are

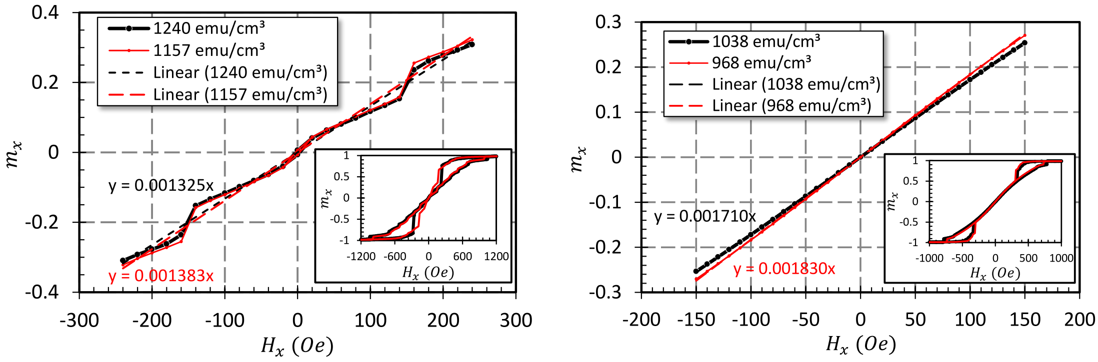

**(a)** Sim. - CoFe $t = 50\,\text{nm}$ **(b)** Sim. - CoFeB $t = 50\,\text{nm}$

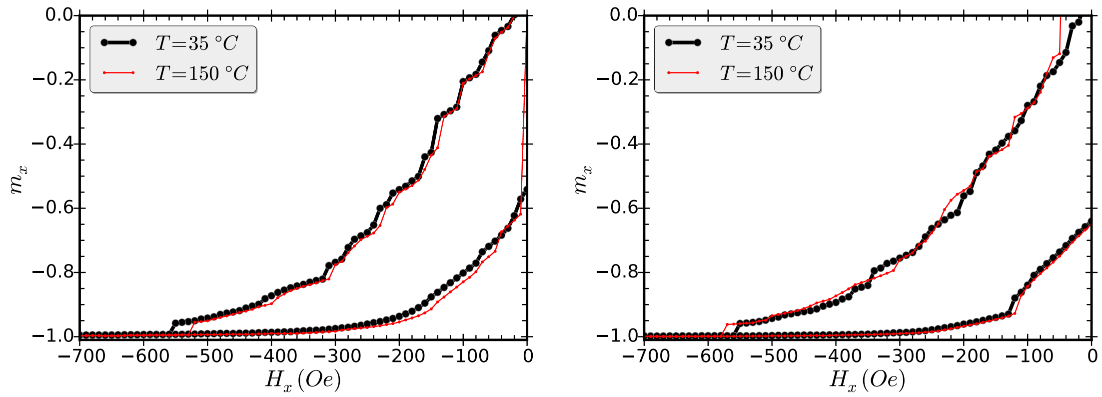

**(c)** Exp. - CoFe $t = 20\,\text{nm}$ **(d)** Exp. - CoFe $t = 20\,\text{nm}$

**Figure 5.8.** (a) Simulations with a reduction of $M_s$ by 6.7 % show that the initial susceptibility is increased only by 4.4 % for CoFe. (b) For CoFeB it is increased by 7.0 %, which corresponds almost exactly to $\Delta M_s$ as to be expected. Trend lines were extracted in the shown range of $m_x \approx \pm 0.3$ (CoFe) or $m_x \approx \pm 0.25$ (CoFeB). The insets show the full hysteresis loops. (c) The experimental measurement further demonstrates the small impact of temperature on the susceptibility. (d) A reversed sense of rotation - visible by varying mini-hysteretic characteristics - can lead to an increase in $H_{an}$. All measured and simulated structures have a diameter of 1.1 µm. Simulation parameters for CoFe are: $K_1 = 5 \times 10^5\,\text{erg/cm}^3$ (in-plane), average crystallite size of 20 nm and $A = 1.53\,\mu\text{erg/cm}$. For CoFeB a magnetically disturbed edge of 15 nm and zero magneto-crystalline anisotropy were applied.

several reasons for this: firstly, large differences in mean values as well as large standard deviations show the influence of the high magneto-crystalline anisotropy with its resulting hysteresis. Secondly, micro-magnetic simulations showed that a reduction of $M_s$ by a certain amount leads to an increase in slope that is not directly proportional. This fact is illustrated by Figure 5.8a. A reduction of $M_s$ by 6.7 % leads to an increase in susceptibility by 4.4 %, which is approximately two thirds of $\Delta M_s$. In contrast, CoFeB shows the expected direct proportionality as illustrated by Figure 5.8b. Consequently, the fitted $\Delta M_s$ values in Table 5.2 are expected to represent an actually larger reduction of $M_s$.

Figure 5.8c illustrates how the temperature-induced change in susceptibility is hardly visible due to the mini-hysteresis of CoFe. The observed changes are very similar in the simulations with reduced $M_s$ as characteristic jumps in the signal remain almost unchanged. Especially for the $m_x$ range from 0 to $-0.25$ the two measurements are nearly identical. During the subsequent reduction of $H_x$, the small jumps occur earlier at the elevated temperature which mainly indicates that a reduction of $M_s$ actually took place. Figure 5.8d illustrates how a reversed sense of rotation of the vortex state at 150 °C leads to an increase of $H_{an}$. Moreover, this example shows that for different senses of rotation the slope of the transfer curve appears to be nearly unaffected by the change in temperature.

To determine the $M_s(T)$ dependence of CoFe more accurately, additional measurements over temperature were performed at devices with 1170 TMR cells in total. Changes in slope around zero field were extracted in the same manner as for the dual disk devices. The resulting value for the 35 nm thick disks is shown in Table 5.2 under '$Fit\ 2\ \varDelta M_s$'. This value has, as expected, a significantly smaller standard deviation. With the assumption that the actual reduction of $M_s$ is about 50 % larger (based on the results shown in Figure 5.8), a $\varDelta M_s$ between 3 and 4 % can be estimated for CoFe. Such an absolute reduction of $M_s$, which is 2 to 3 % smaller compared to CoFeB, is in line with the initial expectations of a higher $T_C$ for CoFe (see Section 5.2.1) and may explain fairly accurately the difference in $\varDelta H_n$ if it is assumed that the thermally induced nucleation field shifts (neglecting the influence of $M_s(T)$) are independent of the material.
In contrast, $H_{an}$ shows drastic differences for the two investigated materials. For CoFeB, both factors - $M_s(T)$ and thermally assisted barrier jumps - reduce the annihilation field. In contrast, only $M_s(T)$ seems to reduce $H_{an}$ for CoFe (at least for 20 and 35 nm thickness). It has been demonstrated that the reason for this can be found in the sense of rotation of the vortex state. Pike and Fernandez showed statistically at cobalt dots that $H_{an}$ is increased for partial hysteresis loops, where the field is reversed when the vortex state has nucleated [50]. They argued that the vortex exits with greater ease on the same side from which it has entered during nucleation. Therefore, the results over temperature in combination with the results from Pike and Fernandez allow the conclusion that the energetically preferred vortex state - in terms of sense of rotation - nucleates with a higher probability at elevated temperatures. Since the field is not reversed in this experiment, the vortex core moves to the 'unfavorable', more stable side of the disk and an increase in $H_{an}$ is observed. Together with the results of the CoFeB system - for 20 nm thickness, the influence of thermally assisted barrier jumps on the annihilation process can be neglected - the small $\varDelta H_{an}$ of CoFe can thus be explained. Future investigations may confirm or disprove this hypothesis.

### 5.2.7 Summary

It was shown that the two effects of a temperature elevation - (1) reduction of $M_s$ and (2) thermally assisted barrier jumps - have different effects on $H_n$ and $H_{an}$ depending on thickness and material. In case of the amorphous CoFeB, both effects add up to a reduction of the average $H_{an}$ (negative $\mathit{\Delta} H_{an}$). However, effect No. (2) plays a negligible role for 20 nm thickness due to the nearly linear course of the vortex core trajectory near the disk edge. For thicker elements the vortex core trajectory becomes non-linear when the vortex core approaches the edge and the core profile gets elongated, which results in a reduced susceptibility. Thus, effect No. (2) has an increased impact and leads to a further reduction of $H_{an}$. The same applies for CoFe but in addition, effect No. (2) leads to the nucleation of a vortex state with reversed direction of rotation at elevated temperatures which in turn allows an increase in $H_{an}$. Thus, the relative $\mathit{\Delta} H_{an}$ values are smaller for CoFe also because the reduction of $M_s$ is smaller.

For both materials, the nucleation field of the 20 nm thick elements has a positive average $\mathit{\Delta} H_n$ which is mainly attributed to the fact that effect No. (1) has almost no influence on $H_n$ for thin elements. Thicker CoFeB disks have a negative $\mathit{\Delta} H_n$, whereas CoFe shows positive values. This difference is mainly attributed to the material dependent characteristics of effect No. (1). The magneto-crystalline anisotropy of CoFe seems to have hardly any impact on the *average* $\mathit{\Delta} H_n$. In contrast, the temperature elevation strongly affects $H_n$ of *individual* CoFe devices: $\mathit{\Delta} H_n$ vs. $H_n$ of individual elements shows a distinct correlation with a large trend line slope over all thicknesses. This is not the case for all CoFeB thicknesses. For CoFeB, a high correlation was only observed for 35 nm, which is expected to be linked to the lowest rate of first-order phase transitions into intermediate states.

## 5.3 Bias Fields

In this section, the influence of constant in-plane magnetic fields is investigated, which are additionally applied and perpendicular to the sensitive axis of the sensor. The orientation of such a $H_y$ bias field is illustrated by the inset in Figure 5.9. The focus of this investigation is on the impact on the nucleation field. In case of an amorphous disk structure with large $H_n$, the impact on $H_n$ is expected to be negligible small, which is demonstrated in Figure 5.9. However, this does not apply to all investigated structures, in particular CoFe elements are significantly influenced by $H_y$ as will be shown in Section 5.3.1.

The motivation for this study was the fact that TMR vortex sensors utilized in a car can be exposed to additional, unintended magnetic fields, for example, due to the electrification of cars. Usually such fields are expected to be constant with respect to the operation frequency of the sensor itself. It is to be expected and shown in Figure 5.9 that the sensitivity of the vortex sensor is nearly unaffected when a 'small' perpendicular in-plane bias field of 80 Oe is applied. This is due to the much larger operating field range, which is proportional to $H_{an}$ in a first approximation. Another important parameter in the application as sensor is $H_n$, which has to be stable under various conditions. There are only few investigations about the effect of magnetic bias fields on the vortex state. Sort et al. reported that no vortex nucleation is observed with perpendicular biasing of magnetic disks (permalloy, $d \leqslant 1\,\mu\mathrm{m}$, $t = 12\,\mathrm{nm}$) [88, 90]. However, as biasing was realized via the exchange bias effect in their studies they could not vary the bias field, which was between about 60 and 90 Oe. It will be shown in the next section that for such thin elements a bias field of $\geqslant 20$ Oe is already sufficient to prevent vortex nucleation. The application of an in-plane bias field, perpendicular to the field of the hysteresis loop, leads to a rotation of external field. Even less has been reported about the influence of rotating fields and

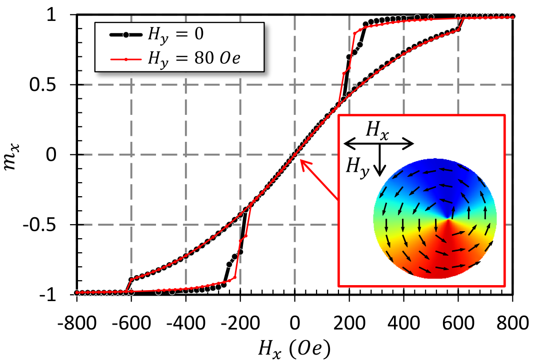

**Figure 5.9.** Simulated hysteresis loops of an amorphous disk element ($d = 1.1\,\mu\mathrm{m}$ and $t = 35\,\mathrm{nm}$) with magnetic properties similar to CoFeB. A $H_y$ bias field of 80 Oe has only a small impact on the nucleation field and susceptibility of the vortex state. The inset illustrates the orientation of $H_y$ in top view and its impact on the vortex state for $H_x = 0$: an offset of the core to the right side due to the anticlockwise direction of rotation. Standard simulation parameters of CoFeB are given in Section 3.3.

how they affect the magnetization reversal of a disk structure. However, it has been shown that rotating fields can decrease the stability of certain magnetic configurations and thus facilitate magnetization reversal [164, 166].
To go one step further, the influence of bias fields is investigated here for different disk thicknesses, different materials - in particular amorphous or with a non-zero magneto-crystalline anisotropy - and also for varying field strength.

### 5.3.1 Bias Field-Induced Nucleation Field Shifts

Double spin-valve structures with 1.1 µm free layer diameter were characterized. Each device was measured ten times without any bias field and ten times with a constant bias field $H_y$ of 80 Oe. This way, the average shifts of $H_n$ and $H_{an}$ were extracted for individual devices (for a detailed description see Section 5.1). A maximum of 25 dual disk devices were measured on each wafer. Additional measurements on devices with 1170 disks were performed with different bias field amplitudes to complete the picture.

Figure 5.10 illustrates how differently the applied bias field can affect vortex nucleation. Again, similar to the influence of an elevation in temperature, positive and negative shifts of $H_n$ are observed. For the 20 nm CoFeB device, shown in Figure 5.10a, vortex nucleation is slightly delayed when coming from positive saturation if a bias field of 80 Oe is applied. When coming from negative saturation, nucleation is accomplished slightly earlier. Furthermore, the general course of hysteresis of the vortex state is nearly unaffected by the bias field. This can be explained by the negligible small reduction of susceptibility when the magnetic field is increased from zero to 80 Oe. The annihilation field is slightly reduced, which is due to the fact that $H_x$ and $H_y$ have to be summed up

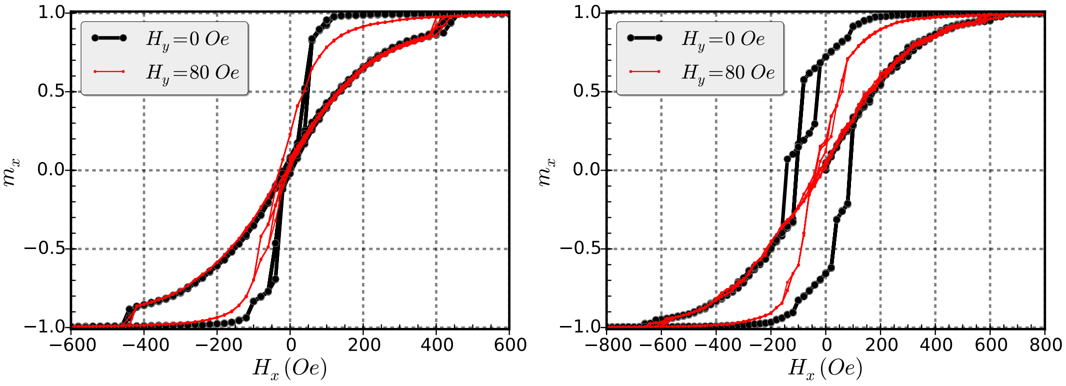

**(a)** CoFeB **(b)** CoFe

**Figure 5.10.** Normalized TMR transfer curves of dual disk devices ($d$ = 1.1 µm and $t$ = 20 nm). Each device was measured ten times with 0 Oe and ten times with 80 Oe applied constant bias field $H_y$.

vectorially. It is also observed that the hysteresis between vortex and non-vortex state is reduced because of the applied bias field in $\hat{y}$-direction, $m_x$ of the free layer is reduced earlier when coming from saturation.
It looks differently for the 20 nm CoFe device shown in Figure 5.10b. In the unbiased loops, vortex nucleation is strongly delayed compared to CoFeB (see influence of the magneto-crystalline anisotropy in Section 4.2.3). For $H_y = 80\,\mathrm{Oe}$, a large shift of $H_n$ to an earlier nucleation is observed. In other words, the applied bias field in $\hat{y}$-direction helps to reduce certain energy barriers during the nucleation process and 'accelerates' the magnetization reversal, which shifts $H_n$ closer to the theoretically possible field value. As might be expected, $H_{an}$ and the general course of hysteresis of the vortex state are nearly unaffected in the same manner as for CoFeB. It has to be noted that the applied bias field of 80 Oe affects the magnetization reversal of the CoFe disks significantly more than an increase in temperature of 115 °C (see Section 5.2.2).

Figure 5.11 shows for CoFe that the observed nucleation field shifts ($\Delta H_n$) are statistically significant. In particular, nearly all 20 nm CoFe devices show a positive $\Delta H_n$. There is also a clear correlation between the unbiased nucleation field value and the absolute value of $\Delta H_n$. This observed correlation is in a way analogous to the reported temperature-induced shifts in Section 5.2.2 but much more pronounced here:

- If the device shows a comparatively early vortex nucleation (large $H_n$ at $H_y = 0$), the additionally applied bias field will increase the absolute value of the external field and thus decrease $H_n$, which results typically in a negative shift.
- In contrast, if the device shows a comparatively delayed vortex nucleation, the applied $H_y$ helps to overcome certain vortex nucleation energy barriers and an earlier vortex nucleation is observed. The observed effect differentiates the vortex

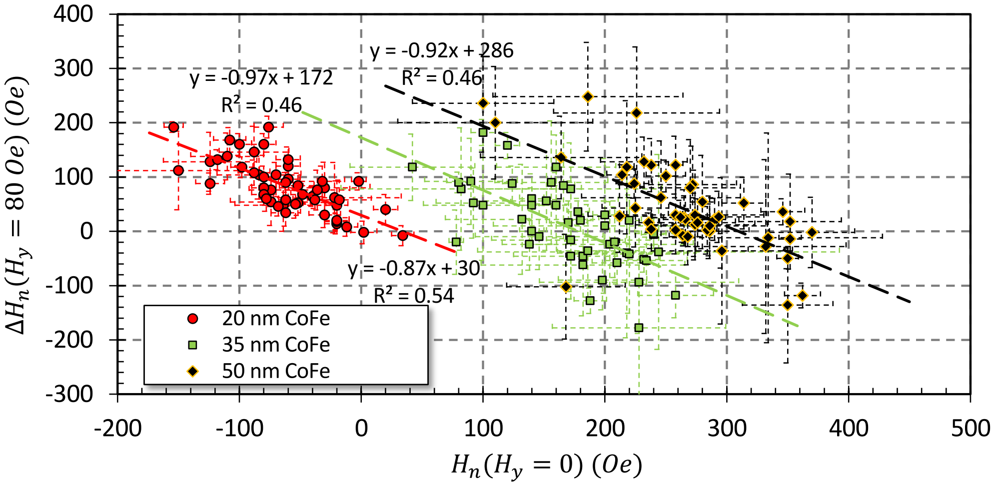

**Figure 5.11.** Shift of $H_n$ for 80 Oe $H_y$ bias field. $\Delta H_n$ is plotted versus the unbiased $H_n$ value for three CoFe thicknesses. A detailed explanation regarding $\Delta H_n$ is given in Section 5.1. Each data point represents the average shift of either $H_{n+}$ or $H_{n-}$ of only one dual disk device ($d = 1.1\,\mu\mathrm{m}$).

sensor concept from traditional sensor concepts with, for example, stripes and elliptical shapes, where bias fields typically lower the sensor performance. Moreover, the effect opens up possibilities when magneto-crystalline free layer materials are used [197]. Mechanisms involved in this effect will be discussed in detail in the next sections.

As it can be observed in Figure 5.11, such a correlation is evident for all three thicknesses. The slopes of the regression lines are nearly identical, and their coefficients of determination share similar levels. However, only 20 nm free layer thickness shows a clear, overall positive shift.

To complete the picture of the varying impact of a magnetic bias field on $H_n$, Figure 5.12 shows the nucleation field shifts for 20, 35, and 50 nm CoFeB free layer thickness. In principle, the scatter plots show the same correlation as for the material CoFe: a negative slope of the regression line. However, the correlation is drastically reduced to barely existent for 35 and 50 nm (see coefficients of determination). Furthermore, only negative average shifts are observed for CoFeB. This is expected to be linked to the fact that, without biasing, vortex nucleation is observed earlier for CoFeB. It will be shown later in this section that positive average shifts are observed for CoFeB as well if smaller bias fields are applied. The CoFeB results are particularly interesting because they indicate that the observed bias field-induced nucleation field shifts of individual disks are not only due to the magneto-crystalline properties of CoFe.

Table 5.3 summarizes the biasing-induced average shifts of $H_n$ and $H_{an}$ for different material systems and free layer thicknesses for the arbitrarily chosen $H_y = 80$ Oe. The values clearly show the general difference between CoFeB and CoFe: a reduction of $H_n$ for CoFeB and an increase for CoFe if the bias field is applied. It should be pointed out

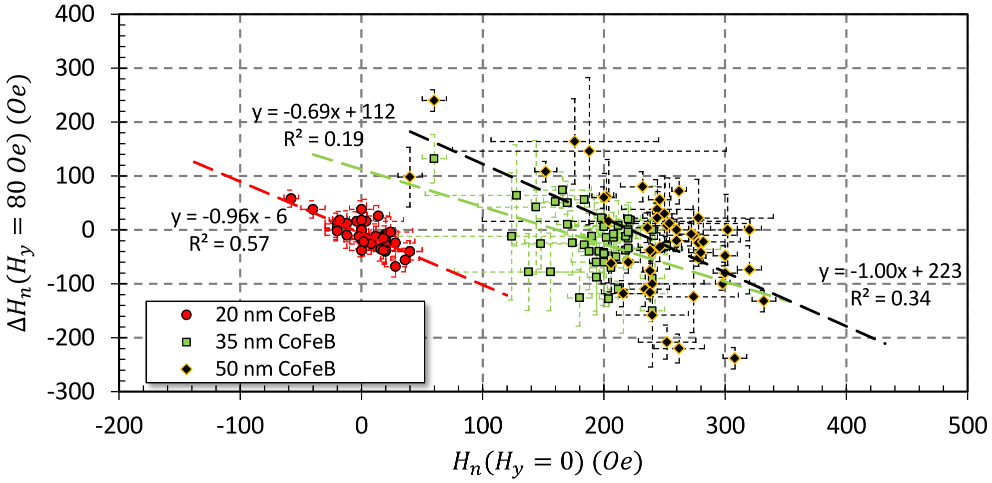

**Figure 5.12.** Shift of $H_n$ for 80 Oe $H_y$ bias field. $\Delta H_n$ is plotted versus the unbiased $H_n$ value for three CoFeB thicknesses. A detailed explanation regarding $\Delta H_n$ is given in Section 5.1. Each data point represents the average shift of either $H_{n+}$ or $H_{n-}$ of only one dual disk device ($d = 1.1\,\mu$m).

**Table 5.3.** Summary of average critical field values $H_n$ and $H_{an}$ without biasing and with an applied $H_y$ bias field of 80 Oe. The given values are the $\hat{x}$-component of the external field ($H_x$), neglecting the $H_y$-component. Measurements were performed on dual disk devices ($d = 1.1\,\mu\text{m}$).

| Material | t (nm) | $H_{n,0\,\text{Oe}}(Oe)$ | $H_{n,80\,\text{Oe}}(Oe)$ | $H_{an,0\,\text{Oe}}(Oe)$ | $H_{an,80\,\text{Oe}}(Oe)$ |
|---|---|---|---|---|---|
| **CoFeB** | **20** | $8 \pm 22$ | $-6 \pm 15$ | $445 \pm 19$ | $438 \pm 19$ |
| **CoFeB** | **35** | $195 \pm 34$ | $172 \pm 37$ | $630 \pm 22$ | $624 \pm 19$ |
| **CoFeB** | **50** | $244 \pm 56$ | $222 \pm 62$ | $798 \pm 26$ | $793 \pm 25$ |
| **CoFe** | **20** | $-61 \pm 39$ | $22 \pm 27$ | $599 \pm 31$ | $590 \pm 35$ |
| **CoFe** | **35** | $169 \pm 49$ | $178 \pm 48$ | $864 \pm 33$ | $854 \pm 30$ |
| **CoFe Ru-coupled** | **35** | $191 \pm 77$ | $156 \pm 115$ | $859 \pm 35$ | $857 \pm 35$ |
| **CoFe** | **50** | $265 \pm 60$ | $306 \pm 59$ | $1065 \pm 53$ | $1063 \pm 54$ |
| **NiFe Ru-coupled** | **35** | $176 \pm 28$ | $164 \pm 38$ | $507 \pm 12$ | $505 \pm 14$ |
| **NiFe Ru-coupled** | **50** | $225 \pm 46$ | $234 \pm 47$ | $595 \pm 15$ | $596 \pm 21$ |

that the $H_n$ values in Table 5.3 neglect the applied $H_y$ field component. As expected, $H_{an}$ is nearly unaffected for all materials. The small reduction that is observed if a bias field is applied is due to the fact that $H_y$ will increase the absolute value of the applied magnetic field. Thus, a smaller $H_x$ value is sufficient to annihilate the vortex.

The Ru-coupled NiFe free layers do not show a clear trend except that the overall shifts are comparatively small. It is interesting that there is a negative $H_n$ shift of the Ru-coupled CoFe free layer in contrast to the positive shift of the uncoupled CoFe free layer. The difference is expected to be linked to some extent to the large unbiased $H_n$ of the coupled CoFe free layer. Furthermore, the coupled CoFe free layer system seems to interact with the applied bias field in a more complicated way since there is also a strong increase of the standard deviation. Thus, it may be of interest to investigate such coupled systems in subsequent works. The observed negative $\Delta H_n$ of the Ru-coupled CoFe free layer system is also interesting in the context that a positive shift was observed with temperature elevation.

So far, a $H_y$ bias field of 80 Oe was discussed. Figure 5.13 gives on overview of how the field amplitude affects the average $\Delta H_n$ for 10 and 20 nm thick CoFe and CoFeB disk structures with 1.1 µm diameter. For this purpose, structures consisting not only of one or two disk-shaped free layer elements but 1170 were characterized. As a consequence, the information about vortex nucleation events of individual disks is lost, but the end of the nucleation field distribution is visible by the vanishing hysteresis (at least for the 20 nm thick elements).

For the 10 nm thick CoFeB (see Figure 5.13a), $H_y = 10\,\text{Oe}$ leads to a slightly earlier vortex nucleation. Moreover, the course of hysteresis of the vortex state (after field reversal at $|H_x| \approx 50\,\text{Oe}$) is identical to the measurement with zero applied bias field. This observation allows the conclusion that actually all individual elements are in the vortex state, which is not the case for $H_y > 10\,\text{Oe}$. Indeed, for the positive branch there

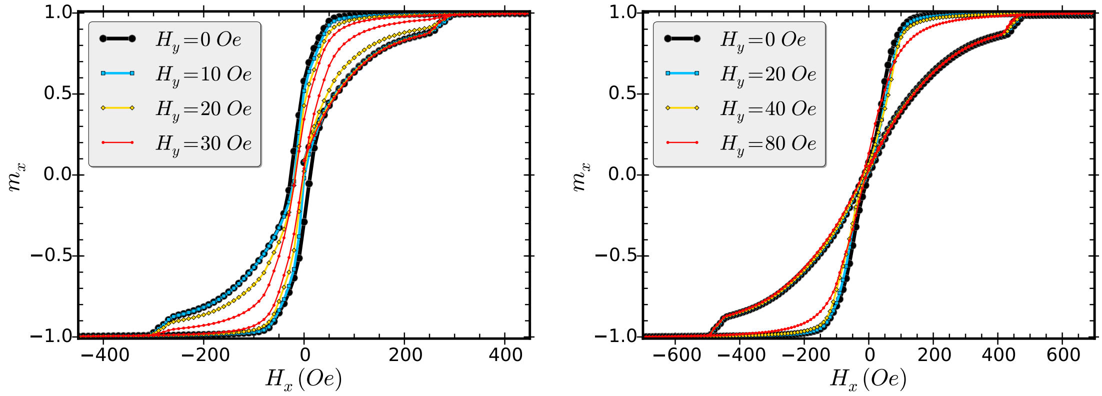

**(a)** CoFeB - $t = 10\,\mathrm{nm}$

**(b)** CoFeB - $t = 20\,\mathrm{nm}$

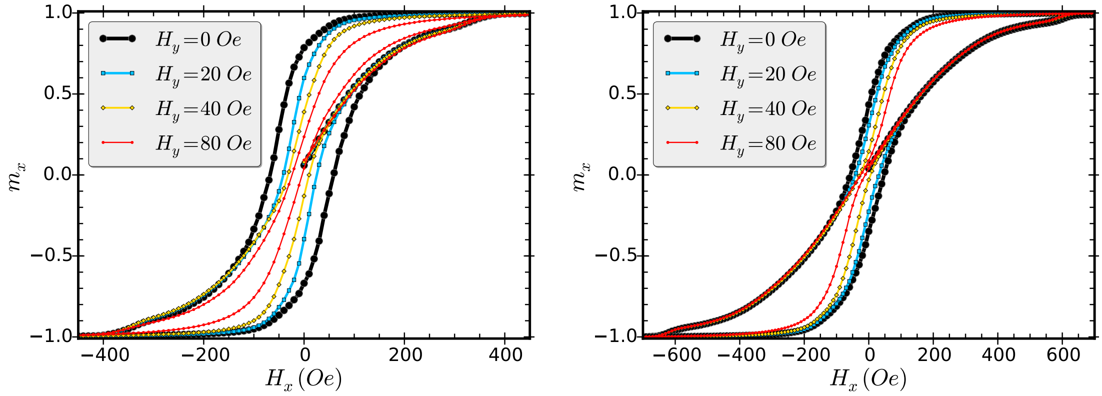

**(c)** CoFe - $t = 10\,\mathrm{nm}$

**(d)** CoFe - $t = 20\,\mathrm{nm}$

**Figure 5.13.** Normalized TMR transfer curves measured on structures which consist in total of 1170 individual spin-valves, each with identical free layer dimensions for various $H_y$ bias field strengths. The disk diameter was always 1.1 µm.

is also one path where $H_y = 20$ and 30 Oe are congruent but this is due to the fact that the measurement starts at zero field.

The bias field measurements on 20 nm thick CoFeB disks indicate that the vortex state is present up to $H_y = 80$ Oe as was to be expected. The measurements also reveal that the positive maximum of $\varDelta H_n$ is reached in the $H_y$ range between 20 Oe and 40 Oe. A more detailed analysis of $\varDelta H_n$ as a function of $H_y$ led to the result that the maximum is slightly below 30 Oe (not shown).

As already discussed, the CoFe elements demonstrate much larger positive nucleation field shifts. Figure 5.13c and 5.13d show how $\varDelta H_n$ increases with increasing amplitude of $H_y$. The results indicate that the maximum of $\varDelta H_n$ is not reached yet for $H_y = 80$ Oe in case of 20 nm thickness. For 10 nm thickness, the measurement with 80 Oe bias field indicates that the vortex state is no longer present for all elements. The observed opening of hysteresis of the positive branch, where a comparison with the starting path is possible, starts at $H_y = 50$ Oe (not shown).

The next sections discuss the different aspects of the bias field-induced $H_n$ shifts. Thus, a summary of the observed effects and corresponding explanations is given in Section 5.3.6.

### 5.3.2 Bias Fields and the Configurational Stability

The question that now arises is how a constant magnetic in-plane bias field perpendicular to the sensing axis facilitates vortex nucleation. To address this question, simulations with and without magneto-crystalline anisotropy were performed. In the following it will be shown that there are several reasons for the observed positive $\Delta H_n$, such as a reduction of the coercivity and remanence of the whole element and a blocking of the formation of intermediate pre-vortex states. A bias field-induced reduction of the coercivity and remanence on crystal grain level is demonstrated in the next section. First, the results for amorphous materials will be discussed as they are expected to be relevant for all types of elements.

Figure 5.14a shows simulated hysteresis loops for an elliptical particle. Due to its shape anisotropy (see e.g. [71]), the easy axis loop shown has a distinct switching behavior. The reason for this is that a rotation of the magnetization increases the stray field energy drastically. Consequently, an antiparallel alignment of the magnetization, with respect to the external field, is stable until a rotation of the magnetization leads to a larger reduction of $E_{\text{Zeeman}}$ (for every possible angle of magnetization) compared to the increase of $E_{\text{demag}}$. When this point is reached the energy barrier between the antiparallel and the parallel alignment is zero and the element switches to the global minimum. This is particularly the case because such small and thin elements behave like uniformly magnetized single-domain particles.

By applying a bias field, the point of switching is reduced since a rotation of the magnetization in hard axis direction is facilitated during magnetization reversal. In other words, a larger reduction of $E_{\text{Zeeman}}$, compared to the increase of $E_{\text{demag}}$, is no longer necessary for every angle of magnetization. For large enough bias fields, the ellipse is saturated in hard axis direction at $H_x = 0$. In such cases, no hysteresis and consequently zero coercivity and zero remanence are observed in the $H_x$ loop (not shown).

The disk elements investigated within this work do not have any shape anisotropy. Still, the observed pre-states, especially the different buckling states such as C- or S-state are able to delay vortex nucleation (see Section 4.1.5), in other words lead to an increased coercivity field. This effect was called *configurational stability* by Ha et al. [164]. One example is the C-state, which is present in the element shown in Figure 5.14b. Without bias field a large coercivity field is observed. By applying a bias field, the coercivity is reduced drastically, similar to the elliptical particle. Ha et al. came to a similar conclusion when they applied rotational fields with constant field amplitude and observed that the configurational stability can be avoided this way [164]. In this context, it needs to be mentioned again that simulations were performed at 0 K. Consequently, energy barriers

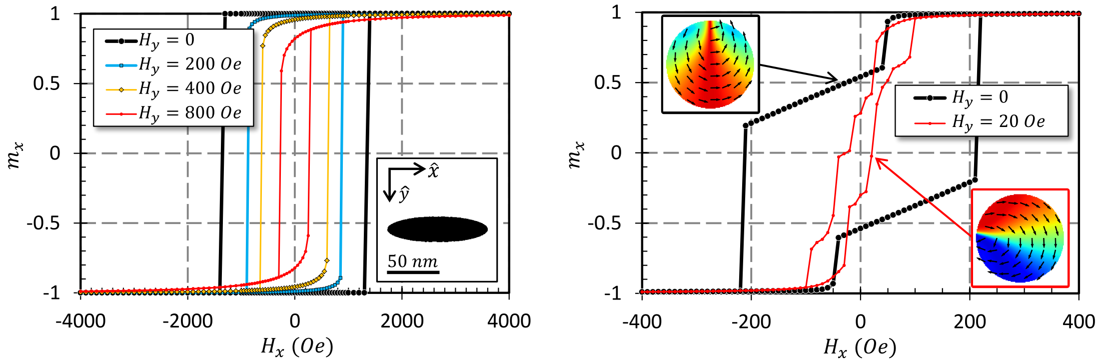

**(a)** Ellipse - 100 nm × 25 nm $t = 2$ nm

**(b)** Disk - $d = 400$ nm $t = 10$ nm

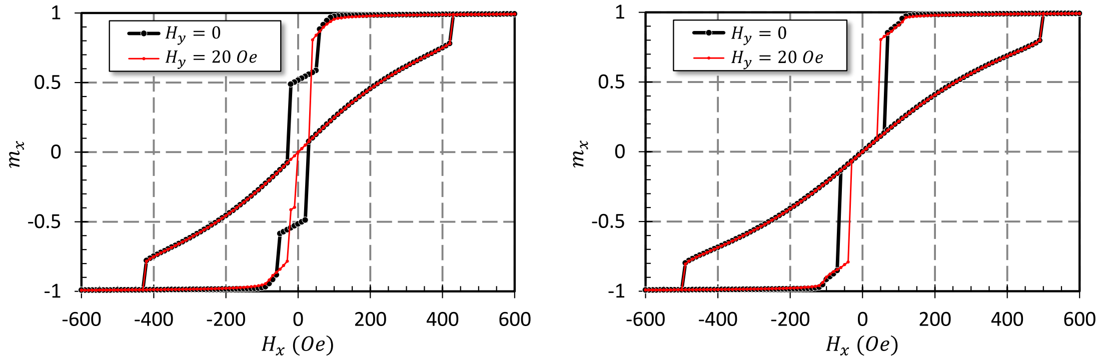

**(c)** Disk - $d = 400$ nm $t = 12$ nm

**(d)** Disk - $d = 400$ nm $t = 14$ nm

**Figure 5.14.** Simulated hysteresis loops of relatively small elements with applied bias fields ($H_y$). (a) The ellipse illustrates how coercivity and remanence are decreasing with increasing bias field strength. (b) For the 10 nm thick disk element magnetization reversal occurs via the C-state (see inset). The bias field leads to a rotation of the C-state which reduces coercivity and remanence, like the ellipse. (c) For the 12 nm thick disk element vortex nucleation occurs after zero-crossing via the C-state if no bias field is applied. By applying a bias field, the C-state formation is skipped or its stability is reduced and an earlier vortex nucleation is observed. (d) The 14 nm thick disk element shows only one first order phase transition previous to annihilation: vortex nucleation itself. Furthermore, $H_n$ is positive. Consequently, by applying a bias field a negative $\varDelta H_n$ is observed. Simulation parameters are as follows: $M_s = 1038\,\mathrm{emu/cm^3}$, $A = 1.53\,\mu\mathrm{erg/cm}$, no magneto-crystalline anisotropy, in-plane edge length of the cells 3.4 nm (disks) or 0.4 nm (ellipse) and out-of-plane below 3 nm. In case of the disk elements a magnetically disturbed edge of 15 nm was applied.

can only be overcome by the changing external magnetic field. Furthermore, vortex nucleation is expected to occur at room temperature for an element with the dimensions of the one shown in Figure 5.14b [52].

The previous findings can now be transferred to a disk element where vortex nucleation is observed via the C-state as it is shown in Figure 5.14c. As expected, the application of a bias field leads to a positive $\varDelta H_n$. If, in contrast, vortex nucleation already occurs before zero-crossing for zero $H_y$ and no additional first-order phase transition into a more stable intermediate state - such as the C-state - takes place, then usually a negative $\varDelta H_n$ is observed. An example of such a case is shown in Figure 5.14d. These results can now be

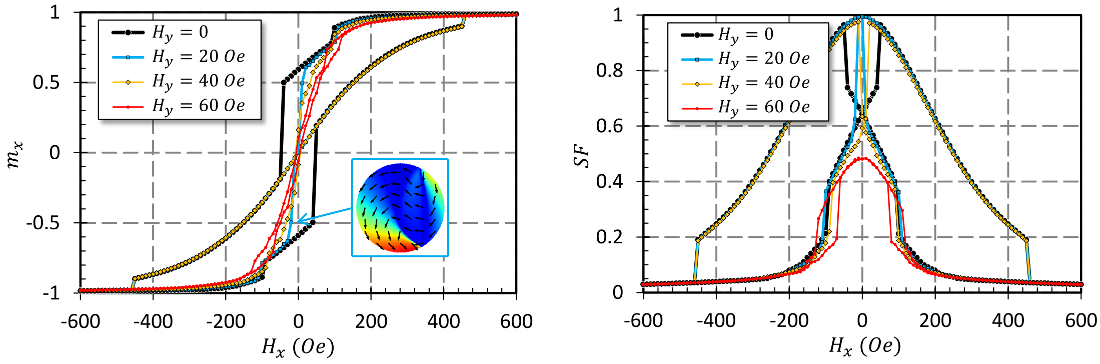

**(a)** Simulation - magnetization **(b)** Simulation - spread function

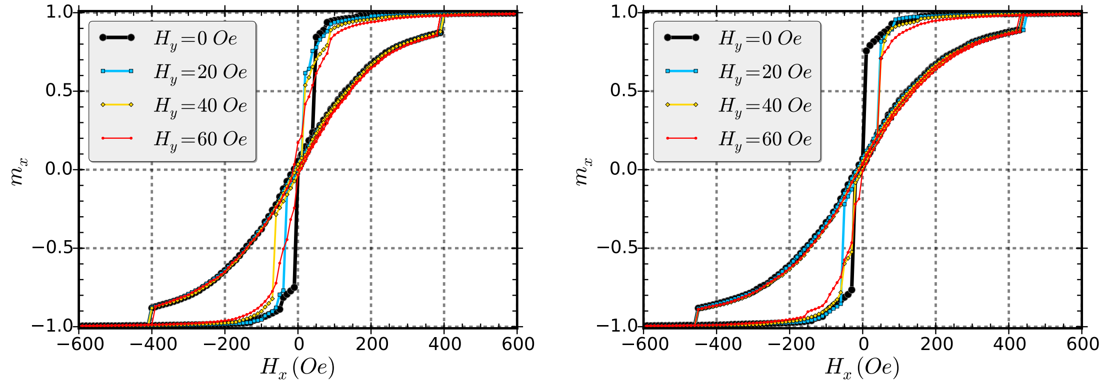

**(c)** Exp. - CoFeB device No. 1 **(d)** Exp. - CoFeB device No. 2

**Figure 5.15.** (a) Simulated hysteresis loops of an amorphous disk structure with applied bias fields ($H_y$). For $H_y = 60$ Oe a coherent rotation of the S-state, without vortex nucleation, takes place. The inset shows an asymmetric S-state for $H_y = -20$ Oe prior to vortex nucleation. (b) Spread function curves of the simulated disk structure. (c-d) Experimental TMR measurements on CoFeB single disk devices. Vortex nucleation is observed also for $H_y =$ 60 Oe. The simulation parameters are as follows: $M_s = 1038\,\text{emu/cm}^3$, $A = 1.53\,\mu\text{erg/cm}$, zero magneto-crystalline anisotropy and a sloped edge with $\alpha = 53°$ (see Section 4.2.7).

transferred to the investigated 1.1 µm diameter elements. The simulated hysteresis loops of such an amorphous disk structure - see Figure 5.15a - show a positive $\Delta H_n$ if small bias fields (20 and 40 Oe) are applied. This is in line with the expectations since $H_n$ is negative for $H_y = 0$ and a first-order phase transition into the S-state takes place. In the example shown, the formation of the S-state is not skipped when a 20 and 40 Oe bias field is applied, but its stability is drastically reduced, which can be explained by the fact that the rotation of the S-state is incoherent for such small bias fields. Due to pinning effects at the element border (see Section 4.2.11), the S-state can become asymmetric (see inset in Figure 5.15a) and thus energetically less favorable, which facilitates vortex nucleation. For $H_y = 60$ Oe, vortex nucleation is no longer observed in the simulation. In this case, a coherent rotation of the S-state takes place during magnetization reversal which was also reported by Sort et al. [88].

It has to be noted that when a magnetically disturbed edge is applied, instead of a sloped edge, similar shifts of $H_n$ are observed. However, vortex nucleation is no longer observed for $H_y = 30\,\mathrm{Oe}$. Consequently, the magnetically disturbed edge reduces the strength of pinning sites at the edge and thus facilitates a coherent rotation of the magnetization.

An additional parameter of the stability of intermediate states is the non-uniformity, which is virtually the opposite of the polarization. It was shown by Ha et al. that the spread function is a good measure of the non-uniformity of a magnetic configuration [164]. The spread function is defined as follows:

$$SF = 1 - {m_x}^2 - {m_y}^2 - {m_z}^2 \tag{5.4}$$

Values of SF lie in the closed interval $[0, 1]$ (proof see [164]). If $SF = 0$, then the magnetization is perfectly uniform while if $SF = 1$, the magnetization is evenly distributed. The second case is valid for the vortex state when neglecting the small $m_z$ component of the core. Consequently, the stability of a magnetic state around zero field should be larger the greater the value of $SF$ is, since this reflects a smaller stray field.

Figure 5.15b shows the spread function for the simulated CoFeB element shown in Figure 5.15a. The bell shape of $SF$, which represents the vortex state, is nearly unaffected by the applied bias fields, but it can be seen clearly that $SF$ becomes smaller for the C-state. A smaller $SF$ results in a larger stray field and is thus energetically less favorable around zero field[3]. Consequently, vortex nucleation occurs earlier if a small bias field is applied. It has to be noted that the chosen type of display of the data set neglects the $H_y$ component and therefore allows to plot a continuous function. However, this type of display makes sense since the applied bias field has to be treated separately from $H_x$, which is the only field component that the sensor is expected to measure. The smaller $SF$ around $H_x = 0$ results from the magnetic polarization which originates from the applied bias field ($|H| > H_x$).

The negative branch of the exemplary TMR measurements of a single disk structure (see Figure 5.15c) show a behavior similar to the simulations: $\mathit{\Delta} H_n$ is positive for $H_y = 20$ and $40\,\mathrm{Oe}$, and for $H_y = 60\,\mathrm{Oe}$ a course of hysteresis can be observed that is similar to the one in Figure 5.15a, which is caused by the almost coherent rotation of the S-state. In contrast to the simulation, vortex nucleation is also observed for $H_y = 60\,\mathrm{Oe}$. Most likely this is due to the influence of thermal fluctuations. The positive branch differs from the negative branch in the experiment as a negative $\mathit{\Delta} H_n$ can be observed. This is expected to be a result of the larger $H_n$ in the experiment for $H_y = 0$.

In summary, the $H_y$ bias field leads to a smaller coercivity for amorphous elements and can therefore facilitate vortex nucleation. In some cases, it was observed that intermediate states were skipped. Lau et al. showed that, if *field dependent* energy barriers are present

---

[3] It has been shown in Section 2.3.2 that the exchange stiffness energy plays a minor role in micrometer sized elements.

which seperate the present magnetic state from other states with lower energy, then a change in sweep rate can affect the probability of the formation of one or the other state [161]. A similar concept can explain a skipping of intermediate states: if an intermediate state - such as the C- or S-state - only forms below a certain threshold field strength, then it is possible to skip this state by applying a bias field which is larger than the threshold field strength.

The previous statements apply primarily to the 10 and 20 nm thick elements. On the one hand because the nucleation field of the double vortex state of the thicker elements is usually larger than 80 Oe. On the other hand because $H_n$ is nearest to the theoretically possible maximum value (see Section 4.1.5) for devices where vortex nucleation occurs via buckling only - with an undulation number $n^* > 2$ - (primary 35 nm).

For the thicker CoFeB elements, a significant correlation between the occurrence and stability of the double vortex state and the applied bias fields was not observed. In some cases, the double vortex state was skipped, if a bias field was applied; in other cases the bias field seemed to induce the double vortex nucleation. For $t = 35$ and 50 nm, the standard deviation is larger for $H_{n,80\,\mathrm{Oe}}$ and $H_{n,0\,\mathrm{Oe}} > \sqrt{(H_{n,80\,\mathrm{Oe}})^2 + (80\,\mathrm{Oe})^2}$ (see Table 5.3). Therefore, it seems reasonable to conclude that the double vortex state is more often induced by the bias field, then it is skipped. Furthermore, it is logical that the $H_y$-induced reduction of coercivity, which is caused by the rotation of the magnetic field, only has a minor impact on elements where vortex nucleation occurs significantly before zero-crossing.

To summarize, a possible explanation of the observed bias field-induced positive $H_n$ shift was discussed: the reduction of the coercivity of intermediate pre-vortex states (configurational stability). A second explanation, the reduction of coercivity caused by the magneto-crystalline texture, is given in the next section. In Section 5.3.6 it is summarized which effects are relevant for the different materials and thicknesses.

### 5.3.3 Bias Fields and Magneto-Crystalline Anisotropy

Simulated hysteresis loops of polycrystalline disk elements with medium magneto-crystalline anisotropy are shown in Figure 5.16a and 5.16b. A reduction of coercivity and hysteresis is observed, similar to amorphous elements, which leads to an average positive $\Delta H_n$ in both cases. However, $\Delta H_n$ is considerably larger for the element with sloped edge due to the increased unbiased nucleation delay. Ultimately, both elements have the approximately same average $H_n$ at $H_y = 80$ Oe, which is below the experimental average $H_n$ of 22 Oe (see Table 5.3). This discrepancy can probably be attributed to thermal excitation in the experiment.

The two CoFe devices shown in Figure 5.16 illustrate again the large $H_n$ distribution. The spectrum of $\Delta H_n$ values is accordingly broad. The device shown in Figure 5.16c shows a comparably large delay of the vortex nucleation for $H_y = 0$. This delay is compensated by applying a bias field of $H_y = 80$ Oe. In contrast, a significantly earlier vortex nucleation

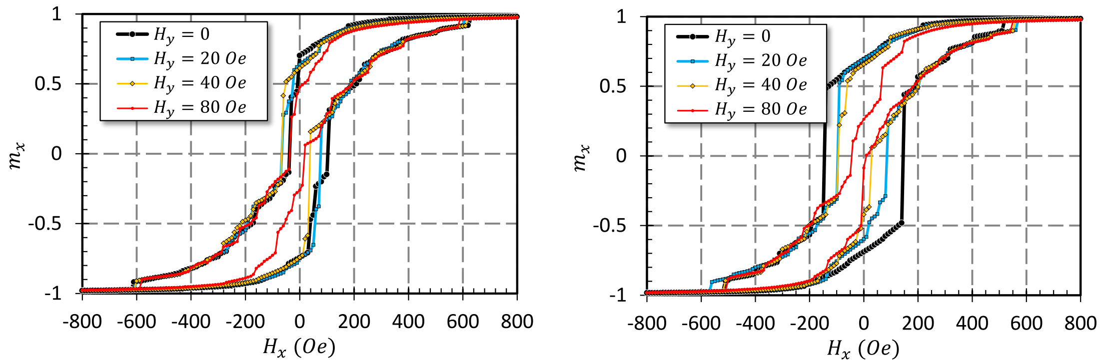

**(a)** Sim. - vertical edge

**(b)** Sim. - sloped edge

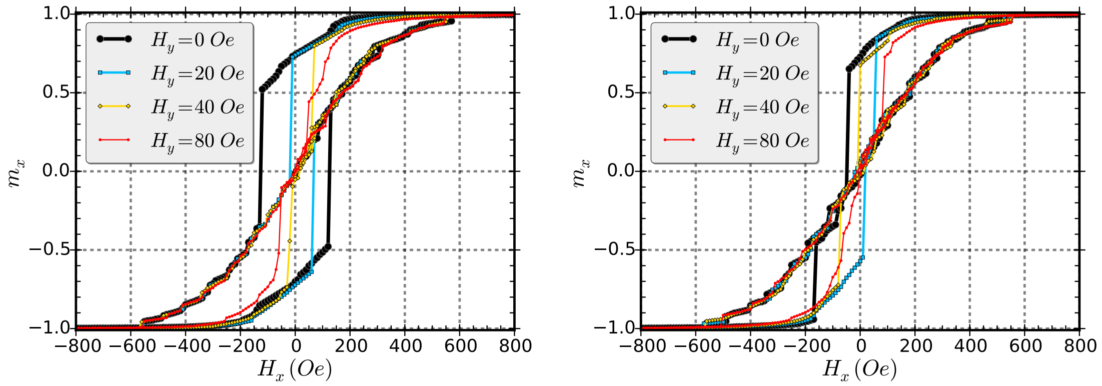

**(c)** Exp. - CoFe device No. 1

**(d)** Exp. - CoFe device No. 2

**Figure 5.16.** (a-b) Simulated hysteresis loops of disk structures ($d = 1.1\,\mu\text{m}$ and $t = 20\,\text{nm}$) with medium magneto-crystalline anisotropy for various bias field strengths ($H_y$). (b) A sloped edge with $\alpha = 53°$ was introduced (see Section 4.2.7). (c-d) Experimental TMR measurements on CoFe single disk devices ($d = 1.1\,\mu\text{m}$ and $t = 20\,\text{nm}$). Standard simulation parameters of CoFe are given in Section 3.3.

is observed in Figure 5.16d for the negative branch. This feature is reversed through a bias field, and simultaneously $H_{n+}$ and $H_{n-}$ become more symmetric. In summary, the various types of $H_n$ shift to a common average value lead to the balancing effect which has already been shown in Figure 5.11.

Additional simulations were performed at 100 nm small thin film elements to address the influence of the magneto-crystalline anisotropy and its interaction with $H_y$ in more detail. A circular shape was chosen in order to avoid any shape anisotropy and the in-plane cell size was below 0.9 nm to reduce the impact of edge and discretization effects (compared to 100 nm particle diameter). An average grain size of 20 nm proved to be reasonable (see Section 4.2.3).
Figure 5.17 shows the results for two elements, each with its own grain texture and its own random distribution of the in-plane anisotropy axes. As was to be expected, hystereses and coercivity fields increase with increasing anisotropy constant $K_1$ as shown in Figure 5.17a ("Coercivity mechanisms in hard magnetic materials" see [198]). Shape and characteristics of the hysteresis clearly varies for different elements (see Figure 5.17b)

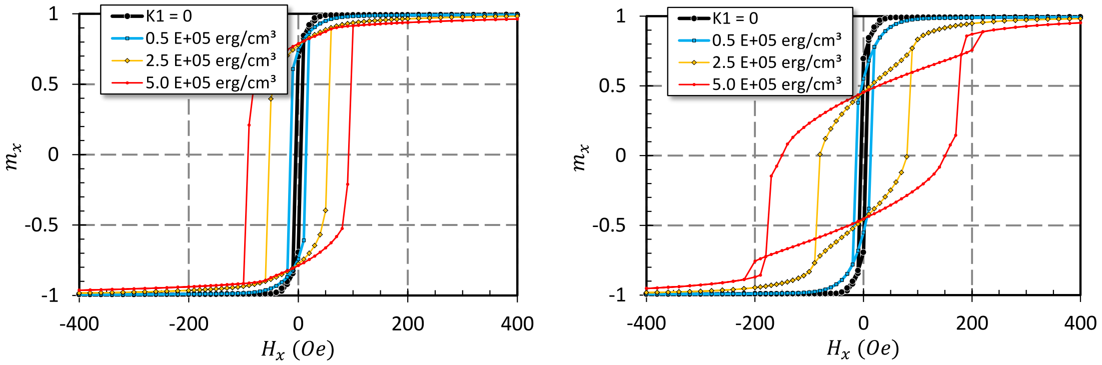

**(a)** Grain texture No. 1 - $H_y = 0$ **(b)** Grain texture No. 2 - $H_y = 0$

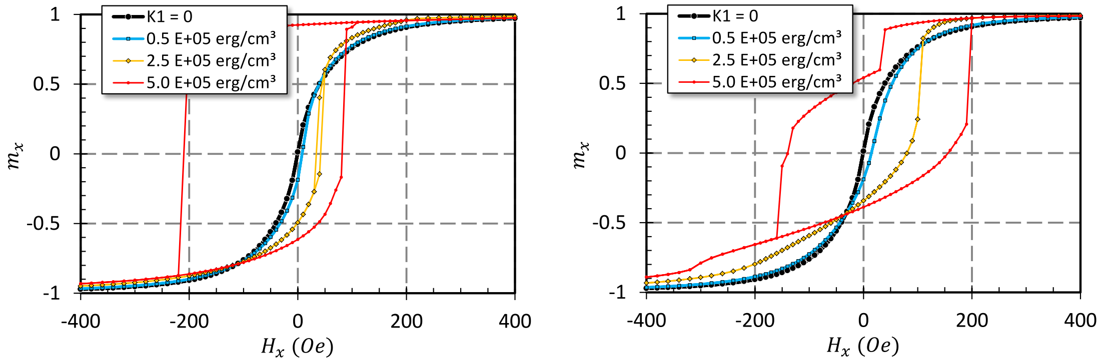

**(c)** Grain texture No. 1 - $H_y = 80\,\mathrm{Oe}$ **(d)** Grain texture No. 2 - $H_y = 80\,\mathrm{Oe}$

**Figure 5.17.** Simulated hysteresis loops of circular-shaped elements with 100 nm diameter, 2 nm thickness and a varying degree of the in-plane uniaxial magnetic anisotropy constant $K_1$. Results for two different, randomly generated grain textures are shown without $H_y$ bias field (a-b) and with an applied bias field of 80 Oe (c-d). Simulation parameters are as follows: $M_s = 1240\,\mathrm{emu/cm^3}$, $A = 1.53\,\mathrm{\mu erg/cm}$, in-plane edge length of the cells 8.4 Å and out-of-plane 2 nm.

since the number of grains is in the two-digit range. By applying a bias field of 80 Oe, the hysteresis is almost vanished for $K_1 \leqslant 2.5 \times 10^5\,\mathrm{erg/cm^3}$. At the same time, the switching field of the element becomes is shifted. The resulting offset is reversed if the sign of the bias field is changed (not shown). For $K_1 = 5 \times 10^5\,\mathrm{erg/cm^3}$ a bias field of 80 Oe is not sufficient to remove the hysteresis or to significantly reduce the coercivity field.

The results can be interpreted as follows. The applied bias fields can drastically reduce hysteresis of small grain clusters, which in turn should lead to a reduction of the coercivity of larger elements and thus facilitate vortex nucleation. Furthermore, the results shown in Figure 5.17 indicate that thermal excitation cannot be neglected in order to fully reproduce the influence of the applied bias fields since hysteresis can become even larger for $K_1 = 5 \times 10^5\,\mathrm{erg/cm^3}$ if a bias field is applied. Another possible conclusion is that $K_1$ is actually smaller for CoFe. In fact, a $K_1$ of $2.5 \times 10^5\,\mathrm{erg/cm^3}$ leads to a slightly increased $\Delta H_n$, but it also drastically reduces the characteristic mini-hysteretic jumps (not shown). Discrepancies may also be attributed to the grain structure as, for example, the grain size distribution may not be reproduced perfectly in the simulations. Such aspects have already been discussed in Section 4.2.3 since the $H_n$ distribution seems to be larger in the experiment. However, the precise quantification of the bias field-induced nucleation field shifts within simulations is beyond the scope of this work. For larger elements ($d = 1.1\,\mu\text{m}$, $t = 2\,\text{nm}$, $K_1 = 5 \times 10^5\,\text{erg/cm}^3$), maximum hysteresis (as a function of $H_x$) is drastically reduced - by approximately a factor of eight - when an 80 Oe bias field is applied (not shown). Such a large difference, compared to the small grain cluster simulations, is expected to be the result of an averaging out due to the much larger number of grains.

Similar hysteresis loops as shown in Figure 5.17, were measured for isotropic aligned Co nanowires by Fang et al. [199]. They also showed that a parallel alignment of the wires, with respect to the applied field, increases hysteresis, coercivity and remanence. The hysteresis loop becomes nearly rectangular, similar to the hysteresis loop of the unbiased ellipse, shown in Figure 5.14a. In contrast, a perpendicular alignment of the wires results in a significant reduction of hysteresis, coercivity, and remanence. Consequently, an anisotropic orientation of $K_1$ - in-plane and perpendicular to the magnetization of the reference system - should lead to a similar, positive $\Delta H_n$ as if a $H_y$ bias field is applied. Such an uniaxial alignment of $K_1$ may be realized, for example, during the deposition of the material. Furthermore, the shown bias field effect may be utilized by adding a magnetic biasing structure [197].

In summary, bias fields cause a significant reduction of coercivity for CoFe, which is linked to its magneto-crystalline structure. A third explanation, an increased number of possible vortex nucleation sites, will be discussed in the following section.

### 5.3.4 Wobbling Fields and Nucleation Sites

Davis et al. pointed out that there is a general difference between the nucleation and annihilation process in circular disk elements [166]: there is no breaking of symmetry during annihilation. The magnetic state, which will be present after the vortex has been annihilated, is known in advance. This does not apply for the nucleation process. Even if the pre-states may indicate the sense of rotation of the subsequently nucleating vortex state, the polarity of the vortex core is unpredictable. Supercooling is associated with the breaking of symmetry during the vortex nucleation. In this context, the term *supercooling* refers to the stability of the different buckling states, causing a delay of the first-order phase transition into the vortex state (see [113] about the different types of phase transitions in a ferromagnetic disk element). The amount of supercooling is influenced by intrinsic factors, such as the thickness of the element, but it also depends on extrinsic factors such as edge roughness as it was demonstrated in Section 4.2.11. The main author [166] primarily investigated superfluidity effects during his former career (see e.g. [200]). His approach led to an interdisciplinary transfer of knowledge about how surface effects affect nucleation and supercooling [184], and allowed to explain why the

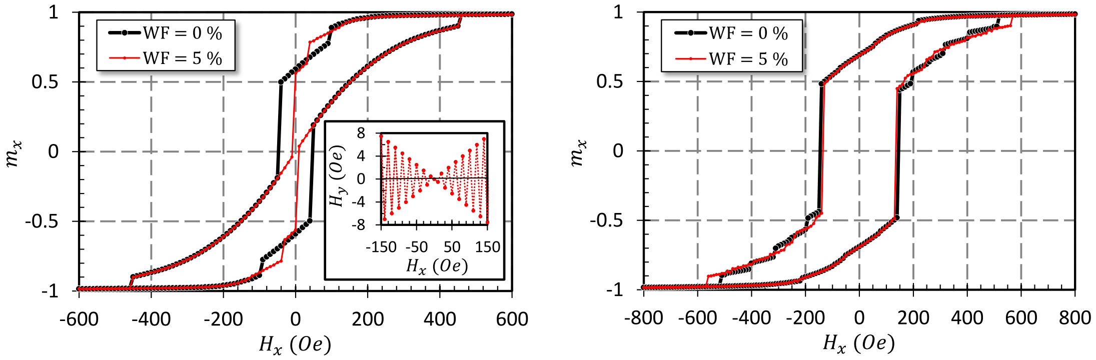

**(a)** Sim. CoFeB - $t = 20\,\mathrm{nm}$ **(b)** Sim. CoFe - $t = 20\,\mathrm{nm}$

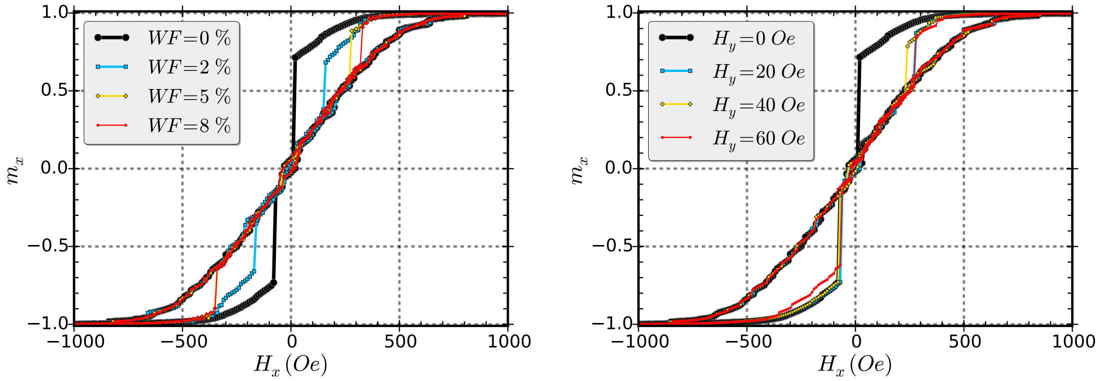

**(c)** Exp. CoFe - $t = 35\,\mathrm{nm}$ **(d)** Exp. CoFe - $t = 35\,\mathrm{nm}$

**Figure 5.18.** (a-b) Simulated hysteresis loops disk structures ($d = 1.1\,\mu\mathrm{m}$) in a wobbling magnetic field (WF): $H_x$ describes a usual hysteresis loop and $H_y$ changes its polarity every field step, whereas the ratio between $|H_y|$ and $|H_x|$ is kept constant. The inset in (a) is illustrating $H_y$ as a function of $H_x$ ($WF = 5\,\%$) for a small section of the applied field range. (c-d) Normalized TMR transfer curves of one $1.1\,\mu\mathrm{m}$ diameter CoFe single disk device for applied wobbling fields and bias fields. Simulation parameters of CoFeB are given in the caption of Figure 5.15 and of CoFe in the caption of Figure 5.16 (sloped edge), respectively.

supercooling effect can be overcome by a rotation of the applied field: in their setup - "nanotorsional resonator torque magnetometry" [201] - a small rotation of the bias field by 2° was causing a wobbling of the field. This in turn shifted the average $H_n$ to larger values. The given explanation was that the wobbling field constantly moves the buckling state and thus increases the number of possible vortex nucleation sites by 'smoothing' the edge of the disk (permalloy, $d = 1\,\mu\mathrm{m}$, $t = 42\,\mathrm{nm}$, crystalline grain roughness of approximately $5\,\mathrm{nm}$) [166].

This type of wobbling field measurement was repeated in simulation and experiment. The results are shown in Figure 5.18. An illustration of the applied wobbling field is given by the inset of Figure 5.18a. For 20 nm CoFeB a positive $\Delta H_n$ is observed (see Figure 5.18a). For 20 nm CoFe a negligible small shift of $H_n$ is observed (see Figure 5.18b). Consequently, the simulations indicate that the shift of the nucleation site can have a positive impact on the nucleation field, similar to the results reported by Davis et al. [166]. However, the coercivity caused by the magneto-crystallinity of the CoFe cannot be

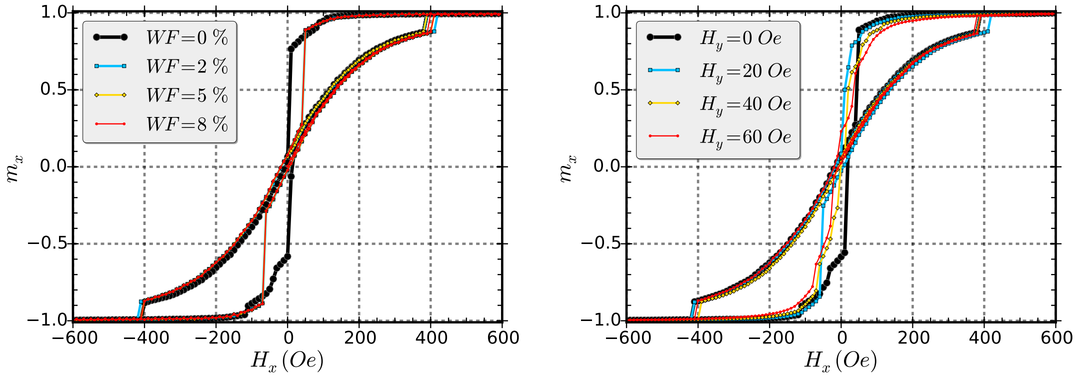

**(a)** CoFeB - device No. 1 **(b)** CoFeB - device No. 1

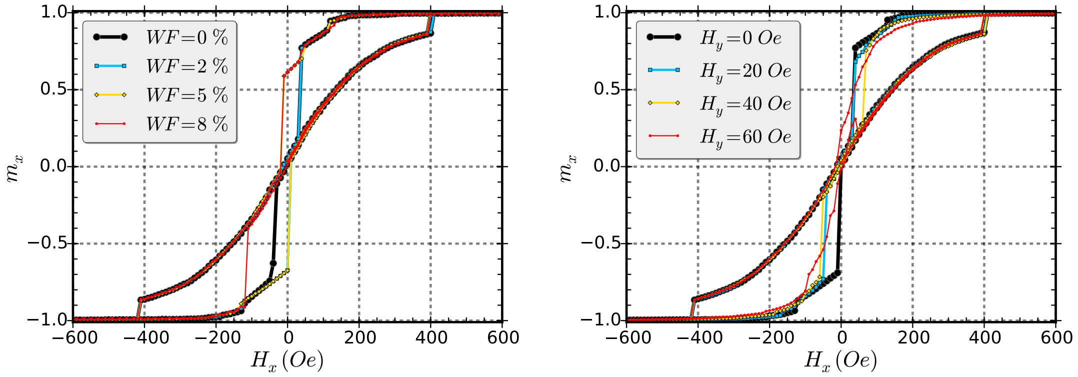

**(c)** CoFeB - device No. 2 **(d)** CoFeB - device No. 2

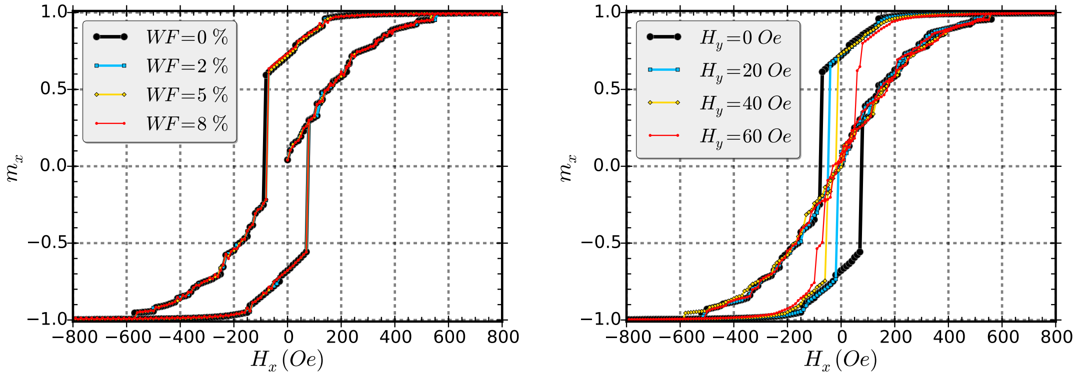

**(e)** CoFe - device No. 3 **(f)** CoFe - device No. 3

**Figure 5.19.** Normalized TMR transfer curves of single disk devices ($d = 1.1\,\mu\text{m}$ and $t = 20\,\text{nm}$) for wobbling fields (WF) and bias fields ($H_y$).

overcome by a wobbling field ($WF = 5\,\%$) for 20 nm disk thickness.

The picture changes drastically for an increased CoFe disk thickness. Figure 5.18c demonstrates how vortex nucleation is facilitated for an element where $H_n$ is initially delayed. The comparison with the measurement of the same element with applied bias fields, instead of a wobbling fields, shows that $\Delta H_n$ is even larger for the applied wobbling fields. Furthermore, the $H_y$ measurement shows an asymmetry regarding $H_n$, which is removed by the $WF$. This is expected to be a result of the asymmetric orientation of the magnetic field in the $H_y$ measurement, which covers only one 'hemisphere', in combination with the randomly distributed anisotropy axes of the CoFe grains. In contrast, the orientation of the magnetic field in the $WF$ measurement covers both hemispheres. Moreover, the $H_y$ component of the $WF$ is directly proportional to $H_x$ and thus becomes larger at larger $H_x$ fields.

It has to be noted that in almost any case where the unbiased $H_n$ was unusually large a negative $\Delta H_n$ was also observed in the $WF$ measurement. This observation coincides with the biasing experiment and allows to conclude that a rotation of the external field can also shift the nucleation site to 'unfavorable' locations.
Figure 5.19 shows experimental data of 20 nm thick disk elements measured with $WF$ and $H_y$. For device No. 1, shown in Figure 5.19a, a significant positive $\Delta H_n$ is observed for an applied $WF$. When $H_y$ is applied (Figure 5.19b), a positive $\Delta H_n$ is also observed but only for one of the two branches, namely for the branch with a delayed vortex nucleation at $H_y = 0$. In contrast, the other branch shows a negative $\Delta H_n$.
However, the wobbling field can also cause negative shifts as demonstrated by Figure 5.19c. In case of device No. 2, only for $WF = 8\,\%$ a significant positive $\Delta H_n$ is observed. It has to be noted that the positive branch shows jumps into intermediate states that seem to be independent of $WF$. It can therefore be concluded that the wobbling field cannot reduce the stability of such states (it can only prevent their formation by an early vortex nucleation). This is in sharp contrast to the bias field measurement, where the stability of such states is decreased as shown in Figure 5.19d.
The measurement of a 20 nm thick CoFe device shown in Figure 5.19e is almost identical to the simulated hysteresis loop shown in Figure 5.18b: $H_n$ is nearly unaffected by $WF$. This is in strong contrast to the bias field measurement of the same device shown in Figure 5.19f.
Other 20 nm thick CoFe devices with a less pronounced delay of the vortex nucleation showed a behavior similar to the CoFeB device shown in Figure 5.19a: widely varying positive and negative shifts of $H_n$ when applying a wobbling field.

In summary, the increasing number of possible vortex nucleation sites as a result of the rotating field plays an important role for $\Delta H_n$ of 35 and 50 nm thick CoFe. Also for 20 nm thick CoFeB, the wobbling field seems to affect $H_n$ in addition to the reduction of the configurational stability. The large positive average shift observed for the 20 nm thick CoFe seems to be mainly caused by the reduced coercivity of the polycrystalline grain structure and less caused by the shift of the vortex nucleation site.

### 5.3.5 Out-of-Plane Bias Fields

To complete the picture, the influence of out-of-plane bias fields is shown in Figure 5.20. It can be observed that for the 20 nm thick disk element $H_n$ is massively shifted by applying a sufficiently large $H_z$ field. A 'small' bias field of 80 Oe has barely any effect (compare

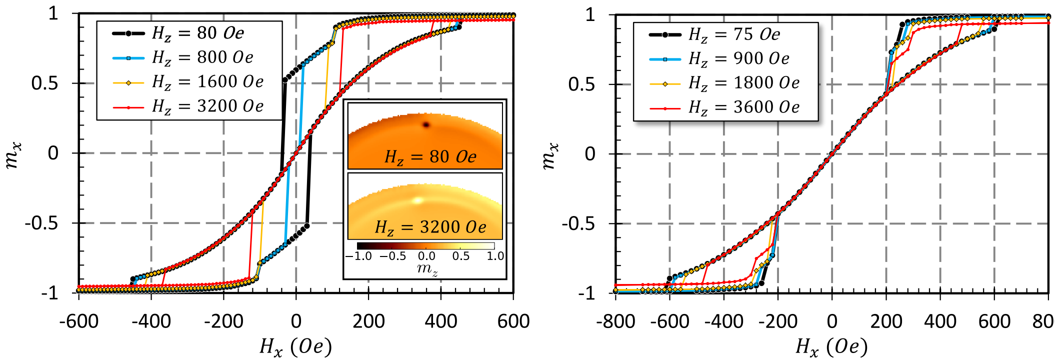

**(a)** $t = 20\,\text{nm}$ **(b)** $t = 35\,\text{nm}$

**Figure 5.20.** Simulated hysteresis loops of amorphous disk elements ($d = 1.1\,\mu\text{m}$) with magnetic properties similar to CoFeB. (a) The application of an out-of-plane bias field ($H_z$) facilitates vortex nucleation in case of 20 nm thickness. The inset shows detail sections (580 nm wide) of $m_z$ for the last simulation steps before annihilation. (b) For $t = 35\,\text{nm}$, $H_n$ is unaffected by $H_z$. Simulation parameters are as follows: $M_s = 1038\,\text{emu/cm}^3$, $A = 1.53\,\mu\text{erg/cm}$ and zero magneto-crystalline anisotropy. For (a) a sloped edge with $\alpha = 53°$ was applied, for (b) a magnetically disturbed edge of 15 nm.

with Figure 5.15a), but with increasing $H_z$, $H_n$ is shifted to an earlier nucleation. This observation allows the conclusion that $H_z$ helps to overcome the vortex nucleation energy barrier by introducing an out-of-plane magnetization at the edge and thus also helps the vortex core to enter the element (for more information about the energy landscape when the vortex core enters the element see [165]).

In case of a thicker element, the application of $H_z$ seems to have no impact on $H_n$ as shown in Figure 5.20b. It can therefore be concluded that for sufficiently thick elements the energy barrier for an out-of-plane rotation of the magnetization vanishes. This observation is consistent with the increasing out-of-plane magnetization of the saturated state as a function of thickness (at the edge of the disk), reported in Section 4.1.5 (see Figure 4.7): at approximately 35 nm, the trend of $|m_z|$ vs. thickness stagnates, indicating that an additionally applied $H_z$ bias field induces the out-of-plane magnetization for thinner elements which is required to facilitate vortex nucleation.

Finally, both elements show a decreasing $H_{an}$ with increasing $H_z$. This observation can be interpreted as follows: since $|H_z|$ is much larger than $|H_x|$, the orientation of the magnetic field is changed for both nucleation and annihilation. Furthermore, $H_z$ facilitates vortex nucleation by reducing the nucleation energy barrier. As a result, the annihilation energy barrier also must be reduced. The results shown agree with literature: Novais et al. investigated $H_{an}$ as a function of perpendicular anisotropy (PA) and showed that an increased PA leads to a decrease of $H_{an}$ [170]. Furthermore, they demonstrated that this effect is caused by a change of the vortex core profile which becomes elongated. This effect is illustrated by the inset in Figure 5.20a. These results indicate that rather the asymmetry of the elongated profile than the profile itself leads to the reduced $H_{an}$: for $H_z = 3200\,\text{Oe}$ the domain wall is closer to the element border on the right side.

### 5.3.6 Summary

It was demonstrated that in-plane bias fields, which are perpendicular to the field axis of the hysteresis loop, can significantly facilitate vortex nucleation. The main reasons for this are (1) the reduction of the coercivity caused by the magneto-crystalline anisotropy, (2) the reduction of the coercivity - or rather configurational stability - of intermediate pre-vortex states (excluding the double vortex state) and (3) the increased number of possible vortex nucleation sites. Depending on the material and thickness of the disk structures, different types of combinations of these effects can act. For 20 nm thick CoFe, reason No. (1) dominates the behavior and leads to the largest observed positive $\varDelta H_n$ (absolute and relative to $H_{an}$). Since vortex nucleation already occurs before zero-crossing for 35 and 50 nm thickness, the influence of reason No. (1) is reduced in these systems, but positive values of the average $\varDelta H_n$ are still observed for CoFe, which is mainly attributed to reason No. (3).

Reason No. (1) naturally does not play a role for the amorphous CoFeB. Consequently, the average $\varDelta H_n$ is much smaller and even negative if a bias field of $H_y = 80\,\mathrm{Oe}$ is applied. For smaller $H_y$, an average positive $\varDelta H_n$ is also observed for CoFeB. Furthermore, the highest correlation between $\varDelta H_n$ and the unbiased $H_n$ was observed for 20 nm CoFeB. This is because for these elements reason No. (2) - a reduction of the stability of C- and S-state - goes hand in hand with reason No. (3) - an increase of the nucleation site area due to the rotating field. Additionally, $H_y$ simply causes a delay of vortex nucleation. For thicker elements, reason No. (2) can be neglected since the formation and stability of the double vortex state seems to be unaffected by a rotating field. Furthermore, reason No. (3) has a drastically reduced impact for thicker CoFeB due to the amorphous edge, which does not retard the formation of a vortex core. This was demonstrated by its insensitivity to $H_z$ bias fields. Consequently, 35 and 50 nm thick CoFeB are nearly unaffected by $H_y$ while $H_n$ is slightly reduced (negative $\varDelta H_n$) due to the resulting increase of the absolute field strength.

# 6 Summary and Outlook

Different aspects of the vortex state, which are relevant for its application in an automotive sensor, were investigated. In the first part, the focus was set on the sensor geometry (diameter $d$ and thickness $t$), material (mainly $Co_{90}Fe_{10}$ and $Co_{60}Fe_{20}B_{20}$), and process influence (different edge effects). In the second part, external factors such as temperature and additional magnetic bias field were examined. In the following, the main results of the different parts are summarized which will be followed by the outlook.

It was observed experimentally that the universal scaling of the annihilation field ($H_{an}$) vs. disk **aspect ratio** is valid, as was to be expected. However, this scaling does not apply for the nucleation field ($H_n$): for 20 nm **thickness**, $H_n$ was independent of the **diameter**. Micro-magnetic simulations confirmed this observation and showed that below a CoFeB thickness of 35 nm the out-of-plane magnetization ($m_z$) at the edge of the disk is reduced which has the following consequences: (1) The suppressed out-of-plane magnetization acts as an energy barrier for vortex nucleation and (2) the stray field energy ($E_{\mathrm{demag}}$) of the saturated state shows a non-linear trend when it is plotted vs. $t$, with low gradient around 20 nm. The observed effect may be of interest regarding the improvement of existing analytical vortex models.
A phase diagram of the pre-vortex states was extracted from micro-magnetic simulations and compared with experimental data. It was shown that for a micrometer-sized CoFeB disk structure the following nucleation modes occur: for a thickness of 10 nm, vortex nucleation occurs via the C- or S-state, which form via first-order phase transitions. For 20 nm, vortex nucleation occurs almost exclusively via the S-state. For 35 nm, the lowest rate of first-order phase transitions into intermediate states was observed and for 50 nm, about one half of the disks showed a first-order phase transition into the double vortex (DV) state and no S-state formation was observed. It was experimentally proven that a first-order phase transition into an intermediate state delays vortex nucleation on average. In addition, micro-magnetic simulations showed that during the formation of the DV state the undulation number of the previous buckling pattern specifies the DV buckling pattern: an even undulation number remains even, and an uneven undulation number remains uneven. But this rule does not apply for buckling to buckling transitions. Finally, for $d = 400$ nm and $t = 50$ nm simulations showed that vortex nucleation occurs directly out of the saturated state.

**Material** parameters were determined by fitting simulated hysteresis loops iteratively to experimental data. It was shown that a good approach to determine the saturation magnetization ($M_s$) is to fit the shape of the hysteresis loop instead of the vortex critical fields. Crystalline properties of the investigated CoFe were also estimated by comparison with micro-magnetic simulations. However, this method is limited because of multiple variables, such as orientation and strength of magneto-crystalline anisotropy, grain size and grain size distribution. Therefore, an exact determination of the material parameters requires further experimental investigations. Nevertheless, it was demonstrated that the magneto-crystalline anisotropy of CoFe (1) leads to a delayed vortex nucleation, (2) causes mini-hysteretic effects which allow to determine whether a change of the direction of rotation of the vortex state occurred, (3) increases the stability of the DV state drastically and (4) can lead to the formation of multiple vortex states with more than two, randomly distributed vortex cores. Factor (3) and (4) can cause crossed/negative hysteresis even after field reversal and even for $t = 50\,\mathrm{nm}$ and are consequently a potential blocking point for the use of CoFe.

Different factors of the process were investigated which affect the edge of the disk structures. Micro-magnetic simulations showed that a magnetic weakening of the edge drastically reduces $H_{an}$ by destabilizing the vortex core when approaching the edge. In a similar manner, a sloped edge reduces $H_{an}$. Both effects explain why $H_{an}$ of CoFeB was smaller than expected. Transmission electron microscopy images confirmed the presence of a sloped edge, but the slope was less pronounced than simulations suggested. Simulations showed that both edge effects affect $H_{an}$ of CoFe significantly less due to the dominant influence of the magneto-crystalline anisotropy, but they can cause a massive reduction of $H_n$, which fits the experimental observations. Consequently, both edge effects appear to be present in both material systems. In addition, the experimentally observed CoFe annihilation jumps suggest that the TMR signal does not include information about the free layer magnetization of a small part of the edge. Finally, the influence of the edge roughness explains the $H_n$ distribution of the amorphous CoFeB, and simulations indicate a reduced influence of roughness for larger thickness.

The investigation of critical fields as a function of **temperature** ($T$) showed for individual elements that both types of nucleation field shifts ($\mathit{\Delta} H_n$) - positive and negative ones - can be observed at elevated $T$. The type of shift depends on which factor dominates either temperature-induced reduction of $M_s$ or thermally assisted energy barrier jumps. Furthermore, the disk thickness determined whether or not a high correlation between $\mathit{\Delta} H_n$ and $H_n$ was observed in the statistic of one wafer which results from the thickness-dependent metastable pre-states and thus the highest correlation was observed for $t = 35\,\mathrm{nm}$, where vortex nucleation occurs most frequently without any additional first-order phase transition. For both materials - CoFe and CoFeB - the average $\mathit{\Delta} H_n$ of one wafer was positive for $20\,\mathrm{nm}$ thickness. This observation can be attributed to the fact that $E_{\mathrm{demag}}$, which is proportional to $M_s$, of the saturated state has almost no influence on $H_n$ in this thickness range. Consequently, thermally assisted energy barrier jumps determine the type of nucleation field shift.

In contrast, it was observed that the trend line of $\mathit{\Delta} H_{an}$ vs. $H_{an}$ gets steeper with increasing $t$. This allowed the conclusion that for 20 nm disk thickness $H_{an}$ vs. $T$ is mainly affected by the $M_s(T)$ dependence whereas for thicker elements thermally assisted energy barrier jumps become more important. Average CoFeB values of $\varDelta H_{an}$ vs. $t$ confirm this conclusion. For CoFe, an increase of $H_{an}$ was sometimes observed at elevated $T$. This observation is expected to be linked to an energetically preferred, more stable direction of rotation of the vortex state, which is accessible with higher probability at higher $T$.

It was demonstrated in experiment and in simulation that in-plane $H_y$ **bias fields** (perpendicular to the magnetization of the reference layer) can facilitate vortex nucleation significantly. Three reasons for positive shifts were found, which contribute differently, depending on the choice of material and thickness: (1) reduction of the coercivity, caused by the magneto-crystalline anisotropy, (2) reduction of the coercivity, caused by the configurational stability and (3) an increased number of possible vortex nucleation sites. The following statements can be made: factor (1) dominates $\varDelta H_n$ of 20 nm CoFe and causes the largest observed positive average $\varDelta H_n$: when applying a bias field of $H_y = 80\,\mathrm{Oe}$ an average shift of $\varDelta H_n \approx 80\,\mathrm{Oe}$ was observed. For 35 and 50 nm thick CoFe the observed shifts were still positive but smaller and can be mainly attributed to factor (3).
For CoFeB, positive average shifts were not observed when applying a bias field of 80 Oe (a smaller $H_y$ also caused average positive shifts), but for $t = 20\,\mathrm{nm}$ the highest correlation between $\varDelta H_n$ and the unbiased $H_n$ was observed, which can be attributed to factor (2) and (3), and to the fact that the applied bias field simply increases the absolute field and thus delays vortex nucleation with respect to $H_x$. For thicker CoFeB, the correlation of $\varDelta H_n$ vs. $H_n$ was drastically reduced. Finally, simulations for 20 nm CoFeB showed a strong increase of $H_n$ when applying out-of-plane bias fields ($H_z$) in the range of thousands of Oersted, whereas for 35 nm no impact of $H_z$ on $H_n$ was found. This observation is consistent with the observed trend of $m_z$ vs. thickness at the edge of the disk of the saturated state.

In the following, a brief outlook of research aspects is given which are related to the vortex state. Further investigations are required regarding the trend of the critical fields for larger thicknesses and smaller diameters including the trend of $E_{\mathrm{demag}}$ vs. $t$ for the saturated state as well as for the vortex state. The influence of the exchange stiffness energy will additionally become important for smaller diameters and cannot be neglected. It could be of interest to continue the phase diagram for $t > 100\,\mathrm{nm}$. The exact determination of the CoFe material parameters requires additional experimental investigations. Furthermore, it will be important to know whether crossed or negative hysteresis of CoFe is still present for a thickness above 50 nm. Experimental investigations are required to prove or disprove the presence of a magnetically disturbed edge. Additionally, the origin of the electrically inactive edge of CoFe requires more experimental research. A direct experimental proof has not been accomplished yet whether for CoFe a preferred direction of rotation of the vortex state is available with increasing temperature. Further investigations are also required regarding (1) the influence of temperature on the magneto-crystalline anisotropy and susceptibility of CoFe and (2) the $T$-influence on the critical fields of materials with lower Curie temperature, such as NiFe. Finally, the patterning process of the edge is particularly crucial due to the large influence on the magnetic behavior of micro- and nanometer-sized elements. Therefore, variations of the patterning process are expected to cause tremendous changes in the vortex hysteresis loop.

This work demonstrated experimentally the feasibility of a TMR vortex sensor. Sensor elements were manufactured which showed nearly zero hysteresis and an easily adjustable linear range of hundreds of Oersted. Still, it is crucial to choose an appropriate layout with sufficiently large free layer thickness, the smallest possible diameter and a material with negligibly small magneto-crystalline anisotropy, for example, CoFeB. Furthermore, it was shown that the nucleation field of the vortex state - a key parameter that defines the operating range - is quite robust against changes in temperature. In addition, the vortex sensor showed superior robustness against magnetic disturbance fields. Therefore, the sensor concept should meet the requirements of automotive applications.

# List of Publications

- Magnetic sensor device and method for a magnetic sensor device having a magneto-resistive structure.
  W. Raberg and T. Wurft.
  *Patent (US, JP, CN, DE) US20170168122A1* (2015)
- Magnetic sensor device and method for a magnetic sensor device having a magneto-resistive structure.
  A. Bachleitner-Hofmann, H. Brückl, K. Prügl, W. Raberg, A. Satz, D. Suess, and T. Wurft.
  *Patent (US, CN, DE) US20170227613A1* (2016)
- The Influence of Edge Inhomogeneities on Vortex Hysteresis Curves in Magnetic Tunnel Junctions.
  T. Wurft, W. Raberg, K. Prügl, A. Satz, G. Reiss, and H. Brückl.
  *IEEE Transactions on Magnetics,* **53** (11) 1-5, DOI: *10.1109/TMAG.2017.2715072* (2017)
- Considering non-uniform current distributions in magnetoresistive sensor designs and their implications for the resistance transfer function.
  A. Bachleitner-Hofmann, C. Abert, H. Brückl, A. Satz, T. Wurft, W. Raberg, K. Prügl, and D. Suess.
  *arXiv ID: 1709.06394* (2017)

# Bibliography

[1] G. Rieger, K. Ludwig, J. Hauch, and W. Clemens. GMR sensors for contactless position detection. *Sensors and Actuators A: Physical*, 91(1-2):7–11, jun 2001. ISSN 09244247. doi: 10.1016/S0924-4247(01)00480-0. URL `http://linkinghub.elsevier.com/retrieve/pii/S0924424701004800`.

[2] C.P.O Treutler. Magnetic sensors for automotive applications. *Sensors and Actuators A: Physical*, 91(1-2):2–6, jun 2001. ISSN 09244247. doi: 10.1016/S0924-4247(01)00621-5. URL `http://linkinghub.elsevier.com/retrieve/pii/S0924424701006215`.

[3] C. Giebeler, D.J. Adelerhof, A.E.T. Kuiper, J.B.A. van Zon, D. Oelgeschläger, and G. Schulz. Robust GMR sensors for angle detection and rotation speed sensing. *Sensors and Actuators A: Physical*, 91(1-2):16–20, jun 2001. ISSN 09244247. doi: 10.1016/S0924-4247(01)00510-6. URL `http://linkinghub.elsevier.com/retrieve/pii/S0924424701005106`.

[4] Konrad Kapser and James Sterling. Integrated GMR based Wheel Speed Sensor for Automotive Applications. In *2007 IEEE Sensors*, pages 848–851. IEEE, 2007. ISBN 978-1-4244-1261-7. doi: 10.1109/ICSENS.2007.4388534. URL `http://ieeexplore.ieee.org/document/4388534/`.

[5] Mitra Djamal and Ramli. Development of Sensors Based on Giant Magnetoresistance Material. *Procedia Engineering*, 32:60–68, 2012. ISSN 18777058. doi: 10.1016/j.proeng.2012.01.1237. URL `http://linkinghub.elsevier.com/retrieve/pii/S1877705812012684`.

[6] Lisa Jogschies, Daniel Klaas, Rahel Kruppe, Johannes Rittinger, Piriya Taptimthong, Anja Wienecke, Lutz Rissing, and Marc Wurz. Recent Developments of Magnetoresistive Sensors for Industrial Applications. *Sensors*, 15(11): 28665–28689, nov 2015. ISSN 1424-8220. doi: 10.3390/s151128665. URL `http://www.mdpi.com/1424-8220/15/11/28665`.

[7] Infineon. Sensing the world (accessed 2018-08-09), 2016. URL `www.infineon.com/dgdl/Sensor_Solutions_BR-2016.pdf?fileId=5546d461590352c501591664f5d40037`.

[8] E. H. Hall. On a New Action of the Magnet on Electric Currents. *American Journal of Mathematics*, 2(3):287, sep 1879. ISSN 00029327. doi: 10.2307/2369245. URL `https://www.jstor.org/stable/2369245?origin=crossref`.

[9] G. Binasch, P. Grünberg, F. Saurenbach, and W. Zinn. Enhanced magnetoresistance in layered magnetic structures with antiferromagnetic interlayer exchange. *Physical Review B*, 39(7):4828–4830, mar 1989. ISSN 0163-1829. doi: 10.1103/PhysRevB.39.4828. URL `https://link.aps.org/doi/10.1103/PhysRevB.39.4828`.

[10] M. N. Baibich, J. M. Broto, A. Fert, F. Nguyen Van Dau, F. Petroff, P. Etienne, G. Creuzet, A. Friederich, and J. Chazelas. Giant Magnetoresistance of (001)Fe/(001)Cr Magnetic Superlattices. *Physical Review Letters*, 61(21):2472–2475, nov 1988. ISSN 0031-9007. doi: 10.1103/PhysRevLett.61.2472. URL `https://link.aps.org/doi/10.1103/PhysRevLett.61.2472`.

[11] Atsufumi Hirohata and Koki Takanashi. Future perspectives for spintronic devices. *Journal of Physics D: Applied Physics*, 47(19):193001, may 2014. ISSN 0022-3727. doi: 10.1088/0022-3727/47/19/193001. URL `http://stacks.iop.org/0022-3727/47/i=19/a=193001?key=crossref.8252e6ac12d7f896edd39b0ab0dd37f8`.

[12] W. Thomson. On the Electro-Dynamic Qualities of Metals:–Effects of Magnetization on the Electric Conductivity of Nickel and of Iron. *Proceedings of the Royal Society of London*, 8(0):546–550, jan 1856. ISSN 0370-1662. doi: 10.1098/rspl.1856.0144. URL `http://rspl.royalsocietypublishing.org/cgi/doi/10.1098/rspl.1856.0144`.

[13] M. Julliere. Tunneling between ferromagnetic films. *Physics Letters A*, 54(3):225–226, sep 1975. ISSN 03759601. doi: 10.1016/0375-9601(75)90174-7. URL `http://linkinghub.elsevier.com/retrieve/pii/0375960175901747`.

[14] S Ikeda, J Hayakawa, Y Ashizawa, Y M Lee, K Miura, H Hasegawa, M Tsunoda, F Matsukura, and H. Ohno. Tunnel magnetoresistance of 604 percent at 300K by suppression of Ta diffusion in CoFeB/MgO/CoFeB pseudo-spin-valves annealed at high temperature. *Applied Physics Letters*, 93(8):082508, aug 2008. ISSN 0003-6951. doi: 10.1063/1.2976435. URL `http://aip.scitation.org/doi/10.1063/1.2976435`.

[15] Christophe Duret and Shintarou Ueno. TMR: A New Frontier for Magnetic Sensing. *NTN Technical Review*, 80(80):64–71, 2012. URL `https://www.ntnglobal.com/en/products/review/pdf/NTN_TR80_en_064_071p.pdf`.

[16] TMR Angle Sensor TAS series (accessed 2018-08-11), 2017. URL `https://product.tdk.com/info/en/catalog/datasheets/sensor_angle-tmr-angle_en.pdf`.

[17] Magnetic Field Sensors (accessed 2018-08-11). URL `http://www.dowaytech.com/en/sensor/magnetic_field_sensors.html`.

[18] TA900 sensor family (accessed 2018-08-11). URL `https://www.sensitec.com/products-solutions/angle-and-length-measurement/ta900-sensor-family`.

[19] Digital TMR Rotation/Speed Sensor Crocus (accessed 2018-08-11). URL `https://crocus-technology.com/digital-tmr-rotation-speed-sensor/`.

[20] Juergen Zimmer, Armin Satz, Wolfgang Raberg, Hubert Brückl, and Dieter Suess. Device, magnetic sensor device and method. *U.S. Patent*, US20150185, dec 2013. URL `https://patents.google.com/patent/US20150185297`.

[21] B. Dieny, V. S. Speriosu, S. S. P. Parkin, B. A. Gurney, D. R. Wilhoit, and D. Mauri. Giant magnetoresistive in soft ferromagnetic multilayers. *Physical Review B*, 43 (1):1297–1300, jan 1991. ISSN 0163-1829. doi: 10.1103/PhysRevB.43.1297. URL `https://link.aps.org/doi/10.1103/PhysRevB.43.1297`.

[22] MarÍa Dolores Cubells-Beltran, Candid Reig, Diego RamÍrez Munoz, Susana Isabel Pinheiro Cardoso de Freitas, and Paulo Jorge Peixeiro de Freitas. Full Wheatstone Bridge Spin-Valve Based Sensors for IC Currents Monitoring. *IEEE Sensors Journal*, 9(12):1756–1762, dec 2009. ISSN 1530-437X. doi: 10.1109/JSEN.2009.2030880. URL `http://ieeexplore.ieee.org/document/5291977/`.

[23] Antonio Lopes, Susana Cardoso, Ricardo Ferreira, Elvira Paz, Francis L. Deepak, Jaime Sanchez, Diego Ramirez, Sergio I. Ravelo, and Paulo P. Freitas. MgO Magnetic Tunnel Junction Electrical Current Sensor With Integrated Ru Thermal Sensor. *IEEE Transactions on Magnetics*, 49(7):3866–3869, jul 2013. ISSN 0018-9464. doi: 10.1109/TMAG.2013.2246550. URL `http://ieeexplore.ieee.org/document/6558990/`.

[24] Dexin Wang, Jay Brown, Tim Hazelton, and Jim Daughton. 360 Degree Angle Sensor Using Spin Valve Materials With SAF Structure. *IEEE Transactions on Magnetics*, 41(10):3700–3702, oct 2005. ISSN 0018-9464. doi: 10.1109/TMAG.2005.854806. URL `http://ieeexplore.ieee.org/document/1519416/`.

[25] Ana V. Silva, Diana C. Leitao, João Valadeiro, José Amaral, Paulo P. Freitas, and Susana Cardoso. Linearization strategies for high sensitivity magnetoresistive sensors. *The European Physical Journal Applied Physics*, 72(1):10601, oct 2015. ISSN 1286-0042. doi: 10.1051/epjap/2015150214. URL `http://www.epjap.org/10.1051/epjap/2015150214`.

[26] Enrique García Vidal, Diego Ramírez Muñoz, Sergio Iván Ravelo Arias, Jaime Sánchez Moreno, Susana Cardoso, Ricardo Ferreira, and Paulo Freitas. Electronic Energy Meter Based on a Tunnel Magnetoresistive Effect (TMR) Current Sensor. *Materials*, 10(10):1134, sep 2017. ISSN 1996-1944. doi: 10.3390/ma10101134. URL `http://www.mdpi.com/1996-1944/10/10/1134`.

[27] K. Yu Guslienko, V. Novosad, Y. Otani, H. Shima, and K. Fukamichi. Field evolution of magnetic vortex state in ferromagnetic disks. *Applied Physics Letters*,

78(24):3848–3850, jun 2001. ISSN 0003-6951. doi: 10.1063/1.1377850. URL `http://aip.scitation.org/doi/10.1063/1.1377850`.

[28] Dieter Suess, Anton Bachleitner-Hofmann, Armin Satz, Herbert Weitensfelder, Christoph Vogler, Florian Bruckner, Claas Abert, Klemens Prügl, Jürgen Zimmer, Christian Huber, Sebastian Luber, Wolfgang Raberg, Thomas Schrefl, and Hubert Brückl. Topologically Protected Vortex Structures to Realize Low-Noise Magnetic Sensors. *arXiv*, dec 2017. URL `http://arxiv.org/abs/1712.07061`.

[29] Continental Automotive - Wheel Speed Sensor (accessed 2018-08-13). URL `https://www.continental-automotive.com/en-gl/Passenger-Cars/Chassis-Safety/Integrated-Safety/Wheel-Speed-Sensor`.

[30] N.A. Usov and S.E. Peschany. Magnetization curling in a fine cylindrical particle. *Journal of Magnetism and Magnetic Materials*, 118(3):L290–L294, jan 1993. ISSN 03048853. doi: 10.1016/0304-8853(93)90428-5. URL `http://linkinghub.elsevier.com/retrieve/pii/0304885393904285`.

[31] L. Landau and E. Lifshits. ON THE THEORY OF THE DISPERSION OF MAGNETIC PERMEABILITY IN FERROMAGNETIC BODIES. *Collected Papers of L.D. Landau*, 59(2):101–114, dec 1965. doi: 10.1016/B978-0-08-010586-4.50023-7. URL `https://doi.org/10.1016/B978-0-08-010586-4.50023-7`.

[32] Charles Kittel. Physical Theory of Ferromagnetic Domains. *Reviews of Modern Physics*, 21(4):541–583, oct 1949. ISSN 0034-6861. doi: 10.1103/RevModPhys.21.541. URL `https://link.aps.org/doi/10.1103/RevModPhys.21.541`.

[33] Charles Kittel. Theory of the Structure of Ferromagnetic Domains in Films and Small Particles. *Physical Review*, 70(11-12):965–971, dec 1946. ISSN 0031-899X. doi: 10.1103/PhysRev.70.965. URL `https://link.aps.org/doi/10.1103/PhysRev.70.965`.

[34] H. A. M. van den Berg. Self consistent domain theory in soft ferromagnetic media. I. Solenoidal distributions in elliptical thin film elements. *Journal of Applied Physics*, 57(6):2168–2173, mar 1985. ISSN 0021-8979. doi: 10.1063/1.334357. URL `http://aip.scitation.org/doi/10.1063/1.334357`.

[35] H A M van den Berg. Domain structures in soft ferromagnetic thin film objects (invited). *Journal of Applied Physics*, 61(8):4194–4199, apr 1987. ISSN 0021-8979. doi: 10.1063/1.338474. URL `http://aip.scitation.org/doi/10.1063/1.338474`.

[36] Alex Hubert and Rudolf Schäfer. *Magnetic Domains*, volume 3. Springer Berlin Heidelberg, Berlin, Heidelberg, feb 1998. ISBN 978-3-540-64108-7. doi: 10.1007/978-3-540-85054-0. URL `http://link.springer.com/10.1007/978-3-540-85054-0`.

[37] E. H. Frei, S. Shtrikman, and D. Treves. Critical Size and Nucleation Field of Ideal Ferromagnetic Particles. *Physical Review*, 106(3):446–455, may 1957. ISSN 0031-899X. doi: 10.1103/PhysRev.106.446. URL `https://link.aps.org/doi/10.1103/PhysRev.106.446`.

[38] William Fuller Brown. Rigorous approach to the theory of ferromagnetic microstructure. *Journal of Applied Physics*, 29(3):470–471, mar 1958. ISSN 00218979. doi: 10.1063/1.1723183. URL `http://aip.scitation.org/doi/10.1063/1.1723183`.

[39] Amikam Aharoni. Magnetostatics of curling in a finite cylinder. *Journal of Applied Physics*, 68(1):255–258, jul 1990. ISSN 0021-8979. doi: 10.1063/1.347125. URL `http://aip.scitation.org/doi/10.1063/1.347125`.

[40] A. Aharoni. Magnetization Curling. *physica status solidi (b)*, 16(1):3–42, 1966. ISSN 03701972. doi: 10.1002/pssb.19660160102. URL `http://onlinelibrary.wiley.com/doi/10.1002/pssb.v16:1/issuetoc`.

[41] I. Eisenstein and A. Aharoni. Magnetization curling in a sphere. *Journal of Applied Physics*, 47(1):321–328, jan 1976. ISSN 0021-8979. doi: 10.1063/1.322318. URL `http://aip.scitation.org/doi/10.1063/1.322318`.

[42] Amikam Aharoni. Angular dependence of nucleation field in magnetic recording particles. *IEEE Transactions on Magnetics*, 22(3):149–150, may 1986. ISSN 0018-9464. doi: 10.1109/TMAG.1986.1064292. URL `http://ieeexplore.ieee.org/document/1064292/`.

[43] A. Aharoni and S. Shtrikman. Magnetization Curve of the Infinite Cylinder. *Physical Review*, 109(5):1522–1528, mar 1958. ISSN 0031-899X. doi: 10.1103/PhysRev.109.1522. URL `https://link.aps.org/doi/10.1103/PhysRev.109.1522`.

[44] Manfred Rührig, Wolfgang Bartsch, Michael Vieth, and Alex Hubert. Elementary magnetization processes in a low-anisotropy circular thin film disk. *IEEE Transactions on Magnetics*, 26(5):2807–2809, 1990. ISSN 00189464. doi: 10.1109/20.104882. URL `http://ieeexplore.ieee.org/document/104882/`.

[45] R. M. H. New. Physical and magnetic properties of submicron lithographically patterned magnetic islands. *Journal of Vacuum Science and Technology B: Microelectronics and Nanometer Structures and Technology B: Microelectronics and Nanometer Structures*, 13(3):1089, may 1995. ISSN 0734211X. doi: 10.1116/1.587908. URL `http://avs.scitation.org/doi/abs/10.1116/1.587908`.

[46] W. Wernsdorfer, K. Hasselbach, A. Sulpice, A. Benoit, J.-E. Wegrowe, L. Thomas, B. Barbara, and D. Mailly. Dynamical measurement of domain-wall nucleation and annihilation in individual amorphous Co particles. *Physical Review B*, 53 (6):3341–3347, feb 1996. ISSN 0163-1829. doi: 10.1103/PhysRevB.53.3341. URL `https://link.aps.org/doi/10.1103/PhysRevB.53.3341`.

[47] K Runge, Y Nozaki, Y Otani, H Miyajima, B Pannetier, T Matsuda, and A Tonomura. High-resolution observation of magnetization processes in 2 $\mu$m x 2 $\mu$m x 0.04 $\mu$m permalloy particles. *Journal of Applied Physics*, 79(8):5075, 1996. ISSN 00218979. doi: 10.1063/1.361921. URL `http://scitation.aip.org/content/aip/journal/jap/79/8/10.1063/1.361921`.

[48] Michel Hehn, Kamel Ounadjela, Jean-pierre Bucher, Françoise Rousseaux, Dominique Decanini, Bernard Bartenlian, Claude Chappert, Michel Hehn, Kamel Ounadjela, Jean-pierre Bucher, Frangoise Rousseaux, Dominique Decanini, Bernard Bartenlian, and Claude Chappert. Nanoscale Magnetic Domains in Mesoscopic Magnets. *Science*, 272(5269):1782–1785, 1996. URL `http://www.jstor.org/stable/2889324`.

[49] A Fernandez, M.R Gibbons, M.a Wall, and C.J Cerjan. Magnetic domain structure and magnetization reversal in submicron-scale Co dots. *Journal of Magnetism and Magnetic Materials*, 190(1-2):71–80, dec 1998. ISSN 03048853. doi: 10.1016/S0304-8853(98)00267-4. URL `http://linkinghub.elsevier.com/retrieve/pii/S0304885398002674`.

[50] Chris Pike and Andres Fernandez. An investigation of magnetic reversal in submicron-scale Co dots using first order reversal curve diagrams. *Journal of Applied Physics*, 85(9):6668–6676, may 1999. ISSN 0021-8979. doi: 10.1063/1.370177. URL `http://aip.scitation.org/doi/10.1063/1.370177`.

[51] R. E. Dunin-Borkowski, M. R. McCartney, B. Kardynal, and David J. Smith. Magnetic interactions within patterned cobalt nanostructures using off-axis electron holography. *Journal of Applied Physics*, 84(1):374–378, jul 1998. ISSN 0021-8979. doi: 10.1063/1.368038. URL `http://aip.scitation.org/doi/10.1063/1.368038`.

[52] R. P. Cowburn, D. K. Koltsov, A. O. Adeyeye, M. E. Welland, and D. M. Tricker. Single-Domain Circular Nanomagnets. *Physical Review Letters*, 83(5):1042–1045, aug 1999. ISSN 0031-9007. doi: 10.1103/PhysRevLett.83.1042. URL `https://link.aps.org/doi/10.1103/PhysRevLett.83.1042`.

[53] A. Fernandez and C. J. Cerjan. Nucleation and annihilation of magnetic vortices in submicron-scale Co dots. *Journal of Applied Physics*, 87(3):1395–1401, feb 2000. ISSN 0021-8979. doi: 10.1063/1.372026. URL `http://aip.scitation.org/doi/10.1063/1.372026`.

[54] Jing Shi, S. Tehrani, and M. R. Scheinfein. Geometry dependence of magnetization vortices in patterned submicron NiFe elements. *Applied Physics Letters*, 76(18):2588–2590, may 2000. ISSN 0003-6951. doi: 10.1063/1.126417. URL `http://aip.scitation.org/doi/10.1063/1.126417`.

[55] Taras Pokhil, Dian Song, and Janusz Nowak. Spin vortex states and hysteretic properties of submicron size NiFe elements. *Journal of Applied Physics*, 87(9): 6319–6321, 2000. ISSN 0021-8979. doi: 10.1063/1.372692. URL `http://aip.scitation.org/doi/10.1063/1.372692`.

[56] T. Shinjo, T. Okuno, R. Hassdorf, K. Shigeto, and T. Ono. Magnetic Vortex Core Observation in Circular Dots of Permalloy. *Science*, 289(5481):930–932, aug 2000. ISSN 00368075. doi: 10.1126/science.289.5481.930. URL `http://www.sciencemag.org/cgi/doi/10.1126/science.289.5481.930`.

[57] M. Schneider, H. Hoffmann, and J. Zweck. Lorentz microscopy of circular ferromagnetic permalloy nanodisks. *Applied Physics Letters*, 77(18):2909–2911, oct 2000. ISSN 0003-6951. doi: 10.1063/1.1320465. URL `http://aip.scitation.org/doi/10.1063/1.1320465`.

[58] J. Raabe, R. Pulwey, R. Sattler, T. Schweinboeck, J. Zweck, and D. Weiss. Magnetization pattern of ferromagnetic nanodisks. *Journal of Applied Physics*, 88(7):4437, 2000. ISSN 00218979. doi: 10.1063/1.1289216. URL `http://scitation.aip.org/content/aip/journal/jap/88/7/10.1063/1.1289216`.

[59] V. Novosad, K.Yu. Guslienko, H. Shima, Y. Otani, K. Fukamichi, N. Kikuchi, O. Kitakami, and Y. Shimada. Nucleation and annihilation of magnetic vortices in sub-micron permalloy dots. *IEEE Transactions on Magnetics*, 37(4):2088–2090, jul 2001. ISSN 00189464. doi: 10.1109/20.951062. URL `http://ieeexplore.ieee.org/document/951062/`.

[60] Ralph Pulwey, Michael Rahm, Josef Biberger, and Dieter Weiss. Switching behavior of vortex structures in nanodisks. *IEEE Transactions on Magnetics*, 37(4):2076–2078, jul 2001. ISSN 00189464. doi: 10.1109/20.951058. URL `http://ieeexplore.ieee.org/document/951058/`.

[61] I. L. Prejbeanu, M. Natali, L. D. Buda, U. Ebels, A. Lebib, Y. Chen, and K. Ounadjela. In-plane reversal mechanisms in circular Co dots. *Journal of Applied Physics*, 91(10):7343, 2002. ISSN 00218979. doi: 10.1063/1.1456041. URL `http://scitation.aip.org/content/aip/journal/jap/91/10/10.1063/1.1456041`.

[62] S.P. Li, M. Natali, A. Lebib, A. Pépin, Y. Chen, and Y.B. Xu. Magnetic nanostructure fabrication by soft lithography and vortex-single domain transition in Co dots. *Journal of Magnetism and Magnetic Materials*, 241(2-3):447–452, mar 2002. ISSN 03048853. doi: 10.1016/S0304-8853(01)00441-3. URL `http://linkinghub.elsevier.com/retrieve/pii/S0304885301004413`.

[63] J Miltat and A Thiaville. Ferromagnetism: Vortex Cores-Smaller Than Small. *Science*, 298(5593):555–555, oct 2002. ISSN 00368075. doi: 10.1126/science.1077704. URL `http://www.sciencemag.org/cgi/doi/10.1126/science.1077704`.

[64] M. Schneider, H. Hoffmann, S. Otto, Th Haug, and J. Zweck. Stability of magnetic vortices in flat submicron permalloy cylinders. *Journal of Applied Physics*, 92 (3):1466–1472, aug 2002. ISSN 0021-8979. doi: 10.1063/1.1490623. URL `http://aip.scitation.org/doi/10.1063/1.1490623`.

[65] A Wachowiak, J Wiebe, M Bode, O Pietzsch, M Morgenstern, and R Wiesendanger. Direct observation of internal spin structure of magnetic vortex cores. *Science (New York, N.Y.)*, 298(5593):577–80, oct 2002. ISSN 1095-9203. doi: 10.1126/science.1075302. URL `http://www.ncbi.nlm.nih.gov/pubmed/12386329`.

[66] M. Rahm, M. Schneider, J. Biberger, R. Pulwey, J. Zweck, D. Weiss, and V. Umansky. Vortex nucleation in submicrometer ferromagnetic disks. *Applied Physics Letters*, 82(23):4110–4112, jun 2003. ISSN 0003-6951. doi: 10.1063/1.1581363. URL `http://aip.scitation.org/doi/10.1063/1.1581363`.

[67] Konstantin Yu. Guslienko and Konstantin L. Metlov. Evolution and stability of a magnetic vortex in a small cylindrical ferromagnetic particle under applied field. *Physical Review B*, 63(10):100403, feb 2001. ISSN 0163-1829. doi: 10.1103/PhysRevB.63.100403. URL `https://link.aps.org/doi/10.1103/PhysRevB.63.100403`.

[68] K. Yu Guslienko, V. Novosad, Y. Otani, H. Shima, and K. Fukamichi. Magnetization reversal due to vortex nucleation, displacement, and annihilation in submicron ferromagnetic dot arrays. *Physical Review B*, 65(2):024414, dec 2001. ISSN 0163-1829. doi: 10.1103/PhysRevB.65.024414. URL `https://link.aps.org/doi/10.1103/PhysRevB.65.024414`.

[69] K. J. Kirk, S. McVitie, J. N. Chapman, and C. D W Wilkinson. Imaging magnetic domain structure in sub-500 nm thin film elements. *Journal of Applied Physics*, 89(11):7174–7176, jun 2001. ISSN 0021-8979. doi: 10.1063/1.1355336. URL `http://aip.scitation.org/doi/10.1063/1.1355336`.

[70] R. P. Cowburn and M. E. Welland. Phase transitions in planar magnetic nanostructures. *Applied Physics Letters*, 72(16):2041–2043, apr 1998. ISSN 0003-6951. doi: 10.1063/1.121258. URL `http://aip.scitation.org/doi/10.1063/1.121258`.

[71] R. P. Cowburn. Property variation with shape in magnetic nanoelements. *Journal of Physics D: Applied Physics*, 33(1):R1–R16, jan 2000. ISSN 0022-3727. doi: 10.1088/0022-3727/33/1/201. URL `http://stacks.iop.org/0022-3727/33/i=1/a=201?key=crossref.942fbeebd7d4e6304f3dc38fb4c690eb`.

[72] Riccardo Hertel. Thickness dependence of magnetization structures in thin Permalloy rectangles. *Zeitschrift für Metallkunde*, 93(10):957–962, oct 2002. ISSN 0044-3093. doi: 10.3139/146.020957. URL `http://www.hanser-elibrary.com/doi/abs/10.3139/146.020957`.

[73] K. J. Kirk, S. McVitie, A. R. Long, and E. Skuras. Magnetization of Co elements sensed by semiconductor transport magnetometry and transmission electron microscopy. *Journal of Applied Physics*, 93(10):7906–7908, may 2003. ISSN 0021-8979. doi: 10.1063/1.1557825. URL `http://aip.scitation.org/doi/10.1063/1.1557825`.

[74] E. R. P. Novais and A. P. Guimarães. Phase diagram of magnetic configurations for soft magnetic nanodots of circular and elliptical shape obtained by micromagnetic simulation. pages 1–8, sep 2009. URL `http://arxiv.org/abs/0909.5686`.

[75] Wen Zhang, Rohit Singh, Noah Bray-Ali, and Stephan Haas. Scaling analysis and application: Phase diagram of magnetic nanorings and elliptical nanoparticles. *Physical Review B*, 77(14):144428, apr 2008. ISSN 1098-0121. doi: 10.1103/PhysRevB.77.144428. URL `https://link.aps.org/doi/10.1103/PhysRevB.77.144428`.

[76] Kuo-Ming Wu, Lance Horng, Jia-Feng Wang, Jong-Ching Wu, Yin-Hao Wu, and Ching-Ming Lee. Influence of asymmetry on vortex nucleation and annihilation in submicroscaled permalloy disk array. *Applied Physics Letters*, 92(26):262507, jun 2008. ISSN 0003-6951. doi: 10.1063/1.2946495. URL `http://aip.scitation.org/doi/10.1063/1.2946495`.

[77] Randy K Dumas, Thomas Gredig, Chang-Peng Li, Ivan K Schuller, and Kai Liu. Angular dependence of vortex-annihilation fields in asymmetric cobalt dots. *Physical Review B*, 80(1):014416, jul 2009. ISSN 1098-0121. doi: 10.1103/PhysRevB.80.014416. URL `https://link.aps.org/doi/10.1103/PhysRevB.80.014416`.

[78] Randy K Dumas, Dustin A Gilbert, Nasim Eibagi, and Kai Liu. Chirality control via double vortices in asymmetric Co dots. *Physical Review B*, 83(6):060415, feb 2011. ISSN 1098-0121. doi: 10.1103/PhysRevB.83.060415. URL `https://link.aps.org/doi/10.1103/PhysRevB.83.060415`.

[79] Chao-Hsien Huang, Kuo-Ming Wu, Jong-Ching Wu, and Lance Horng. Vortex annihilation in magnetic disks with different degrees of asymmetry. *Journal of Applied Physics*, 113(10):103905, mar 2013. ISSN 0021-8979. doi: 10.1063/1.4795115. URL `http://aip.scitation.org/doi/10.1063/1.4795115`.

[80] Sebastia Agramunt-Puig, Nuria Del-Valle, Carles Navau, and Alvaro Sanchez. Controlling vortex chirality and polarity by geometry in magnetic nanodots. *Applied Physics Letters*, 104(1):012407, jan 2014. ISSN 0003-6951. doi: 10.1063/1.4861423. URL `http://aip.scitation.org/doi/10.1063/1.4861423`.

[81] M. Huber, J. Zweck, and D. Weiss. Experimental observation of switching in ferromagnetic nanoscale double disks. *Physical Review B*, 77(5):054407, feb 2008. ISSN 1098-0121. doi: 10.1103/PhysRevB.77.054407. URL `https://link.aps.org/doi/10.1103/PhysRevB.77.054407`.

[82] W. Jung, F. J. Castaño, and C. A. Ross. Current-in-plane magnetoresistance of spin valve elliptical rings. *Applied Physics Letters*, 91(15):152508, oct 2007. ISSN 0003-6951. doi: 10.1063/1.2798495. URL `http://aip.scitation.org/doi/10.1063/1.2798495`.

[83] S. Jain and A. O. Adeyeye. Magnetoresistance behavior of elliptical ring nanomagnets in close proximity with magnetic elements. *Journal of Applied Physics*, 105(7):07E904, apr 2009. ISSN 0021-8979. doi: 10.1063/1.3072753. URL `http://aip.scitation.org/doi/10.1063/1.3072753`.

[84] Chao Hsien Huang, Nian Jia Cheng, Feng Sheng Wu, Jong Ching Wu, and Lance Horng. Study of Vortex Configuration and Switching Behavior in Submicro-Scaled Asymmetric Permalloy Ring. *IEEE Transactions on Magnetics*, 48(11):3648–3650, nov 2012. ISSN 0018-9464. doi: 10.1109/TMAG.2012.2204044. URL `http://ieeexplore.ieee.org/document/6332748/`.

[85] Jaroslav Tóbik, Vladimír Cambel, and Goran Karapetrov. Dynamics of vortex nucleation in nanomagnets with broken symmetry. *Physical Review B*, 86(13):134433, oct 2012. ISSN 1098-0121. doi: 10.1103/PhysRevB.86.134433. URL `https://link.aps.org/doi/10.1103/PhysRevB.86.134433`.

[86] T. Ščepka, T. Polakovič, J. Šoltýs, J. Tóbik, M. Kulich, R. Kúdela, J. Dérer, and V. Cambel. Individual vortex nucleation/annihilation in ferromagnetic nanodots with broken symmetry observed by micro-Hall magnetometry. *AIP Advances*, 5(11):117205, nov 2015. ISSN 2158-3226. doi: 10.1063/1.4935437. URL `http://aip.scitation.org/doi/10.1063/1.4935437`.

[87] Jaroslav Tóbik, Vladimir Cambel, and Goran Karapetrov. Asymmetry in Time Evolution of Magnetization in Magnetic Nanostructures. *Scientific Reports*, 5(1):12301, dec 2015. ISSN 2045-2322. doi: 10.1038/srep12301. URL `http://www.nature.com/articles/srep12301`.

[88] J. Sort, A. Hoffmann, S.-H. Chung, K. S. Buchanan, M. Grimsditch, M. D. Baró, B. Dieny, and J. Nogués. Magnetization Reversal in Submicron Disks: Exchange Biased Vortices. *Physical Review Letters*, 95(6):067201, aug 2005. ISSN 0031-9007. doi: 10.1103/PhysRevLett.95.067201. URL `https://link.aps.org/doi/10.1103/PhysRevLett.95.067201`.

[89] Zhi-Pan Li, Oleg Petracic, Johannes Eisenmenger, and Ivan K. Schuller. Reversal behavior of exchange-biased submicron dots. *Applied Physics Letters*, 86(7):072501, 2005. ISSN 00036951. doi: 10.1063/1.1863449. URL `http://scitation.aip.org/content/aip/journal/apl/86/7/10.1063/1.1863449`.

[90] J. Sort, G. Salazar-Alvarez, M. D. Baró, B. Dieny, A. Hoffmann, V. Novosad, and J. Nogués. Controlling magnetic vortices through exchange bias. *Applied Physics*

*Letters*, 88(4):042502, jan 2006. ISSN 0003-6951. doi: 10.1063/1.2165290. URL `http://aip.scitation.org/doi/10.1063/1.2165290`.

[91] Dustin A. Gilbert, Li Ye, Aïda Varea, Sebastià Agramunt-Puig, Nuria del Valle, Carles Navau, José Francisco López-Barbera, Kristen S. Buchanan, Axel Hoffmann, Alvar Sánchez, Jordi Sort, Kai Liu, and Josep Nogués. A new reversal mode in exchange coupled antiferromagnetic/ferromagnetic disks: distorted viscous vortex. *Nanoscale*, 7(21):9878–9885, 2015. ISSN 2040-3364. doi: 10.1039/C5NR01856K. URL `http://xlink.rsc.org/?DOI=C5NR01856K`.

[92] M. Tanase, A. K. Petford-Long, O. Heinonen, K. S. Buchanan, J. Sort, and J. Nogués. Magnetization reversal in circularly exchange-biased ferromagnetic disks. *Physical Review B*, 79(1):014436, jan 2009. ISSN 1098-0121. doi: 10.1103/PhysRevB.79.014436. URL `https://link.aps.org/doi/10.1103/PhysRevB.79.014436`.

[93] G. Salazar-Alvarez, J. J. Kavich, J. Sort, A. Mugarza, S. Stepanow, A. Potenza, H. Marchetto, S. S. Dhesi, V. Baltz, B. Dieny, A. Weber, L. J. Heyderman, J. Nogués, and P. Gambardella. Direct evidence of imprinted vortex states in the antiferromagnet of exchange biased microdisks. *Applied Physics Letters*, 95(1):012510, jul 2009. ISSN 0003-6951. doi: 10.1063/1.3168515. URL `http://aip.scitation.org/doi/10.1063/1.3168515`.

[94] K. Yu Guslienko, B. A. Ivanov, V. Novosad, Y. Otani, H. Shima, and K. Fukamichi. Eigenfrequencies of vortex state excitations in magnetic submicron-size disks. *Journal of Applied Physics*, 91(10):8037, 2002. ISSN 00218979. doi: 10.1063/1.1450816. URL `http://scitation.aip.org/content/aip/journal/jap/91/10/10.1063/1.1450816`.

[95] S.-B. Choe. Vortex Core-Driven Magnetization Dynamics. *Science*, 304(5669): 420–422, apr 2004. ISSN 0036-8075. doi: 10.1126/science.1095068. URL `http://www.sciencemag.org/cgi/doi/10.1126/science.1095068`.

[96] K Yu Guslienko, X F Han, D J Keavney, R Divan, and S D Bader. Magnetic Vortex Core Dynamics in Cylindrical Ferromagnetic Dots. *Physical Review Letters*, 96(6): 067205, feb 2006. ISSN 0031-9007. doi: 10.1103/PhysRevLett.96.067205. URL `https://link.aps.org/doi/10.1103/PhysRevLett.96.067205`.

[97] V Novosad, F Y Fradin, P E Roy, K. S. Buchanan, K Yu Guslienko, and S D Bader. Magnetic vortex resonance in patterned ferromagnetic dots. *Physical Review B - Condensed Matter and Materials Physics*, 72(2):024455, mar 2005. ISSN 10980121. doi: 10.1103/PhysRevB.72.024455. URL `https://link.aps.org/doi/10.1103/PhysRevB.72.024455`.

[98] Keisuke Yamada, Shinya Kasai, Yoshinobu Nakatani, Kensuke Kobayashi, Hiroshi Kohno, André Thiaville, and Teruo Ono. Electrical switching of the vortex core in

a magnetic disk. *Nature Materials*, 6(4):270–273, apr 2007. ISSN 1476-1122. doi: 10.1038/nmat1867. URL `http://www.nature.com/articles/nmat1867`.

[99] Manu Sushruth, Jasper P. Fried, Abdelmadjid Anane, Stephane Xavier, Cyrile Deranlot, Mikhail Kostylev, Vincent Cros, and Peter J. Metaxas. Electrical measurement of magnetic-field-impeded polarity switching of a ferromagnetic vortex core. *Physical Review B*, 94(10):100402, sep 2016. ISSN 2469-9950. doi: 10.1103/PhysRevB.94.100402. URL `https://link.aps.org/doi/10.1103/PhysRevB.94.100402`.

[100] K. Nakano, D. Chiba, N. Ohshima, S. Kasai, T. Sato, Y. Nakatani, K. Sekiguchi, K. Kobayashi, and T. Ono. All-electrical operation of magnetic vortex core memory cell. *Applied Physics Letters*, 99(26):262505, dec 2011. ISSN 0003-6951. doi: 10.1063/1.3673303. URL `http://aip.scitation.org/doi/10.1063/1.3673303`.

[101] Kunihiro Nakano, Kenji Tanabe, Ryo Hiramatsu, Daichi Chiba, Norikazu Ohshima, Shinya Kasai, Tomonori Sato, Yoshinobu Nakatani, Koji Sekiguchi, Kensuke Kobayashi, and Teruo Ono. Real-time observation of electrical vortex core switching. *Applied Physics Letters*, 102(7):072405, feb 2013. ISSN 0003-6951. doi: 10.1063/1.4793212. URL `http://aip.scitation.org/doi/10.1063/1.4793212`.

[102] Young-Sang Yu, Hyunsung Jung, Ki-Suk Lee, Peter Fischer, and Sang-Koog Kim. Memory-bit selection and recording by rotating fields in vortex-core cross-point architecture. *Applied Physics Letters*, 98(5):052507, jan 2011. ISSN 0003-6951. doi: 10.1063/1.3551524. URL `http://aip.scitation.org/doi/10.1063/1.3551524`.

[103] K. Kuepper, M. Buess, J. Raabe, C. Quitmann, and J. Fassbender. Dynamic Vortex-Antivortex Interaction in a Single Cross-Tie Wall. *Physical Review Letters*, 99(16):167202, oct 2007. ISSN 0031-9007. doi: 10.1103/PhysRevLett.99.167202. URL `https://link.aps.org/doi/10.1103/PhysRevLett.99.167202`.

[104] Jun Ichiro Ohe, Stewart E. Barnes, Hyun Woo Lee, and Sadamichi Maekawa. Electrical measurements of the polarization in a moving magnetic vortex. *Applied Physics Letters*, 95(12):123110, sep 2009. ISSN 00036951. doi: 10.1063/1.3237166. URL `http://aip.scitation.org/doi/10.1063/1.3237166`.

[105] A. S. Jenkins, E. Grimaldi, P. Bortolotti, R. Lebrun, H. Kubota, K. Yakushiji, A. Fukushima, G. de Loubens, O. Klein, S. Yuasa, and V. Cros. Controlling the chirality and polarity of vortices in magnetic tunnel junctions. *Applied Physics Letters*, 105(17):172403, oct 2014. ISSN 0003-6951. doi: 10.1063/1.4900743. URL `http://aip.scitation.org/doi/10.1063/1.4900743`.

[106] Hyunsung Jung, Youn-Seok Choi, Ki-Suk Lee, Dong-Soo Han, Young-Sang Yu, Mi-Young Im, Peter Fischer, and Sang-Koog Kim. Logic Operations Based on Magnetic-Vortex-State Networks. *ACS Nano*, 6(5):3712–3717, may 2012. ISSN 1936-0851. doi: 10.1021/nn3000143. URL `http://pubs.acs.org/doi/10.1021/nn3000143`.

[107] Norinobu Hasegawa, Satoshi Sugimoto, Hiroaki Fujimori, Kouta Kondou, Yasuhiro Niimi, and Yoshichika Otani. Selective mode excitation in three-chained magnetic vortices. *Applied Physics Express*, 8(6):063005, jun 2015. ISSN 1882-0778. doi: 10.7567/APEX.8.063005. URL `http://stacks.iop.org/1882-0786/8/i=6/a=063005?key=crossref.cc2adad80b1cff8de80ad9da9da4f859`.

[108] J. F. Pulecio, P. Warnicke, S. D. Pollard, D. A. Arena, and Y. Zhu. Coherence and modality of driven interlayer-coupled magnetic vortices. *Nature Communications*, 5:1–8, apr 2014. ISSN 2041-1723. doi: 10.1038/ncomms4760. URL `http://www.nature.com/doifinder/10.1038/ncomms4760`.

[109] X Liu, M. M. Steiner, R Sooryakumar, G. A. Prinz, R. F. C. Farrow, and G. Harp. Exchange stiffness, magnetization, and spin waves in cubic and hexagonal phases of cobalt. *Physical Review B*, 53(18):12166–12172, may 1996. ISSN 0163-1829. doi: 10.1103/PhysRevB.53.12166. URL `https://link.aps.org/doi/10.1103/PhysRevB.53.12166`.

[110] Jaehun Cho, Jinyong Jung, Shin-Yong Cho, and Chun-Yeol You. Effect of annealing temperature on exchange stiffness of CoFeB thin films. *Journal of Magnetism and Magnetic Materials*, 395:18–22, dec 2015. ISSN 03048853. doi: 10.1016/j.jmmm.2015.06.073. URL `http://linkinghub.elsevier.com/retrieve/pii/S0304885315302833`.

[111] J.A.J. Burgess, J.E. Losby, and M.R. Freeman. An analytical model for vortex core pinning in a micromagnetic disk. *Journal of Magnetism and Magnetic Materials*, 361:140–149, jun 2014. ISSN 03048853. doi: 10.1016/j.jmmm.2014.02.078. URL `http://linkinghub.elsevier.com/retrieve/pii/S0304885314001991`.

[112] Konstantin L. Metlov and Konstantin Yu Guslienko. Stability of magnetic vortex in soft magnetic nano-sized circular cylinder. *Journal of Magnetism and Magnetic Materials*, 242-245:1015–1017, apr 2002. ISSN 03048853. doi: 10.1016/S0304-8853(01)01360-9. URL `http://linkinghub.elsevier.com/retrieve/pii/S0304885301013609`.

[113] Sergey Savel'ev and Franco Nori. Magnetic and mechanical buckling: Modified Landau theory approach to study phase transitions in micromagnetic disks and compressed rods. *Physical Review B*, 70(21):214415, dec 2004. ISSN 1098-0121. doi: 10.1103/PhysRevB.70.214415. URL `https://link.aps.org/doi/10.1103/PhysRevB.70.214415`.

[114] K Yu Guslienko. Magnetic Vortex State Stability, Reversal and Dynamics in Restricted Geometries. *Journal of Nanoscience and Nanotechnology*, 8(6):2745–2760, jun 2008. ISSN 1533-4880. doi: 10.1166/jnn.2008.003. URL `http://www.ingentaconnect.com/content/10.1166/jnn.2008.003`.

[115] J. A J Burgess, D. C. Fortin, J. E. Losby, D. Grombacher, J. P. Davis, and M. R. Freeman. Thermally activated decay of magnetic vortices. *Physical Review B*, 82 (14):144403, oct 2010. ISSN 1098-0121. doi: 10.1103/PhysRevB.82.144403. URL `https://link.aps.org/doi/10.1103/PhysRevB.82.144403`.

[116] T. Kimura, Y. Otani, and J. Hamrle. Determination of magnetic vortex chirality using lateral spin-valve geometry. *Applied Physics Letters*, 87(17):172506, oct 2005. ISSN 0003-6951. doi: 10.1063/1.2120911. URL `http://aip.scitation.org/doi/10.1063/1.2120911`.

[117] Anton Bachleitner-Hofmann, Hubert Brückl, Klemens Prügl, Wolfgang Raberg, Armin Satz, Dieter Suess, and Tobias Wurft. Magnetic sensor device and method for a magnetic sensor device having a magneto-resistive structure. *U.S. Patent*, dec 2016. URL `https://patents.google.com/patent/US20170227613A1`.

[118] Anton Bachleitner-Hofmann, Claas Abert, Hubert Brückl, Armin Satz, Tobias Wurft, Wolfgang Raberg, Klemens Prügl, and Dieter Suess. Considering non-uniform current distributions in magnetoresistive sensor designs and their implications for the resistance transfer function. *arXiv*, sep 2017. URL `http://arxiv.org/abs/1709.06394`.

[119] F Oyster. Two-current model for parallel and anti-parallel alignment of the magnetizations (accessed 2018-08-02), 2014. URL `https://en.wikipedia.org/wiki/Tunnel_magnetoresistance#/media/File:TunnelSchema_TMR.svg`.

[120] J F Gregg, I Petej, E Jouguelet, and C Dennis. Spin electronics a review. *Journal of Physics D: Applied Physics*, 35(18):R121–R155, sep 2002. ISSN 0022-3727. doi: 10.1088/0022-3727/35/18/201. URL `http://stacks.iop.org/0022-3727/35/i=18/a=201?key=crossref.4304df46f7cad601ee53146d7613308d`.

[121] Stuart S. P. Parkin, Christian Kaiser, Alex Panchula, Philip M. Rice, Brian Hughes, Mahesh Samant, and See-Hun Yang. Giant tunnelling magnetoresistance at room temperature with MgO (100) tunnel barriers. *Nature Materials*, 3(12):862–867, dec 2004. ISSN 1476-1122. doi: 10.1038/nmat1256. URL `http://www.nature.com/articles/nmat1256`.

[122] A. Thomas, H. Brückl, M. D. Sacher, J. Schmalhorst, and G. Reiss. Aluminum oxidation by a remote electron cyclotron resonance plasma in magnetic tunnel junctions. *Journal of Vacuum Science and Technology B: Microelectronics and Nanometer Structures*, 21(5):2120, 2003. ISSN 0734211X. doi: 10.1116/1.1609480. URL `http://scitation.aip.org/content/avs/journal/jvstb/21/5/10.1116/1.1609480`.

[123] Dexin Wang, Cathy Nordman, J.M. Daughton, Zhenghong Qian, Jonathon Fink, Dexin Wang, Cathy Nordman, J.M. Daughton, Zhenghong Qian, and Jonathon Fink. 70Free and Reference Layers. *IEEE Transactions on Magnetics*, 40(4):

2269–2271, jul 2004. ISSN 0018-9464. doi: 10.1109/TMAG.2004.830219. URL `http://ieeexplore.ieee.org/document/1325474/`.

[124] W. H. Butler, X.-G. Zhang, T. C. Schulthess, and J. M. MacLaren. Spin-dependent tunneling conductance of Fe|MgO|Fe sandwiches. *Physical Review B*, 63(5):054416, jan 2001. ISSN 0163-1829. doi: 10.1103/PhysRevB.63.054416. URL `https://link.aps.org/doi/10.1103/PhysRevB.63.054416`.

[125] X.-G. Zhang and W. H. Butler. Large magnetoresistance in bcc Co / MgO / Co and FeCo / MgO / FeCo tunnel junctions. *Physical Review B*, 70(17):172407, nov 2004. ISSN 1098-0121. doi: 10.1103/PhysRevB.70.172407. URL `https://link.aps.org/doi/10.1103/PhysRevB.70.172407`.

[126] S. Yuasa and D. D. Djayaprawira. Giant tunnel magnetoresistance in magnetic tunnel junctions with a crystalline MgO(0 0 1) barrier. *Journal of Physics D: Applied Physics*, 40(21):R337–R354, nov 2007. ISSN 0022-3727. doi: 10.1088/0022-3727/40/21/R01. URL `http://stacks.iop.org/0022-3727/40/i=21/a=R01?key=crossref.5e4ad43797a155e306a576b1744a6d26`.

[127] William H Butler. Tunneling magnetoresistance from a symmetry filtering effect. *Science and Technology of Advanced Materials*, 9(1):014106, jan 2008. ISSN 1468-6996. doi: 10.1088/1468-6996/9/1/014106. URL `http://www.tandfonline.com/doi/full/10.1088/1468-6996/9/1/014106`.

[128] Shinji Yuasa, Yoshishige Suzuki, Toshikazu Katayama, and Koji Ando. Characterization of growth and crystallization processes in CoFeB/MgO/CoFeB magnetic tunnel junction structure by reflective high-energy electron diffraction. *Applied Physics Letters*, 87(24):242503, dec 2005. ISSN 0003-6951. doi: 10.1063/1.2140612. URL `http://aip.scitation.org/doi/10.1063/1.2140612`.

[129] H. Jaffrès, D Lacour, F. Nguyen Van Dau, J Briatico, F Petroff, and A. Vaurès. Angular dependence of the tunnel magnetoresistance in transition-metal-based junctions. *Physical Review B*, 64(6):064427, jul 2001. ISSN 0163-1829. doi: 10.1103/PhysRevB.64.064427. URL `https://link.aps.org/doi/10.1103/PhysRevB.64.064427`.

[130] W. H. Meiklejohn and C. P. Bean. New Magnetic Anisotropy. *Physical Review*, 105(3):904–913, feb 1957. ISSN 0031-899X. doi: 10.1103/PhysRev.105.904. URL `https://link.aps.org/doi/10.1103/PhysRev.105.904`.

[131] J Nogués, J Sort, V Langlais, V Skumryev, S Suriñach, J.S. Muñoz, and M.D. Baró. Exchange bias in nanostructures. *Physics Reports*, 422(3):65–117, dec 2005. ISSN 03701573. doi: 10.1016/j.physrep.2005.08.004. URL `http://linkinghub.elsevier.com/retrieve/pii/S0370157305003303`.

[132] J. Hayakawa, S. Ikeda, Y. M. Lee, F. Matsukura, and H. Ohno. Effect of high annealing temperature on giant tunnel magnetoresistance ratio of CoFeB/MgO/CoFeB

magnetic tunnel junctions. *Applied Physics Letters*, 89(23):232510, dec 2006. ISSN 0003-6951. doi: 10.1063/1.2402904. URL `http://aip.scitation.org/doi/10.1063/1.2402904`.

[133] Sarah M Thompson. The discovery, development and future of GMR: The Nobel Prize 2007. *Journal of Physics D: Applied Physics*, 41 (9):093001, may 2008. ISSN 0022-3727. doi: 10.1088/0022-3727/41/9/093001. URL `http://stacks.iop.org/0022-3727/41/i=9/a=093001?key=crossref.e81e7c8f22afb14e30b406657fab7e50`.

[134] Daniel K Schreiber, Young Suk Choi, Yuzi Liu, Ann N Chiaramonti, David N Seidman, and Amanda K. Petford-Long. Effects of elemental distributions on the behavior of MgO-based magnetic tunnel junctions. In *Journal of Applied Physics*, volume 109, page 103909, may 2011. ISBN 0021-8979. doi: 10.1063/1.3583569. URL `http://aip.scitation.org/doi/10.1063/1.3583569`.

[135] M. A. Ruderman and C. Kittel. Indirect Exchange Coupling of Nuclear Magnetic Moments by Conduction Electrons. *Physical Review*, 96(1):99–102, oct 1954. ISSN 0031-899X. doi: 10.1103/PhysRev.96.99. URL `https://link.aps.org/doi/10.1103/PhysRev.96.99`.

[136] Tadao Kasuya. A Theory of Metallic Ferro- and Antiferromagnetism on Zener's Model. *Progress of Theoretical Physics*, 16(1):45–57, jul 1956. ISSN 0033-068X. doi: 10.1143/PTP.16.45. URL `https://academic.oup.com/ptp/article-lookup/doi/10.1143/PTP.16.45`.

[137] Kei Yosida. Magnetic Properties of Cu-Mn Alloys. *Physical Review*, 106(5):893–898, jun 1957. ISSN 0031-899X. doi: 10.1103/PhysRev.106.893. URL `https://link.aps.org/doi/10.1103/PhysRev.106.893`.

[138] Stuart Parkin, Xin Jiang, Christian Kaiser, Alex Panchula, Kevin Roche, and Mahesh Samant. Magnetically engineered spintronic sensors and memory. *Proceedings of the IEEE*, 91(5):661–680, may 2003. ISSN 0018-9219. doi: 10.1109/JPROC.2003.811807. URL `http://ieeexplore.ieee.org/document/1200120/`.

[139] Ke Wang, Zhan Xu, Ya Huang, Yuzhen Qiu, and Shuo Dong. Magnetic, thermal, electrical properties and crystallization kinetics of Co60Fe20B20 alloy films. *Science China Materials*, 59(8):639–647, aug 2016. ISSN 2095-8226. doi: 10.1007/s40843-016-5052-1. URL `http://link.springer.com/10.1007/s40843-016-5052-1`.

[140] T. Okuno, K. Shigeto, T. Ono, K. Mibu, and T. Shinjo. MFM study of magnetic vortex cores in circular permalloy dots: behavior in external field. *Journal of Magnetism and Magnetic Materials*, 240(1-3):1–6, feb 2002. ISSN 03048853. doi: 10.1016/S0304-8853(01)00708-9. URL `http://linkinghub.elsevier.com/retrieve/pii/S0304885301007089`.

[141] Dmitriy Mitin. Advanced scanning magnetoresistive microscopy as a multifunctional magnetic characterization method. *Thesis*, 2016. URL `http://www.qucosa.de/fileadmin/data/qucosa/documents/22498/Dissertation_Dmitriy_Mitin.pdf`.

[142] D. Mitin, M. Grobis, and M. Albrecht. Scanning magnetoresistive microscopy: An advanced characterization tool for magnetic nanosystems. *Review of Scientific Instruments*, 87(2), 2016. ISSN 10897623. doi: 10.1063/1.4941292. URL `http://dx.doi.org/10.1063/1.4941292`.

[143] D Mitin, A Kovacs, T Schrefl, A Ehresmann, D Holzinger, and M Albrecht. Magnetic properties of artificially designed magnetic stray field landscapes in laterally confined exchange-bias layers. *Nanotechnology*, 29(35):355708, aug 2018. ISSN 0957-4484. doi: 10.1088/1361-6528/aacb67. URL `http://stacks.iop.org/0957-4484/29/i=35/a=355708?key=crossref.29de561ada2544e23ed2499997d74ed9`.

[144] K. Shigeto, T. Okuno, K. Mibu, T. Shinjo, and T. Ono. Magnetic force microscopy observation of antivortex core with perpendicular magnetization in patterned thin film of permalloy. *Applied Physics Letters*, 80(22):4190–4192, jun 2002. ISSN 0003-6951. doi: 10.1063/1.1483386. URL `http://aip.scitation.org/doi/10.1063/1.1483386`.

[145] V. Novosad, M. Grimsditch, J. Darrouzet, J. Pearson, S. D. Bader, V. Metlushko, K. Guslienko, Y. Otani, H. Shima, and K. Fukamichi. Shape effect on magnetization reversal in chains of interacting ferromagnetic elements. *Applied Physics Letters*, 82(21):3716–3718, may 2003. ISSN 0003-6951. doi: 10.1063/1.1577808. URL `http://aip.scitation.org/doi/10.1063/1.1577808`.

[146] M. Miyata, K. Kiseki, S. Yakata, H. Wada, and T. Kimura. Formations of magnetic vortices in a chain array of triangle Py dots and an isosceles triangle Py dot. *Journal of Applied Physics*, 111(7):07B902, apr 2012. ISSN 0021-8979. doi: 10.1063/1.3673349. URL `http://aip.scitation.org/doi/10.1063/1.3673349`.

[147] D. V. Berkov, K. Ramstöcck, and A. Hubert. Solving Micromagnetic Problems. Towards an Optimal Numerical Method. *Physica Status Solidi (a)*, 137(1):207–225, may 1993. ISSN 00318965. doi: 10.1002/pssa.2211370118. URL `http://doi.wiley.com/10.1002/pssa.2211370118`.

[148] D Berkov. MicroMagus - software for micromagnetic simulation. 2008. URL `https://www.researchgate.net/publication/271367785_MicroMagus_-_software_for_micromagnetic_simulation`.

[149] Dmitri V. Berkov. Magnetization Dynamics Including Thermal Fluctuations: Basic Phenomenology, Fast Remagnetization Processes and Transitions Over High-energy Barriers. In *Handbook of Magnetism and Advanced Magnetic Materials*. John Wiley and Sons, Ltd, Chichester, UK, dec 2007. ISBN 9780470022184.

doi: 10.1002/9780470022184.hmm204. URL `http://doi.wiley.com/10.1002/9780470022184.hmm204`.

[150] J E Miltat and M J Donahue. Numerical Micromagnetics: Finite Difference Methods. *Handbook of Magnetism and Advanced Magnetic Materials*, pages 1–23, 2007. doi: 10.1002/9780470022184. URL `https://doi.org/10.1002/9780470022184.hmm202`.

[151] Wenyong Wang and Curt A Richter. Magnetic tunnel junctions with self-assembled molecules. *Journal of nanoscience and nanotechnology*, 9(2):1008–10, feb 2009. ISSN 1533-4880. doi: 10.1002/9780470022184. URL `http://doi.wiley.com/10.1002/9780470022184`.

[152] D. Kumar and A. O. Adeyeye. Techniques in micromagnetic simulation and analysis. *Journal of Physics D: Applied Physics*, 50(34):343001, aug 2017. ISSN 0022-3727. doi: 10.1088/1361-6463/aa7c04. URL `http://stacks.iop.org/0022-3727/50/i=34/a=343001?key=crossref.895e826297c2ed97e5e1fb9b8a921392`.

[153] Thomas Schrefl, Gino Hrkac, Simon Bance, Dieter Suess, Otmar Ertl, and Josef Fidler. Numerical Methods in Micromagnetics (Finite Element Method). *Handbook of Magnetism and Advanced Magnetic Materials*, pages 1–30, 2007. doi: 10.1002/9780470022184.hmm203. URL `http://onlinelibrary.wiley.com/doi/10.1002/9780470022184.hmm203/full%5Cnhttp://doi.wiley.com/10.1002/9780470022184.hmm203`.

[154] R. D. McMichael and B. B. Maranville. Edge saturation fields and dynamic edge modes in ideal and non-ideal magnetic film edges. In *INTERMAG 2006 - IEEE International Magnetics Conference*, number June, pages 931–931. IEEE, may 2006. ISBN 1-4244-1479-2. doi: 10.1109/INTMAG.2006.374962. URL `http://ieeexplore.ieee.org/document/4262364/`.

[155] S.-H. Chung, R. D. McMichael, D. T. Pierce, and J. Unguris. Phase diagram of magnetic nanodisks measured by scanning electron microscopy with polarization analysis. *Physical Review B*, 81(2):024410, jan 2010. ISSN 1098-0121. doi: 10.1103/PhysRevB.81.024410. URL `https://link.aps.org/doi/10.1103/PhysRevB.81.024410`.

[156] H. Hoffmann and F. Steinbauer. Single domain and vortex state in ferromagnetic circular nanodots. *Journal of Applied Physics*, 92(9):5463–5467, nov 2002. ISSN 0021-8979. doi: 10.1063/1.1510559. URL `http://aip.scitation.org/doi/10.1063/1.1510559`.

[157] W. Scholz, K.Yu Guslienko, V. Novosad, D. Suess, T. Schrefl, R.W Chantrell, and J. Fidler. Transition from single-domain to vortex state in soft magnetic cylindrical nanodots. *Journal of Magnetism and Magnetic Materials*, 266(1-2):155–163, oct 2003. ISSN 03048853. doi: 10.1016/S0304-8853(03)00466-9. URL `http://linkinghub.elsevier.com/retrieve/pii/S0304885303004669`.

[158] Jonathan Kin Ha, Riccardo Hertel, and J. Kirschner. Micromagnetic study of magnetic configurations in submicron permalloy disks. *Physical Review B*, 67 (22):224432, jun 2003. ISSN 0163-1829. doi: 10.1103/PhysRevB.67.224432. URL `https://link.aps.org/doi/10.1103/PhysRevB.67.224432`.

[159] F. Porrati and M. Huth. Diagram of the states in arrays of iron nanocylinders. *Applied Physics Letters*, 85(15):3157–3159, oct 2004. ISSN 0003-6951. doi: 10.1063/1.1805697. URL `http://aip.scitation.org/doi/10.1063/1.1805697`.

[160] Meng Zhu, Christoph Mathieu, Werner Scholz, Sridhar Dubbaka, and Michael Kautzky. Vortex state formation and stability in single and double layer nanorings and nanodisks. *Journal of Applied Physics*, 113(17):17B905, may 2013. ISSN 0021-8979. doi: 10.1063/1.4798247. URL `http://aip.scitation.org/doi/10.1063/1.4798247`.

[161] J. W. Lau, M. Beleggia, and Y. Zhu. Common reversal mechanisms and correlation between transient domain states and field sweep rate in patterned Permalloy structures. *Journal of Applied Physics*, 102(4):043906, aug 2007. ISSN 0021-8979. doi: 10.1063/1.2769779. URL `http://aip.scitation.org/doi/10.1063/1.2769779`.

[162] S. R. Bakaul, B. L. Wu, G. C. Han, and Y. H. Wu. Probing magnetization reversal process in ferromagnetic disk by superconductor-ferromagnet junction. *Applied Physics Letters*, 97(4):042503, jul 2010. ISSN 0003-6951. doi: 10.1063/1.3463474. URL `http://aip.scitation.org/doi/10.1063/1.3463474`.

[163] Marek Vaňatka, Michal Urbánek, Roman Jíra, Lukáš Flajšman, Meena Dhankhar, Mi-Young Im, Jan Michalička, Vojtěch Uhlĩr, and Tomáš Šikola. Magnetic vortex nucleation modes in static magnetic fields. *AIP Advances*, 7(10):105103, oct 2017. ISSN 2158-3226. doi: 10.1063/1.5006235. URL `http://aip.scitation.org/doi/10.1063/1.5006235`.

[164] Jonathan Kin Ha, Riccardo Hertel, and J. Kirschner. Configurational stability and magnetization processes in submicron permalloy disks. *Physical Review B*, 67 (6):064418, feb 2003. ISSN 0163-1829. doi: 10.1103/PhysRevB.67.064418. URL `https://link.aps.org/doi/10.1103/PhysRevB.67.064418`.

[165] R. Dittrich, T. Schrefl, M. Kirschner, D. Suess, G. Hrkac, F. Dorfbauer, O. Ertl, and J. Fidler. Thermally induced vortex nucleation in permalloy elements. *IEEE Transactions on Magnetics*, 41(10):3592–3594, oct 2005. ISSN 0018-9464. doi: 10.1109/TMAG.2005.854736. URL `http://ieeexplore.ieee.org/document/1519380/`.

[166] J. P. Davis, D. Vick, J. A J Burgess, D. C. Fortin, P. Li, V. Sauer, W. K. Hiebert, and M. R. Freeman. Observation of magnetic supercooling of the transition to the vortex state. *New Journal of Physics*, 12(9):093033, sep 2010. ISSN 1367-2630. doi: 10.1088/1367-2630/12/9/093033. URL `http://stacks.iop.org/1367-2630/12/i=9/a=093033?key=crossref.6bdabfa1b514dab23479a2a8f8e81622`.

[167] P. Ehrenfest. Phasenumwandlungen im ueblichen und erweiterten Sinn, classifiziert nach den entsprechenden Singularitaeten des thermo-dynamischen Potentiales. *Verhandelingen der Koninklijke Akademie van Wetenschappen*, 36(153):157, 1933.

[168] Onuttom Narayan and a. P. Young. Free energies in the presence of electric and magnetic fields. *American Journal of Physics*, 73(4):293–298, apr 2005. ISSN 0002-9505. doi: 10.1119/1.1819934. URL `http://aapt.scitation.org/doi/10.1119/1.1819934`.

[169] Gregg Jaeger. The Ehrenfest Classification of Phase Transitions: Introduction and Evolution. *Archive for History of Exact Sciences*, 53(1):51–81, may 1998. ISSN 0003-9519. doi: 10.1007/s004070050021. URL `http://link.springer.com/10.1007/s004070050021`.

[170] E. R. P. Novais, S. Allende, D. Altbir, P. Landeros, F. Garcia, and A. P. Guimarães. Effect of perpendicular uniaxial anisotropy on the annihilation fields of magnetic vortices. *Journal of Applied Physics*, 114(15):153905, oct 2013. ISSN 0021-8979. doi: 10.1063/1.4824803. URL `http://dx.doi.org/10.1063/1.4824803`.

[171] J. F. Pulecio, S. D. Pollard, P. Warnicke, D. A. Arena, and Y. Zhu. Symmetry breaking of magnetic vortices before annihilation. *Applied Physics Letters*, 105 (13):132403, sep 2014. ISSN 0003-6951. doi: 10.1063/1.4893422. URL `http://aip.scitation.org/doi/10.1063/1.4893422`.

[172] T. Wurft, W. Raberg, K. Prugl, A. Satz, G. Reiss, and H. Bruckl. The Influence of Edge Inhomogeneities on Vortex Hysteresis Curves in Magnetic Tunnel Junctions. *IEEE Transactions on Magnetics*, 53(11):1–5, nov 2017. ISSN 0018-9464. doi: 10.1109/TMAG.2017.2715072. URL `http://ieeexplore.ieee.org/document/7947144/`.

[173] A. Helmer, S. Cornelissen, T. Devolder, J.-V. Kim, W. van Roy, L. Lagae, and C. Chappert. Quantized spin-wave modes in magnetic tunnel junction nanopillars. *Physical Review B*, 81(9):094416, mar 2010. ISSN 1098-0121. doi: 10.1103/PhysRevB.81.094416. URL `https://link.aps.org/doi/10.1103/PhysRevB.81.094416`.

[174] S. Ingvarsson, Gang Xiao, S.S.P Parkin, and W.J Gallagher. Thickness-dependent magnetic properties of Ni81Fe19, Co90Fe10 and Ni65Fe15Co20 thin films. *Journal of Magnetism and Magnetic Materials*, 251(2):202–206, oct 2002. ISSN 03048853. doi: 10.1016/S0304-8853(02)00577-2. URL `http://linkinghub.elsevier.com/retrieve/pii/S0304885302005772`.

[175] Ricardo Ferré. Large scale micromagnetic calculations for finite and infinite 3Dferromagnetic systems using FFT. *Computer Physics Communications*, 105(2-3): 169–186, oct 1997. ISSN 00104655. doi: 10.1016/S0010-4655(97)00072-6. URL `http://linkinghub.elsevier.com/retrieve/pii/S0010465597000726`.

[176] Gavin S. Abo, Yang-Ki Hong, Jihoon Park, Jaejin Lee, Woncheol Lee, and Byoung-Chul Choi. Definition of Magnetic Exchange Length. *IEEE Transactions on Magnetics*, 49(8):4937–4939, aug 2013. ISSN 0018-9464. doi: 10.1109/TMAG.2013.2258028. URL `http://ieeexplore.ieee.org/document/6497624/`.

[177] Thomas Uhlig, M. Rahm, Christian Dietrich, Rainer Höllinger, Martin Heumann, Dieter Weiss, and Josef Zweck. Shifting and Pinning of a Magnetic Vortex Core in a Permalloy Dot by a Magnetic Field. *Physical Review Letters*, 95(23):237205, nov 2005. ISSN 0031-9007. doi: 10.1103/PhysRevLett.95.237205. URL `https://link.aps.org/doi/10.1103/PhysRevLett.95.237205`.

[178] A.K. Petford-Long and J.N. Chapman. *Magnetic Microscopy of Nanostructures*. NanoScience and Technology. Springer Berlin Heidelberg, Berlin, Heidelberg, 2005. ISBN 978-3-540-40186-5. doi: 10.1007/b137837. URL `http://link.springer.com/10.1007/b137837`.

[179] Yuan-Tsung Chen, Jiun-Yi Tseng, Tzer-Shin Sheu, Y.C. Lin, and S.H. Lin. Effect of grain size on magnetic properties and microstructure of Ni80Fe20 thin films. *Thin Solid Films*, 544:602–605, oct 2013. ISSN 00406090. doi: 10.1016/j.tsf.2012.12.058. URL `http://dx.doi.org/10.1016/j.tsf.2012.12.058`.

[180] Weisheng Zhao, Xiaoxuan Zhao, Boyu Zhang, Kaihua Cao, Lezhi Wang, Wang Kang, Qian Shi, Mengxing Wang, Yu Zhang, You Wang, Shouzhong Peng, Jacques-Olivier Klein, Lirida de Barros Naviner, and Dafine Ravelosona. Failure Analysis in Magnetic Tunnel Junction Nanopillar with Interfacial Perpendicular Magnetic Anisotropy. *Materials*, 9(1):41, jan 2016. ISSN 1996-1944. doi: 10.3390/ma9010041. URL `http://www.mdpi.com/1996-1944/9/1/41`.

[181] J. W. Lau, R. D. McMichael, M. A. Schofield, and Y. Zhu. Correlation of edge roughness to nucleation field and nucleation field distribution in patterned Permalloy elements. *Journal of Applied Physics*, 102(2):023916, jul 2007. ISSN 0021-8979. doi: 10.1063/1.2761850. URL `http://aip.scitation.org/doi/10.1063/1.2761850`.

[182] C. A.F. Vaz, C Athanasiou, J. A.C. Bland, and G. Rowlands. Energetics of magnetic ring and disk elements: Uniform versus vortex state. *Physical Review B - Condensed Matter and Materials Physics*, 73(5):054411, feb 2006. ISSN 10980121. doi: 10.1103/PhysRevB.73.054411. URL `https://link.aps.org/doi/10.1103/PhysRevB.73.054411`.

[183] Robert D. McMichael, C. A. Ross, and Vivian P. Chuang. Thickness dependence of magnetic film edge properties in Ni80Fe20 stripes. *Journal of Applied Physics*, 103(7):07C505, 2008. ISSN 00218979. doi: 10.1063/1.2833314. URL `http://scitation.aip.org/content/aip/journal/jap/103/7/10.1063/1.2833314`.

[184] P. Schiffer and D. D. Osheroff. Nucleation of the AB transition in superfluid 3He: Surface effects and baked Alaska. *Reviews of Modern Physics*, 67(2):491–501, apr 1995. ISSN 0034-6861. doi: 10.1103/RevModPhys.67.491. URL `https://link.aps.org/doi/10.1103/RevModPhys.67.491`.

[185] D. Meyners, H. Brückl, and G. Reiss. Influence of boundary roughness on the magnetization reversal in submicron sized magnetic tunnel junctions. *Journal of Applied Physics*, 93(5):2676–2680, mar 2003. ISSN 0021-8979. doi: 10.1063/1.1544424. URL `http://aip.scitation.org/doi/10.1063/1.1544424`.

[186] Jason Gadbois and Jian-Gang Zhu. Effect of edge roughness in nano-scale magnetic bar switching. *IEEE Transactions on Magnetics*, 31(6):3802–3804, 1995. ISSN 00189464. doi: 10.1109/20.489777. URL `http://ieeexplore.ieee.org/document/489777/`.

[187] Serban Lepadatu. Effective field model of roughness in magnetic nano-structures. *Journal of Applied Physics*, 118(24):243908, dec 2015. ISSN 0021-8979. doi: 10.1063/1.4939093. URL `http://aip.scitation.org/doi/10.1063/1.4939093`.

[188] A R Wazzan, A Bristoti, L B Robinson, and A Ahmedieh. Temperature dependence of the single-crystal elastic constants of Co-rich Co-Fe alloys. *Journal of Applied Physics*, 44(5):2018–2024, may 1973. ISSN 0021-8979. doi: 10.1063/1.1662508. URL `http://aip.scitation.org/doi/10.1063/1.1662508`.

[189] J. M. Leger, C. Loriers-Susse, and B. Vodar. Pressure Effect on the Curie Temperatures of Transition Metals and Alloys. *Physical Review B*, 6(11):4250–4261, dec 1972. ISSN 0556-2805. doi: 10.1103/PhysRevB.6.4250. URL `https://link.aps.org/doi/10.1103/PhysRevB.6.4250`.

[190] CHIH-WEN CHEN. METALLURGY OF SOFT MAGNETIC MATERIALS. In *Magnetism and Metallurgy of Soft Magnetic Materials*, volume 1161, pages 171–367. Elsevier, 1977. doi: 10.1016/B978-0-7204-0706-8.50012-5. URL `http://linkinghub.elsevier.com/retrieve/pii/B9780720407068500125`.

[191] J. F. Sierra, V. V. Pryadun, S. E. Russek, M. García-Hernández, F. Mompean, R. Rozada, O. Chubykalo-Fesenko, E. Snoeck, G. X. Miao, J. S. Moodera, and F. G. Aliev. Interface and Temperature Dependent Magnetic Properties in Permalloy Thin Films and Tunnel Junction Structures. *Journal of Nanoscience and Nanotechnology*, 11(9):7653–7664, sep 2011. ISSN 15334880. doi: 10.1166/jnn.2011.4754. URL `http://www.ingentaconnect.com/content/asp/jnn/2011/00000011/00000009/art00014`.

[192] C A Neugebauer. Temperature dependence of the saturation magnetization of nickel films of thickness less than 100A. *Journal of Applied Physics*, 31(5):S152–S153, may 1960. ISSN 00218979. doi: 10.1063/1.1984641. URL `http://aip.scitation.org/doi/10.1063/1.1984641`.

[193] G. Mihajlović, M. S. Patrick, J. E. Pearson, V. Novosad, S. D. Bader, M. Field, G. J. Sullivan, and A. Hoffmann. Temperature dependent nucleation and annihilation of individual magnetic vortices. *Applied Physics Letters*, 96(11):112501, mar 2010. ISSN 0003-6951. doi: 10.1063/1.3360841. URL `http://aip.scitation.org/doi/10.1063/1.3360841`.

[194] Tiago S. Machado, Tatiana G. Rappoport, and Luiz C. Sampaio. Vortex core magnetization dynamics induced by thermal excitation. *Applied Physics Letters*, 100(11):112404, mar 2012. ISSN 0003-6951. doi: 10.1063/1.3694757. URL `http://aip.scitation.org/doi/10.1063/1.3694757`.

[195] G. N. Kakazei, M. Ilyn, O. Chubykalo-Fesenko, J. Gonzalez, A. A. Serga, A. V. Chumak, P. A. Beck, B. Laegel, B. Hillebrands, and K. Y. Guslienko. Slow magnetization dynamics and energy barriers near vortex state nucleation in circular permalloy dots. *Applied Physics Letters*, 99(5):052512, aug 2011. ISSN 0003-6951. doi: 10.1063/1.3619846. URL `http://aip.scitation.org/doi/10.1063/1.3619846`.

[196] Mathias. Getzlaff. *Fundamentals of magnetism.* Springer, 2010. ISBN 9783642068270. URL `https://www.springer.com/de/book/9783540311508`.

[197] Wolfgang Raberg and Tobias Wurft. Magnetic sensor device and method for a magnetic sensor device having a magneto-resistive structure. *U.S. Patent*, US20170168, 2015. URL `https://patents.google.com/patent/US20170168122`.

[198] D. GIVORD, M. F. ROSSIGNOL, and D. W. TAYLOR. Coercivity mechanisms in hard magnetic materials. *Le Journal de Physique IV*, 02(C3):C3–95–C3–104, dec 1992. ISSN 1155-4339. doi: 10.1051/jp4:1992314. URL `http://www.edpsciences.org/10.1051/jp4:1992314`.

[199] Weiqing Fang, Ioannis Panagiotopoulos, Frédéric Ott, François Boué, Kahina Ait-Atmane, Jean-Yves Piquemal, Guillaume Viau, and Florent Dalmas. Optimization of the magnetic properties of aligned Co nanowires/polymer composites for the fabrication of permanent magnets. *Journal of Nanoparticle Research*, 16(2):2265, feb 2014. ISSN 1388-0764. doi: 10.1007/s11051-014-2265-x. URL `http://link.springer.com/10.1007/s11051-014-2265-x`.

[200] J. P. Davis, J. Pollanen, B. Reddy, K. R. Shirer, H. Choi, and W. P. Halperin. Stability of the axial phase of superfluid 3He in aerogel with globally anisotropic scattering. *Physical Review B*, 77(14):140502, apr 2008. ISSN 1098-0121. doi: 10.1103/PhysRevB.77.140502. URL `https://link.aps.org/doi/10.1103/PhysRevB.77.140502`.

[201] J. P. Davis, D. Vick, D. C. Fortin, J. A J Burgess, W. K. Hiebert, and M. R. Freeman. Nanotorsional resonator torque magnetometry. *Applied Physics Letters*,

96(7):072513, feb 2010. ISSN 0003-6951. doi: 10.1063/1.3319502. URL `http://aip.scitation.org/doi/10.1063/1.3319502`.